

REPORT DOCUMENTATION PAGE		READ INSTRUCTIONS BEFORE COMPLETING FORM
1. REPORT NUMBER Report 4	2. GOVT ACCESSION NO.	3. RECIPIENT'S CATALOG NUMBER
4. TITLE (and Subtitle) Turbulent Flow Over Small Amplitude Solid Waves		5. TYPE OF REPORT & PERIOD COVERED Technical
		6. PERFORMING ORG. REPORT NUMBER
7. AUTHOR(s) Jonathan Abrams and Thomas J. Hanratty, Project Supervisor		8. CONTRACT OR GRANT NUMBER(s) N00014-88-82-K-0324
9. PERFORMING ORGANIZATION NAME AND ADDRESS Department of Chemical Engineering University of Illinois Urbana, Illinois 61801		10. PROGRAM ELEMENT, PROJECT, TASK AREA & WORK UNIT NUMBERS NR 657-728
11. CONTROLLING OFFICE NAME AND ADDRESS Office of Naval Research Fluid Dynamics Program - Dr. M. M. Reischman Arlington, VA 22217		12. REPORT DATE January, 1984
		13. NUMBER OF PAGES 261
14. MONITORING AGENCY NAME & ADDRESS (if different from Controlling Office)		15. SECURITY CLASS. (of this report) Unclassified
		15a. DECLASSIFICATION/DOWNGRADING SCHEDULE
16. DISTRIBUTION STATEMENT (of this Report) Approved for distribution unlimited public release		
17. DISTRIBUTION STATEMENT (of the abstract entered in Block 20, if different from Report)		
18. SUPPLEMENTARY NOTES		
19. KEY WORDS (Continue on reverse side if necessary and identify by block number) turbulence, waves		
20. ABSTRACT (Continue on reverse side if necessary and identify by block number) see reverse side		

TURBULENT FLOW OVER SMALL AMPLITUDE SOLID WAVES

Measurements have been made of the variation of wall shear stress and of the root mean square level of the fluctuating shear stress along a solid wavy surface with an amplitude of 0.014 in. and a wavelength of 2 in.

The phase angle associated with the spatial variation of the wave induced shear stress passes through a well defined maximum when measured as a function of the dimensionless wave number, $\alpha = 2\pi v/\lambda u^*$. The measurements of the wall shear stress and in particular the location of this maximum provide an extremely sensitive test of turbulence models which pay particular attention to the viscous wall region.

The use of a quasi-laminar assumption, whereby the wave induced changes of the Reynolds stresses are ignored gives good agreement with the measurements of the variation of the wall shear stress for large values of α . An equilibrium turbulence assumption in which the wave induced Reynolds stresses are assumed to adjust instantaneously to changes in flow conditions along the wave surface is valid for only small values of α . In the range of $5 \times 10^{-4} < \alpha < 0.2$ it is necessary to use a model for the wave induced Reynolds stresses which takes account of the fact that the turbulence does not respond immediately to changes in the flow conditions. The mixing length model of Loyd et al. [42] provides the best fit of the data. A modification of this model which takes into account the effect of streamline curvature on the mixing length, as suggested by Bradshaw [8], is shown to provide an improved fit of the available pressure measurements over a wavy surface.

TURBULENT FLOW OVER SMALL AMPLITUDE SOLID WAVES

LIBRARY
RESEARCH REPORTS DIVISION
NAVAL POSTGRADUATE SCHOOL
MONTEREY, CALIFORNIA 93943

PREPARED BY
JONATHAN ABRAMS
THOMAS J. HANRATTY, PROJECT SUPERVISOR
FOR
THE OFFICE OF NAVAL RESEARCH, ARLINGTON, VA 22217
CONTRACT N00014-88-82-K-0324
PROJECT NR 657-728



REPORT 4

DEPARTMENT OF CHEMICAL ENGINEERING

UNIVERSITY OF ILLINOIS

URBANA, ILLINOIS

61801

JANUARY 1984

APPROVED FOR PUBLIC RELEASE, DISTRIBUTION UNLIMITED

TURBULENT FLOW OVER SMALL AMPLITUDE SOLID WAVES

Prepared by

Jonathan Abrams
Thomas J. Hanratty, Project Supervisor

for

The Office of Naval Research, Arlington, VA 22217
Contract N00014-88-K-0324
Project NR 657-728

Report 4

Department of Chemical Engineering
University of Illinois
Urbana, Illinois
61801

January, 1984

Approved for public release, distribution unlimited

TABLE OF CONTENTS

<u>Chapter</u>		<u>Page</u>
1	INTRODUCTION.....	1
2	LITERATURE.....	5
	(a) Effects of Pressure Gradient and Curvature.....	5
	(b) Models for Flow Over Wavy Surfaces.....	8
3	THEORY.....	11
	(a) Coordinate System and Basic Equations.....	11
	(b) Linearized Equations.....	14
	(c) Models for Turbulent Stresses.....	19
	c.1 Constant Reynolds Stress Assumption Model A.....	19
	c.2 Zero Equation Models.....	21
	c.3 K- ϵ Model.....	27
	(d) Streamline Curvature.....	33
	(e) Finite Boundary Layer Calculation.....	35
	e.1 Mean Flow.....	35
	e.2 Eddy Viscosity.....	36
4	EXPERIMENTAL MEASUREMENTS AND RESULTS.....	38
	(a) Flow Loop.....	39
	(b) Test Section.....	43
	(c) Electrochemical Technique.....	51
	(d) Data Acquisition.....	55
	(e) Shear Stress Measurements.....	58
5	NUMERICAL ANALYSIS.....	91
	(a) Numerical Solution of the Wave Induced Flow.....	94

<u>Chapter</u>	<u>Page</u>
	(b) Orthonormalization Procedure..... 100
	(c) Gram-Schmidt Orthogonalization Procedure..... 104
	(d) Numerical Solution of the Mean Energy and Mean Dissipation Equations..... 108
6	RESULTS..... 114
	(a) Quasi-Laminar Model: Model A..... 114
	(b) Model C*..... 115
	(c) Equilibrium Turbulence Model..... 124
	(d) Model D* and Relaxation Turbulence Model..... 133
	(e) K- ϵ Model..... 142
	(f) Curvature Effects..... 160
7	DISCUSSION OF RESULTS..... 176
 APPENDIX	
A	CONDITIONS FOR LINEARITY..... 183
B	FORMULATION OF OUTER BOUNDARY CONDITION..... 185
C	DERIVATION OF TURBULENT ENERGY AND DISSIPATION EQUATIONS..... 188
D	DERIVATION OF STREAMLINE CURVATURE..... 194
E	FINITE BOUNDARY LAYER CALCULATION..... 199
F	TABULATED DATA..... 205
G	ELECTROCHEMICAL MEASUREMENTS..... 227
H	ANALYSIS OF RAW DATA..... 229
I	LEAST SQUARES ANALYSIS..... 232
J	CORRECTION OF INTENSITY DATA..... 234
K	NUMERICAL FORMULATION OF WAVE INDUCED EQUATIONS..... 237

APPENDIX

Page

L	RELATIONSHIP BETWEEN TURBULENT ENERGY AND VELOCITY GRADIENT AT THE WAVE SURFACE.....	248
	NOMENCLATURE.....	251
	REFERENCES.....	256
	VITA.....	262

LIST OF TABLES

<u>Table</u>		<u>Page</u>
F.1.	Wave Profile Measurements.....	206
F.2.	Summary of Average Shear Stress Measurements.....	207
F.3.	Summary of Average Shear Stress Measurements.....	208
F.4.	Summary of Average Shear Stress Measurements.....	209
F.5.	Summary of Average Shear Stress Measurements.....	210
F.6.	Summary of Fluctuating Shear Stress Measurements.....	211
F.7.	Average Shear Stress Measurements.....	212
F.8.	Average Shear Stress Measurements.....	213
F.9.	Average Shear Stress Measurements.....	214
F.10.	Average Shear Stress Measurements.....	215
F.11.	Average Shear Stress Measurements.....	216
F.12.	Average Shear Stress Measurements.....	217
F.13.	Average Shear Stress Measurements.....	218
F.14.	Average Shear Stress Measurements.....	219
F.15.	Average Shear Stress Measurements.....	220
F.16.	Average Shear Stress Measurements.....	221
F.17.	Average Shear Stress Measurements.....	222
F.18.	Average Shear Stress Measurements.....	223
F.19.	Fluctuating Shear Stress Measurements.....	224
F.20.	Fluctuating Shear Stress Measurements.....	225
F.21.	Fluctuating Shear Stress Measurements.....	226
G.1.	Physical and Chemical Properties of Electrolyte.....	228
J.1.	Correction of Fluctuating Shear Stress Measurements....	235
J.2.	Correction of Fluctuating Shear Stress Measurements....	236

LIST OF FIGURES

<u>Figure</u>		<u>Page</u>
3.1.	Boundary Layer Coordinate System.....	12
4.1.	Schematic Diagram of Flow Loop.....	41
4.2.	Photograph of Pumping Network.....	42
4.3.	Cross Sectional View of Cutting Tool.....	44
4.4.	Cross Sectional View of End Cutting Tool.....	44
4.5.	Cross Sectional View of Wave Surface.....	45
4.6.	Electrode Pattern.....	47
4.7.	Profile of Wave 6.....	48
4.8.	Profile of Wave 8.....	49
4.9.	Profile of Wave 9.....	50
4.10.	Photograph of Front View of Wave Section.....	52
4.11.	Photograph of Back View of Wave Section.....	53
4.12.	Electronic Circuit for Shear Stress Measurements.....	56
4.13.	Schematic Diagram of Data Acquisition System.....	57
4.14.	Shear Stress Distribution for $Re = 5,970$	59
4.15.	Shear Stress Distribution for $Re = 6,680$	60
4.16.	Shear Stress Distribution for $Re = 8,450$	61
4.17.	Shear Stress Distribution for $Re = 9,650$	62
4.18.	Shear Stress Distribution for $Re = 13,000$	63
4.19.	Shear Stress Distribution for $Re = 14,600$	64
4.20.	Shear Stress Distribution for $Re = 15,700$	65
4.21.	Shear Stress Distribution for $Re = 19,800$	66
4.22.	Shear Stress Distribution for $Re = 20,600$	67
4.23.	Shear Stress Distribution for $Re = 27,950$	68

<u>Figure</u>		<u>Page</u>
4.24.	Shear Stress Distribution for $Re = 30,620$	69
4.25.	Shear Stress Distribution for $Re = 34,700$	70
4.26.	Shear Stress Distribution for $Re = 36,000$	71
4.27.	Shear Stress Distribution for $Re = 58,000$	72
4.28.	Shear Stress Distribution for $Re = 64,000$	73
4.29.	Shear Stress Distribution for $Re = 71,000$	74
4.30.	Shear Stress Distribution for $Re = 73,500$	75
4.31.	Shear Stress Distribution for $Re = 84,500$	76
4.32.	Shear Stress Distribution for $Re = 102,500$	77
4.33.	Shear Stress Distribution for $Re = 114,500$	78
4.34.	Shear Stress Distribution for $Re = 122,500$	79
4.35.	Fluctuating Shear Stress Distribution for $Re = 6,680$	80
4.36.	Fluctuating Shear Stress Distribution for $Re = 8,450$	81
4.37.	Fluctuating Shear Stress Distribution for $Re = 9,650$	82
4.38.	Fluctuating Shear Stress Distribution for $Re = 13,000$	83
4.39.	Fluctuating Shear Stress Distribution for $Re = 15,700$	84
4.40.	Fluctuating Shear Stress Distribution for $Re = 19,800$	85
4.41.	Phase Angle of Average Shear Stress Measurements as a Function of Reynolds Number.....	87
4.42.	Amplitude of Average Shear Stress Measurements as a Function of Reynolds Number.....	88
4.43.	Phase Angle of Fluctuating Shear Stress Measurements as a Function of Reynolds Number.....	89
4.44.	Amplitude of Fluctuating Shear Stress Measurements as a Function of Reynolds Number.....	90

<u>Figure</u>		<u>Page</u>
5.1.	Grid Used for Integrating Mean K-ε Model Equations.....	110
6.1.	$ \hat{\tau}(o) $ for Quasi-Laminar Model.....	116
6.2.	$\hat{\tau}(o)$ Phase Angle for Quasi-Laminar Model.....	117
6.3.	Real $(\hat{u} e^{i\alpha x})$ for Quasi-Laminar Model for $\alpha = 0.1$	118
6.4.	Real $(\hat{u} e^{i\alpha x})$ for Quasi-Laminar Model for $\alpha = 0.01$	119
6.5.	Real $(\hat{u} e^{i\alpha x})$ for Quasi-Laminar Model for $\alpha = 0.0045$	120
6.6.	Real $(\hat{u} e^{i\alpha x})$ for Quasi-Laminar Model for $\alpha = 0.001$	121
6.7.	$ \hat{p}(o) $ for Quasi-Laminar Model.....	122
6.8.	$\hat{p}(o)$ Phase Angle for Quasi-Laminar Model.....	123
6.9.	$ \hat{\tau}(o) $ for Model C*.....	125
6.10.	$\hat{\tau}(o)$ Phase Angle for Model C*.....	126
6.11.	$\hat{p}(o)$ Phase Angle for Model C*.....	127
6.12.	$ \hat{p}(o) $ for Model C*.....	128
6.13.	Real $(\hat{u} e^{i\alpha x})$ for Model C* for $\alpha = 0.01$	129
6.14.	Real $(\hat{u} e^{i\alpha x})$ for Model C* for $\alpha = 0.0045$	130
6.15.	Real $(\hat{u} e^{i\alpha x})$ for Model C* for $\alpha = 0.001$	131
6.16.	$\hat{\tau}(o)$ Phase Angle for Equilibrium Turbulence Model for Different Values of k_1	132
6.17.	$\hat{\tau}(o)$ Phase Angle for Model D* for $k_1 = -35$ and $k_L = 1800$	134
6.18.	$ \hat{\tau}(o) $ for Model D* for $k_1 = -35$ and $k_L = 1800$	135
6.19.	$\hat{p}(o)$ Phase Angle for Model D* for $k_1 = -35$ and $k_L = 1800$	136
6.20.	$ \hat{p}(o) $ for Model D* for $k_1 = -35$ and $k_L = 1800$	137
6.21.	Real $(\hat{u} e^{i\alpha x})$ for Model D* for $k_1 = -35$, $k_L = 1800$ and $\alpha = 0.01$	138

<u>Figure</u>	<u>Page</u>
6.22. Real ($\hat{u} e^{i\alpha x}$) for Model D* for $k_1 = -35$, $k_L = 1800$ and $\alpha = 0.0045$	139
6.23. Real ($\hat{u} e^{i\alpha x}$) for Model D* for $k_1 = -35$, $k_L = 1800$ and $\alpha = 0.001$	140
6.24. Real ($\hat{u} e^{i\alpha x}$) For Model D* for $k_1 = -35$, $k_L = 1800$ and $\alpha = 0.0006$	141
6.25. $\hat{\tau}(o)$ Phase Angle for Relaxation Model for $k_1 = -20$ and $k_R = 4200$	143
6.26. $ \hat{\tau}(o) $ for Relaxation Model for $k_1 = -20$ and $k_R = 4200$	144
6.27. Effect of k_1 and k_R on $\hat{\tau}(o)$ Phase Angle for Relaxation Model.....	145
6.28. Effect of k_1 and k_R on $ \hat{\tau}(o) $ for Relaxation Model.....	146
6.29. $\hat{p}(o)$ Phase Angle for Relaxation Model for $k_1 = -20$ and $k_R = 4200$	147
6.30. $ \hat{p}(o) $ for Relaxation Model for $k_1 = -20$ and $k_R = 4200$	148
6.31. Real ($\hat{u} e^{i\alpha x}$) for Relaxation Model for $k_1 = -20$, $k_R = 4200$ and $\alpha = 0.01$	149
6.32. Real ($\hat{u} e^{i\alpha x}$) for Relaxation Model for $k_1 = -20$, $k_R = 4200$ and $\alpha = 0.0045$	150
6.33. Real ($\hat{u} e^{i\alpha x}$) for Relaxation Model for $k_1 = -20$, $k_R = 4200$ and $\alpha = 0.001$	151
6.34. Real ($\hat{u} e^{i\alpha x}$) for Relaxation Model for $k_1 = -20$, $k_R = 4200$ and $\alpha = 0.0006$	152
6.35. Mean Velocity Profile for K- ϵ Model.....	153
6.36. Mean Energy Profile for K- ϵ Model.....	154
6.37. Mean Dissipation Profile for K- ϵ Model.....	155
6.38. $\hat{\tau}(o)$ Phase Angle for K- ϵ Model.....	156
6.39. $ \hat{\tau}(o) $ for K- ϵ Model.....	157
6.40. $\hat{p}(o)$ Phase Angle for K- ϵ Model.....	158

<u>Figure</u>	<u>Page</u>
6.41. $ \hat{p}(o) $ for K- ϵ Model.....	159
6.42. $\hat{k}(o)$ Phase Angle for K- ϵ Model.....	161
6.43. $ \hat{k}(o) $ for K- ϵ Model.....	162
6.44. $\hat{p}(o)$ Phase Angle for Model C* for Different Values of β_c	163
6.45. $ \hat{p}(o) $ for Model C* for Different Values of β_c	164
6.46. $\hat{\tau}(o)$ Phase Angle for Model C* for Different Values of β_c	165
6.47. $ \hat{\tau}(o) $ for Model C* for Different Values of β_c	166
6.48. $\hat{p}(o)$ Phase Angle for Model C* for $\beta_c = 6$ and Different Values of k_c	168
6.49. $ \hat{p}(o) $ for Model C* for $\beta_c = 6$ and Different Values of k_c	169
6.50. $\hat{\tau}(o)$ Phase Angle for Model C* for $\beta_c = 6$ and Different Values of k_c	170
6.51. $ \hat{\tau}(o) $ for Model C* for $\beta_c = 6$ and Different Values of k_c	171
6.52. $\hat{\tau}(o)$ Phase Angle for Model D* for $k_1 = -30$, $k_L = 1550$, $\beta_c = 2$ and $k_c = 0$	172
6.53. $ \hat{\tau}(o) $ for Model D* for $k_1 = -30$, $k_L = 1550$, $\beta_c = 2$ and $k_c = 0$	173
6.54. $\hat{p}(o)$ Phase Angle for Model D* for $k_1 = -30$, $k_L = 1550$, $\beta_c = 2$ and $k_c = 0$	174
6.55. $ \hat{p}(o) $ for Model D* for $k_1 = -30$, $k_L = 1550$, $\beta_c = 2$ and $k_c = 0$	175
7.1. Comparison of Several Calculation Models with the Data for Shear Stress Phase Angle.....	177
7.2. Comparison of Several Calculation Models with the Data for Shear Stress Amplitude.....	178
7.3. Comparison of Phase Angle of Pressure Gradient and Effective Pressure Gradient for Model D*.....	179

<u>Figure</u>	<u>Page</u>
7.4. Comparison of Predicted Phase Angle of $\hat{p}(o)$ Model D* With and Without Curvature Correction.....	181
B.1. Diagram for Development of Outer Boundary Condition.....	186
E.1. Effect of Finite Boundary Layer Thickness on $\hat{\tau}(o)$ Phase Angle for Model D* $k_1 = -35$ and $k_L = 1800$	201
E.2. Effect of Finite Boundary Layer Thickness on $ \hat{\tau}(o) $ for Model D* $k_1 = -35$ and $k_L = 1800$	202
E.3. Effect of Finite Boundary Layer Thickness on $\hat{p}(o)$ Phase Angle for Model D* $k_1 = -35$ and $k_L = 1800$	203
E.4. Effect of Finite Boundary Layer Thickness on $ \hat{p}(o) $ for Model D* $k_1 = -35$ and $k_L = 1800$	204

CHAPTER 1

INTRODUCTION

When a turbulent fluid interacts with a sinusoidal solid wave spatial variations of the pressure and the shear stress occur at the surface. If the wave is of small enough amplitude a linear response can be expected in that the hydrodynamic quantities can be described by single harmonics with characteristic phases and amplitudes. The analysis for this case is, therefore, greatly simplified. The principal theoretical problem is the determination of the Reynolds stresses close to the surface. In previous studies by Cook [15] and Thorsness [70] it was shown that the phase angle associated with the spatial variation of the surface shear stress provides a particularly sensitive test of the theory used.

The primary purpose of this thesis is to obtain surface shear stress measurements for turbulent flow over small amplitude solid waves, over a wide range of conditions and to compare these measurements in a meaningful way with predictions derived from various turbulence models. These measurements provide a particularly sensitive test of current turbulence models in the neighborhood of a solid boundary. The results find application in understanding the generation of water waves at a gas liquid interface.

Various attempts have been made to measure surface shear stress and pressure profiles over a solid wavy surface. Motzfield [49], Larras and Claria [36] and Zagustin et al. [76] measured pressure profiles. Their measurements indicate a linear response for amplitude, a_d , to wavelength, λ , ratios of $2 a_d/\lambda \leq 0.05$. Kendall [34], who was concerned mainly with moving

waves, made a limited number of pressure and shear stress measurements at zero wave speed. A wave of $\lambda = 4$ inches and $2 a_d/\lambda = 0.062$ was used in this study. Sigal [65], using two geometrically similar waves with $2 a_d/\lambda = 0.055$ and wavelengths of 6 and 12 inches, measured both surface shear stress and pressure profiles. Hsu and Kennedy [26] carried out a similar set of experiments to Sigal using waves of $2 a_d/\lambda = 0.022$ and 0.044 on the wall of a pipe. In this laboratory Zilker [77] and Cook [15] used electrochemical techniques to determine shear stress profiles over waves with $2 a_d/\lambda = 0.0312, 0.05, 0.125$ and 0.2 and a wavelength of $\lambda = 2$ inches. The major limitation of the above measurements, with the exception of the shear stress measurements of Zilker and Cook, is that they were not carried out over a large enough range of flow conditions to be suitable for testing solutions of the momentum equations. Another limitation is that the height of the waves was such that the appearance of higher order harmonics in the shear stress profiles made comparison of these measurements with linear theory difficult.

Thorsness [70] and Morrisroe [48] obtained a set of shear stress measurements using a wave surface with $2 a_d/\lambda = 0.012$ and a wavelength, $\lambda = 2$ inches. These experiments provide the first detailed set of measurements appropriate for testing models of the wave induced variation of the Reynolds stress.

The analysis carried out by Thorsness indicates that for thick boundary layers the phase angle characterizing the shear stress variation is a unique function of a wave number, $\alpha = 2\pi\nu/\lambda u^*$, made dimensionless with the kinematic viscosity, ν , and the friction velocity, u^* . The amplitude of the shear stress variation, made dimensionless using ν and u^* , is found to vary linearly with $a = \alpha u^*/\nu$. The ratio of this

dimensionless amplitude to α is a unique function of α . A major limitation of the measurements of Thorsness is that they were obtained in a range of α which was not entirely suitable to discriminate amongst various turbulence models. Analysis suggests that the variation of the shear stress phase angle passes through a well defined maximum and that the prediction of this maximum should provide a sensitive test of turbulence models. The experiments performed in this research are an improvement over the work of Thorsness in that they covered a wide enough range of α to determine this maximum. This was accomplished by using the same wavelength, solid waves of $\lambda = 2$ inches, and by increasing the maximum value of u^* by a factor of four.

Many turbulence models use the kinetic energy of the turbulence fluctuations as a primary variable in estimating the Reynolds stress. Very few measurements are available of this quantity close to a solid surface. This lack of experimental data makes the evaluation of these models more difficult. Therefore, additional experiments were carried out to determine the streamwise component of the turbulent kinetic energy at the wave surface.

The measurements of the time average shear stress and root mean square value of the fluctuations were obtained in a rectangular channel two inches high and twenty four inches wide. The measurements were obtained utilizing an electrochemical technique developed in this laboratory by Reis [57], Mitchell and Hanratty [58] and Cook [15]. This technique makes use of an electrochemical solution as the transducing medium. The solution flowed over a train of eleven waves comprising the bottom wall of the test section. Each wave had an amplitude of 0.014 inches and a wavelength of 2 inches.

The presence of waves on the solid surface causes differences in the turbulence properties from what would exist for turbulent flow over a flat plate. This is due to the wave induced pressure variations and the wave induced curvature of the streamlines. A periodic pressure variation occurs along the wave surface due to the compression of the streamlines at the wave crest and the rarefaction of the streamlines at the wave trough. Experimental studies of Jones and Launder [32] and Anderson, Kays and Moffat [3] have shown that these negative and positive pressure gradients lead respectively to a damping and enhancement of the turbulence. Similarly the alternating positive and negative curvature of the streamlines can also lead to alternating enhancement and damping of the turbulence. The problem of predicting the influence of a wavy surface on the turbulence is further complicated in that the turbulence does not adjust instantaneously to the change in the pressure gradient and the streamline curvature.

Two approaches are explored to evaluate the Reynolds stress. The first is an extension of Thorsness [70] Model D in which he applied the ideas of Loyd, Moffat and Kays [42] mixing length theory to flow over waves. The second is a modification of the Jones and Launder [31] K- ϵ Model.

The advantage of the Loyd et al. mixing length approach is the simple manner in which the effects of the pressure gradient, streamline curvature and the relaxation can be taken into account. The disadvantage of this approach is the ad hoc manner in which the relaxation effects are introduced. The K- ϵ Model avoids the arbitrary approach of introducing relaxation phenomena by solving transport equations for the turbulence properties which define the turbulent viscosity.

CHAPTER 2

LITERATURE

(a) Effects of Pressure Gradient and Curvature

Experiments carried out in order to understand the effects of pressure gradient and streamline curvature on a turbulent boundary layer have led to the development of turbulence models which have been applied to flow over wavy surfaces. A short review of these experiments, the models developed, and their applications is also presented.

An extensive review of momentum and thermal boundary layers subject to pressure gradients and transpiration has been given by Kays and Moffat [33]. Jones [28], Launder and Stinchcombe [37], Badri Narayanan and Ramjee [4], Julien, Kays and Moffat [32], Launder and Jones [39], Loyd, Moffat and Kays [42] and Jones and Launder [30] have measured velocity profiles and skin friction in a turbulent boundary layer which has been accelerated by flowing through a plane-walled convergent channel. The interest in these flows stems from the fact that they approach a state in which the local Reynolds number, the skin friction and the shape factor are invariant with flow direction and therefore constitute one of the simplest flows in which to study the effect of pressure gradient. These flows are a special case of an equilibrium boundary layer and are often referred to as sink flows or asymptotically accelerated boundary layers. The strength of the acceleration is characterized by the magnitude of the parameter, K , defined as $U^{-2} \nu (dU/dx)$, where U is the local free-stream velocity and ν is the kinematic viscosity of the fluid.

The velocity measurements indicate that for moderate acceleration, $K \approx 1 \times 10^{-6}$, the boundary layer remains turbulent; however, the viscous

sublayer becomes thicker in terms of the distance, y , made dimensionless with wall parameters. The velocity profiles lie above the universal logarithmic law of the wall. As the acceleration is increased the deviation from logarithmic behavior becomes more evident with distinction between the viscous sublayer and the fully turbulent region of the velocity profiles becoming less clear. Eventually a state is reached in which a turbulent boundary layer can no longer be sustained and the flow is said to have undergone relaminarization.

Anderson, Kays and Moffat [3] have measured velocity profiles and skin friction in unfavorable pressure gradients without separation. In contrast to accelerating flows, the velocity profiles remain logarithmic and experience a thinning of the viscous dominated sublayer in terms of the dimensionless distance, y .

The effect of streamline curvature on a turbulent boundary layer has been thoroughly reviewed by Bradshaw [8] and later by Gillis et al. [24]. Bradshaw [7] has shown that a flow subjected to mild longitudinal curvature with a ratio of boundary layer thickness, δ , to surface curvature, R_c , of $\delta/R_c = 1/300$ can significantly effect the length scale distribution. So and Mellor [66] have demonstrated that a convex surface inhibits turbulence while a concave surface enhances it. Eskinazi and Yeh [19] found that the wall shear stress is larger on the concave wall than on the convex wall of a curved duct. Ellis and Joubert [18] have shown that the width of the logarithmic region is curvature dependent. Convex curvature causes the velocity profiles to become wake like at a lower value of y than does concave curvature. Ramaprian and Shivaprasad [56,57] have shown that the effects of curvature are far more significant on the outer region of a boundary layer than on the region close to the wall.

Gillis et al. [24] carried out experiments to determine how a boundary layer responds to strong convex curvature followed by a flat section. The experiments show that both the shear stress in the outer part of the boundary layer and the wall shear stress are strongly diminished on encountering the curved surface. When the surface becomes flat again both wall shear and shear stress profiles recover very slowly to flat plate conditions.

The first models of turbulent boundary layers close to a solid wall have used Van Driest's [73] modification of Prandtl's mixing length hypothesis. This approach, which assumes a universality of the wall region in terms of wall parameters, fails to predict flows subject to mild pressure gradient and streamline curvature. Various workers have proposed modifications to the Van Driest formula to better account for these effects.

Patankar and Spalding [53] proposed that the local value of the shear stress rather than the wall value be used in the exponent of the Van Driest damping function. This modification has the correct qualitative behavior. In favorable pressure gradients the shear stress decreases from its value at the wall, so that this formulation does result in a thickening of the viscous wall region. However, calculations carried out using this formulation show that it does not produce a large enough effect.

Launder and Jones [38], Cebeci and Smith [12], Julien et al. [32] and Loyd et al. [42] began experimenting with the idea that the constant A in the Van Driest mixing length model is related to the thickness of the viscous sublayer in wall coordinates which in turn depends on the dimensionless pressure gradient, $\frac{dp}{dx}$. These workers deduced a functional dependency

of A on $\frac{dp}{dx}$ by examining a large number of equilibrium velocity profiles subject to both positive and negative pressure gradients.

In nondimensional flows where the pressure gradient is changing rapidly Loyd et al. [42], Julien et al. [32] and Launder and Jones [38] have proposed that a first order lag equation be used to predict an effective sublayer thickness, A_{eff} .

Bradshaw [7] has modified the Van Driest mixing length proposal to account for the effect of streamline curvature on the turbulence. The flat wall mixing length is multiplied by an empirical function built around the curvature Richardson number. In a situation in which the surface curvature is not constant, Bradshaw suggests that an effective radius of curvature be computed from a first order lag equation.

Jones and Launder [29,31] abandoned the mixing length approach by arguing that the prediction of nondimensional flows could not be achieved with a transport hypothesis based so firmly on equilibrium notions. They assumed that the turbulent viscosity is the product of the square root of the turbulent kinetic energy and an appropriate length scale. The turbulence length scale is calculated by solving transport equations for the turbulent kinetic energy and the turbulent dissipation rate. Launder et al. [40] have modified this model to account for streamline curvature, by redefining the curvature Richardson number in terms of turbulence quantities. Several workers have developed alternate higher order closure schemes. These have been reviewed by Reynolds [59,60]

(b) Models for Flow Over Wavy Surfaces

Benjamin [6] and Miles [46] considered the wave induced flow caused by small amplitude waves. They formulated the problem in a curvilinear

coordinate system and included the effects of turbulence only in the specification of the mean velocity profile.

Hussain and Reynolds [27] incorporated the effects of turbulence on the perturbed flow. The eddy viscosity distribution is assumed to be set up by the mean flow. The mean eddy viscosity is then assumed to act on the perturbed velocity gradient generating a wave induced Reynolds stress.

Other workers to examine flow over wavy surfaces include Davis [16] and Townsend [72]. Their models have been reviewed by Thorsness [70].

Thorsness [70] formulated the problem in a curvilinear coordinate system and investigated several turbulence models for the wave induced Reynolds stress. Three particular models are of interest. They are labeled as Model A, Model C, and Model D. Model A is essentially the quasilaminar model of Benjamin described above. Model C evaluates the wave induced Reynolds stress by using the Van Driest mixing length model. A wave induced eddy viscosity results because the shear stress used in the damping function is the local wall shear stress. Model D is an adaptation of the mixing length model of Loyd et al. This model uses the wave induced pressure gradient and wall shear stress in evaluating the mixing length.

Markatos [44] solved the full nonlinear problem using a curvilinear coordinate system. In order to avoid the difficulty of modeling the turbulence in the viscous wall region the high Reynolds number form of the Jones and Launder two equation model is matched to the logarithmic law of the wall.

Cary et al. [11] have used the mixing length model of Loyd et al. and the two equation model of Jones and Launder. Their study is

primarily concerned with the investigation of a wavy surface as a possible drag reducing device. Their analysis suggests that neither of the two models describe flow over large amplitude waves.

Caponi et al. [10] have developed a model for laminar flow over an arbitrarily shaped periodic surface. An orthogonal transformation is used to map the physical domain under consideration to a rectangular region. Because of the periodic nature of the problem, the dependent variables are expanded in terms of Fourier series. The model successfully predicts viscous flow over both a moving liquid and solid wave surface.

McLean [45] has extended the laminar flow calculations of Caponi et al. to include turbulent flow by using the mixing length model of Loyd et al. A comparison of this theory with the shear stress measurements of Thorsness and Zilker indicates that the model successfully predicts flow over small amplitude waves. However, in the case of large amplitude waves the discrepancy between the theory and experiments is more apparent.

CHAPTER 3

THEORY

In this chapter a theoretical framework for the description of turbulent flow over a small amplitude wave surface is presented. The problem is formulated in a boundary layer coordinate system. A number of models for the wave induced Reynolds stresses are developed. The results of the alternate approaches and their comparative success in predicting the experimental results is reserved for presentation in Chapter 6 and Chapter 7. The various numerical techniques used in integrating the equations are presented in Chapter 5.

(a) Coordinate System and Basic Equations

The boundary layer coordinate system used in formulating the problem is shown in Figure 3.1. The x direction is taken parallel to the wave surface while the y axis is perpendicular to it. For convenience $x = 0$ is taken as the wave crest with the positive x axis being in the direction of flow. The flow field is assumed to be two dimensional.

Unless otherwise stated all the variables are made nondimensional with respect to wall parameters. Velocities are made dimensionless with respect to the friction velocity, $u^* = \sqrt{\tau_{wd}/\rho}$. Lengths are made dimensionless with respect to ν/u^* , where ν is the kinematic viscosity. Pressure, stresses and the turbulent kinetic energy are considered multiples of ρu^{*2} .

The time averaged continuity and momentum equations in the boundary layer coordinate system with surface curvature, κ , are:

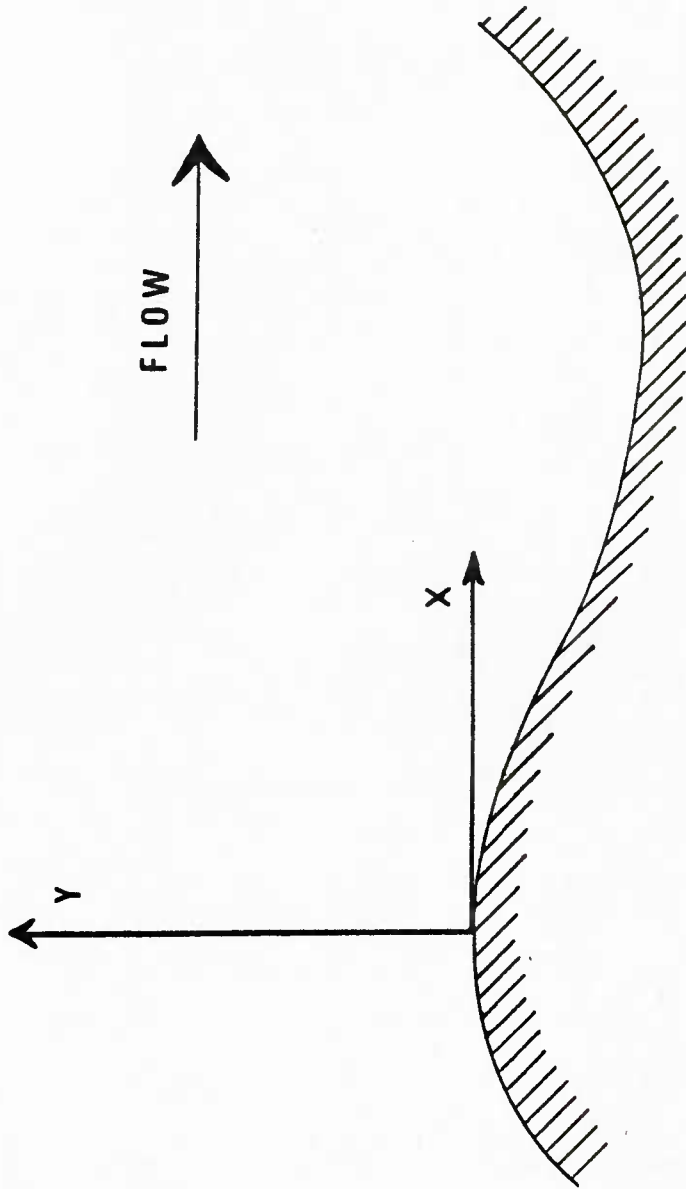


Figure 3.1. Boundary Layer Coordinate System

$$\frac{\partial U}{\partial x} + \frac{\partial}{\partial y} [(1 + \kappa y)V] = 0, \quad (3.1)$$

$$\begin{aligned} & \frac{1}{1 + \kappa y} U \frac{\partial U}{\partial x} + V \frac{\partial U}{\partial y} + \frac{\kappa}{1 + \kappa y} UV \\ &= - \frac{1}{1 + \kappa y} \frac{\partial P}{\partial x} + \left[\frac{1}{(1 + \kappa y)^2} \frac{\partial^2 U}{\partial x^2} + \frac{\partial^2 U}{\partial y^2} \right. \\ & \quad - \frac{y}{(1 + \kappa y)^3} \frac{\partial \kappa}{\partial x} \frac{\partial U}{\partial x} + \frac{\kappa}{1 + \kappa y} \frac{\partial U}{\partial y} - \frac{\kappa^2}{(1 + \kappa y)^2} U \\ & \quad \left. + \frac{1}{(1 + \kappa y)^3} \frac{\partial \kappa}{\partial x} V + \frac{2\kappa}{(1 + \kappa y)^2} \frac{\partial V}{\partial x} \right] \\ & \quad + \frac{1}{1 + \kappa y} \frac{\partial}{\partial x} (-\overline{u'u'}) + \frac{\partial}{\partial y} (-\overline{u'v'}) + \frac{2\kappa}{1 + \kappa y} (-\overline{u'v'}), \quad (3.2) \end{aligned}$$

$$\begin{aligned} & \frac{1}{1 + \kappa y} U \frac{\partial V}{\partial x} + V \frac{\partial V}{\partial y} - \frac{\kappa}{1 + \kappa y} U^2 \\ &= - \frac{\partial P}{\partial y} + \left[\frac{1}{(1 + \kappa y)^2} \frac{\partial^2 V}{\partial x^2} + \frac{\partial^2 V}{\partial y^2} - \frac{y}{(1 + \kappa y)^3} \frac{\partial \kappa}{\partial x} \frac{\partial V}{\partial x} \right. \\ & \quad + \frac{\kappa}{1 + \kappa y} \frac{\partial V}{\partial y} - \frac{\kappa^2}{(1 + \kappa y)^2} V - \frac{1}{(1 + \kappa y)^3} \frac{\partial \kappa}{\partial x} U \\ & \quad \left. - \frac{2\kappa}{(1 + \kappa y)^2} \frac{\partial U}{\partial x} \right] + \frac{1}{1 + \kappa y} \frac{\partial}{\partial x} (-\overline{u'v'}) + \frac{\partial}{\partial y} (-\overline{v'v'}) \\ & \quad - \frac{\kappa}{1 + \kappa y} (-\overline{u'u'}) + \frac{\kappa}{1 + \kappa y} (-\overline{v'v'}), \quad (3.3) \end{aligned}$$

where U and V are the velocities in the x and y directions respectively. The quantities, $-\overline{u'u'}$, $-\overline{u'v'}$ and $-\overline{v'v'}$ are the Reynolds stresses and P is the static pressure.

(b) Linearized Equations

The necessary conditions for the flow field to be described by a linear form of the Navier Stokes equations are that the wave amplitude be small compared to both the wavelength and the boundary layer thickness. These conditions are developed in Appendix A.

The time averaged velocities, U, V , the turbulent stresses, R_{ij} , and the pressure gradients, $\partial P/\partial x, \partial P/\partial y$, are assumed to be the sum of a component averaged over a wavelength at a constant value of y and a periodic spatially varying wave induced component. The general form of the wave induced component is $a\hat{n}e^{i\alpha x}$ where \hat{n} is a complex number whose real and imaginary parts are at most functions of y . Thus the velocities, stresses and pressure gradients are given by

$$U = \bar{U}(y) + a\hat{u}(y)e^{i\alpha x} \quad (3.4.1)$$

$$V = a\hat{v}(y)e^{i\alpha x} \quad (3.4.2)$$

$$-\overline{u'_i u'_j} = R_{ij} = \bar{R}_{ij}(y) + a\hat{r}_{ij}(y)e^{i\alpha x} \quad (3.4.3)$$

$$\frac{\partial P}{\partial y} = \frac{\partial \bar{P}}{\partial y} + a \frac{d\hat{p}(y)}{dy} e^{i\alpha x} \quad (3.4.4)$$

$$\frac{\partial P}{\partial x} = \frac{\partial \bar{P}}{\partial x} + a i \alpha \hat{p}(y) e^{i\alpha x} \quad (3.4.5)$$

If the equations (3.4.1)-(3.4.5) are substituted into the continuity and momentum equations (3.1)-(3.3) and the terms of $O(a^2)$ are neglected, a system of equations which is linear in the wave induced components results. The continuity, the x momentum and the y momentum equations are respectively

$$a [i\alpha \hat{u} + \hat{v}'] e^{i\alpha x} = 0, \quad (3.5)$$

$$\begin{aligned}
& a [i\alpha\bar{U}\hat{u} + \hat{v}\bar{U}'] e^{i\alpha x} = -\frac{\partial\bar{P}}{\partial x} + \bar{U}'' + \bar{R}'_{xy} \\
& + a [-i\alpha\hat{p} - \alpha^2\hat{u} + \alpha^2\bar{U}' + \alpha^2y \frac{\partial\bar{P}}{\partial x} + \hat{u}'' \\
& + 2R_{xy}\alpha^2 + i\alpha\hat{r}_{xx} + \hat{r}'_{xy}] e^{i\alpha x} , \tag{3.6}
\end{aligned}$$

$$\begin{aligned}
& a [i\alpha\bar{U}\hat{v} - \alpha^2\bar{U}^2] e^{i\alpha x} = -\frac{\partial\bar{P}}{\partial y} + \bar{R}'_{yy} \\
& + a [\hat{v}'' - \alpha^2\hat{v} - i\alpha^3\bar{U} - \hat{p}' + \hat{r}'_{yy} + \bar{R}_{yy}\alpha^2 + i\alpha\hat{r}_{xy} \\
& - \alpha^2\bar{R}_{xx}] e^{i\alpha x} . \tag{3.7}
\end{aligned}$$

The primes denote differentiation with respect to the y direction. The continuity equation (3.5) can be satisfied by the introduction of the stream function

$$\Psi = \int_0^y \bar{U}(y) dy + a F(y) e^{i\alpha x} , \tag{3.8}$$

with

$$U = \frac{1}{h_y} \frac{\partial\Psi}{\partial y} \tag{3.9.1}$$

and

$$V = \frac{-1}{h_x} \frac{\partial\Psi}{\partial x} \tag{3.9.2}$$

where h_x and h_y are the metric functions. The linearized metrics are:

$$h_x = 1 \quad (3.10.1)$$

and

$$h_y = 1 + a\alpha^2 y e^{i\alpha x}. \quad (3.10.2)$$

Substituting equations (3.10.1) and (3.10.2) into equations (3.9.1)-(3.9.2) and using the definition of the stream function equation (3.8), the U and V velocities to 0 (a) are respectively,

$$U = \bar{U} + aF'e^{i\alpha x} \quad (3.11.1)$$

and

$$V = -aiaFe^{i\alpha x}. \quad (3.11.2)$$

The linearized momentum equations (3.6) and (3.7) can be combined to eliminate the pressure terms in the following manner. Equation (3.6) is multiplied by $(1 + a\alpha^2 y e^{i\alpha x})$ and then differentiated with respect to y. Equation (3.7) is differentiated with respect to x and multiplied by (-1). The resulting equations are then added. Substituting the definitions of the velocities in terms of the stream function (3.11.1) and (3.11.2) into the resulting equation and collecting terms of similar order the following equations defining F(y) are obtained:

$$\bar{U}''' + \bar{R}''_{xy} = 0, \quad (3.12)$$

$$\begin{aligned}
& i\alpha [\bar{U}(F'' - \alpha^2 F) - \bar{U}''F + \alpha^2 \bar{U}^2] \\
& = F'''' - 2\alpha^2 F'' + \alpha^4 F + 2\alpha^2 \bar{U}'' - \alpha^4 \bar{U} + R, \quad (3.13)
\end{aligned}$$

$$R = i\alpha^3 \bar{R}_{xx} + 3\alpha^2 \bar{R}'_{xy} + i\alpha (\hat{r}'_{xx} - \hat{r}'_{yy}) + \alpha^2 \hat{r}_{xy} + \hat{r}''_{xy} - i\alpha^3 \bar{R}_{yy}. \quad (3.14)$$

Equation (3.13) is similar to the well known Orr-Sommerfeld equation used in stability calculations except for the appearance of additional terms which arise due to the use of the curvilinear coordinate system and due to the inclusion of the Reynolds stresses.

Solution of equations (3.12) and (3.13) requires the specification of the Reynolds stresses and the boundary conditions. The average velocity profile, $\bar{U}(y)$, and the average Reynolds stress, $\bar{R}_{xy}(y)$, appearing in equations (3.12) and (3.13) are taken to be the same as would exist if the surface were flat. This specification is consistent with the linearization assumption in that the leading order wave averaged terms are the same in both a boundary layer and cartesian coordinate system. Furthermore it is assumed that the wave averaged shear stress, $\bar{\tau}(y)$, does not vary in the y direction. This implies that the wave averaged pressure gradient, $\partial\bar{P}/\partial x$ is zero. Equation (3.12) can therefore be integrated once to yield

$$\bar{U}'' + \bar{R}'_{xy} = 0. \quad (3.15)$$

The specification of the Reynolds stress is dealt with in the next section.

At the wave surface no slip and no penetration boundary conditions are invoked.

$$F = 0 \text{ and } F' = 0 \quad \text{at } y = 0. \quad (3.16)$$

The outer boundary condition is such that the flow field far away from the surface is unaffected by the presence of the wave. Therefore the velocity field in the boundary layer coordinate system must be equated to an undisturbed velocity field that would exist if the wave surface were not present. This is accomplished in two steps. Firstly the velocity field in the boundary layer coordinate system is transformed into cartesian coordinates. Secondly the transformed velocity field is then equated to a linearized velocity field in cartesian coordinates, see Appendix B. The linearized boundary conditions for the flow far from the wave surface are then obtained as

$$F = \bar{U} \quad \text{and} \quad F' = \bar{U}' \quad \text{for large } y. \quad (3.17)$$

The shear stress at the surface is evaluated from the component of the rate of strain tensor, S_{xy} ,

$$\tau_w = 2 S_{xy} \Big|_{y=0} = \left[h_x \frac{\partial}{\partial y} \left(\frac{U}{h_x} \right) + \frac{1}{h_x} \frac{\partial V}{\partial x} \right]_{y=0}. \quad (3.18)$$

Neglecting terms of $O(a^2)$ and using the surface boundary conditions equation (3.16),

$$\tau_w = \bar{\tau}(0) + a\hat{\tau}(0)e^{i\alpha x} = \bar{U}'(0) + aF''(0)e^{i\alpha x}. \quad (3.19)$$

The wave induced variation of the wall shear stress is

$$a\hat{\tau}(0)e^{i\alpha x} = aF''(0)e^{i\alpha x}. \quad (3.20)$$

The wave induced variation of the pressure at the solid surface is found by evaluating equation (3.6) at $y = 0$

$$a\hat{p}(0)e^{i\alpha x} = \frac{-i}{\alpha} [F'''(0) + \alpha^2 \bar{U}'(0)] ae^{i\alpha x}. \quad (3.21)$$

(c) Models for Turbulent Stresses

c.1 Constant Reynolds Stress Assumption Model A

The simplest assumption to make is the quasi-laminar assumption of Miles and Benjamin that the effects of turbulence enter the problem only in the specification of the mean velocity profile $\bar{U}(y)$. In this case $R = 0$. A slightly different approach is taken here in that only the fluctuating component of the Reynolds stress, \hat{r}_{ij} , is set equal to zero. Consequently

$$R = 3\alpha^2 \bar{R}'_{xy}, \quad (3.22)$$

if the normal stresses, \bar{R}_{xx} and \bar{R}_{yy} , are neglected.

For a thick boundary layer

$$\bar{U}'' = -\bar{R}'_{xy} \quad (3.23)$$

so

$$R = -3\alpha^2 \bar{U}'' \quad (3.24)$$

Thorsness [70] has argued that the constant stress model formulated in a boundary layer coordinate system, which he designated as Model A, is closely related to the assumption that the Reynolds stresses are frozen along a streamline as discussed by Davis [16]. In a cartesian coordinate system the constant stress assumption reduces to the quasi-laminar model of Miles and Benjamin.

A major shortcoming of the constant stress model (Model A) is that there is no interaction between the wave and the turbulence. Several models are now explored which take this interaction into account. These models are all based on the assumption that the Reynolds stresses are described by a Newtonian constitutive equation of the form

$$R_{ij} = -\frac{1}{3} q^2 \delta_{ij} + \frac{\nu_t}{\nu} 2S_{ij} \quad (3.25)$$

where q^2 is the turbulent kinetic energy and ν_t is a turbulent or eddy viscosity and S_{ij} is the rate of strain tensor defined in Appendix C.

Since turbulent stresses are important only close to the wave surface, use is made of the boundary layer assumption that the normal stresses, R_{xx} and R_{yy} , can be neglected. Here the only component contributing to the Reynolds stress tensor is R_{xy} where

$$R_{xy} = \frac{\nu_t}{\nu} 2S_{xy} \quad (3.26)$$

In order to account for the spatial variation of the turbulence properties along the wave surface the concept of a wave induced eddy viscosity is introduced

$$\frac{\nu_t}{\nu} = \overline{\frac{\nu_t}{\nu}} + a \frac{\hat{\nu}_t}{\nu} e^{i\alpha x} \quad (3.27)$$

Decomposing the rate of strain S_{xy} into its wave averaged and fluctuating components

$$S_{xy} = \overline{S}_{xy} + a \hat{s}_{xy} e^{i\alpha x} \quad (3.28)$$

the Reynolds stress, R_{xy} , is related to the eddy viscosity and the rate of strain as follows

$$R_{xy} = \frac{\bar{v}_t}{\nu} 2 \bar{S}_{xy} + a \left(\frac{\hat{v}_t}{\nu} 2 \bar{S}_{xy} + \frac{\bar{v}_t}{\nu} 2 \hat{s}_{xy} \right) e^{i\alpha x}. \quad (3.29)$$

The wave induced variation of the Reynolds stress is

$$a \hat{r}_{xy} e^{i\alpha x} = a \left(\frac{\hat{v}_t}{\nu} 2 \bar{S}_{xy} + \frac{\bar{v}_t}{\nu} 2 \hat{s}_{xy} \right) e^{i\alpha x}. \quad (3.30)$$

The average and wave induced rates of strain are respectively

$$2 \bar{S}_{xy} = \bar{U}', \quad (3.31)$$

$$2a \hat{s}_{xy} e^{i\alpha x} = a (F'' + \alpha^2 F - \alpha^2 \bar{U}) e^{i\alpha x}. \quad (3.32)$$

The Reynolds stress term, R , equation (3-14), can now be written as

$$R = 3\alpha^2 \left[\frac{\bar{v}_t}{\nu} \bar{U}' \right]' + \alpha^2 \left[\frac{\bar{v}_t}{\nu} (F'' + \alpha^2 F - \alpha^2 \bar{U}) + \frac{\hat{v}_t}{\nu} \bar{U}' \right] + \left[\frac{\bar{v}_t}{\nu} (F'' + \alpha^2 F - \alpha^2 \bar{U}) + \frac{\hat{v}_t}{\nu} \bar{U}' \right]'' \quad (3.33)$$

Before equation (3.12) to (3.14) can be solved for the fluctuating flow the eddy viscosity must be specified. Two approaches are explored.

c.2 Zero Equation Models

At this level of turbulence modeling the Prandtl mixing length hypothesis is frequently used.

$$v_t = \ell_o^2 |2 S_{xy}| \quad (3.34)$$

where ℓ_o is "the mixing length." Close to a solid boundary where viscous effects are important several workers have adopted the Van Driest mixing length model

$$\ell_o = \kappa y [1 - \exp(-D_m)] \quad (3.35)$$

where κ is the Von Karman constant and, D_m , is a damping function introduced to account for the effects of the wall in suppressing turbulent transport.

Van Driest's original proposal was that $D_m = \frac{y}{A} \tau_w^{1/2}$ where a value of $A = \bar{A} = 26$ is suggested for flow over a flat plate. Thorsness [70] has applied this formulation of the Van Driest mixing length hypothesis, which he labeled as Model C, to flow over small amplitude waves. This formulation is not expected to be correct for flow over wavy surfaces because the presence of pressure gradients causes a large variation of τ with distance from the boundary and a drastic change in the production of turbulence in the wall region. This can be taken into account by redefining the damping function as

$$D_m = \frac{y}{A} \tau^{1/2}(y) \quad (3.36)$$

where the local shear stress, $\tau(y)$, is used instead of the value at the surface, τ_w . The local shear stress is the sum of viscous and turbulent stresses

$$\tau = 2 S_{xy} + \frac{v_t}{v} 2 S_{xy} \quad (3.37)$$

For small amplitude waves the local shear stress can be separated into an average and a wave induced component. The average shear stress is simply equal to its value at the surface

$$\bar{\tau} = \left(1 + \frac{\bar{v}_t}{v} \right) 2 \bar{S}_{xy} = 1 \quad (3.38)$$

and the wave induced component of τ is

$$a \hat{\tau}(y) e^{i\alpha x} = 2a \left[\frac{\hat{v}_t}{v} \bar{S}_{xy} + \left(1 + \frac{\bar{v}_t}{v} \right) \hat{s}_{xy} \right] e^{i\alpha x} . \quad (3.39)$$

The mixing length to $O(a)$ is

$$l_o = \bar{l}_o + a \hat{l}_o e^{i\alpha x} . \quad (3.40)$$

Using the definitions of v_t , l_o and D_m , equations (3.34), (3.35) and (3.36) respectively, and neglecting terms of $O(a^2)$ the average components of the mixing length, \bar{l}_o , and the eddy viscosity, \bar{v}_t , are respectively

$$\bar{l}_o = \kappa y [1 - \exp(-y/\bar{A})] \quad (3.41)$$

and

$$\bar{v}_t = \bar{l}_o^2 \bar{U}' . \quad (3.42)$$

The wave induced components of l_o and v_t are respectively

$$a \hat{l}_o e^{i\alpha x} = \kappa y \exp(-y/\bar{A}) \frac{y}{\bar{A}} \left(\frac{\hat{\tau}}{2} \right) e^{i\alpha x} \quad (3.43)$$

and

$$\frac{a\hat{v}_t}{\bar{v}} e^{i\alpha x} = a \left[\frac{\hat{s}_{xy}}{\bar{s}_{xy}} + \frac{2 \exp(-y/\bar{A})}{[1 - \exp(-y/\bar{A})]} \left(\frac{y}{\bar{A}} \right) \frac{\hat{\tau}}{2} \right] \frac{\bar{v}_t}{v} e^{i\alpha x} \quad (3.44)$$

where

$$\frac{\hat{s}_{xy}}{\bar{s}_{xy}} = \frac{F'' + \alpha^2 F - \alpha^2 \bar{U}}{\bar{U}'} \quad (3.45)$$

Eliminating the eddy viscosity, \hat{v}_t , between equations (3.39) and (3.44) an explicit result for the variation of the wave induced shear stress is obtained.

$$\hat{\tau}(y) e^{i\alpha x} = \frac{a \left[\left(2 \frac{\bar{v}_t}{v} + 1 \right) 2 \hat{s}_{xy} \right]}{\left[1 - \frac{\bar{v}_t}{v} \frac{2 \bar{s}_{xy} \exp(-y/\bar{A}) y}{[1 - \exp(-y/\bar{A})] \bar{A}} \right]} e^{i\alpha x} \quad (3.46)$$

Equation (3.44) and (3.46) defining \hat{v}_t and $\hat{\tau}$ respectively are designated as Model C*. If $\hat{\tau}$ is evaluated at the wall Model C* reduces to Model C.

For equilibrium boundary layers Loyd et al. suggest the following functional dependence of A on pressure gradient

$$A = \bar{A} \left[1 + k_1 \left(\frac{dP}{dx} \right) + k_2 \left(\frac{dP}{dx} \right)^2 \right] \quad (3.47)$$

where \bar{A} is the flat plate value.

For flow over small amplitude waves A can be expressed as

$$A = \bar{A} + a\hat{A}e^{i\alpha x} \quad (3.48.1)$$

where

$$a\hat{A}e^{i\alpha x} = a\bar{A}k_1 i\alpha\hat{p}(0)e^{i\alpha x} . \quad (3.48.2)$$

The damping function is

$$D_m = y \frac{[1 + a\hat{t}e^{i\alpha x}]^{1/2}}{\bar{A} + a\hat{A}e^{i\alpha x}} . \quad (3.49)$$

Using equation (3.35) and (3.36) and neglecting terms of $O(a^2)$ the wave induced mixing length and eddy viscosity are respectively

$$a\hat{\lambda}_0 e^{i\alpha x} = aky \exp(-y/\bar{A}) \frac{y}{\bar{A}} \left[\frac{\hat{t}}{2} - \frac{\hat{A}}{\bar{A}} \right] e^{i\alpha x} \quad (3.50)$$

and

$$a \frac{\hat{v}_t}{\nu} e^{i\alpha x} = a \frac{\bar{v}_t}{\nu} \left[\frac{\hat{s}_{xy}}{\bar{s}_{xy}} + \frac{2 \exp(-y/\bar{A})}{[1 - \exp(-y/\bar{A})]} \left(\frac{y}{\bar{A}} \right) \left(\frac{\hat{t}}{2} - \frac{\hat{A}}{\bar{A}} \right) \right] e^{i\alpha x} . \quad (3.51)$$

Eliminating the eddy viscosity between equations (3.39) and (3.51) the wave induced shear stress is

$$a\hat{\tau}(y)e^{i\alpha x} = \frac{a \left[\left(2 \frac{\bar{v}_t}{\nu} + 1 \right) 2 \hat{s}_{xy} - \frac{2 \frac{\bar{v}_t}{\nu} \bar{U}' \exp(-y/\bar{A})}{[1 - \exp(-y/\bar{A})]} \left(\frac{y}{\bar{A}} \right) \frac{\hat{A}}{\bar{A}} \right]}{\left[1 - \frac{\bar{v}_t}{\nu} \bar{U}' \exp(-y/\bar{A}) \left(\frac{y}{\bar{A}} \right) \right]} e^{i\alpha x} . \quad (3.52)$$

Equations (3.51), (3.52) and (3.48.2) represent an equilibrium eddy viscosity model for flow over a small amplitude wave.

In situations where the pressure is varying rapidly Loyd et al. [42] (see literature survey) have suggested that the flow close to the wall sees an effective pressure gradient,

$$\frac{d}{dx} \left(\frac{dP}{dx} \right)_{\text{eff}} = \frac{\frac{dP}{dx} - \left(\frac{dP}{dx} \right)_{\text{eff}}}{k_L} \quad (3.53)$$

where k_L is a lag constant.

Solving for a periodic pressure gradient

$$a \hat{p}_{\text{eff}} e^{i\alpha x} = \frac{a \hat{p} e^{i\alpha x}}{[1 + i\alpha k_L]} \quad (3.54)$$

and thus replacing \hat{p} with \hat{p}_{eff} equation (3.48.2) becomes

$$a \hat{A}_{\text{eff}} e^{i\alpha x} = \frac{a \bar{A} k_L i \alpha \hat{p}}{[1 + i\alpha k_L]} e^{i\alpha x} . \quad (3.55)$$

Thorsness [70] has labeled the above formulation for \hat{A}_{eff} together with equation (3.51) and equation (3.52) evaluated at the wall Model D. Abrams, Frederick and Hanratty [2], using the local value of the shear stress equation (3.52) together with equation (3.51) and (3.55), have labeled this formulation Model D*.

A slightly different approach is also explored in this research. Instead of accounting for the nonequilibrium effects in the boundary layer by relaxing the pressure gradient, the complete Reynolds stress term, R , is relaxed, by introducing an effective, R_{eff} , satisfying the following first order rate equation.

$$\frac{d}{dx} \left(R_{\text{eff}} a e^{i\alpha x} \right) = \frac{(R - R_{\text{eff}})}{k_R} a e^{i\alpha x}. \quad (3.56)$$

Solving for a periodic variation yields,

$$R_{\text{eff}} = \frac{R}{[1 + i\alpha k_R]}. \quad (3.57)$$

Equations (3.52), (3.51), (3.48.2) and (3.57) for \hat{v}_t , $\hat{\tau}$, \hat{A} , and R_{eff} define a nonequilibrium relaxation model for flow over a small amplitude wave.

The mean velocity profile to be used with the above turbulence models is obtained by integrating the wave averaged momentum equation (3.15). This results in the well known Van Driest velocity profile.

$$\bar{U}(y) = \int_0^y \frac{2 dy}{1 + \sqrt{(1 + 4\kappa^2 y^2 [1 - \exp(-y/\bar{A})])^2}} \quad (3.58)$$

c.3 K-ε Model

The basic high Reynolds number K-ε model used in this thesis is the model proposed by Jones and Launder [29,31]. Several workers have extended the basic model to include the low Reynolds number viscous wall region. Patel et al. [54] have tested many of these models against data sets obtained in a variety of external pressure gradients. The most successful low Reynolds number model tested is the one proposed by Chien [13]. This is the model adopted for use in this thesis.

The K-ε model requires that a partial differential equation be developed for the turbulent kinetic energy

$$K = \frac{1}{2} \overline{u'_i u'_i} \quad (3.59)$$

and for the isotropic turbulent energy dissipation rate

$$\epsilon = \overline{\frac{\partial u'_i}{\partial x_j} \frac{\partial u'_i}{\partial x_j}} \quad (3.60)$$

Equations for the kinetic energy and dissipation rate are presented in Appendix C together with the necessary closure assumptions. The closed form of the energy and dissipation equations in boundary layer coordinates are respectively

$$\begin{aligned} & \text{I} \qquad \qquad \qquad \text{II} \qquad \qquad \qquad \text{II} \\ & \frac{U}{(1+\kappa y)} \frac{\partial K}{\partial x} + v \frac{\partial K}{\partial y} = \frac{1}{(1+\kappa y)} \frac{\partial}{\partial x} \left(\frac{1}{(1+\kappa y)} \frac{\partial K}{\partial x} \right) + \frac{1}{(1+\kappa y)} \frac{\partial}{\partial y} \left((1+\kappa y) \frac{\partial K}{\partial y} \right) \\ & \qquad \qquad \qquad \text{III} \qquad \qquad \qquad \text{III} \\ & + \frac{1}{(1+\kappa y)} \frac{\partial}{\partial x} \left(\frac{1}{(1+\kappa y)} \frac{v_t}{v\sigma_K} \frac{\partial K}{\partial x} \right) + \frac{1}{(1+\kappa y)} \frac{\partial}{\partial y} \left((1+\kappa y) \frac{v_t}{v\sigma_K} \frac{\partial K}{\partial y} \right) \\ & \qquad \qquad \qquad \text{IV} \\ & - \overline{u'v'} \left(\frac{\partial U}{\partial y} - \frac{\kappa U}{(1+\kappa y)} + \frac{1}{(1+\kappa y)} \frac{\partial V}{\partial x} \right) \\ & \qquad \qquad \qquad \text{IV} \qquad \qquad \qquad \text{IV} \qquad \qquad \qquad \text{V} \\ & - \overline{u'^2} \left(\frac{1}{(1+\kappa y)} \frac{\partial U}{\partial x} + \frac{\kappa V}{(1+\kappa y)} \right) - \overline{v'^2} \frac{\partial V}{\partial y} - \epsilon - \frac{2K}{y^2} \end{aligned}$$

and

(3.61)

$$\begin{aligned} & \text{I} \qquad \qquad \qquad \text{II} \qquad \qquad \qquad \text{II} \\ & \frac{U}{(1+\kappa y)} \frac{\partial \epsilon}{\partial x} + v \frac{\partial \epsilon}{\partial y} = \frac{1}{(1+\kappa y)} \frac{\partial}{\partial x} \left(\frac{1}{(1+\kappa y)} \frac{\partial \epsilon}{\partial x} \right) + \frac{1}{(1+\kappa y)} \frac{\partial}{\partial y} \left((1+\kappa y) \frac{\partial \epsilon}{\partial y} \right) \\ & \qquad \qquad \qquad \text{III} \qquad \qquad \qquad \text{III} \\ & + \frac{1}{(1+\kappa y)} \frac{\partial}{\partial x} \left(\frac{1}{(1+\kappa y)} \frac{v_t}{v\sigma_\epsilon} \frac{\partial \epsilon}{\partial x} \right) + \frac{1}{(1+\kappa y)} \frac{\partial}{\partial y} \left((1+\kappa y) \frac{v_t}{v\sigma_\epsilon} \frac{\partial \epsilon}{\partial y} \right) \end{aligned}$$

$$\begin{aligned}
& + C_1 \frac{\varepsilon}{K} \left[\overbrace{(-\overline{u'v'})}^{\text{IV}} \left(\frac{\partial U}{\partial y} - \frac{\kappa U}{(1+\kappa y)} + \frac{1}{(1+\kappa y)} \frac{\partial V}{\partial x} \right) - \overline{u'^2} \left(\frac{1}{(1+\kappa y)} \frac{\partial U}{\partial x} + \frac{\kappa V}{(1+\kappa y)} \right) \right. \\
& \left. \overbrace{\frac{1}{v'^2} \frac{\partial V}{\partial y}}^{\text{IV}} \right] - \frac{\varepsilon^2}{K} C_2 f_o - \frac{2\varepsilon}{y^2} f_d \quad (3.62)
\end{aligned}$$

where

$$f_o = 1 - 0.4/1.8 \exp(-K^4/36\varepsilon^2) \quad (3.63.1)$$

$$f_d = \exp(-C_4 y \tau_w) \quad (3.63.2)$$

Terms I = advection of K or ε by time averaged flow

Terms II = viscous diffusion of K or ε

Terms III = turbulent diffusion of K or ε by pressure
and velocity fluctuations

Terms IV = production of K or ε by time averaged flow

Terms V = dissipation of K or ε

The eddy viscosity v_t is defined as

$$\frac{v_t}{\nu} = \frac{C_\mu K^2}{\varepsilon} [1 - \exp(-C_3 y \tau_w)] \quad (3.64)$$

In summary, the turbulence model is assumed to be governed by equations

(3.61) - (3.64) with the constants $\sigma_K = 1$, $\sigma_\varepsilon = 1.3$, $C_\mu = 0.09$, $C_1 = 1.35$,
 $C_2 = 1.8$, $C_3 = 0.0115$, and $C_4 = 0.5$. The values used are those suggested
by Chien [13].

For flow over small amplitude waves it is possible to define a mean and fluctuating component of the turbulent energy and dissipation rate

$$K = \bar{K}(y) + a\hat{k}(y)e^{i\alpha x} \quad (3.65)$$

$$\varepsilon = \bar{\varepsilon}(y) + a\hat{\varepsilon}(y)e^{i\alpha x} \quad (3.66)$$

Substituting equations (3.65) and (3.66) into equations (3.60)-(3.61), collecting terms of like order and neglecting $O(a^2)$ terms, the following equations for the mean and fluctuating energy and dissipation rate result.

Mean energy equation:

$$0 = \left[(1 + \bar{v}_t / \nu \sigma_K) \bar{K}' \right]' + \bar{R}_{xy} \bar{U}' - \bar{\varepsilon} - \frac{2\bar{K}}{y^2} \quad (3.67)$$

Mean dissipation equation:

$$0 = \left[(1 + \bar{v}_t / \nu \sigma_\varepsilon) \bar{\varepsilon}' \right]' + \frac{C_1 \bar{\varepsilon}}{\bar{K}} \bar{R}_{xy} \bar{U}' - \frac{C_2 \bar{f}_o \bar{\varepsilon}^2}{\bar{K}} - \frac{2\bar{\varepsilon} \bar{f}_d}{y^2} \quad (3.68)$$

where

$$\bar{f}_o = \left[1 - \frac{0.4}{1.8} \exp \left(\frac{-\bar{K}^4}{36\bar{\varepsilon}^2} \right) \right] \quad (3.69.1)$$

$$\bar{f}_d = \exp(-C_4 y) \quad (3.69.2)$$

$$\frac{\bar{v}_t}{\nu} = C_\mu \frac{\bar{K}^2}{\bar{\varepsilon}} [1 - \exp(-C_3 y)] \quad (3.69.3)$$

are

$$\bar{K} = \bar{\varepsilon} = 0 \quad \text{at} \quad y = 0 \quad (3.70)$$

and at large y the energy and dissipation distribution must be such as to yield a constant stress region

$$\bar{K} = C_{\mu}^{-1/2} \quad \text{for large } y. \quad (3.71)$$

$$\bar{\varepsilon} = 1/\kappa y.$$

Fluctuating energy equation:

$$\begin{aligned} a [i\alpha \bar{U} \hat{k} + \bar{K}' \hat{v}] e^{i\alpha x} = a \left[-\alpha^2 \left(1 + \frac{\bar{v}_t}{\nu \sigma_K} \right) \hat{k} + \alpha^2 \frac{\bar{v}_t}{\nu \sigma_K} \bar{K}' \right. \\ \left. + \left(\frac{\hat{v}_t}{\nu \sigma_K} \bar{K}' + \frac{\bar{v}_t}{\nu \sigma_K} \hat{k}' \right)' \right. \\ \left. + \bar{K}' \alpha^2 + \hat{k}'' + P_k - \hat{\varepsilon} + 2\hat{k}/y^2 \right] e^{i\alpha x} \quad (3.72) \end{aligned}$$

Fluctuating dissipation equation:

$$\begin{aligned} a [i\alpha \bar{U} \hat{\varepsilon} + \bar{\varepsilon}' \hat{v}] e^{i\alpha x} = a \left[-\alpha^2 \left(1 + \frac{\bar{v}_t}{\nu \sigma_{\varepsilon}} \right) \hat{\varepsilon} + \alpha^2 \frac{\bar{v}_t}{\nu \sigma_{\varepsilon}} \bar{\varepsilon}' + \bar{\varepsilon}' \alpha^2 \right. \\ \left. + \hat{\varepsilon}'' + \left(\frac{\hat{v}_t}{\nu \sigma_{\varepsilon}} \bar{\varepsilon}' + \frac{\bar{v}_t}{\nu \sigma_{\varepsilon}} \hat{\varepsilon}' \right)' + \frac{C_1 \bar{\varepsilon}}{\bar{K}} \bar{R}_{xy} \bar{U}' \left(\frac{\hat{\varepsilon}}{\bar{\varepsilon}} - \frac{\hat{k}}{\bar{K}} \right) \right. \\ \left. + \frac{C_1 \bar{\varepsilon}}{\bar{K}} P_k - \frac{C_2 \bar{\varepsilon}^2}{\bar{K}} \bar{f}_0 \left(\frac{2\hat{\varepsilon}}{\bar{\varepsilon}} - \frac{\hat{k}}{\bar{K}} \right) \right] \end{aligned}$$

$$\begin{aligned}
& - \frac{C_2 \bar{\epsilon}^{-2}}{\bar{K}} \frac{(.22)}{36} \exp \left(\frac{-\bar{K}^4}{36 \bar{\epsilon}^2} \right) \left(\frac{4 \hat{k}}{\bar{K}} - \frac{2 \hat{\epsilon}}{\bar{\epsilon}} \right) \frac{\bar{K}^4}{\bar{\epsilon}^2} \\
& - \left. \frac{2 \hat{\epsilon}}{y^2} \bar{f}_d + \frac{2 \bar{\epsilon}}{y^2} \exp(-C_4 y) C_4 y \frac{F''(0)}{2} \right] e^{i\alpha x} \quad (3.73)
\end{aligned}$$

where

$$\begin{aligned}
\frac{\hat{v}_t}{v} &= \frac{C_\mu \bar{K}^2}{\bar{\epsilon}} [1 - \exp(-C_3 y)] \left(\frac{2 \hat{k}}{\bar{K}} - \frac{\hat{\epsilon}}{\bar{\epsilon}} \right) \\
&+ C_3 C_\mu \frac{\bar{K}^2}{\bar{\epsilon}} \exp(-C_3 y) \frac{y}{2} F''(0) \quad (3.74)
\end{aligned}$$

and

$$\begin{aligned}
P_k &= 2 \bar{R}_{xy} \hat{s}_{xy} + 2 \hat{r}_{xy} \bar{S}_{xy} \\
&+ \bar{R}_{xx} \hat{s}_{xx} + \bar{R}_{yy} \hat{s}_{yy} \quad (3.75)
\end{aligned}$$

Assuming that the normal stresses are small and using equation (3.30) the production term becomes

$$P_k = \frac{\bar{v}_t}{v} (\bar{U}')^2 \left[\frac{2 \hat{s}_{xy}}{\bar{S}_{xy}} + \frac{\hat{v}_t}{v_t} \right] \quad (3.76)$$

The velocity field is obtained by solving the stream function equation (3.13) simultaneously with equations (3.71)-(3.76).

The boundary conditions at the wave surface and at large values of y for the fluctuating energy and dissipation are

$$\hat{k} = \hat{\epsilon} = 0 \quad \text{at } y = 0 \quad (3.77.1)$$

and

$$\hat{k} = \hat{\epsilon} = 0 \quad \text{for large } y \quad (3.77.2)$$

Since equations (3.72) and (3.73) are singular at $y = 0$ the boundary conditions at the wave surface cannot be used in the form presented in equation (3.77.2). If a Taylor series expansion is made on equations (3.70) and (3.71) about $y = 0$ the following boundary conditions are arrived at

$$k - \frac{\delta_d k'}{2} = 0 \quad (3.78.1)$$

$$\text{at } y = \delta_d$$

$$\hat{\epsilon} - \frac{\delta_d \hat{\epsilon}'}{2} = 0 \quad (3.78.2)$$

where δ_d is a small distance from the wave surface.

(d) Streamline Curvature

The influence of streamline curvature is taken into account at the zero equation level of turbulence modeling by modifying the plane shear mixing length relation equation (3.35) in the manner suggested by Bradshaw.

$$l = l_0 (1 - \beta_c R_{i_c}) \quad (3.79)$$

Here β_c is an empirical constant and R_{i_c} is the curvature Richardson number defined as

$$R_{i_c} = \frac{2U}{R_c \frac{\partial U}{\partial y}} \quad (3.80)$$

where $1/R_c$ is the curvature of the streamlines. For small amplitude waves

$$1/R_c = -a \frac{(F - \bar{U})}{\bar{U}} \alpha^2 e^{i\alpha x} \quad (3.81)$$

in boundary layer coordinates. The details of this derivation are given in Appendix D.

Bradshaw suggests that an effective radius of curvature, R_{eff} , satisfying a first order lag equation be used

$$\frac{d}{dx} \frac{1}{R_{c_{eff}}} = \frac{\frac{1}{R_c} - \frac{1}{R_{c_{eff}}}}{k_c} \quad (3.82)$$

Here k_c is the curvature lag constant. Solving the above equation for a periodic variation, the effective radius of curvature of the streamlines is

$$\frac{1}{R_{c_{eff}}} = \frac{1}{R_c (1 + i\alpha k_c)} \quad (3.83)$$

Using, $1/R_{c_{eff}}$ in equation (3.80) and neglecting terms of $O(a^2)$, the curvature Richardson number can be written as

$$R_{i_c} = a \hat{R}_{i_c} e^{i\alpha x} \quad (3.84)$$

where

$$a \hat{R}_{i_c} e^{i\alpha x} = - \frac{a^2 (F - \bar{U})}{\bar{U}' (1 + i\alpha k_c)} e^{i\alpha x} \quad (3.85)$$

The wave induced mixing length, eddy viscosity and shear stress distribution incorporating the effect of curvature are respectively

$$a \hat{\ell} e^{i\alpha x} = a \left[\kappa y \exp(-y/\bar{A}) \left(\frac{y}{\bar{A}} \right) \left(\frac{\hat{\tau}}{2} - \frac{\hat{A}}{\bar{A}} \right) - \bar{\ell}_o \beta_c \hat{R}_{1c} \right] e^{i\alpha x}, \quad (3.86)$$

$$a \frac{\hat{v}_t}{v} e^{i\alpha x} = a \left[\frac{\hat{s}_{xy}}{\bar{s}_{xy}} + \frac{2 \exp(-y/\bar{A})}{[1 - \exp(-y/\bar{A})]} \left(\frac{y}{\bar{A}} \right) \left(\frac{\hat{\tau}}{2} - \frac{\hat{A}}{\bar{A}} \right) - 2\beta_c \hat{R}_{1c} \right] \frac{\bar{v}_t}{v} e^{i\alpha x}, \quad (3.87)$$

$$a \hat{\tau} e^{i\alpha x} = a \left[(2\bar{v}_t/v + 1) 2\hat{s}_{xy} - \frac{2\bar{v}_t/v \bar{U}' \exp(-y/\bar{A})}{[1 - \exp(-y/\bar{A})]} \left(\frac{y}{\bar{A}} \right) \frac{\hat{A}}{\bar{A}} - 2\beta_c \hat{R}_{1c} \right] e^{i\alpha x}$$

$$\left[1 - \frac{\bar{v}_t \bar{U}' \exp(-y/\bar{A})}{[1 - \exp(-y/\bar{A})]} \left(\frac{y}{\bar{A}} \right) \right] \quad (3.88)$$

(e) Finite Boundary Layer Calculation

The calculations thus far have assumed that the boundary layer is sufficiently deep such that in the region where the wave induced flow is negligible the average velocity profile is still logarithmic. The problem has therefore been characterized by a single parameter the wave number, α . In this section the requirement of an infinite boundary layer thickness is relaxed.

e.1 Mean Flow

The average velocity profile is assumed to be given by the Coles proposal (see Cebeci and Smith [12]).

$$U = \int_0^y \frac{2 dy}{1 + \sqrt{1 + 4 \kappa^2 y^2 (1 - \exp(-y/\bar{A}))^2}} + \frac{2\Pi}{\kappa} \sin^2 \left[\frac{\Pi}{2} \frac{y}{\delta} \right] \quad (3.89)$$

where $\Pi = 0.55$ for a zero pressure gradient boundary layer and δ is the boundary layer thickness.

e.2 Eddy Viscosity

A finite boundary layer consists of two parts: a fully turbulent inner region, where the Reynolds stress distribution is calculated from equations (3.51) and (3.52) for the average and wave induced flows respectively and an outer region, where Cebeci [12] suggests that the mixing length is given as

$$\ell_o = \gamma \delta \quad y_c \leq y \leq \delta . \quad (3.90)$$

Here γ is an empirically determined constant approximately equal to 0.075 and y_c is obtained from the continuity of ℓ_o . The eddy viscosity is found using (3.34) to be

$$\left(\frac{v_t}{v} \right) = \gamma^2 \delta^2 |2 s_{xy}| \quad y_c \leq y \leq \delta \quad (3.91)$$

Neglecting terms of $O(a^2)$ the average eddy viscosity is

$$\left(\frac{\bar{v}_t}{v} \right) = \gamma^2 \delta^2 \bar{U}' \quad y_c \leq y \leq \delta \quad (3.92)$$

and the wave induced eddy viscosity is

$$a \left(\frac{\hat{v}_t}{v} \right) e^{i\alpha x} = a \gamma^2 \delta^2 2 \hat{s}_{xy} e^{i\alpha x} \quad y_c \leq y < \delta . \quad (3.93)$$

Using equation (3.30) the wave induced Reynolds stress in the outer region of the boundary layer becomes

$$a \hat{r}_{xy} e^{i\alpha x} = \frac{a \bar{v}}{\nu} 4 \hat{s}_{xy} e^{i\alpha x} \quad y_c \leq y \leq \delta \quad (3.94)$$

The details of the finite boundary layer calculation are presented in Appendix E.

CHAPTER 4

EXPERIMENTAL MEASUREMENTS AND RESULTS

The purpose of the experimental effort was to obtain data which can be used to compare the various turbulence models developed in Chapter 3 for the wave induced Reynolds stresses. The data consist of time average shear stress profiles and profiles of the root mean square value of the fluctuating velocity gradient at the wave surface. The measurements were made in the large aspect ratio channel used by Thorsness [70]. Wall stresses were measured with electrochemical techniques.

To test the theory developed, data had to be obtained over the range of dimensionless wave numbers of $0.0005 < \alpha = \frac{2\pi v}{\lambda u^*} < 0.01$. It was possible to meet the above requirement by modifying existing equipment in one of two ways. The facility could be redesigned so as to increase the range of friction velocities attainable by a factor of four or waves of four times the previously used wavelength could be employed. Cook [15] has shown that for a given channel the minimum channel height to wavelength ratio that can be used before the upper wall interferes with the measurements at the wave surface is $\frac{h}{\lambda} = 1$. This condition would have required the construction of a new channel if waves of longer wavelength were to be used. For this reason it was decided to use the existing channel and to install a pumping network that would provide the necessary range of friction velocities.

Since the measurements are to be compared with linear theory, the amplitude of the wave model used in gathering the data had to be sufficiently small so as to prevent the appearance of higher order harmonics in the data. Zilker has demonstrated that provided the

dimensionless amplitude, $\frac{a_d u^*}{\nu} < 30$, the contribution of second and higher order harmonics to the total shear stress profile is negligible.

(a) Flow Loop

The flow loop used in this study was originally built by G. W. Cook and modified by D. P. Zilker. The modifications necessary to carry out the experiments reported in this thesis are reported in detail by J. J. Buckles [9]. Consequently the description given here is limited to the essential features.

The flow loop shown in Figure 4.1 consists of a rectangular channel having a cross sectional area of 2 in. \times 24 in. and a length of 27.5 ft. The channel was originally designed to handle liquid flows for which the velocity profiles could be considered fully developed in the neighborhood of the test section. This portion of the channel consists of a 24 in. \times 27 in. removable section located at the far end of the 27.5 ft. run. It is here that the wave model used in the experiments was inserted.

Two pumps connected in parallel were used in the experiments. The smaller pump is a Worthington 6 CNG84 centrifugal, 316 stainless steel model. It was driven by a 5 h.p. motor. This pump was used to deliver flow rates of up to 800 (g.p.m.) corresponding to a channel Reynolds number, $\frac{U_b h/2}{\nu} = 42,000$, at room temperature. The larger pump constructed from 316 stainless steel is a Worthington model 1050-D centrifugal pump and is driven by a 60 h.p. motor. This pump is able to deliver flow rates of up to 2700 (g.p.m.) corresponding to $\frac{U_b h/2}{\nu} = 120,000$. The range of friction velocities obtained with the two pumps is 2.93×10^{-2} ft/sec $< u^* < 5.86 \times 10^{-1}$ ft/sec. The pumping network is shown in Figure 4.2. All piping and fittings were either 6 in. or 8 in. Celanese schedule

Figure 4.1. Schematic Diagram of Flow Loop

1. Down stream rectangular to round diffuser
2. Removable wave surface
3. Test section
4. Channel
5. Honeycomb
6. Up stream rectangular to round diffuser
7. Annubar flow meter
8. Butterfly throttling valve
9. Removable blanking plate
10. Diaphragm valve
11. Small pump
12. By pass diaphragm valve
13. Large pump
14. Cooling coils
15. Reservoir tank

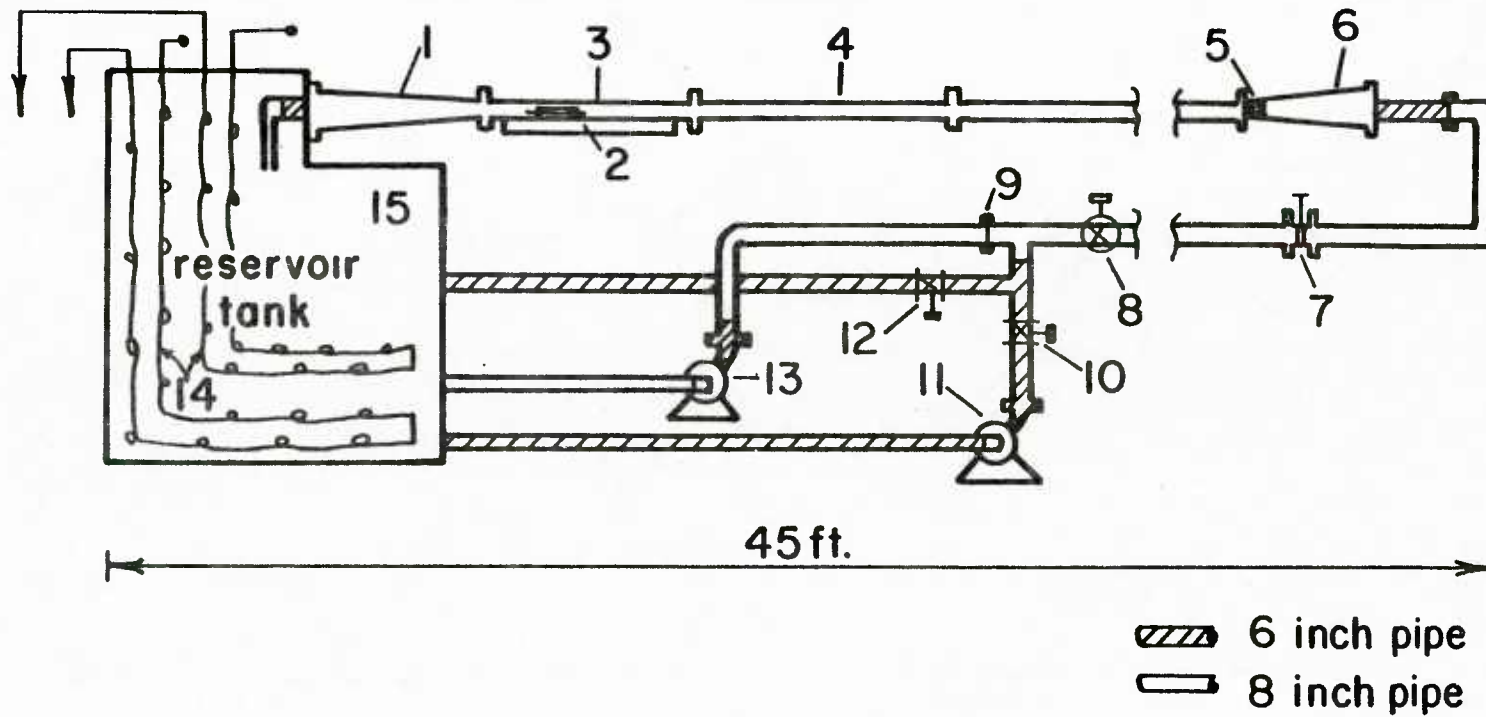


Figure 4.1. Schematic Diagram of Flow Loop

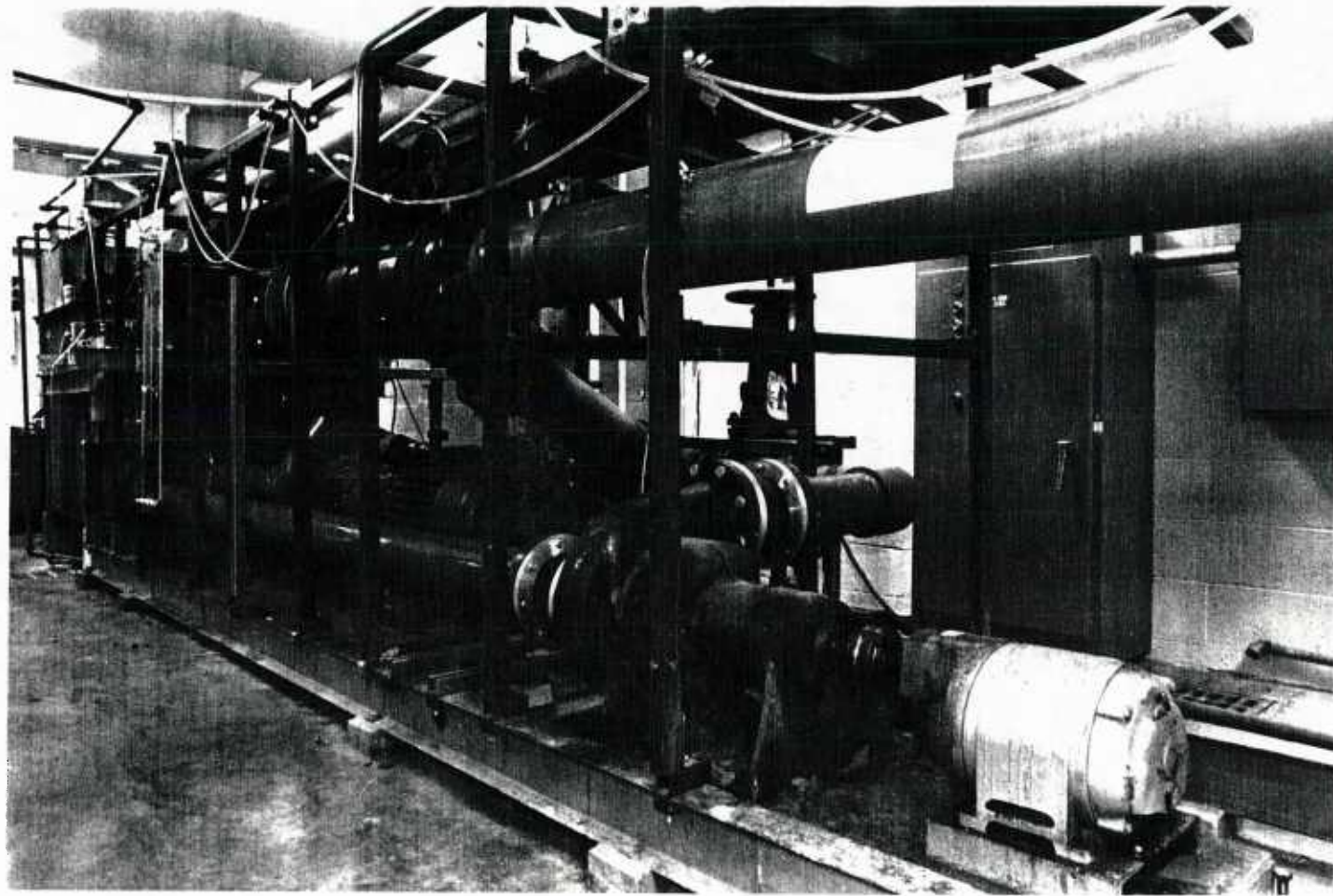


Figure 4.2. Photograph of Pumping Network

80 P.V.C. Provisions were available for flow rate and temperature control. An additional set of cooling coils had to be installed in the recirculating tank to maintain temperature control when running with the large pump. The flow rate was monitored by using an annubar connected to either a mercury or mirriam oil filled manometer.

(b) Test Section

A wave with a $\frac{2 a_d}{\lambda}$ ratio of 0.014 and a wavelength of 2 in. was used in this study. Six cutting tools were made for the fabrication of the wave surface. Four of the cutting tools were used to construct complete waves, Figure 4.3, while the remaining two, Figure 4.4, were used so as to mesh the leading and lagging waves into the flat portion of the wave section which lined up with the channel. The cutting tools were made from hardened steel using a new approach. A computer controlled mill which automatically compensated for the radius of curvature of the mill was used to generate the tools. The tools were 2 in. in length and machined according to the relationship $y = a_d \sin (2\pi x/\lambda)$. The cutting edge of the tools had a $9\frac{1}{2}^\circ$ slope and therefore the amplitude of the tools had to be compensated for in order to provide the required wave amplitude. The formula used to calculate this compensation is $a_d(\text{actual wave}) = a_d(\text{cutting tool})/\cos(\theta)$, where θ is the angle of the cutting tool edge.

The tools were placed in a rotary cutter assembly and a wave train consisting of ten complete wavelengths was machined into a 27 in. \times 24 in. \times 2 in. thick plexiglass section. The waves were machined perpendicular to the mean flow direction. Finally the two waves which meshed into the flat portions of the wave section were machined. A cross sectional view of the wave pattern is shown in Figure 4.5.

Amplitude of Cutting Tool Exaggerated

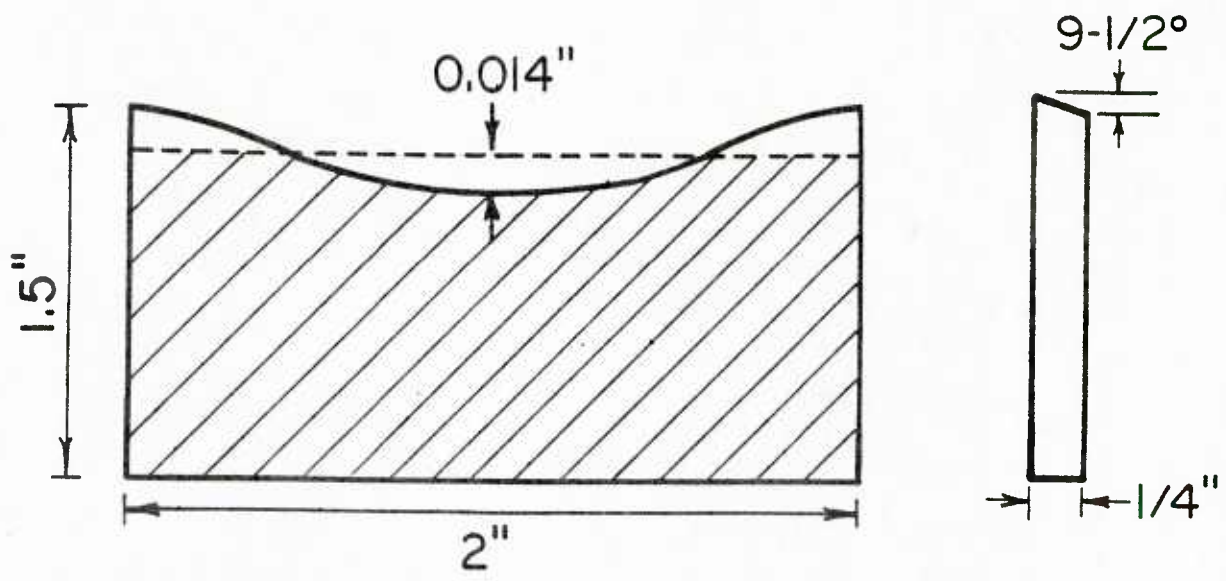


Figure 4.3. Cross Sectional View of Cutting Tool

Amplitude of Tool Exaggerated

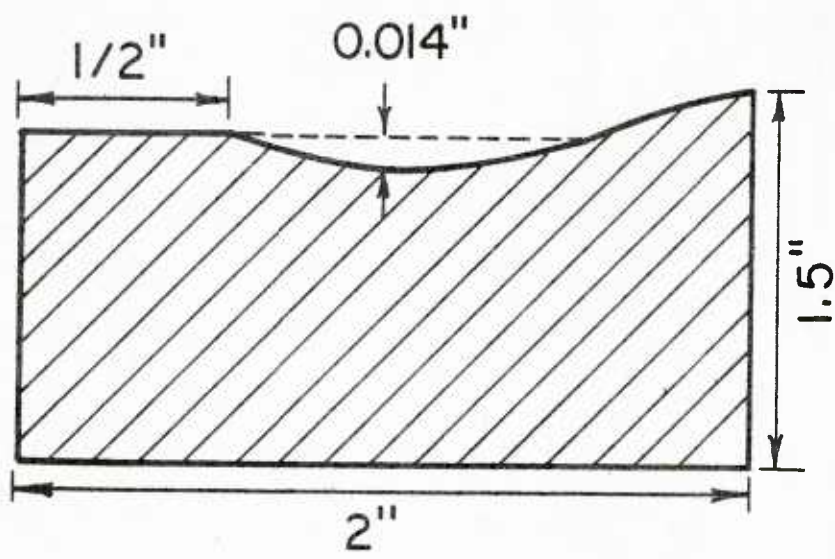


Figure 4.4. Cross Sectional View of End Cutting Tool

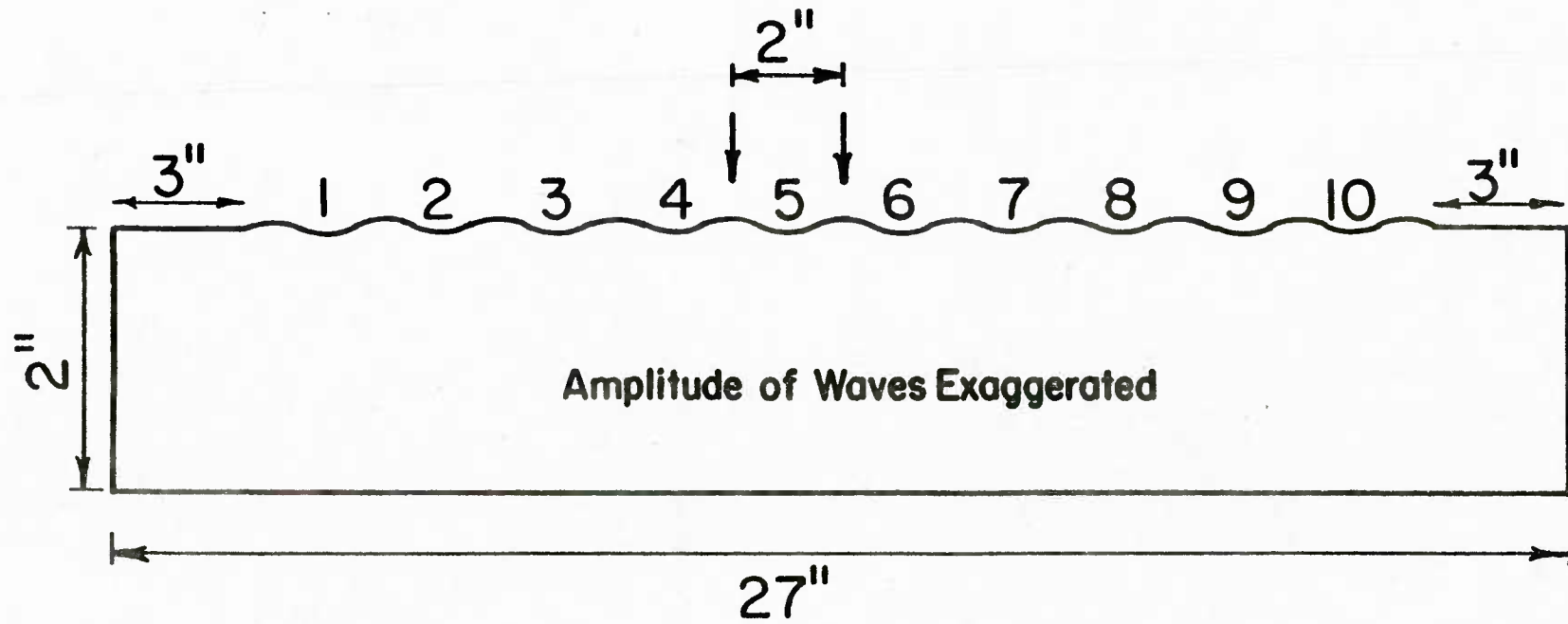


Figure 4.5. Cross Sectional View of Wave Surface

Holes for the electrodes were drilled into the wave surface according to the following pattern. Twenty-one holes of 0.025 in. diameter were drilled into the third and sixth waves respectively while a combined total of forty-one holes were drilled into the eighth and ninth waves. The electrode pattern shown in Figure 4.6 was chosen so as to minimize the interference between the electrodes and to test whether a fully developed flow field existed.

Platinum electrodes, 0.020 in. diameter, were epoxied into each of the holes using Techkits A-12 epoxy as follows. The epoxy was injected into a hole. Before the epoxy dried, a two inch piece of platinum wire, soldered onto a twelve inch coated copper wire, was inserted into the hole from the back of the wave section. A small amount of platinum wire was allowed to protrude on the wave side. The platinum wire was coated with a thin layer of epoxy prior to insertion into the holes.

Once dry the electrodes were filed down flush with the wave surface using a soft file. This had the advantage of not damaging the plexi-glass while removing the excess platinum. Once the electrodes were flush, the surface was sanded down with progressively finer grades of sandpaper, polished with DUPONT 0861N Rubbing Compound, and DUPONT 0761N Polishing Compound, and finally polished with Mirror Glaze Plastic Cleaner and Polish. On completion of the polishing, the profile of the waves was checked using a dial indicator.

The shear stress measurements were made over the sixth, eighth and ninth waves. Figure 4.7, 4.8 and 4.9 show the profiles of the above waves respectively as a function of x/λ , taking the wave trough to be

ELECTRODE PATTERN

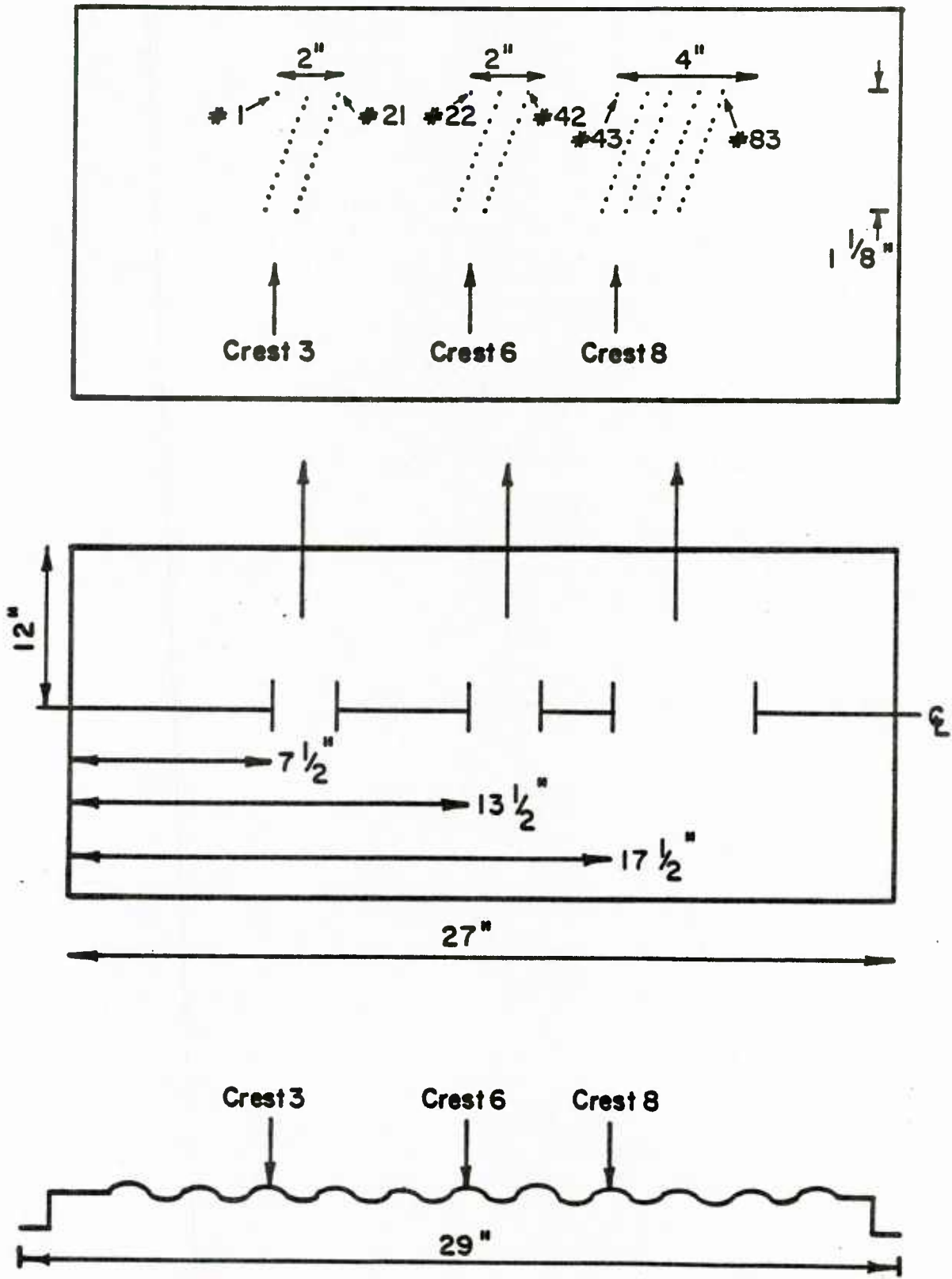


Figure 4.6. Electrode Pattern

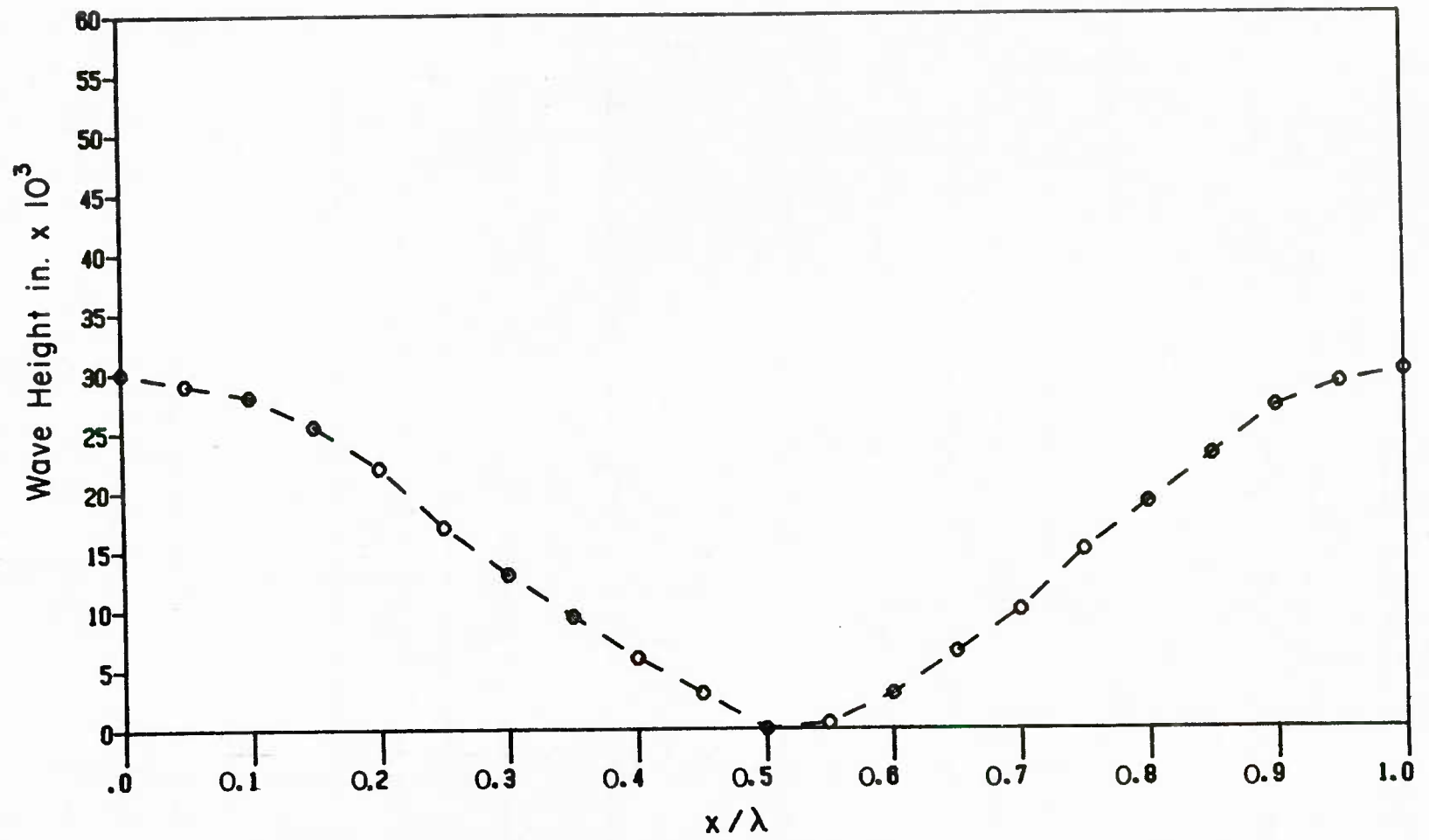


Figure 4.7. Profile of Wave 6

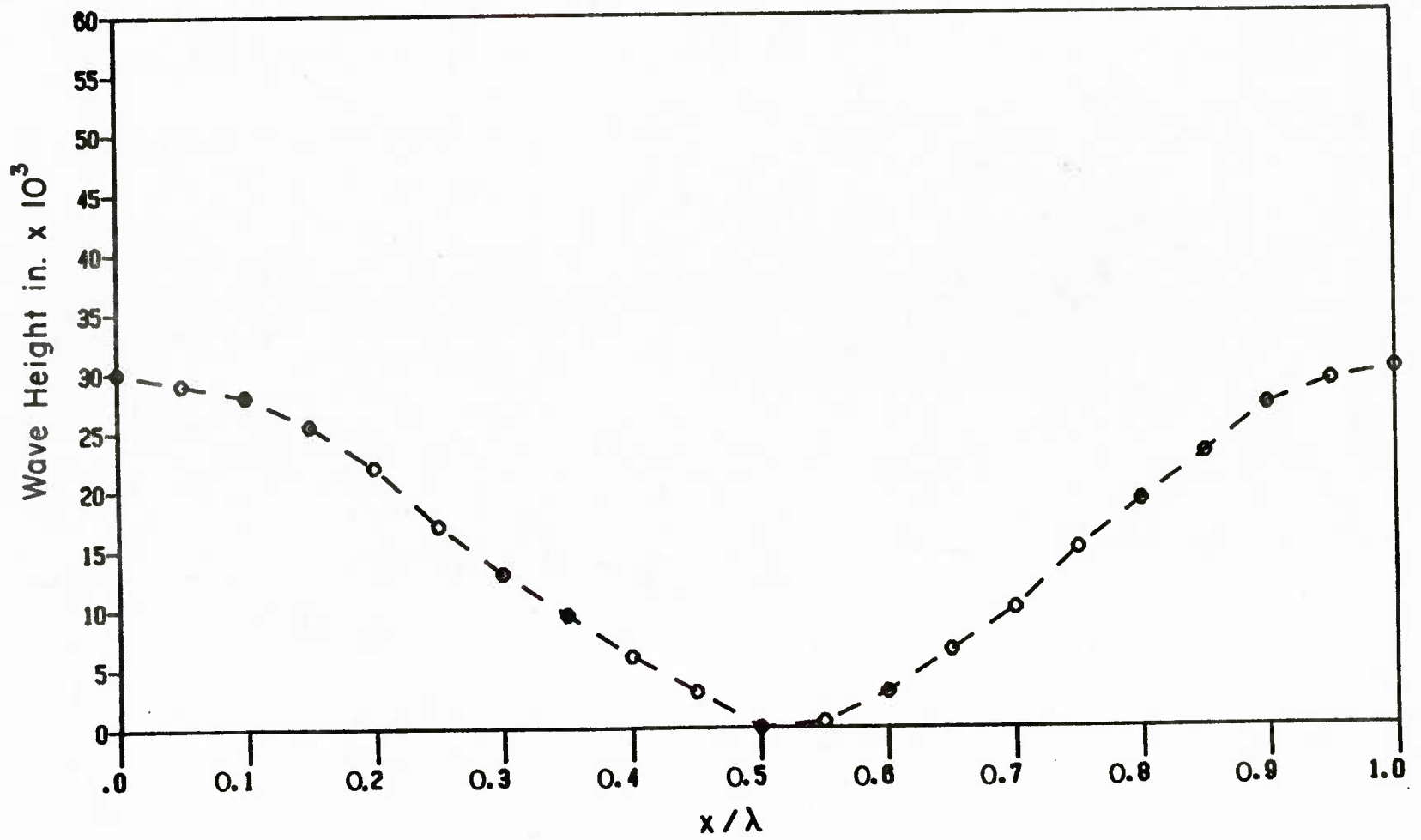


Figure 4.8. Profile of Wave 8

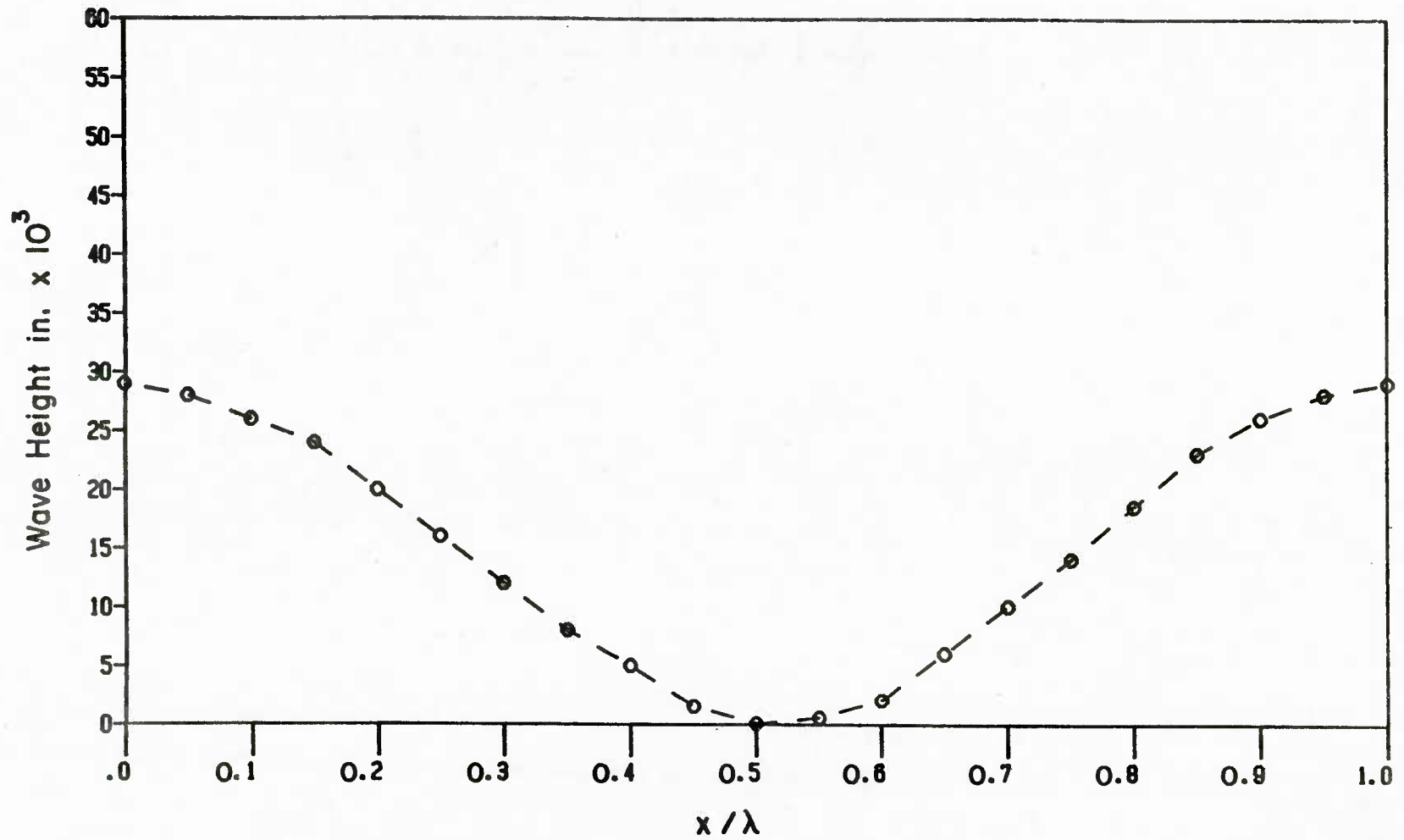


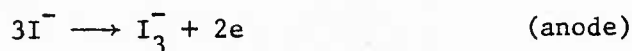
Figure 4.9. Profile of Wave 9

zero. The amplitude of each wave was estimated by performing a least squares analysis of the wave profile data. The maximum relative phase shift among the three wave profiles is less than 3° . The tabulated wave profile data is listed in Appendix F. Figures 4.10 and 4.11 show the front and back view of the completed wave section.

(c) Electrochemical Technique

The electrochemical technique which uses a diffusion controlled electrode for the measurement of wall shear stress was developed by Reiss [58] and Mitchell and Hanratty [47]. A chemical reaction occurs on an electrode which is embedded flush with the surface. The resulting reaction current is related to the wall shear stress. The electrochemical reaction employed is an oxidation reduction couple employing a large excess of supporting electrolyte. The cathode which is the shear stress probe is much smaller than the anode which makes the cathodic reaction the limiting step. By suitably adjusting the applied potential the concentration of active specie at the surface can be made equal to zero. The result is that the reaction rate and hence current flow becomes a function only of the rate of diffusion to the cathode. Consequently the current flow can be related directly to the mass flux at the surface and the physical properties of the system.

The redox reaction used in this study is the potassium iodide and iodine reaction system, in which the following reactions occur.



The approximate concentrations of I_3^- and the potassium iodide supporting electrolyte were 0.0015m and 0.2m respectively. The properties of the electrolyte are summarized in Appendix G.

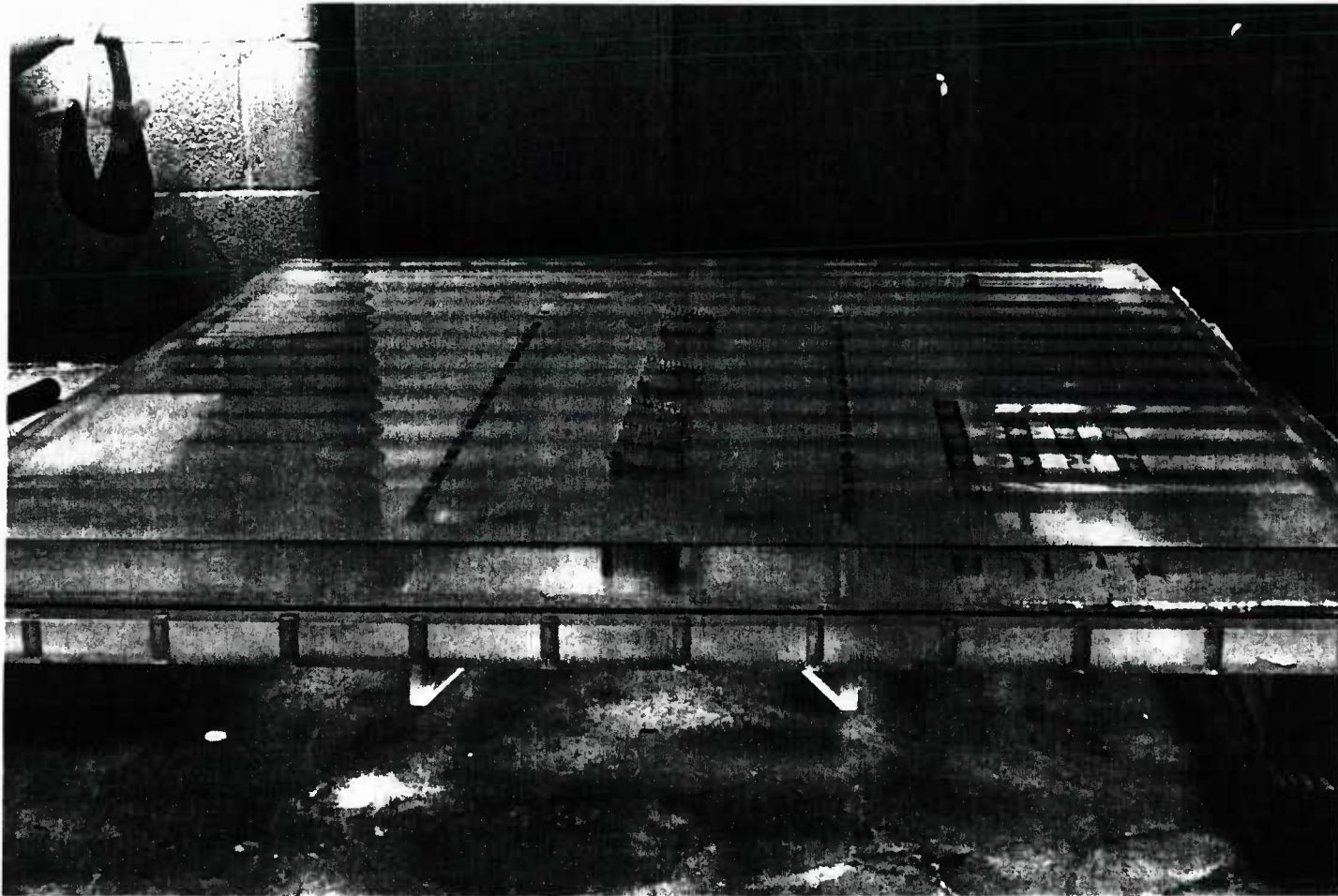


Figure 4.10. Photograph of Front View of Wave Section

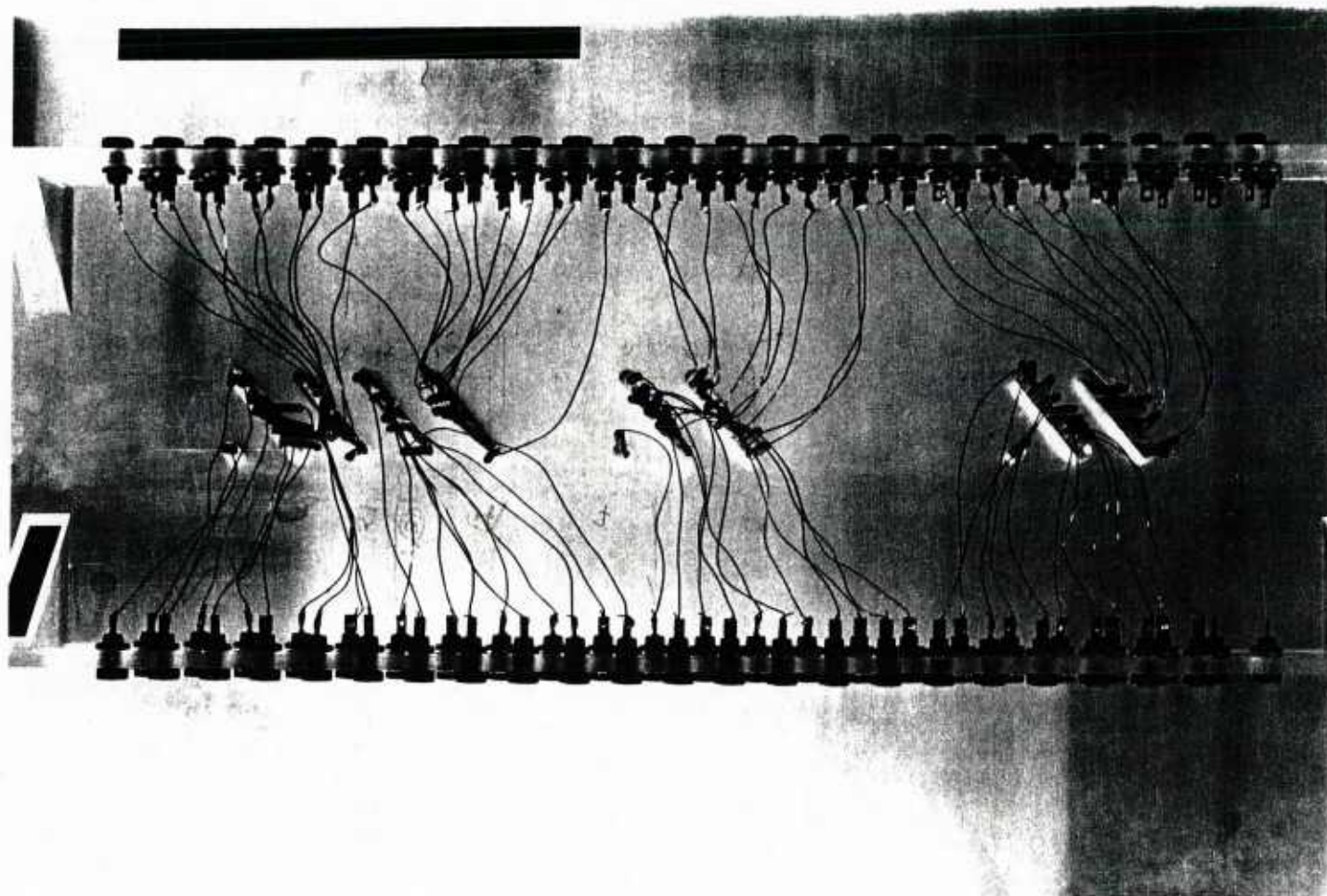


Figure 4.11. Photograph of Back View of Wave Section

Under these conditions a mass transfer coefficient may be defined by the relationship

$$K_m = \frac{I}{n_e F_a A_e C_b} \quad (4.1)$$

where I is the current at the cathode, n_e is the number of electrons involved in the reaction, F_a is Faraday's constant, A_e is the area of the electrode and C_b is the bulk electrolyte concentration. Through a solution of the mass balance equations Mitchell and Hanratty [47] have shown that the instantaneous mass transfer coefficient is related to the wall shear stress as follows

$$\tau_{w_d} = \left(\frac{2\Gamma(4/3) K_m^3}{3} \right) \left(\frac{9 L_e \mu}{D^2} \right) \quad (4.2)$$

where μ is the viscosity of the fluid, D is the diffusion coefficient for the reacting species and L_e is the equivalent length of the electrode, equal to 0.816 times the diameter of the electrode. Using equations (4.1) and (4.2) and neglecting the transverse component of the fluctuating stress τ'_{z_d} the current measured can be related to the wall shear stress as follows

$$I = C (\bar{\tau}_{w_d} + \tau'_{x_d})^{1/3} \quad (4.3)$$

where C is a proportionality constant and $\bar{\tau}_{w_d}$ and τ'_{x_d} are the time averaged and fluctuating wall shear stresses respectively. Furthermore if

$$\left(\frac{\tau'_{x_d}}{\bar{\tau}_{w_d}} \right)^2 \ll \left(\frac{\tau'_{x_d}}{\bar{\tau}_{w_d}} \right) \quad (4.4)$$

$$\bar{I} = C \bar{\tau}_{wd}^{-1/3} \quad (4.5)$$

and

$$\frac{I - \bar{I}}{\bar{I}} = \frac{1}{3} \frac{\tau'_{xd}}{\bar{\tau}_{wd}} \quad (4.6)$$

Equations (4.5) and (4.6) are the design equations used to determine the average and root-mean square value of the wall shear stress respectively.

(d) Data Acquisition

The electronic equipment used to measure the electrode currents was the same as that described in previous work, (Zilker [77]). Figure 4.12 gives a schematic representation of the basic electronics. A 118A amplifier was used to apply a negative potential to the alternate electrodes and to act as a current to voltage converter. The applied potential was set by the adjustment of a Helipot so that the potential was always kept in the mass transfer controlled plateau region. A feedback resistor, R_f , was used such that the output voltage, V_o , was between 2.5 and 3.5 volts. The output voltage was sampled with an Isaac-Cyborg twelve bit analog to digital, A/D, converter. The A/D converter was in turn linked to an Apple II plus computer. Up to sixteen channels could be sampled simultaneously at a sampling rate of 1 KHz . A block diagram representation of the data acquisition process is shown in Figure 4.13.

Data was stored in an integer basic format which allowed the Apple II to store approximately 22,000 data points in memory. A 6502 assembly language program was written for the purpose of analyzing the data. The program is able to calculate the mean and the variance of the output

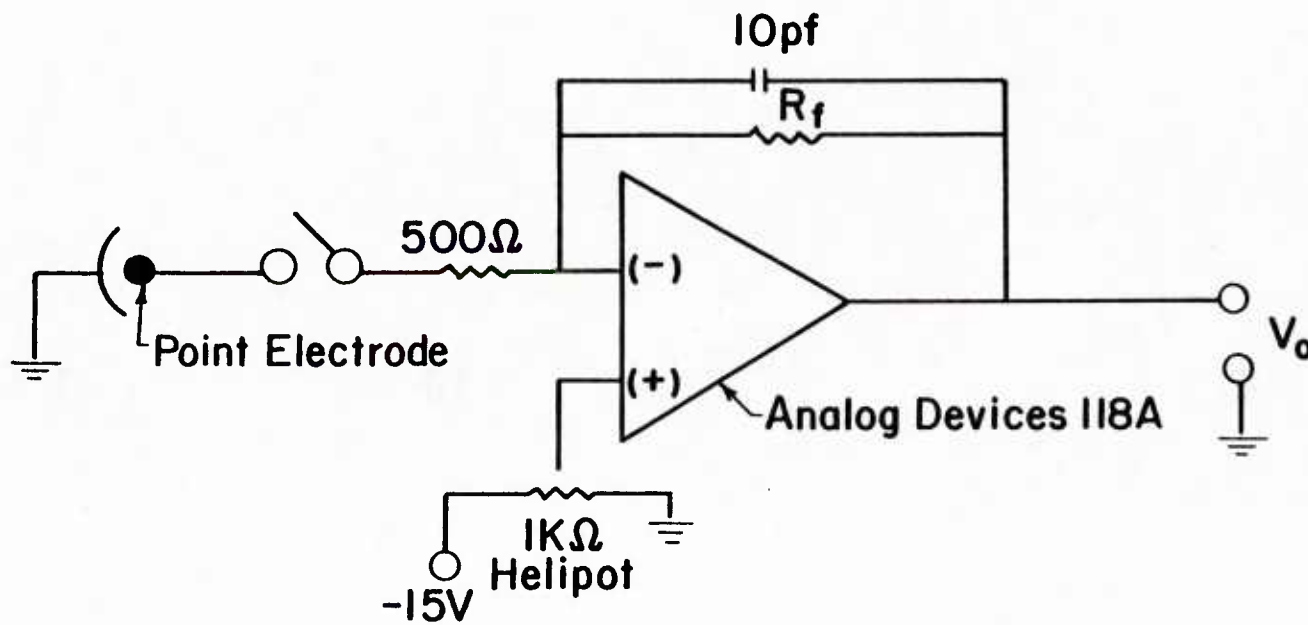


Figure 4.12. Electronic Circuit for Shear Stress Measurements

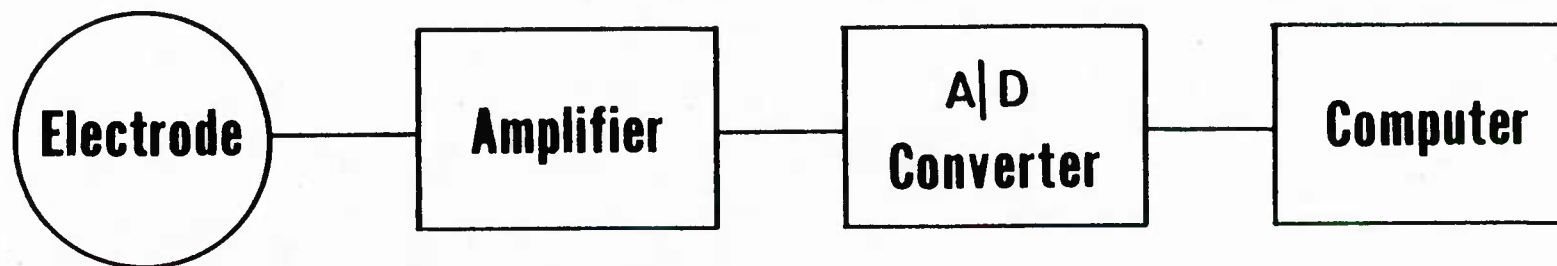


Figure 4.13. Schematic Diagram of Data Acquisition System

voltage minus the applied voltage, $(V_o - V_{app})$. Using these values and the design equations, (4.5) and (4.6) the average shear stress and the root mean square value of the fluctuating shear stress can be obtained as described in Appendix H. Provision was also made to transfer the raw data to a floppy disc so as to allow for further analysis if necessary.

(e) Shear Stress Measurements

Shear stress measurements were obtained using the previously described wave surface. Before each run was made the wave surface was cleaned with soapy water using a soft sponge. This was followed by thoroughly rinsing the wave surface with deionized water. The channel was filled with electrolyte and allowed to run for a period of time in order to remove any entrapped bubbles. The temperature was maintained at $(26 \pm 0.2) \text{ C}^\circ$. At the conclusion of a run a sample of fluid was taken and the required chemical and physical tests were performed as outlined in Appendix G.

Figures 4.14 through 4.34 show the measured time average shear stress profiles of selected number of runs. Measurements of the root mean square level of the fluctuating shear stress are shown in Figures 4.35 through 4.40. The average and fluctuating shear stress measurements are normalized with the wave averaged shear stress. The data are plotted with respect to a cosine wave such that $x/\lambda = 0$ corresponds to the upstream crest and $x/\lambda = 1$ corresponds to the downstream crest. On each plot a line is drawn through the points representing the best sinusoidal fit of the data. The curves were obtained by performing a least squares analysis of the data. The details of this analysis are presented in Appendix I.

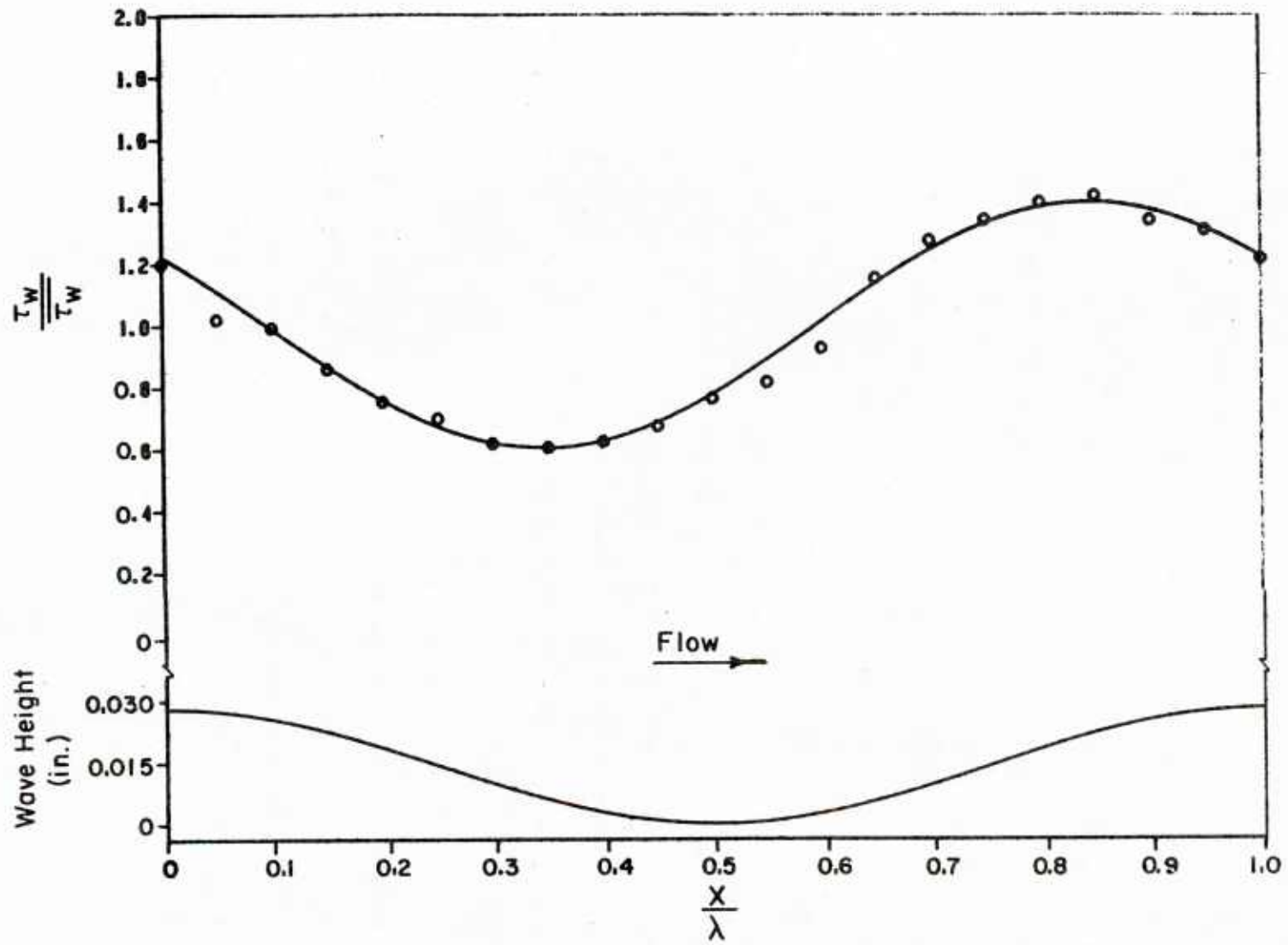


Figure 4.14. Shear Stress Distribution for $Re = 5,970$

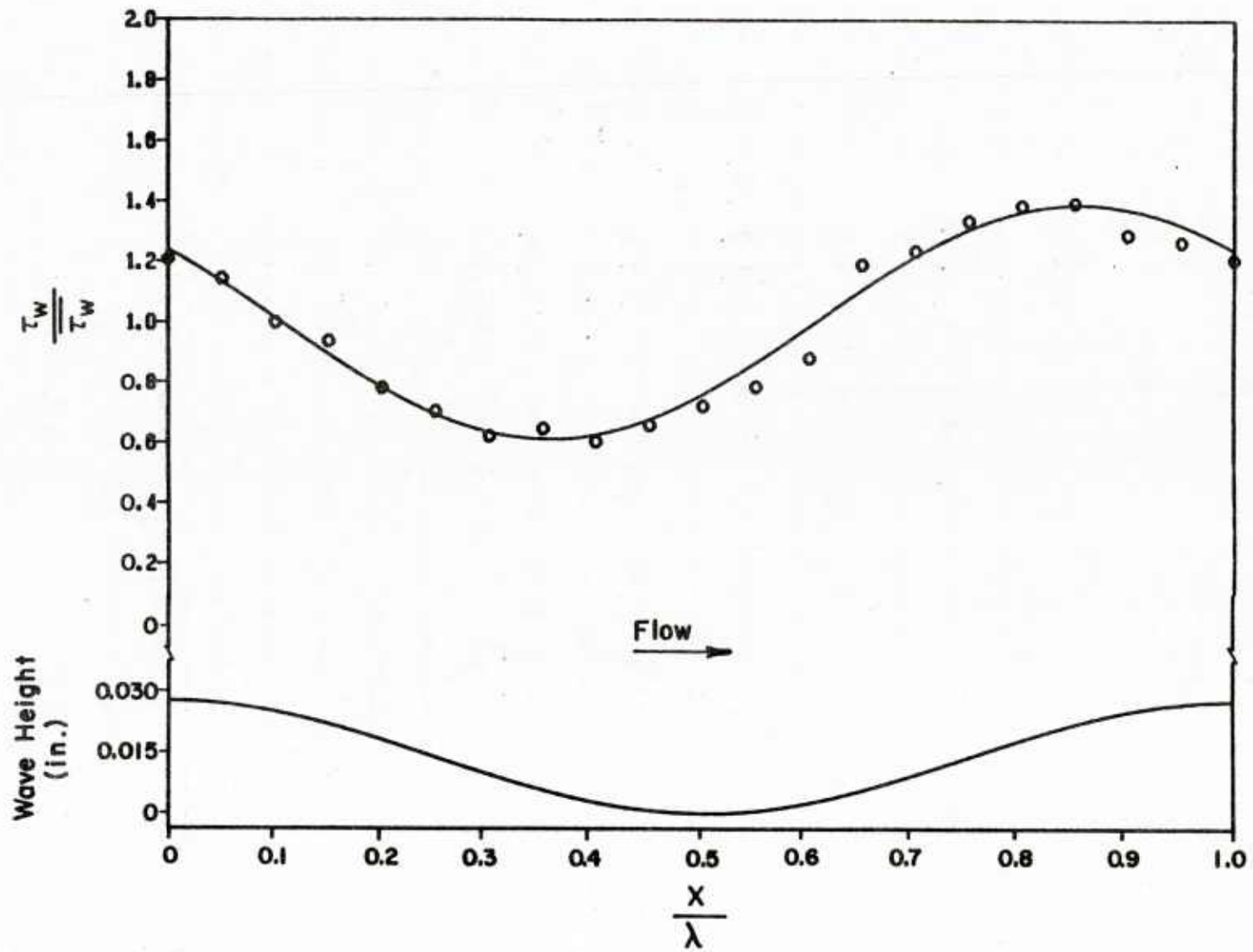


Figure 4.15. Shear Stress Distribution for $Re = 6,680$

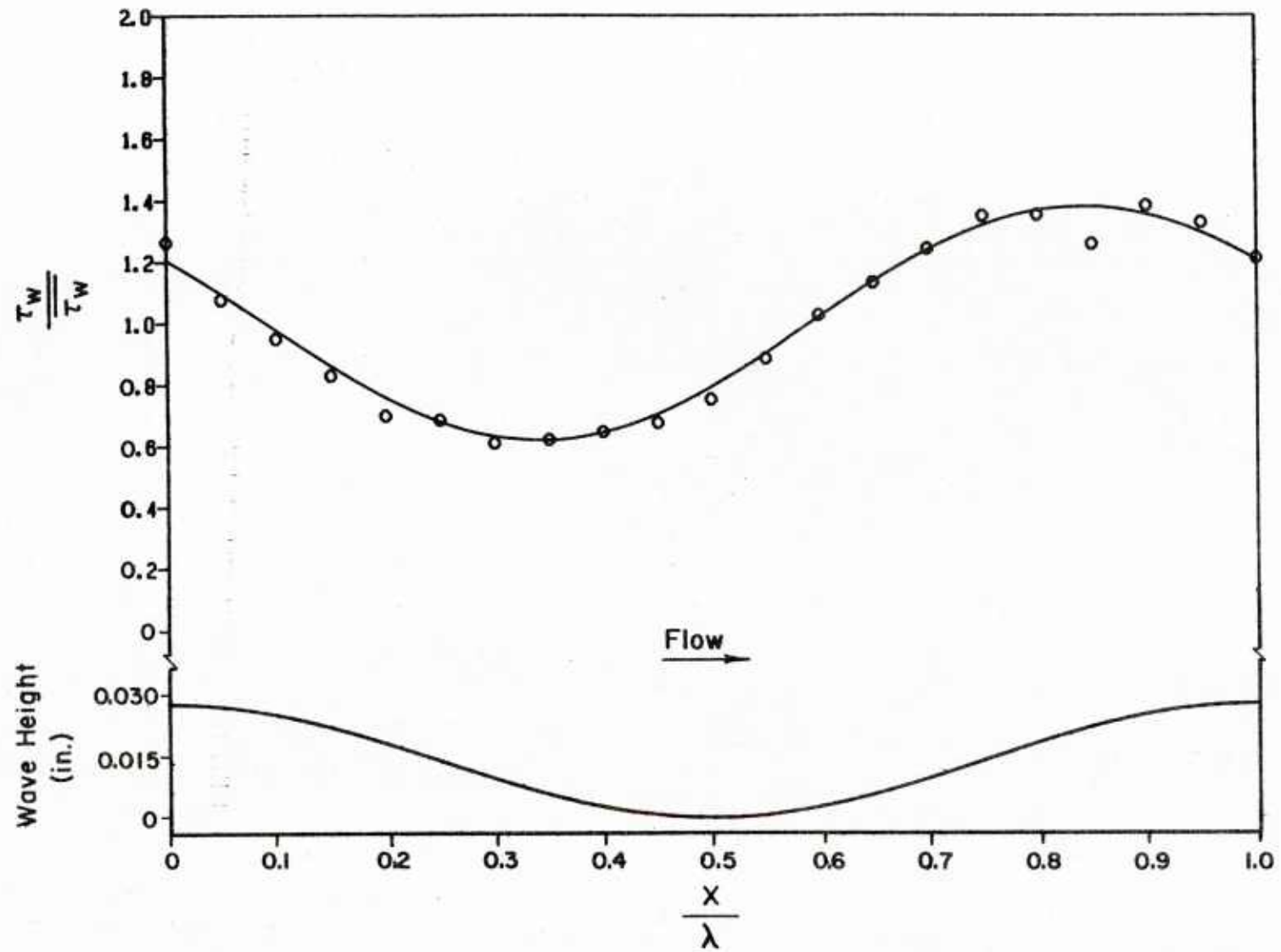


Figure 4.16. Shear Stress Distribution for $Re = 8,450$

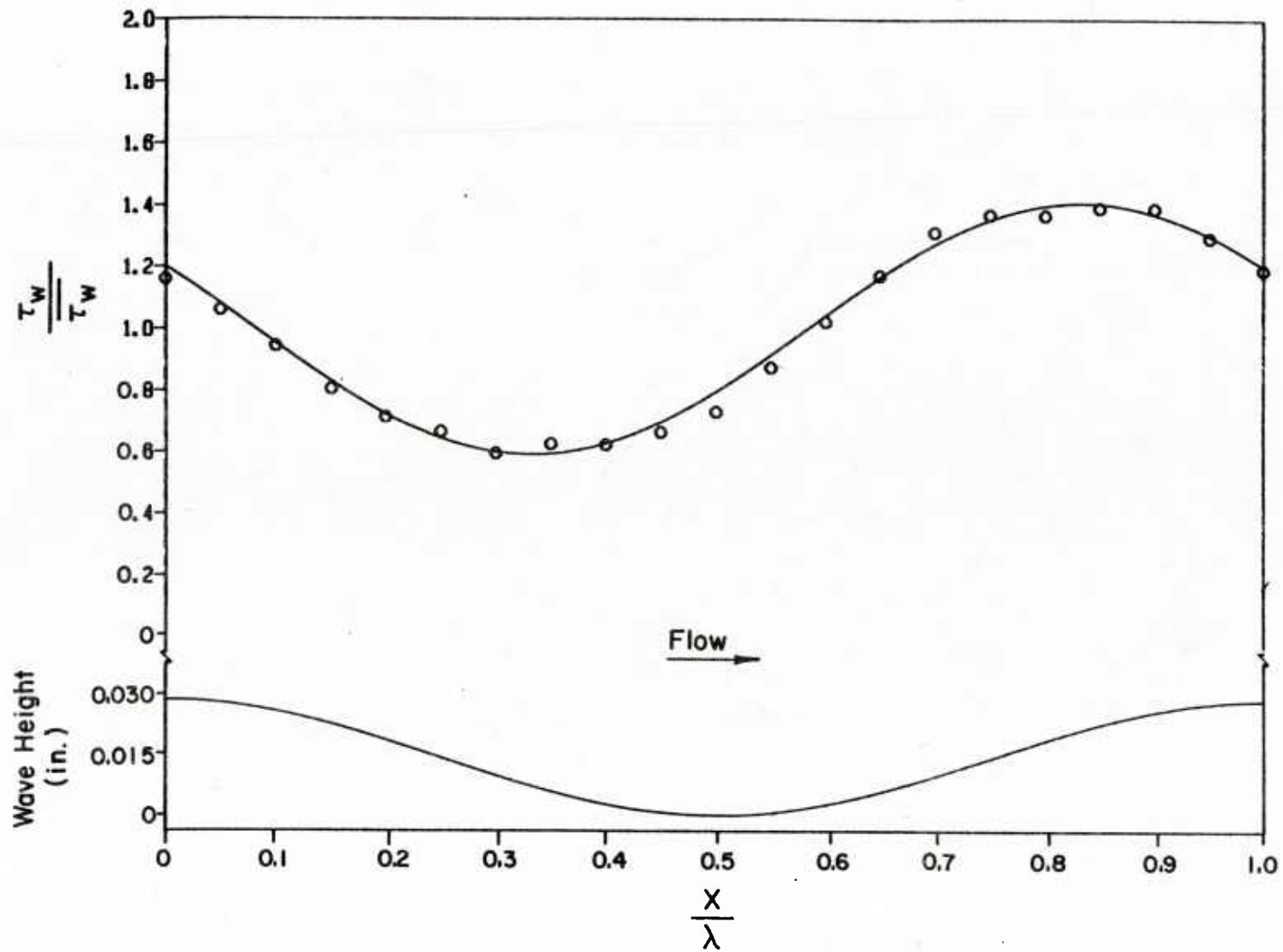


Figure 4.17. Shear Stress Distribution for $Re = 9,650$

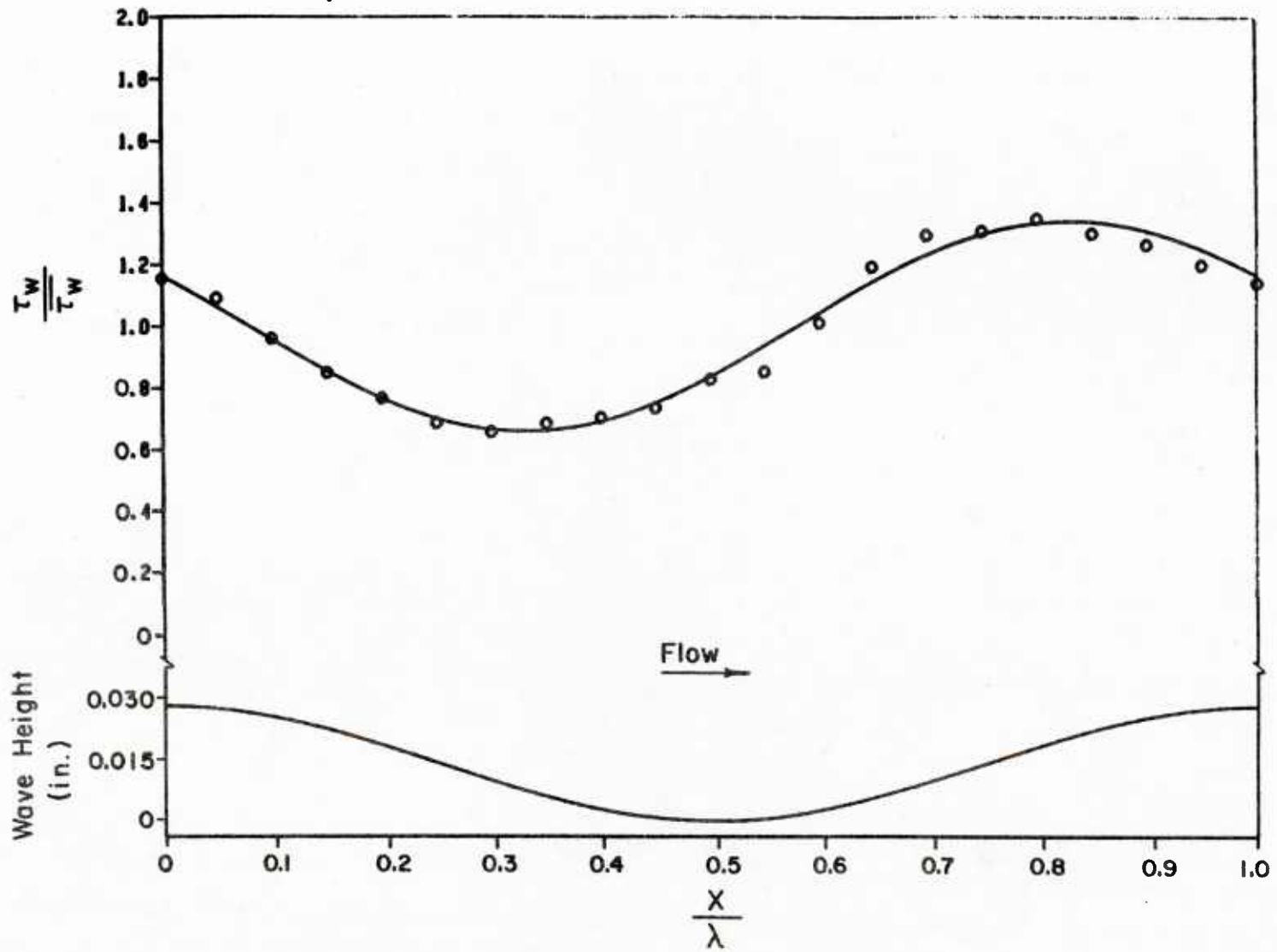


Figure 4.18. Shear Stress Distribution for $Re = 13,000$

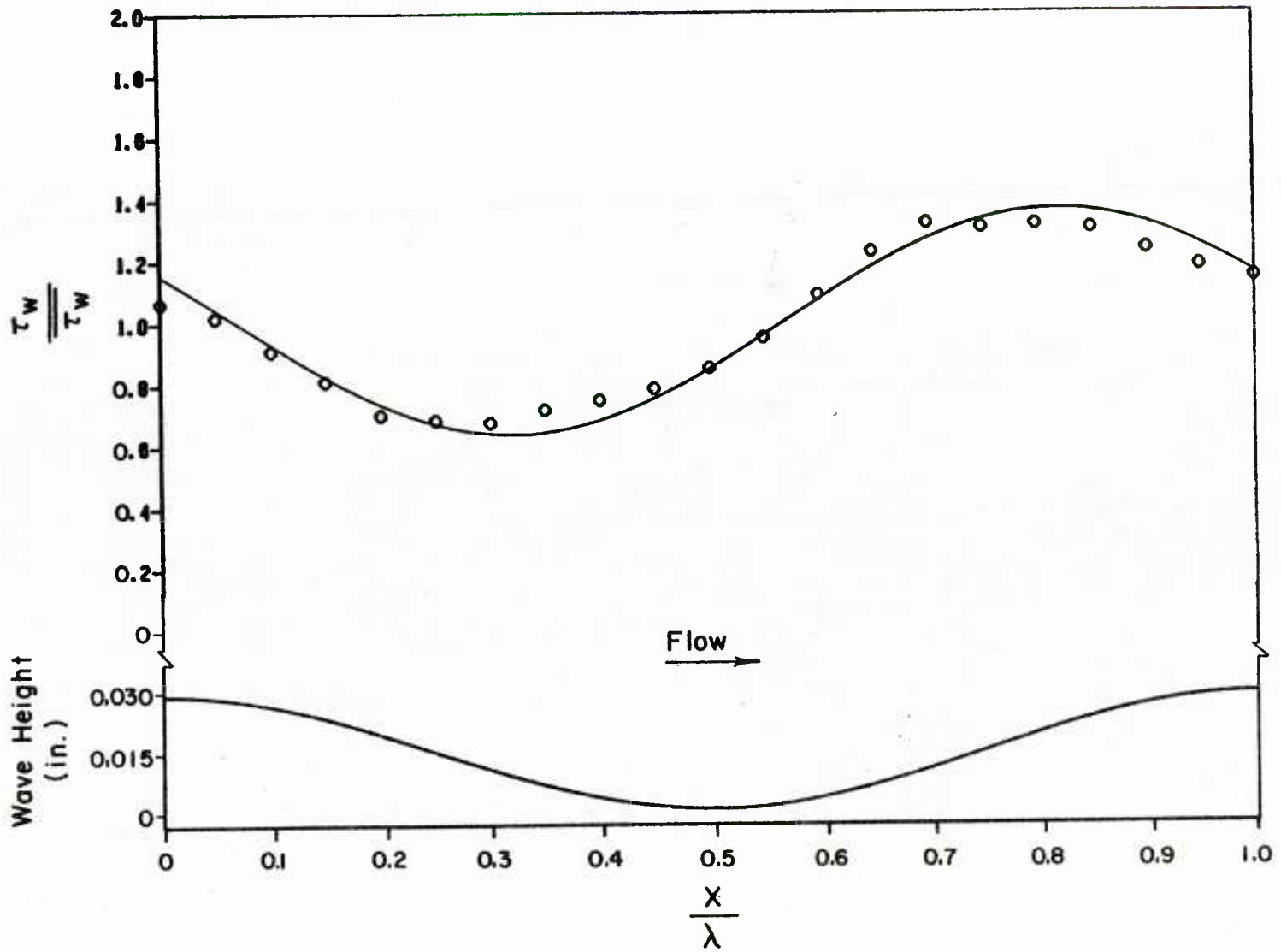


Figure 4.19. Shear Stress Distribution for $Re = 14,600$

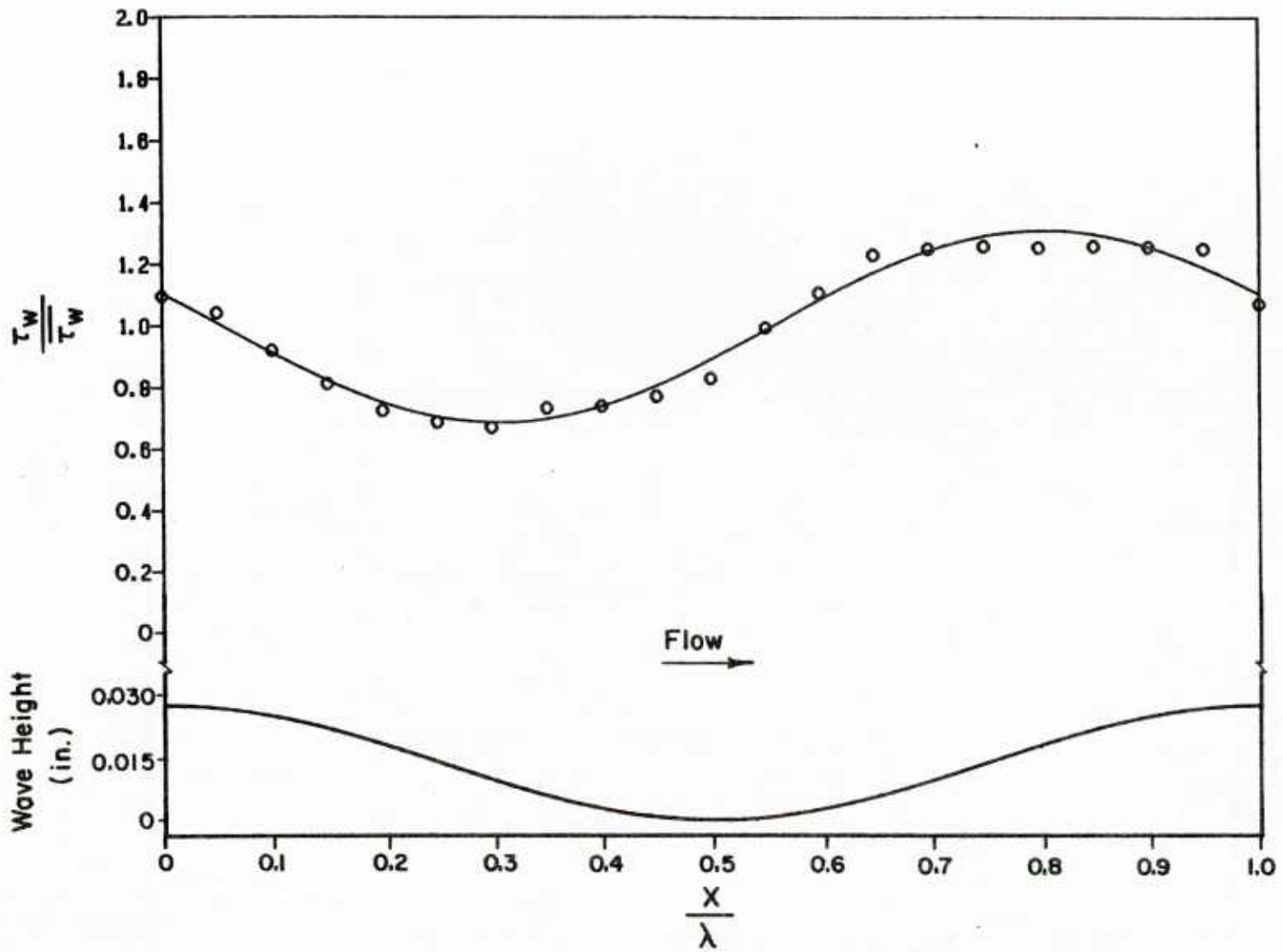


Figure 4.20. Shear Stress Distribution for $Re = 15,700$

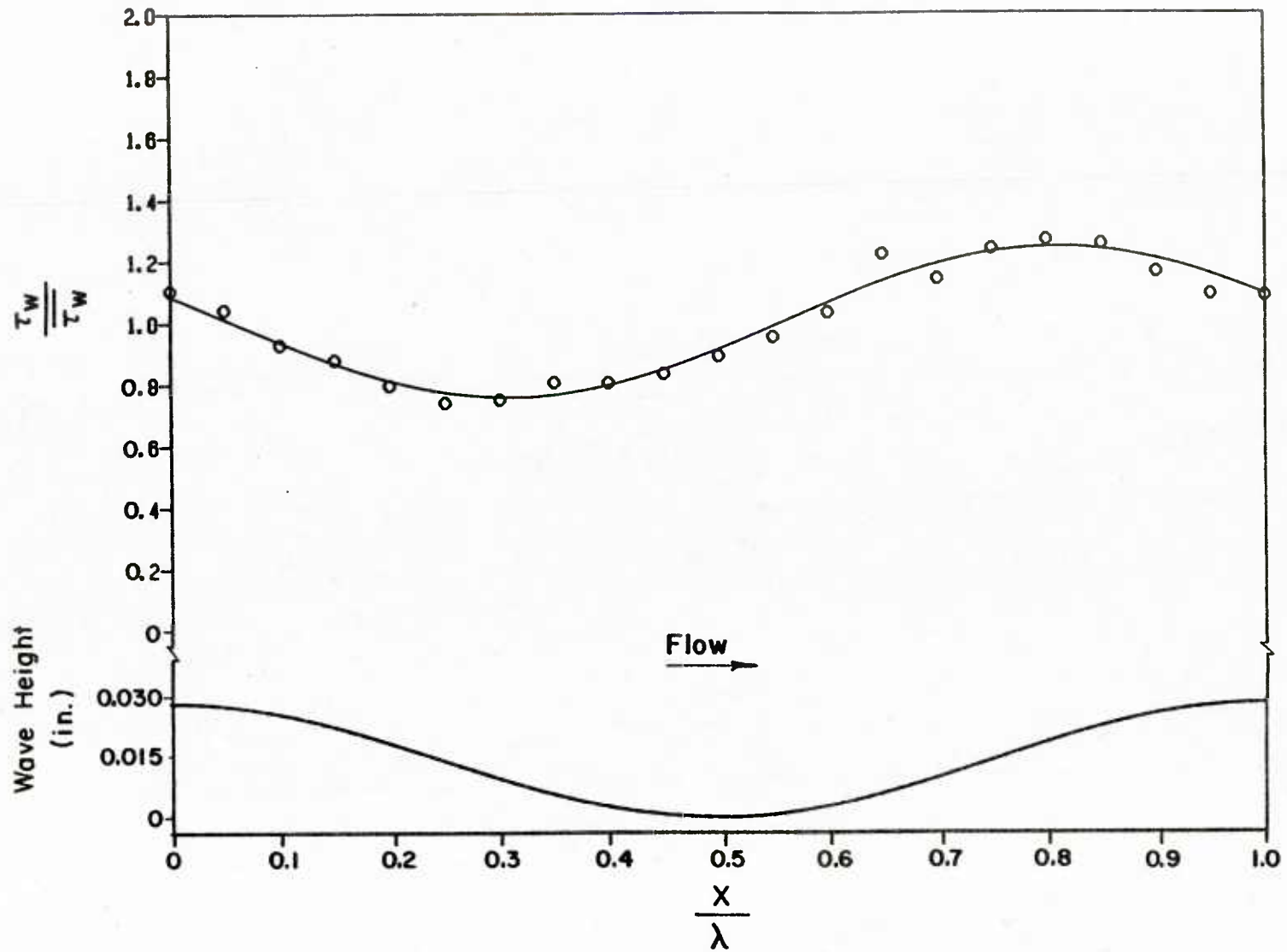


Figure 4.21. Shear Stress Distribution for $Re = 19,800$

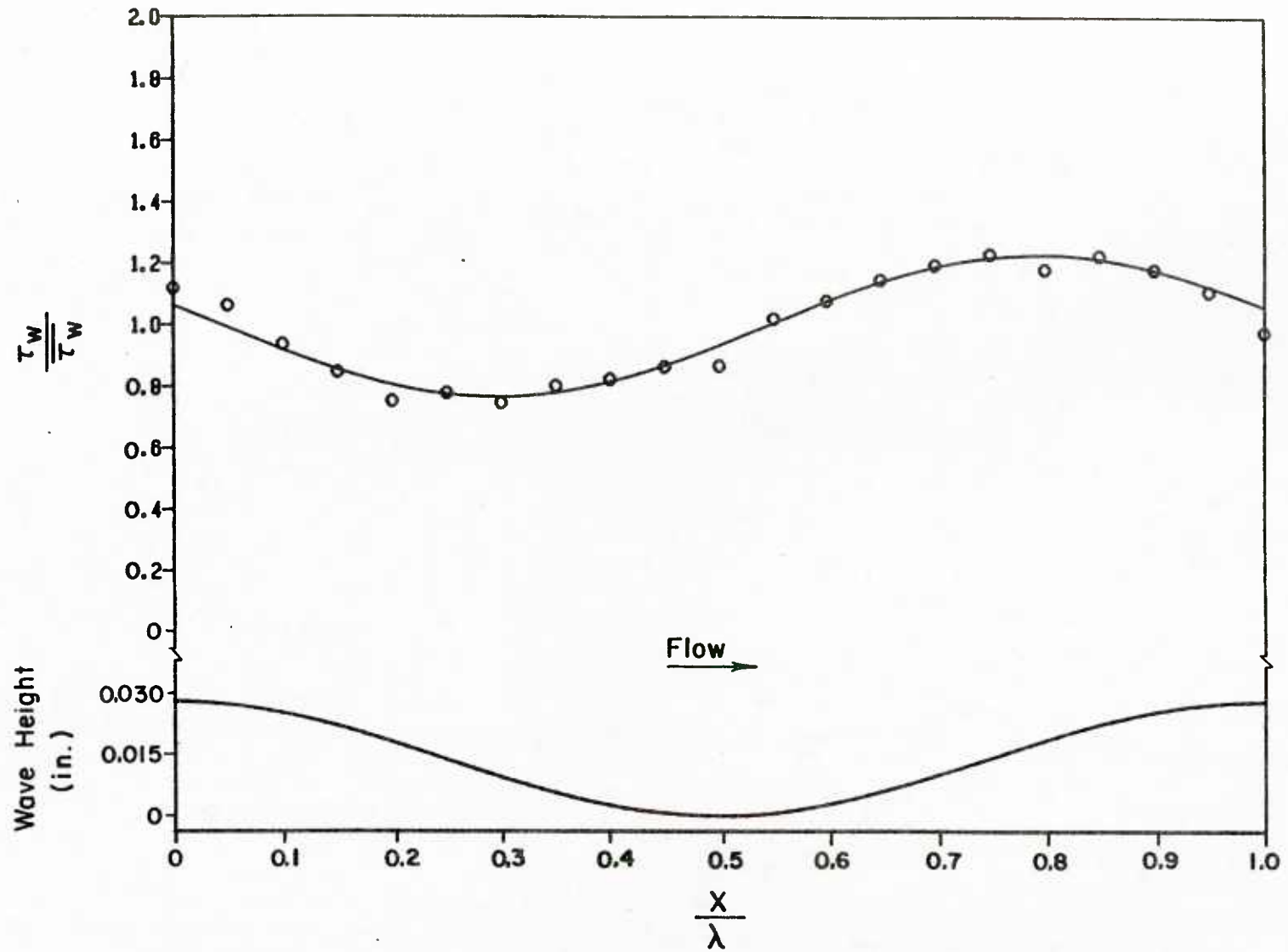


Figure 4.22. Shear Stress Distribution for $Re = 20,600$

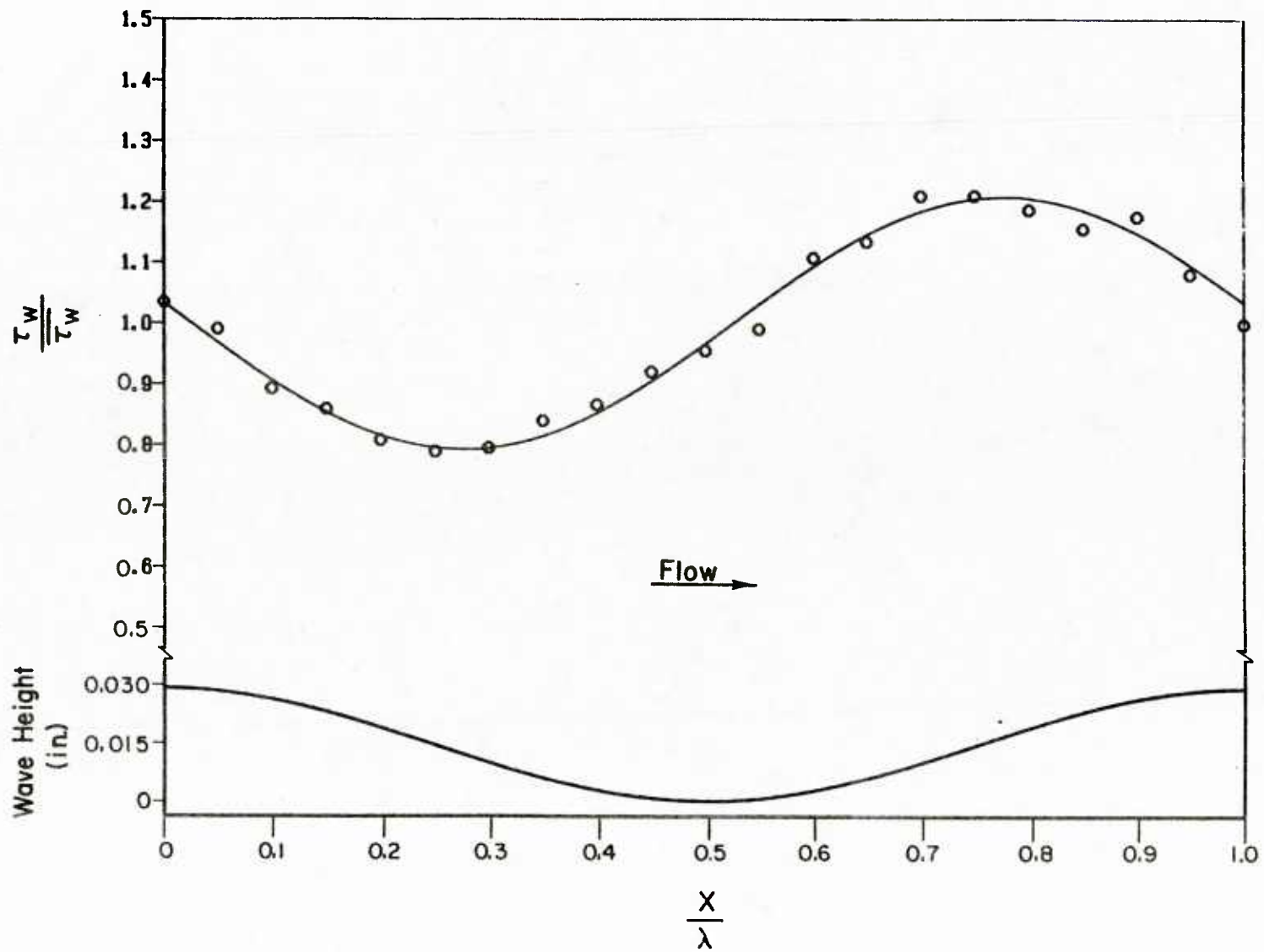


Figure 4.23. Shear Stress Distribution for $Re = 27,950$

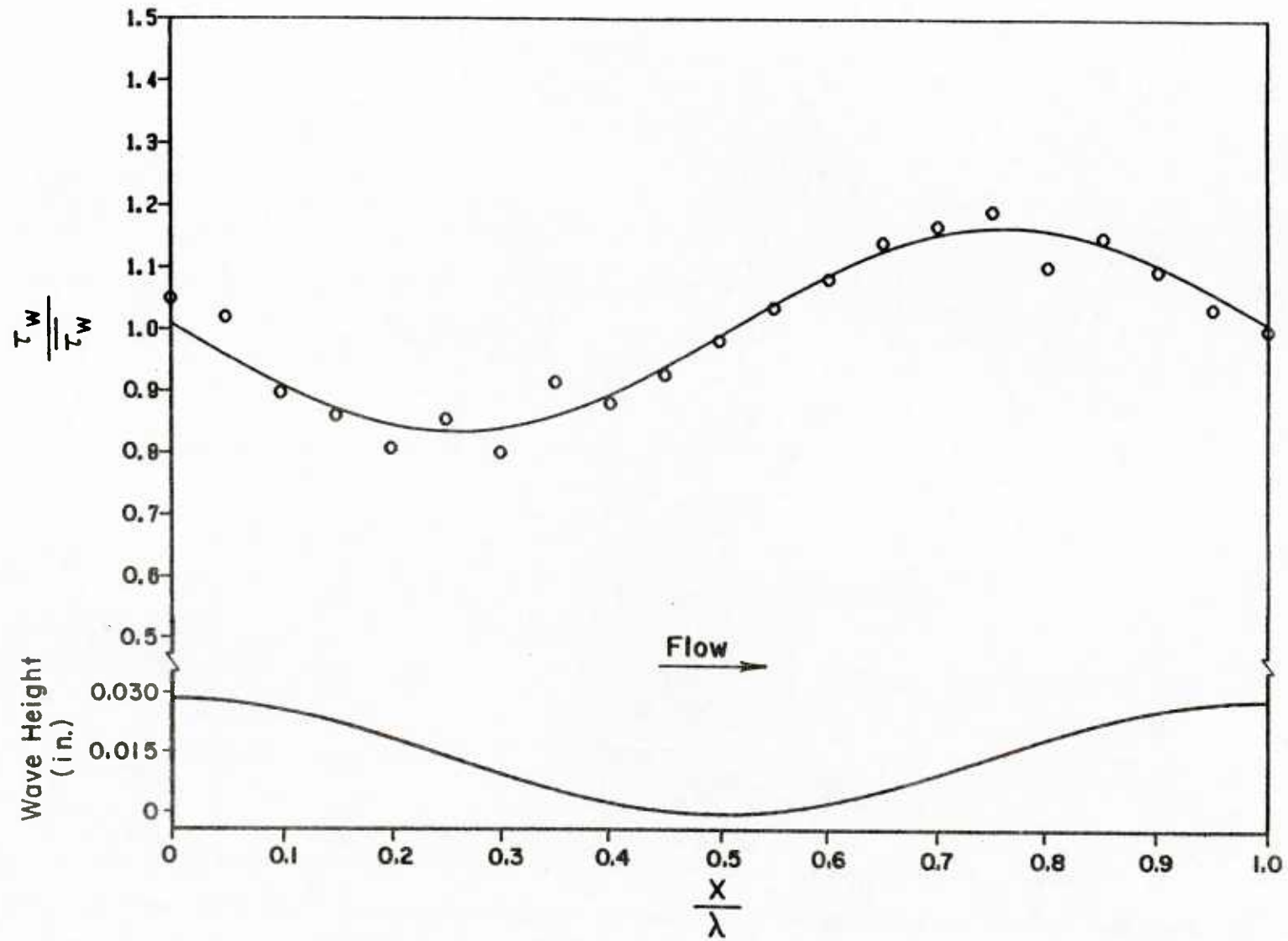


Figure 4.24. Shear Stress Distribution for $Re = 30,620$

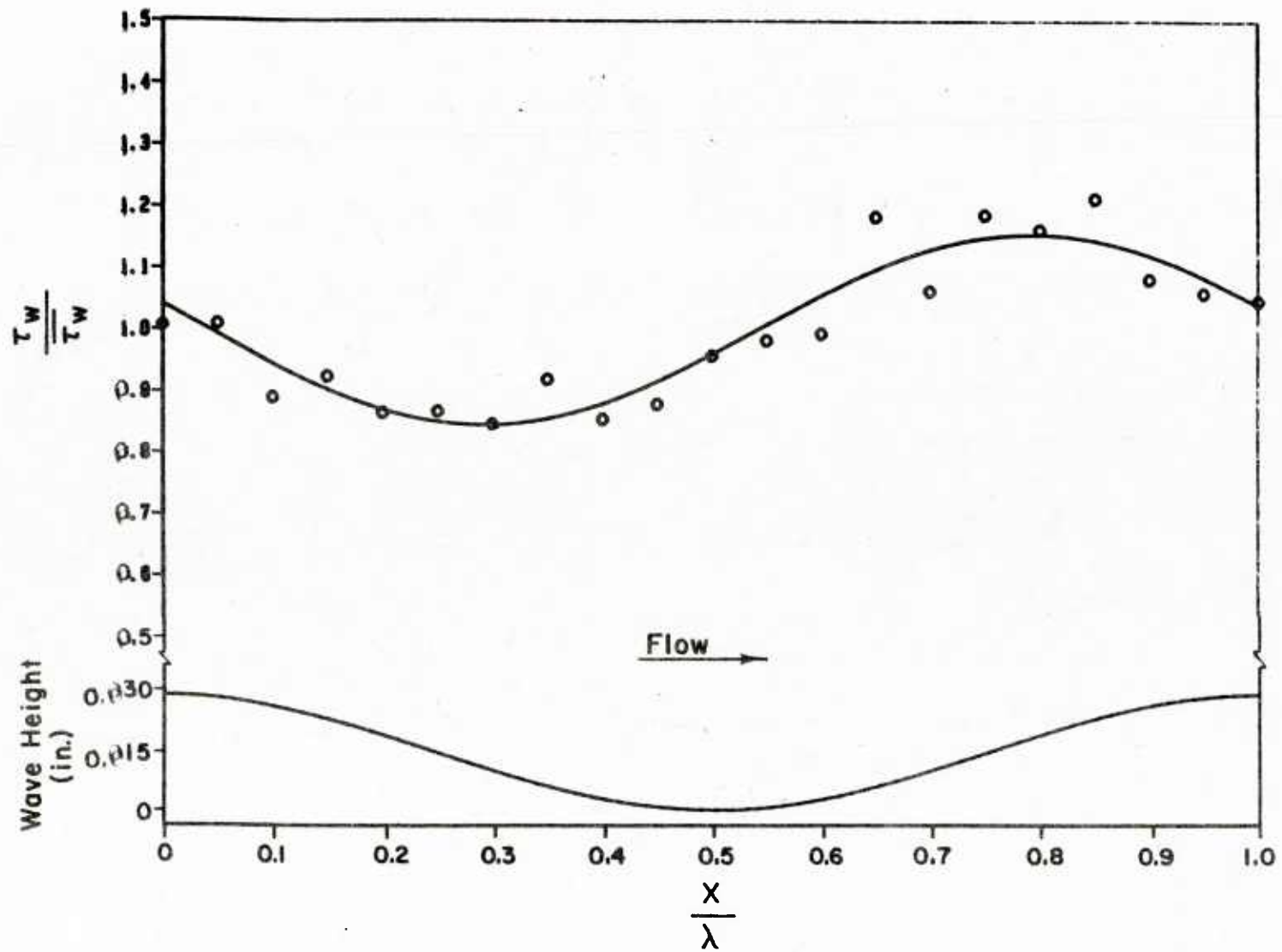


Figure 4.25. Shear Stress Distribution $Re = 34,700$

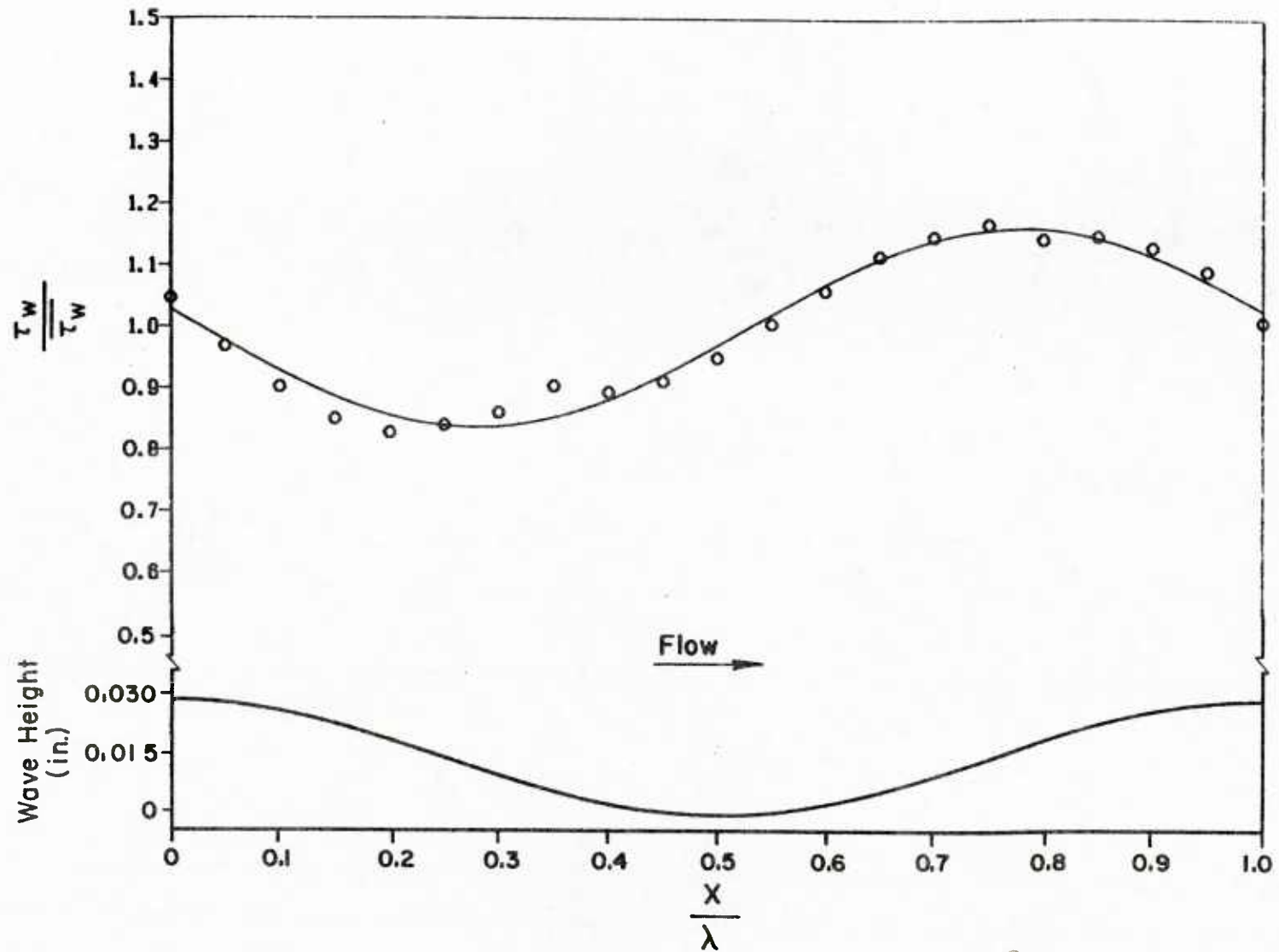


Figure 4.26. Shear Stress Distribution for $Re = 36,000$

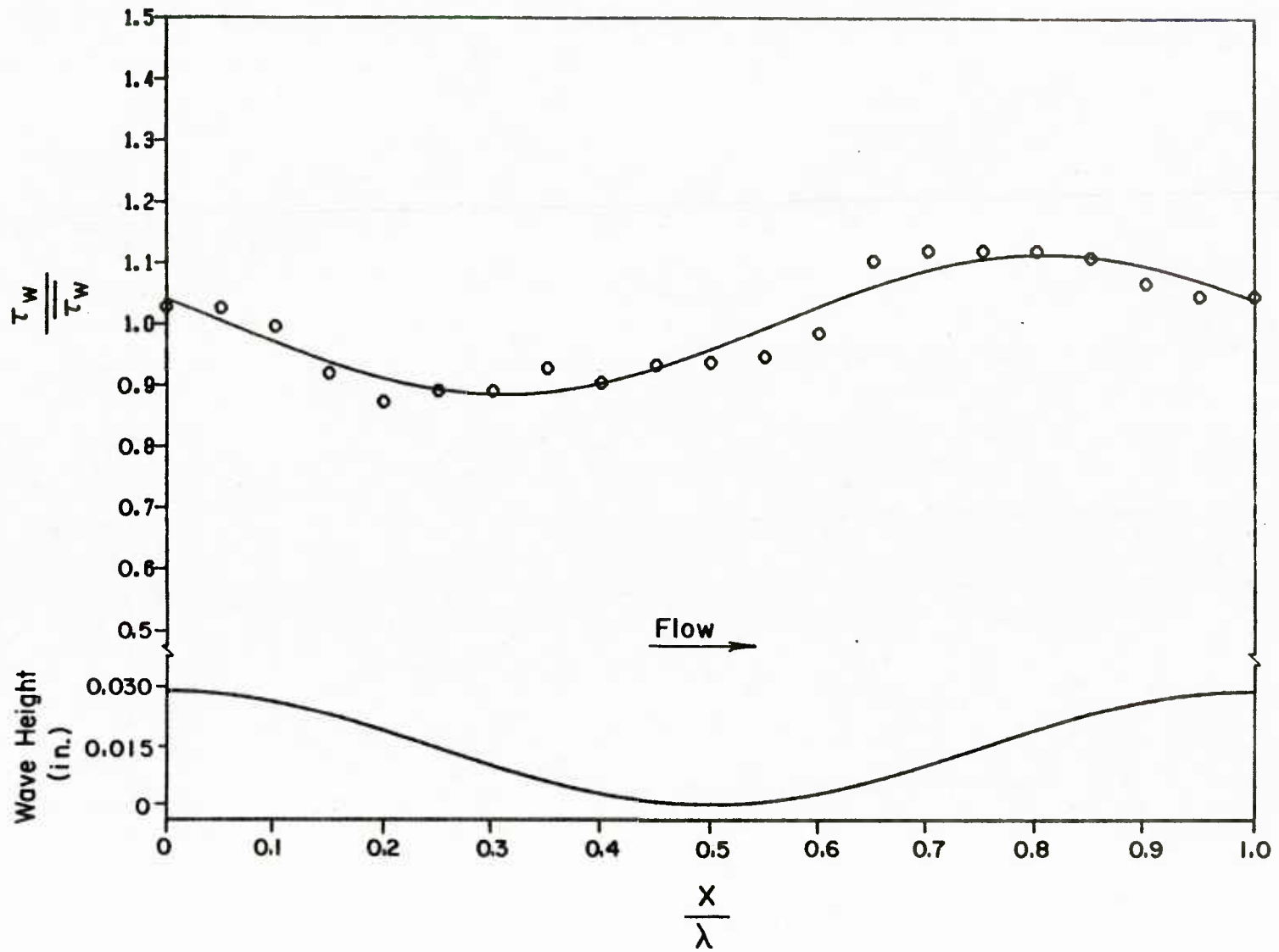


Figure 4.27. Shear Stress Distribution for $Re = 58,000$

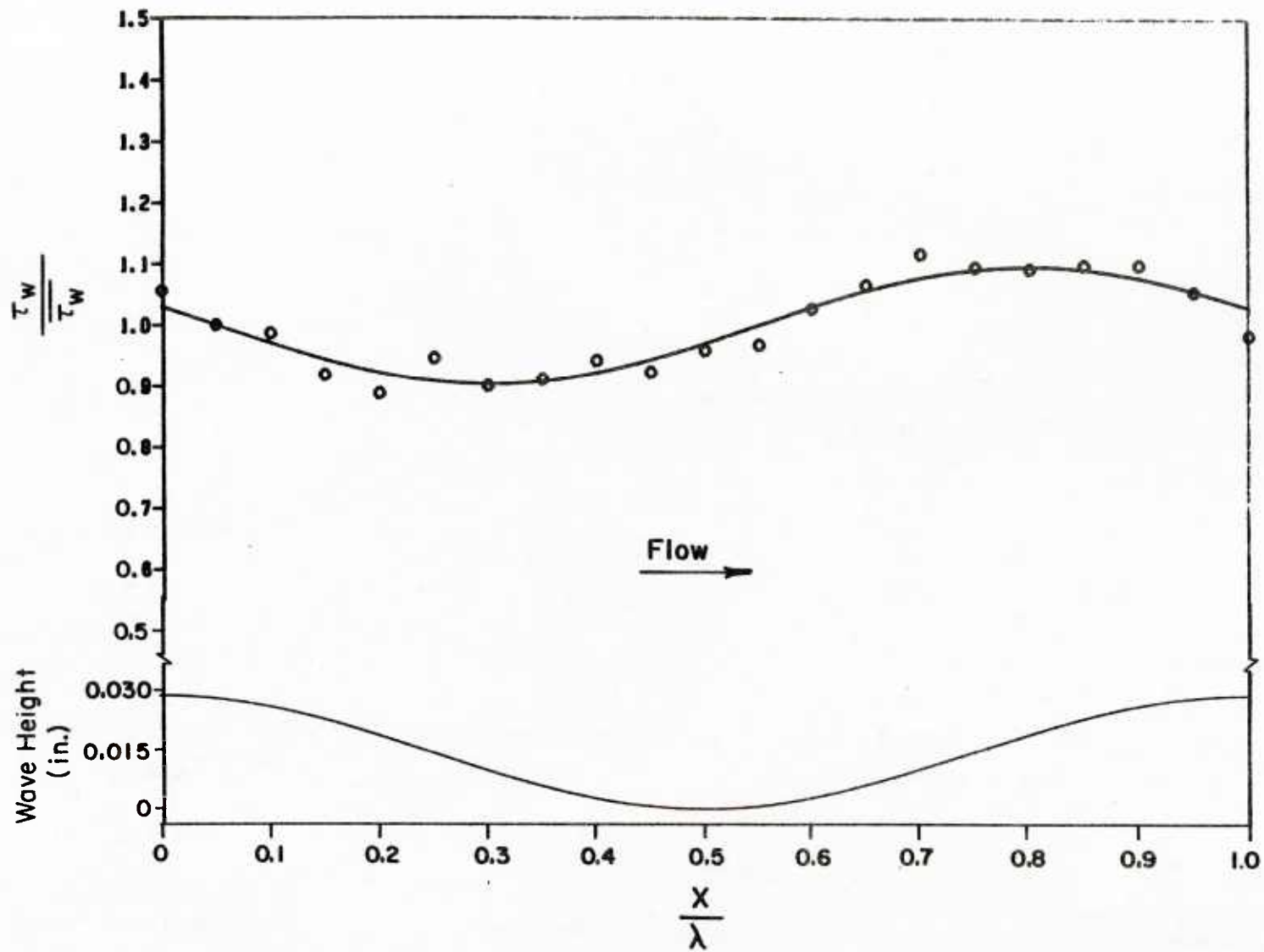


Figure 4.28. Shear Stress Distribution for $Re = 64,000$

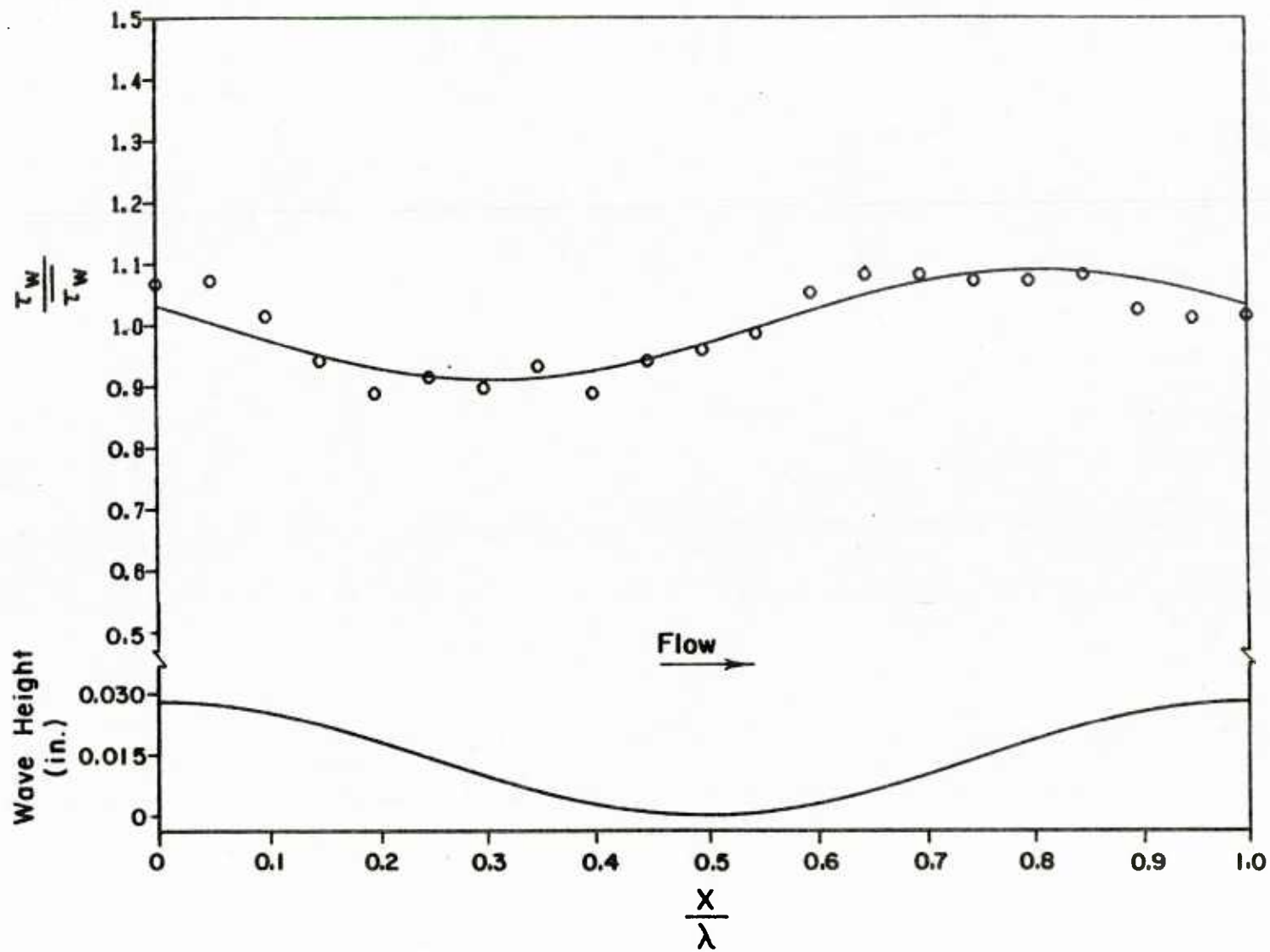


Figure 4.29. Shear Stress Distribution for $Re = 71,000$

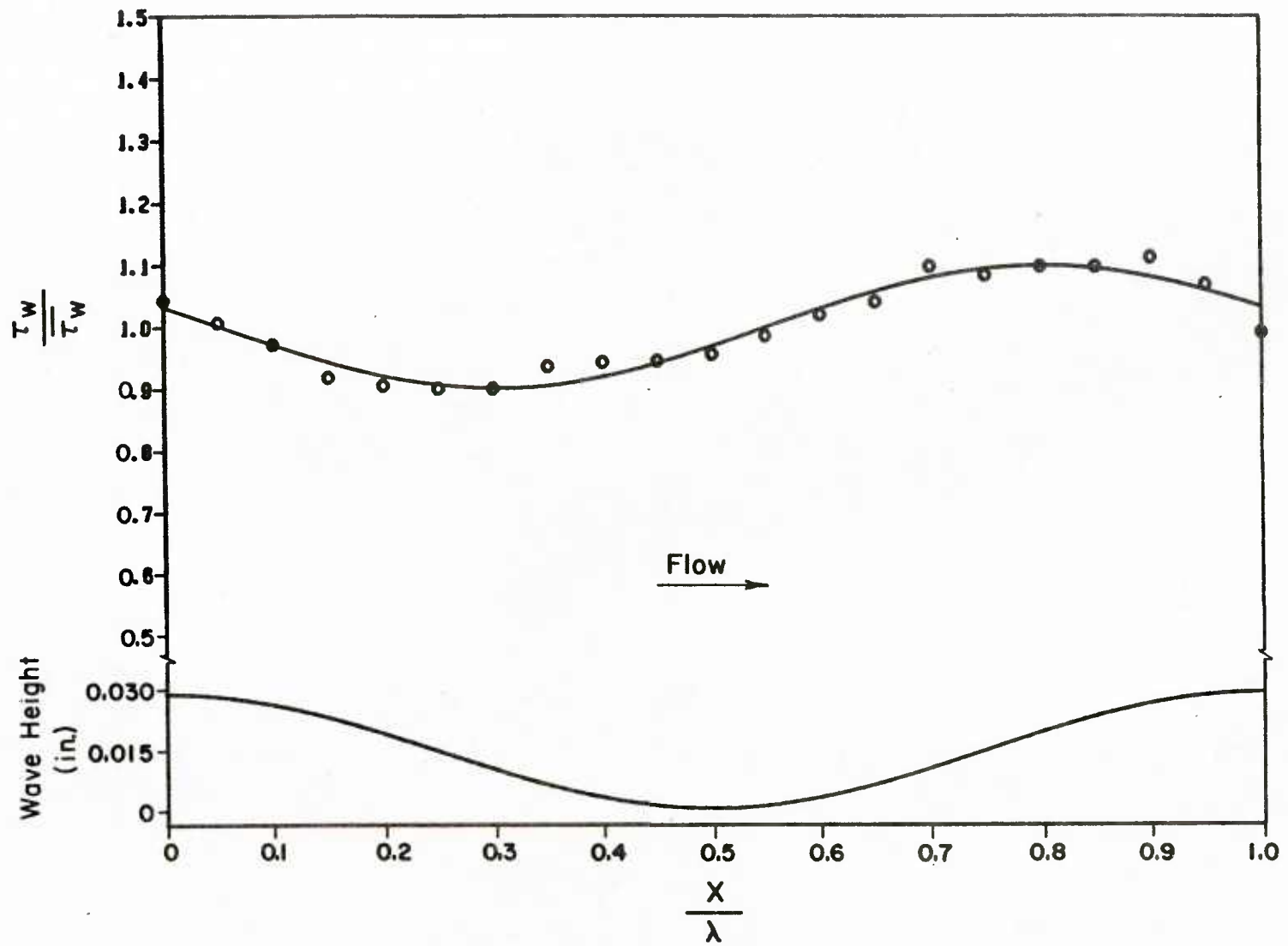


Figure 4.30. Shear Stress Distribution for $Re = 73,500$

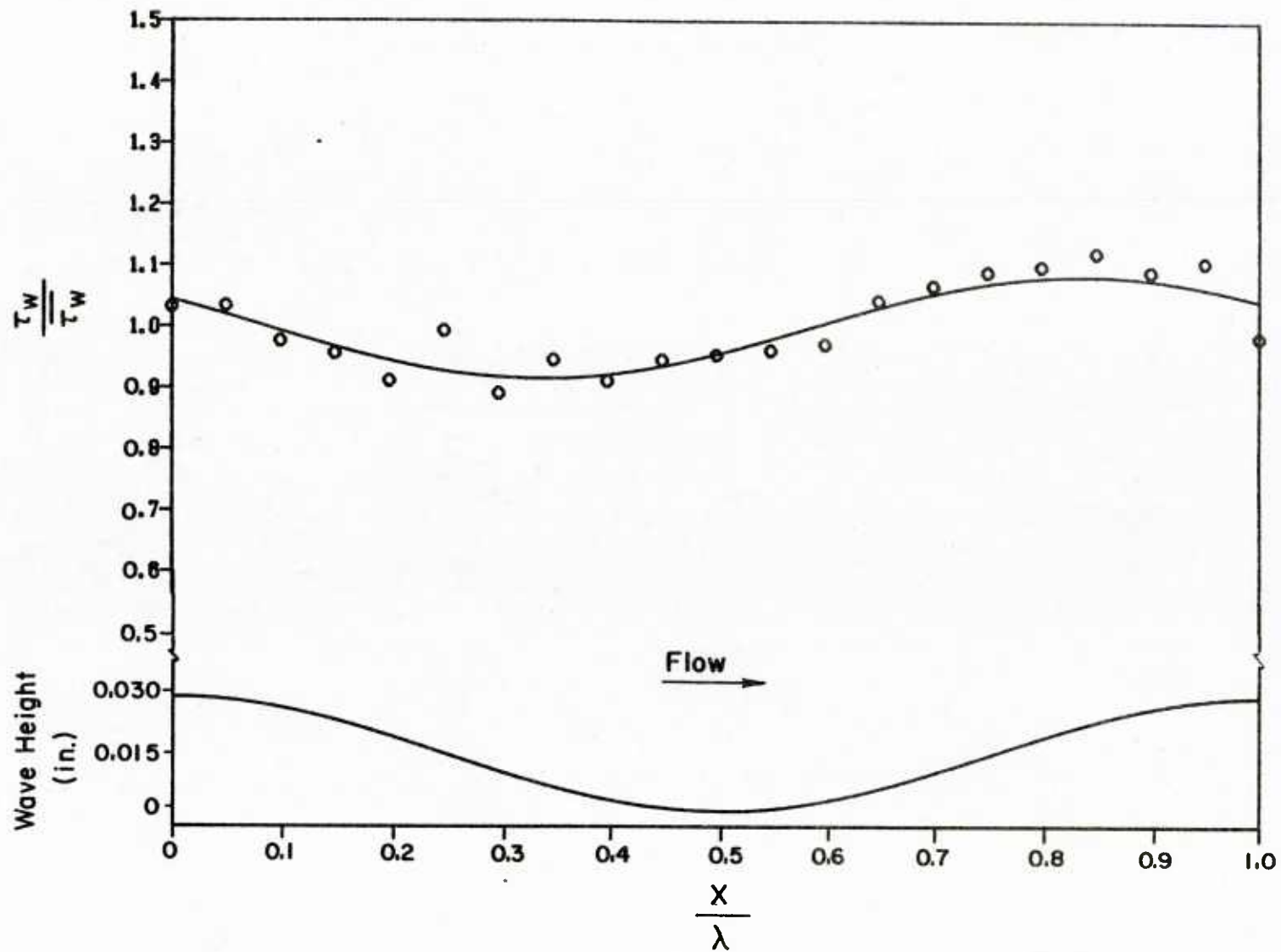


Figure 4.31. Shear Stress Distribution for $Re = 84,500$

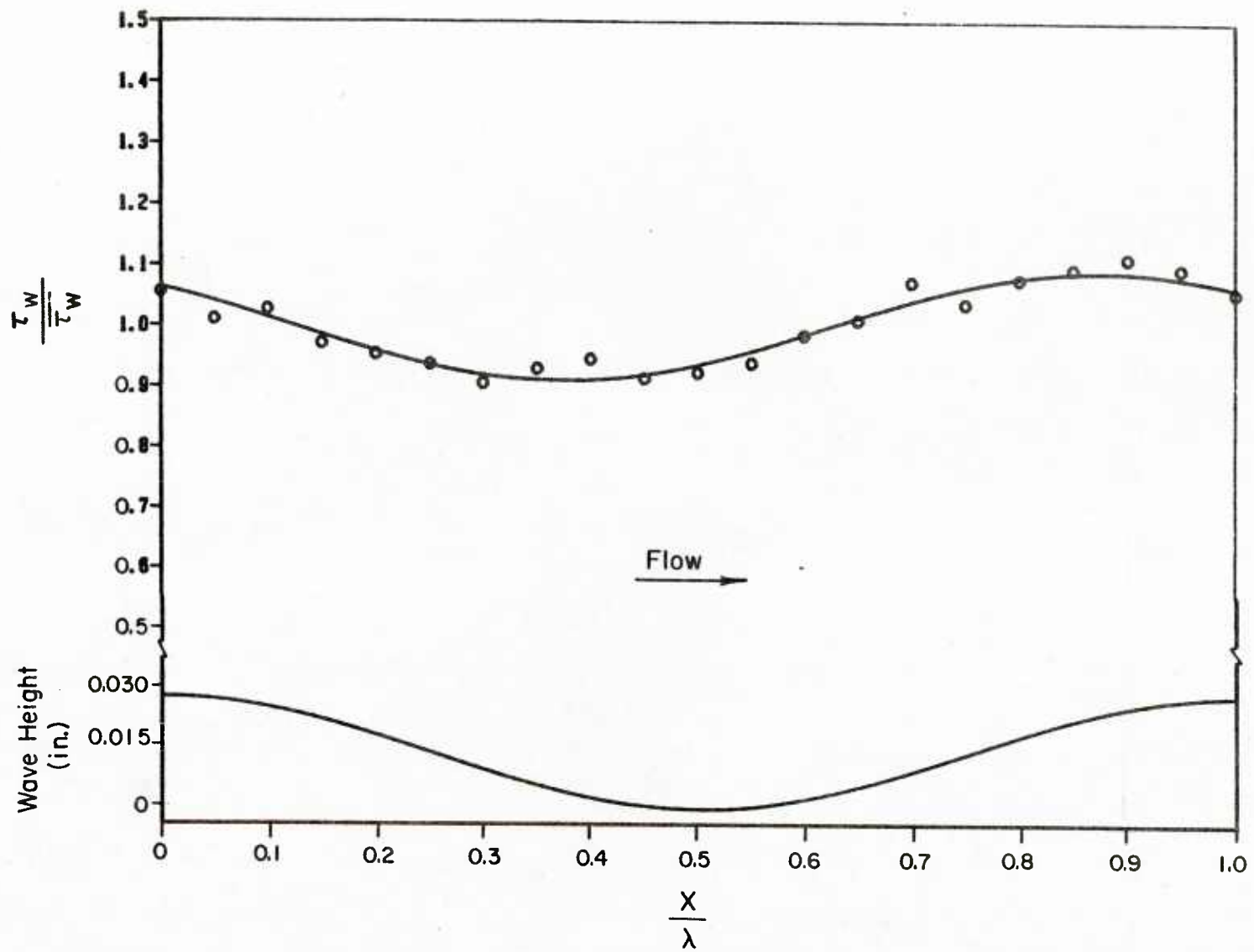


Figure 4.32. Shear Stress Distribution for $Re = 102,500$

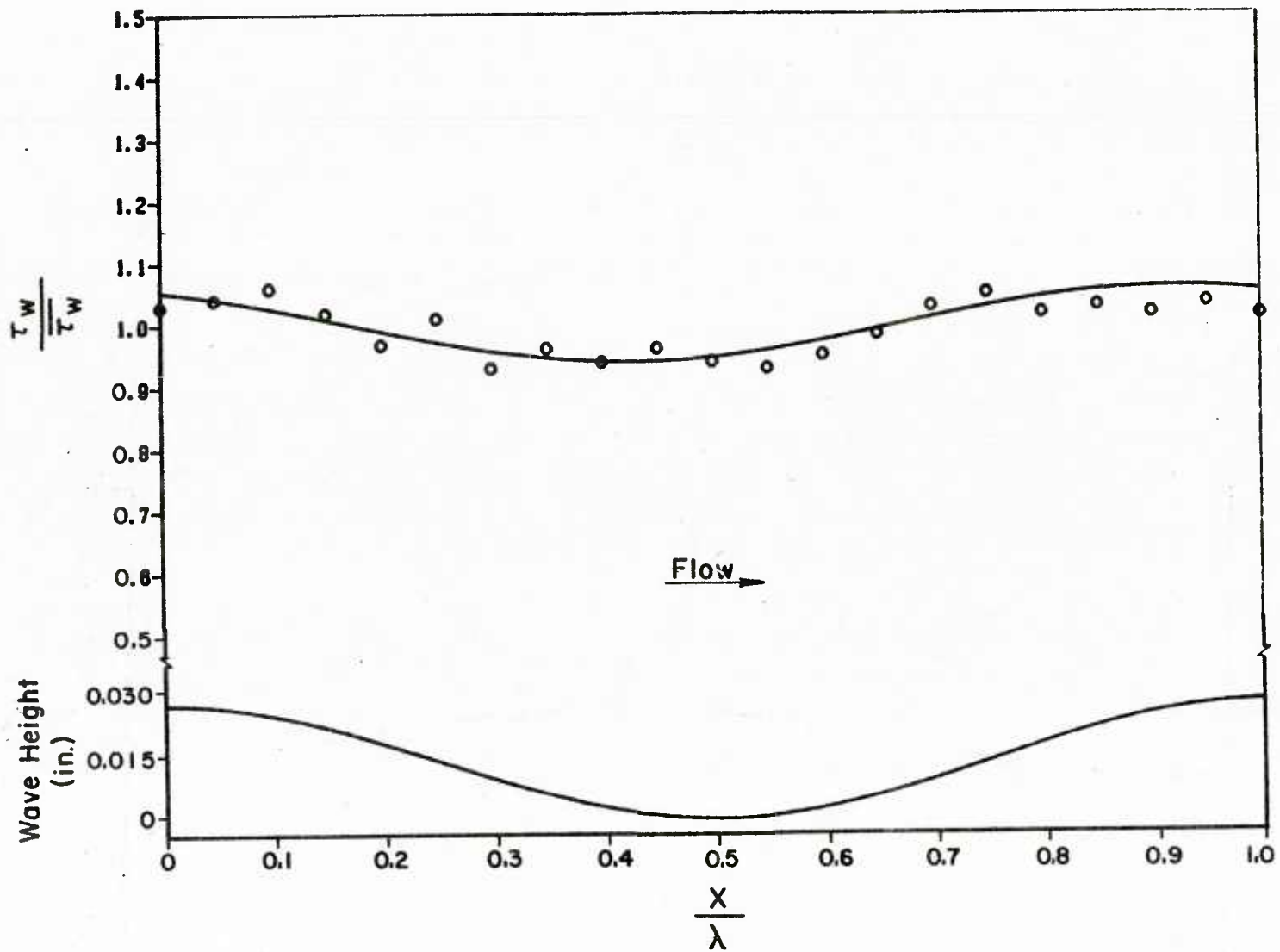


Figure 4.33. Shear Stress Distribution for $Re = 114,500$

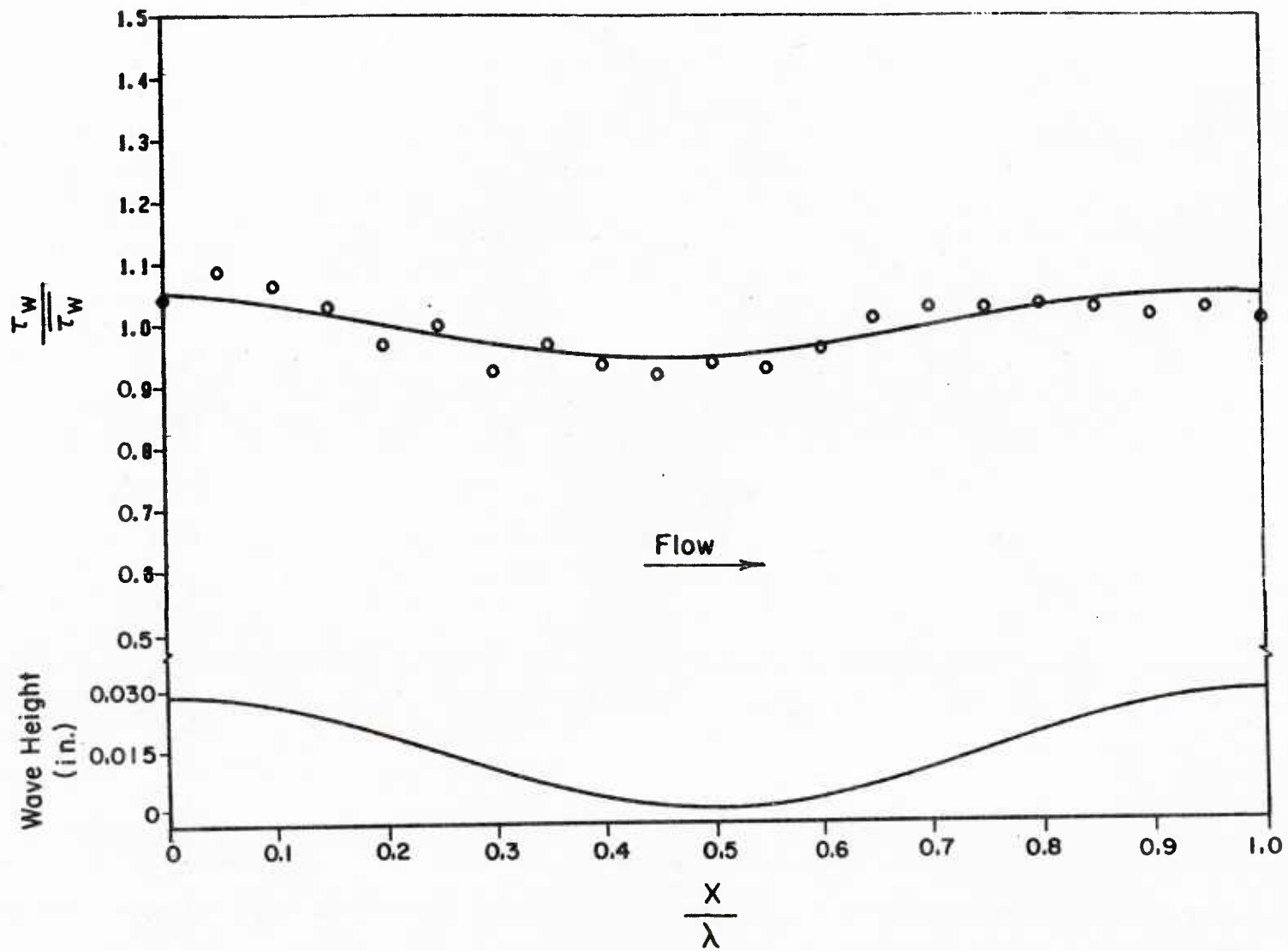


Figure 4.34. Shear Stress Distribution for $Re = 122,500$

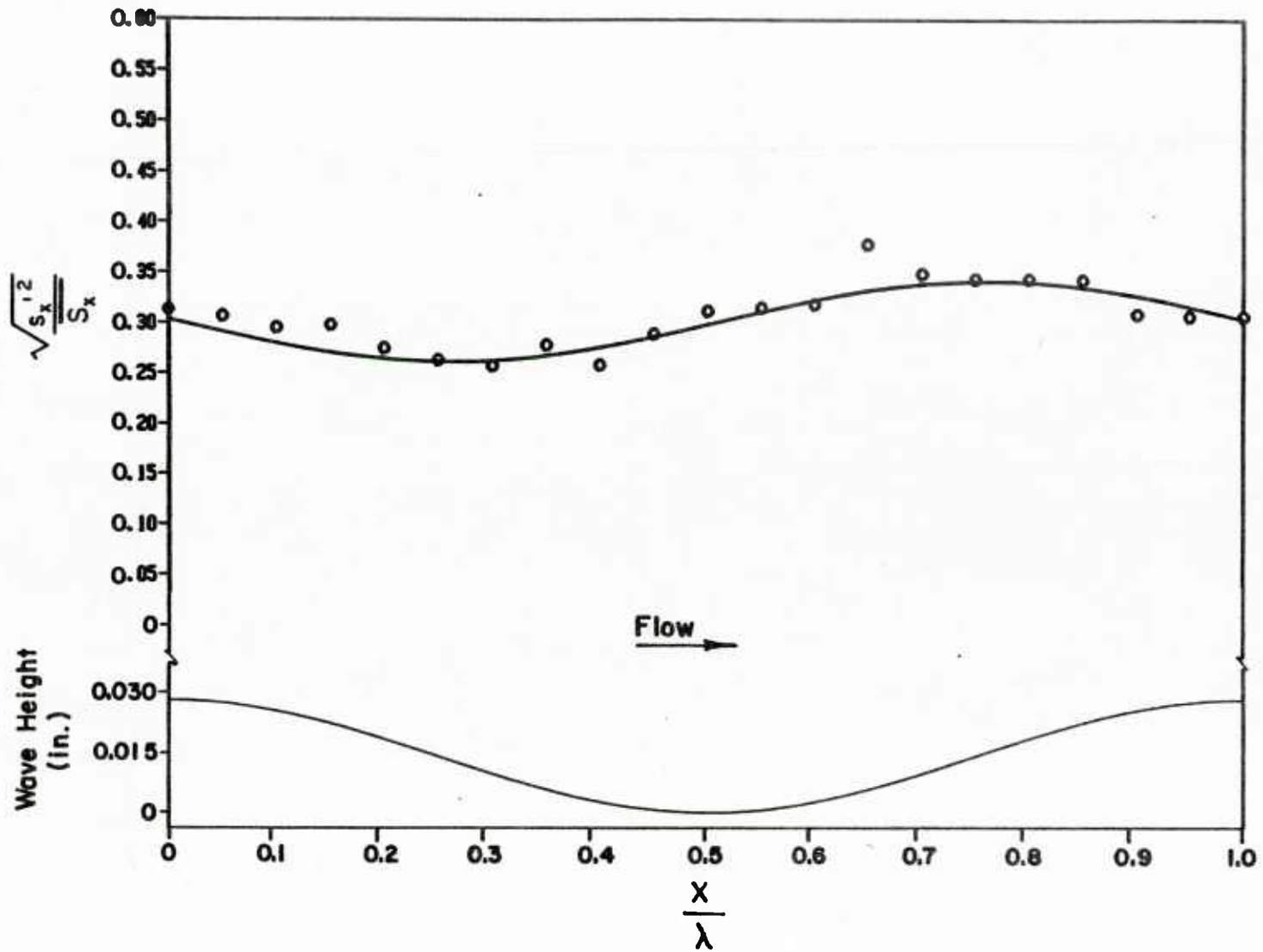


Figure 4.35. Fluctuating Shear Distribution for $Re = 6,680$

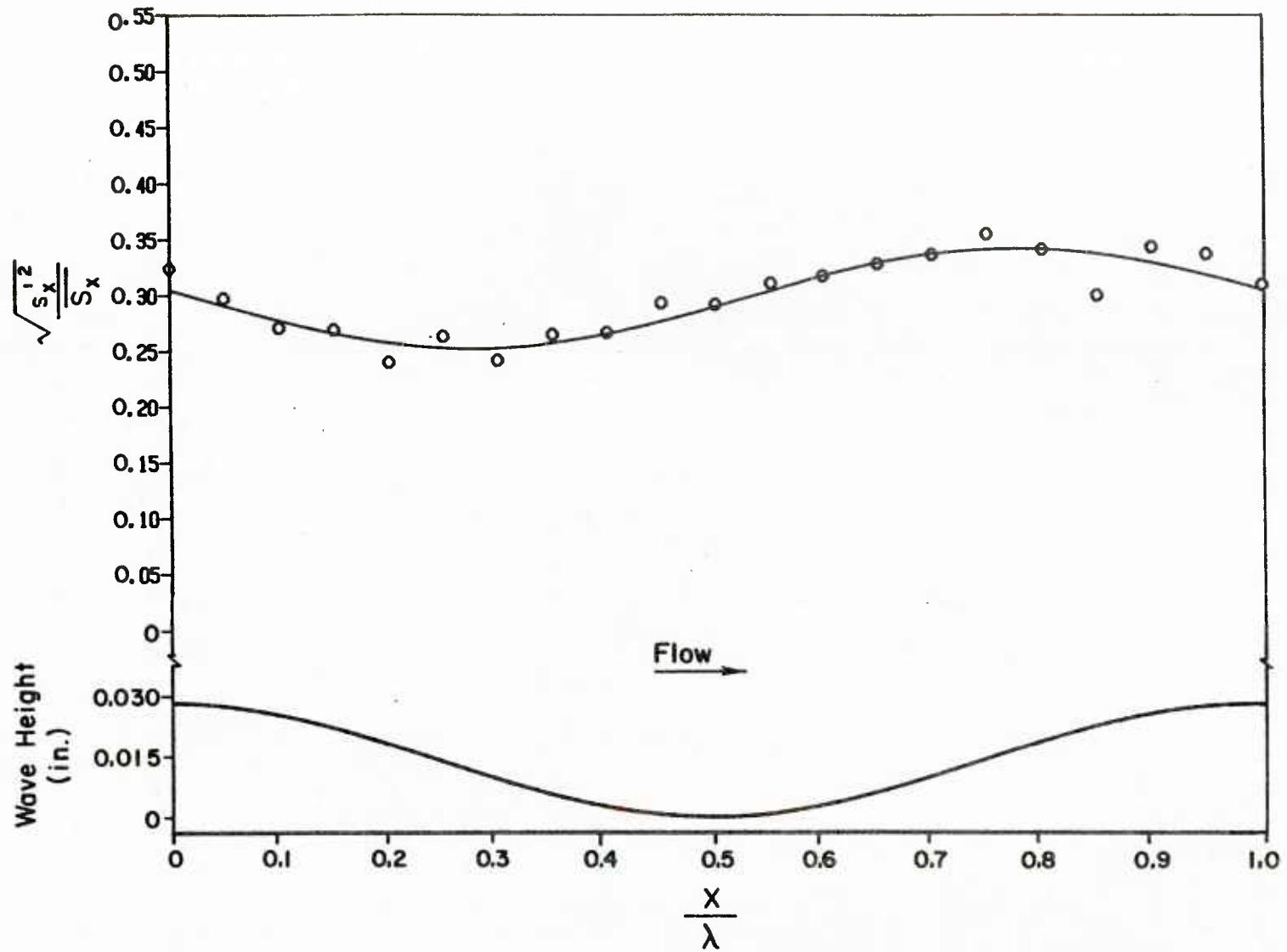


Figure 4.36. Fluctuating Shear Stress Distribution for $Re = 8,450$

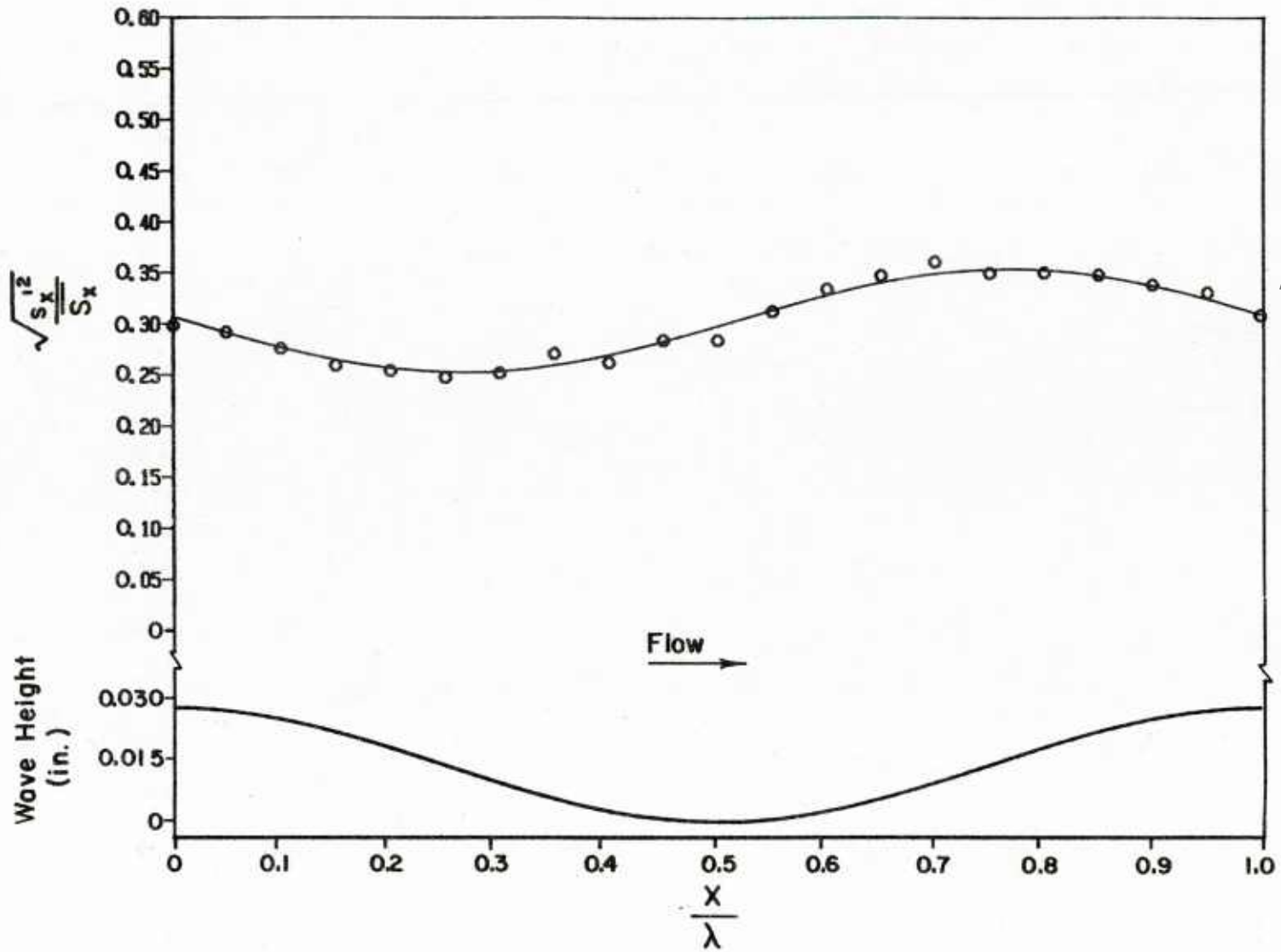


Figure 4.37. Fluctuating Shear Stress Distribution for $Re = 9,650$

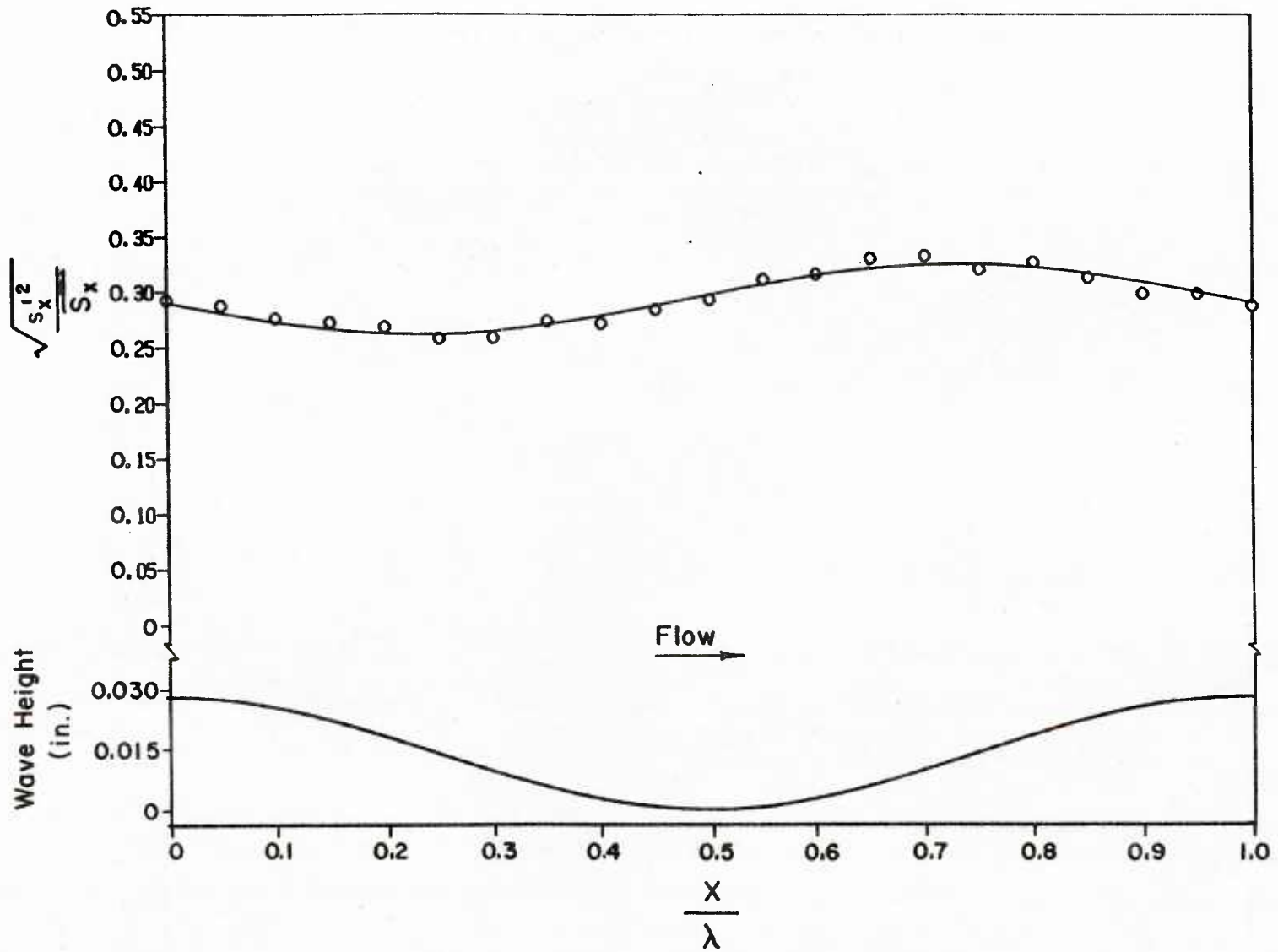


Figure 4.38. Fluctuating Shear Stress Distribution for $Re = 13,000$

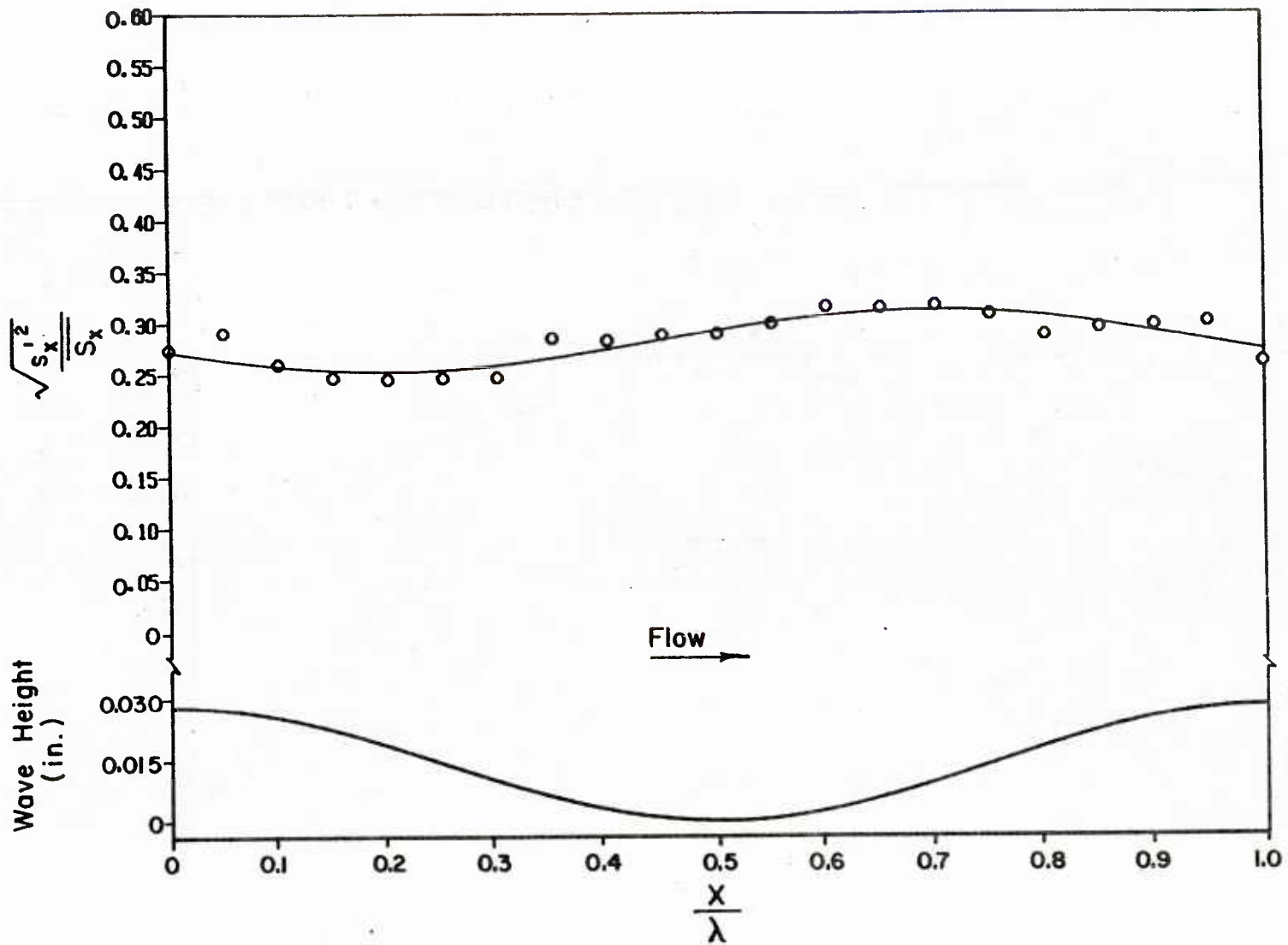


Figure 4.39. Fluctuating Shear Stress Distribution for $Re = 15,700$

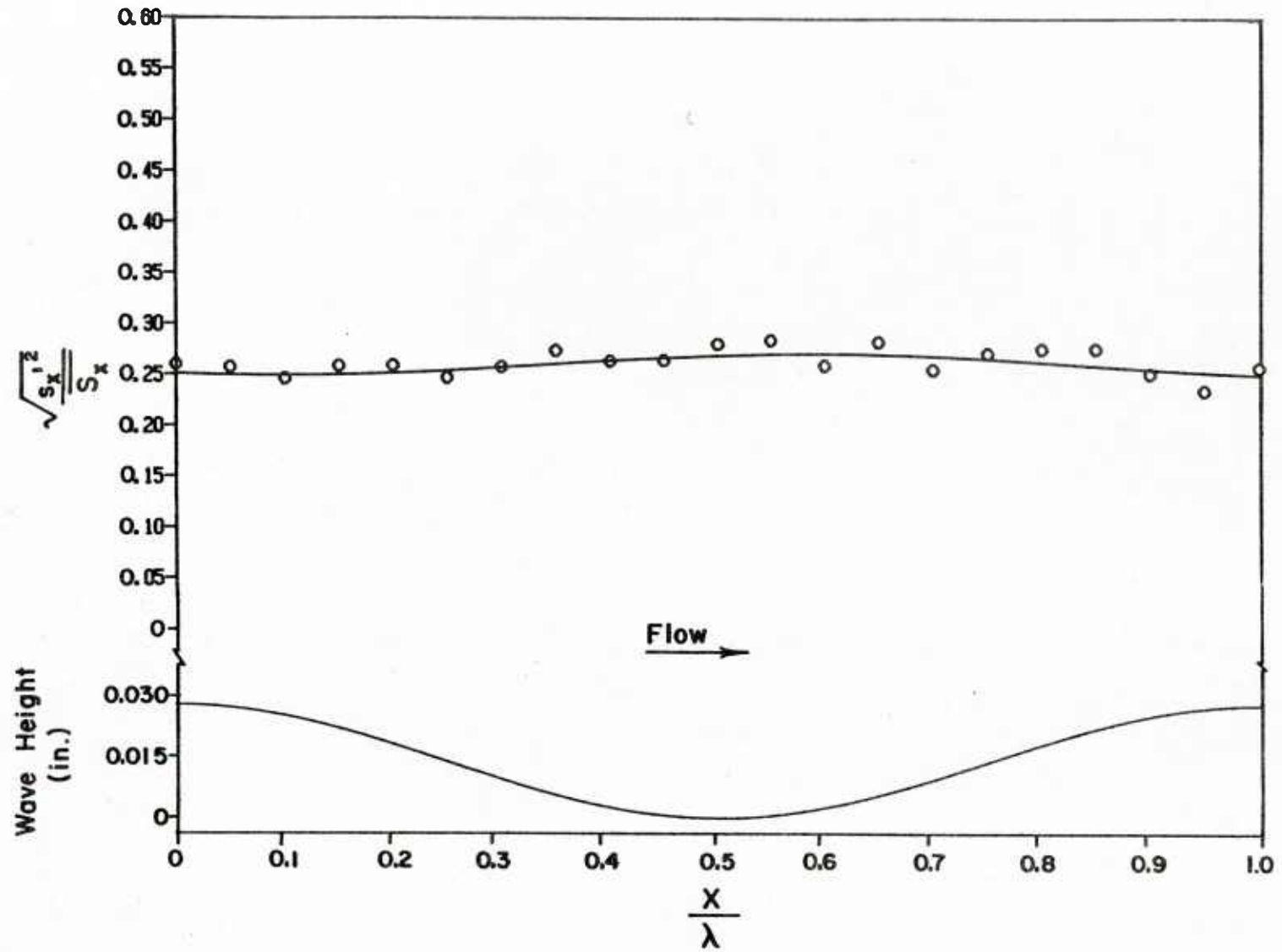


Figure 4.40. Fluctuating Shear Stress Distribution for $Re = 19,800$

Figures 4.41 and 4.42 summarize the average shear stress data by plotting the phase angles and amplitudes of the sinusoidal curves fitted to the wall shear stress measurements as a function of Reynolds number. The phase angle is measured with respect to the wave surface, with shifts in the direction opposite the flow direction taken as positive. The magnitude of the variation of shear stress decreases with Reynolds number while the phase angle increases initially, passes through a maximum at about a Reynolds number of 35,000 and then decreases.

Figures 4.43 and 4.44 summarize the phase angles and amplitudes of the fluctuating shear stress measurements. An error in the amplitudes of these measurements is expected due to the spatial averaging of the velocity fluctuations over the surface of the electrode and due to the problem of frequency response. Mitchell and Hanratty [47] have shown how to correct for both of these effects. Figure 4.47 also shows the corrected amplitudes. The details of the corrections are given in Appendix J. The magnitudes of the fluctuations decrease with increasing Reynolds number while the phase angles increase with Reynolds number.

The shear stress and intensity data are tabulated in Appendix F.

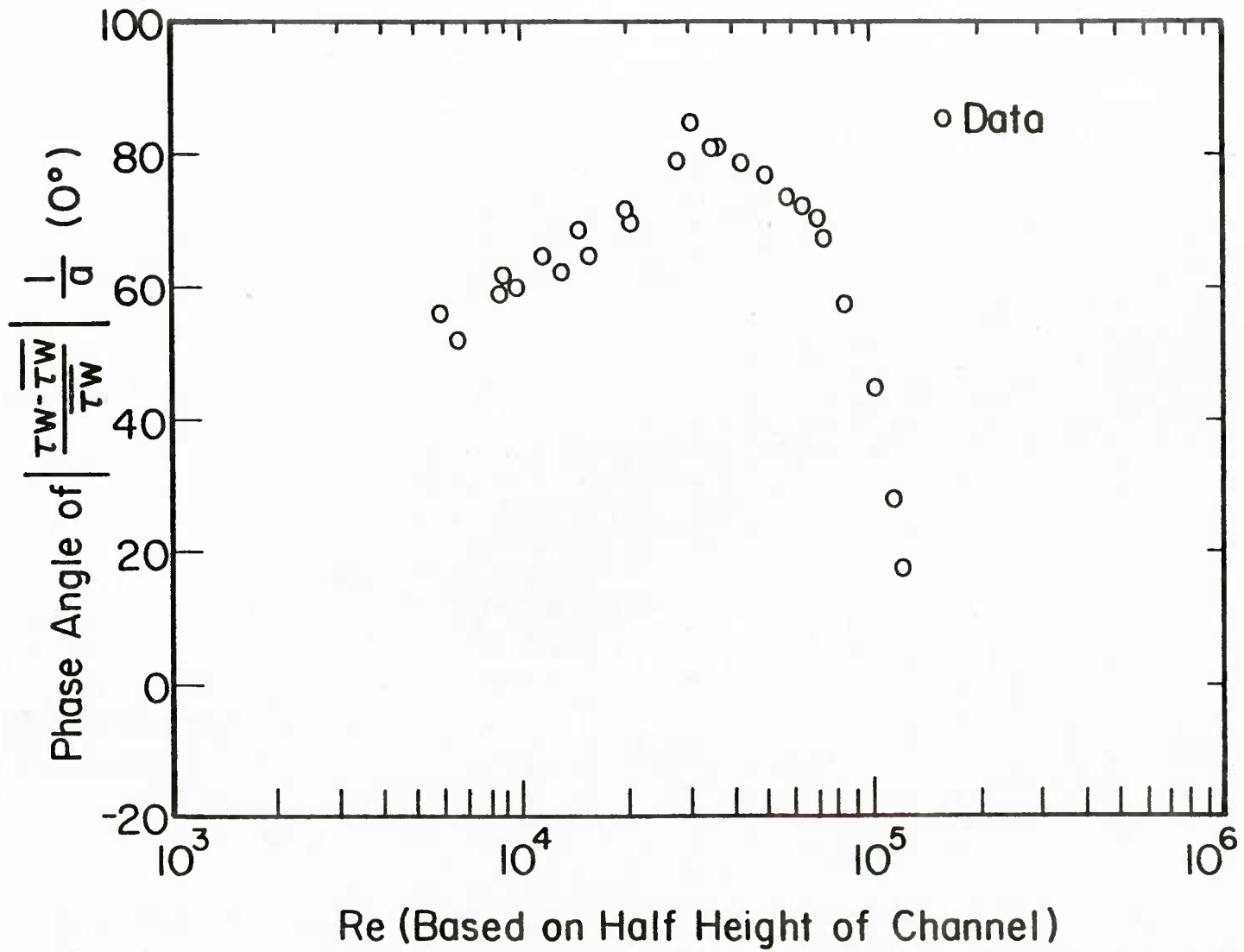


Figure 4.41. Phase Angle of Average Shear Stress Measurements as a Function of Reynolds Number

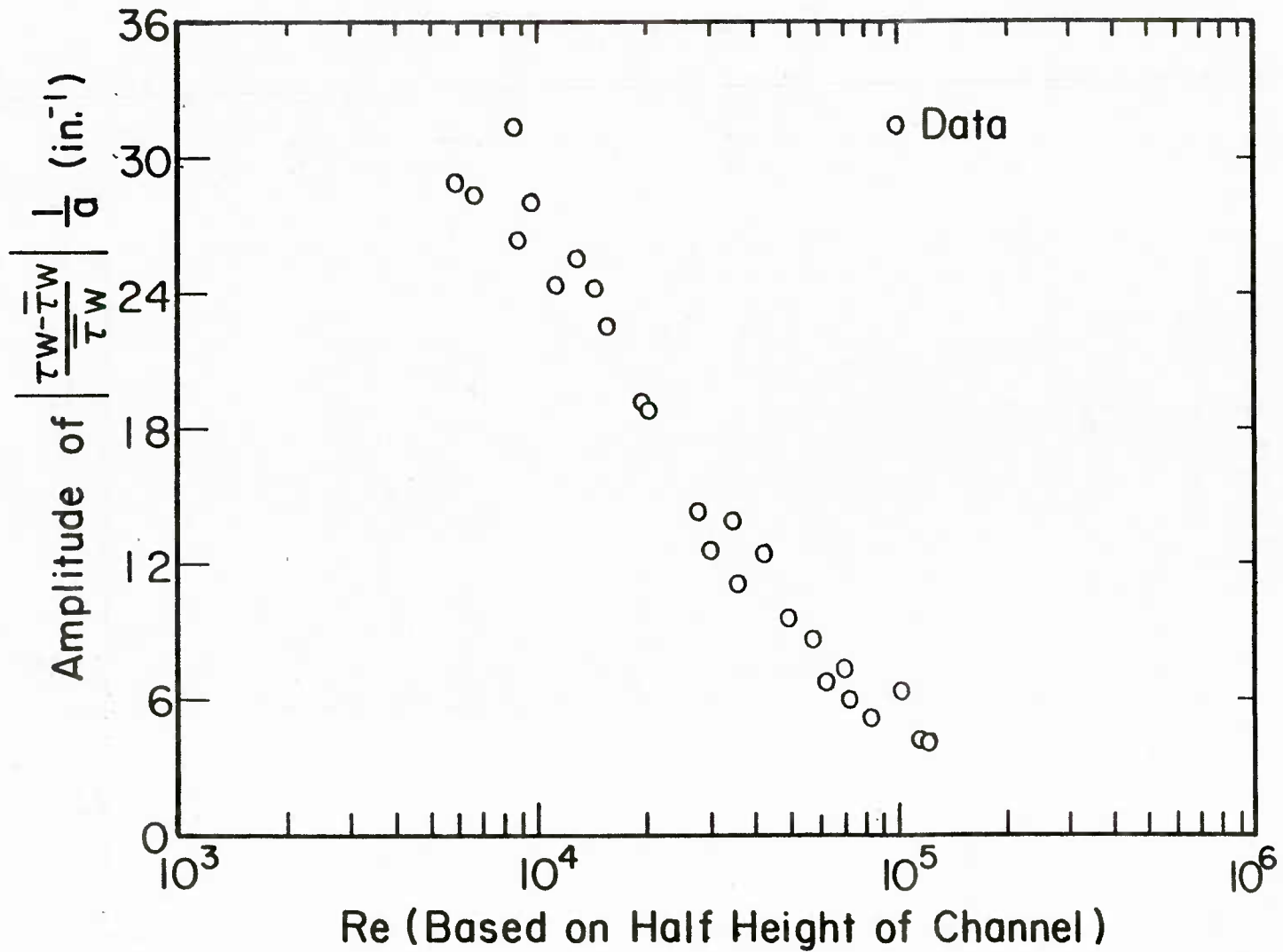
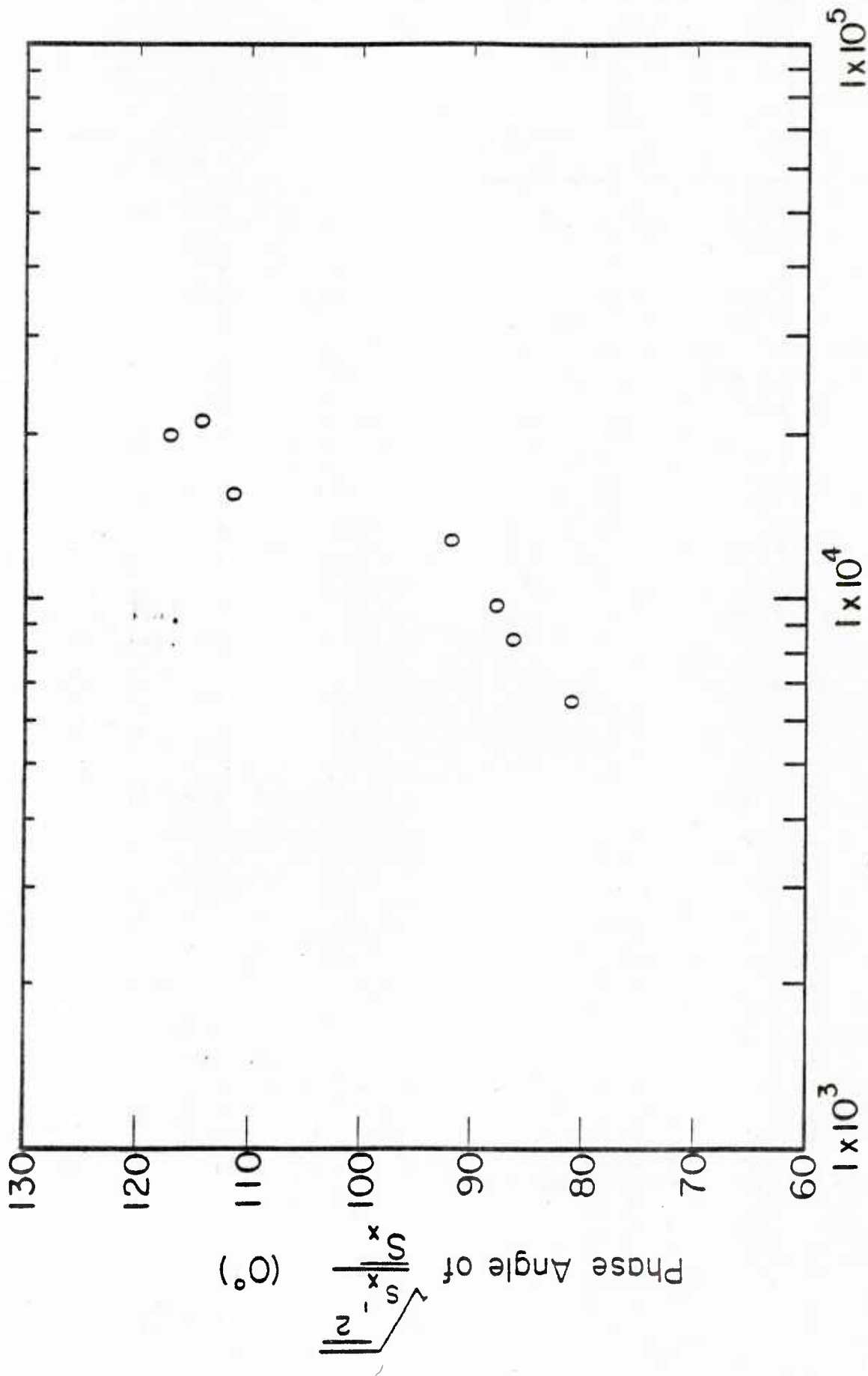


Figure 4.42. Amplitude of Average Shear Stress Measurements as a Function of Reynolds Number



Re (Based on Half Height of Channel)

Figure 4.43. Phase Angle of Fluctuating Shear Stress Measurements as a Function of Reynolds Number

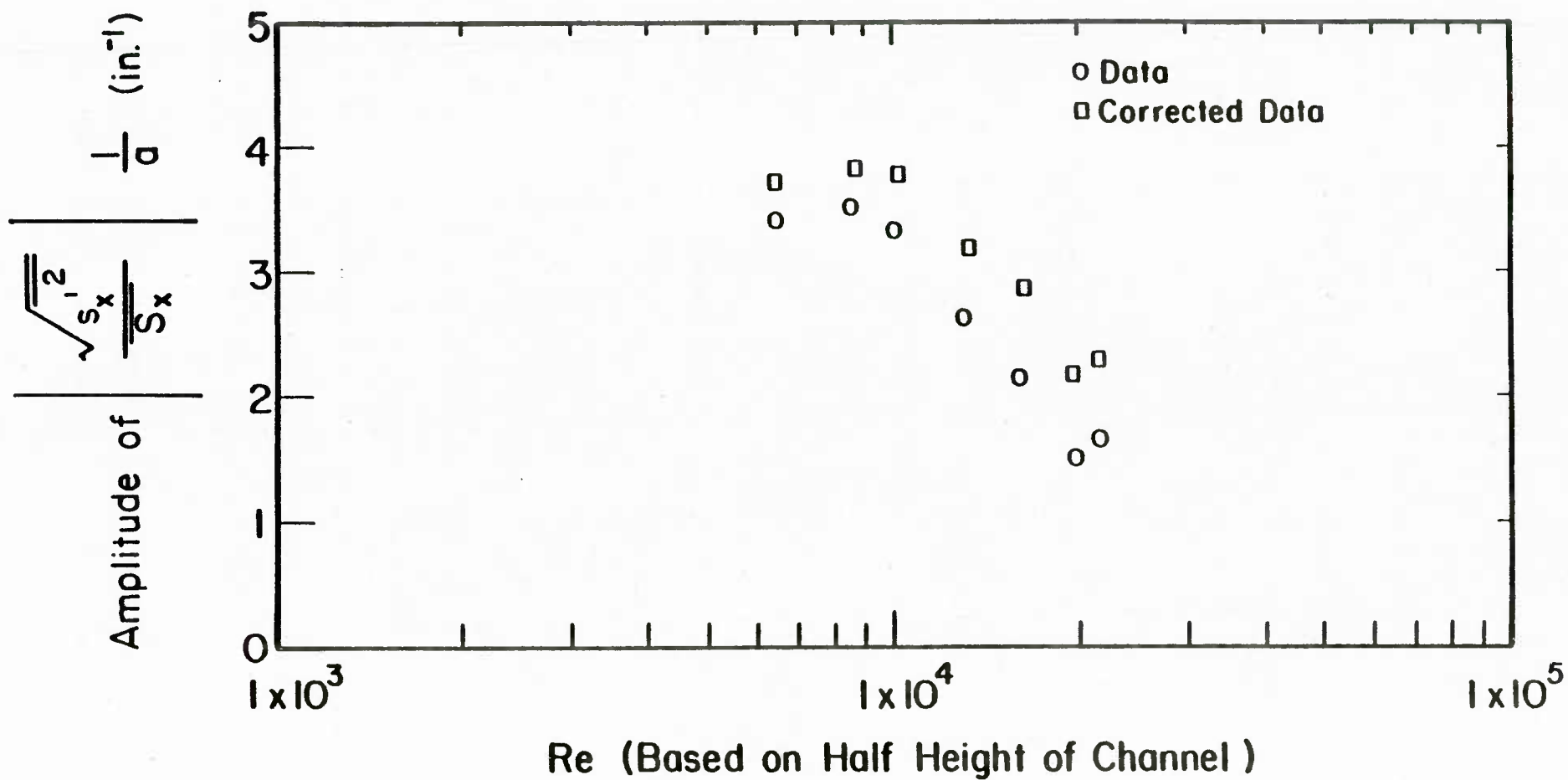


Figure 4.44. Amplitude of Fluctuating Shear Stress Measurements as a Function of Reynolds Number

CHAPTER 5

NUMERICAL ANALYSIS

In this chapter the numerical methods used in solving the differential equations developed in Chapter 3 are presented. These equations include both linear and nonlinear boundary value problems of the form

$$\frac{d^n y(x)}{dx^n} = f \left[y(x), y'(x), \dots, y^{n-1}(x), g(x) \right] \quad (5.1)$$

where $(y^j(x) \ j = 1, \dots, n)$ represents the j th derivative and $g(x)$ is a function of x . Three main classes of methods have been suggested and used in the literature for the solution of these problems. A brief description of these methods is given along with the details of the algorithms used in solving the specific equations. The first class of methods known as projection methods seeks an approximation to the solution of a differential equation in the form

$$y(x) = \sum_{j=0}^n c_j \phi_j(x) . \quad (5.2)$$

The basis functions, $\phi_j(x)$, are specified and chosen to satisfy the boundary conditions. The basis functions are either simple polynomials, trigonometric functions or most commonly spline functions. The problem is then to determine the coefficients, c_j , in the linear combination. Two widely used projection methods are the method of Collocation and Galerkin's method.

In the method of Collocation the approximate solution, $y(x)$, is required to satisfy the differential equation in question at a fixed

number of points in the range x_1, \dots, x_n . This leads to a system of, n , algebraic equations which can then be solved for the coefficients, c_j . The system of algebraic equations will be linear provided the differential equation being solved is linear. Villadsen and Michelsen [74] provide a detailed review of this method.

Galerkin's method (Strang and Fix [68]) is based on the orthogonality of functions. If $y(x)$ represents an exact solution to

$$\frac{d^n f(x)}{dx^n} = g(f(x), \dots, f^n(x), v(x)) , \quad (5.3)$$

then $y(x)$ has an associated residual, $r(x)$, defined as

$$r(x) = \frac{d^n y(x)}{dx^n} - g(y(x), \dots, y^n(x), v(x)) , \quad (5.4)$$

which is identically equal to zero for all x , (since $y(x)$ represents an exact solution). Therefore, the residual, $r(x)$, is orthogonal to every function and in particular it would be orthogonal to the set of basis functions. Hence

$$\int_a^b r(x) \phi_i(x) dx = 0 \quad i = 1, \dots, n. \quad (5.5)$$

Since, $y(x)$, is a linear combination of basis functions it is not expected to be an exact solution of the differential equation being solved. What Galerkin's method does is to choose a $y(x)$ which has a residual that is orthogonal to all basis functions, $\phi_1(x), \dots, \phi_n(x)$, respectively. This procedure, which requires the vanishing of a number of integrals, again leads to the solution of a system of algebraic

equations for the unknown constants, c_j . Further details regarding the above projection methods can be found in Prenter [55], Lucas and Reddisen [43], Russel [6], and Ortega and Poole [52].

The next class of methods are the so called shooting methods where the basic aim is to always solve an initial value problem by using any one of the standard forward integration techniques. This is achieved by guessing any parameters which are needed to make this possible, and by adjusting the guesses, directly with linear problem or iteratively with nonlinear problems, such that all the boundary conditions are satisfied. There are many variations of the basic idea. These include direct shooting or the method of superposition for linear problems, (Scott and Watts [63], Na [50]). For nonlinear problems direct shooting must be used in conjunction with Newtons method, (Na [50]). Alternatively several workers including Bellman and Kalaba [5] and Scott and Watts [62] have suggested using the method of superposition together with quasilinearization.

In the final class of methods low-order finite difference formulae are used and applied as approximations to the differential equation at a number of discreet points in the range. The boundary conditions are satisfied exactly if they do not involve derivatives or approximately if they do. The result of approximating the differential equation by finite difference formulae, is a set of linear algebraic equations in the case of a linear differential equation and a set of nonlinear algebraic equations in the case of a nonlinear differential equation. The method is then, to solve the resulting set of algebraic equations directly for linear problems and iteratively for nonlinear problems, to give

approximations to the solution of the differential equation simultaneously at all mesh points. The method had been reviewed by Ortega and Poole [52] and Fox [20].

The linear differential equations (3.13)-(3.17) and (3.72)-(3.77) which specify the wave induced stream function, $F(y)$, for the Zero Equation and $K-\epsilon$ Models were solved using a modified version of the method of superposition to be discussed in the next section. The main advantage of the method of superposition (direct shooting) is the existence of very good and well programmed methods for solving systems of initial value problems. These integrators are programmed to adjust the step by step intervals so as to provide the desired level of accuracy required by the user.

The nonlinear differential equations (3.67)-(3.71) which specify the mean flow field when using the $K-\epsilon$ Model were solved by combining finite difference techniques with quasilinearization, to be discussed in a subsequent section. Initial attempts were made to solve this problem using direct shooting and Newton's method. However, due to the nature of the equations, if the initial conditions are not known accurately the solution blows up very fast. An alternate method suggested by Scott [64], but not tried, is the method of parallel shooting.

(a) Numerical Solution of the Wave Induced Flow

A linear boundary value problem such as equations (3.13)-(3.17) or equations (3.72)-(3.77) may be written as a system of first order equations and expressed in the following form, (see Appendix K),

$$y'(x) = F(x) y(x) + g(x), \quad (5.6)$$

$$Ay(a) = \alpha, \quad (5.7)$$

$$By(b) = \beta, \quad (5.8)$$

where $y(x)$ is a column vector of length n , $F(x)$ is an $n \times n$ matrix of rank k , A is an $(n - k) \times n$ matrix of rank $(n - k)$, B is $k \times n$ matrix of rank k , and α and β are column vectors of $(n - k)$ and k components respectively.

Applying the method of superposition any solution of equations (5.6)-(5.8) can be expressed as

$$y(x) = v(x) + c_1 y^1(x) + c_2 y^2(x) \dots c_k y^k(x) \quad (5.9)$$

$$= v(x) + U(x)c \quad (5.10)$$

where c is a vector with k components, $v(x)$ is a solution of the nonhomogeneous system

$$v'(x) = F(x) v(x) + g(x), \quad (5.11)$$

$$Av(a) = \alpha \quad (5.12)$$

and $U(x)$ is an $n \times k$ matrix whose columns $y^1(x) \dots, y^k(x)$ are solutions of the homogeneous system

$$U'(x) = F(x) U(x), \quad (5.13)$$

$$AU(a) = 0. \quad (5.14)$$

The constant vector c is determined by satisfying the final boundary condition at $x = b$, equation (5-8).

$$By(b) = BU(b)c + Bv(b) = \beta \quad (5.15)$$

It should be mentioned that in classical superposition n homogeneous solutions would have to be generated. However by suitably choosing the initial conditions, equations (5.12) and (5.14), it is possible to generate only k homogeneous solutions. If the direction of integration is reversed (i.e. from b to a) then $(n-k)$ solutions are required. For simple boundary conditions [equations (3.16), (3.17) and (3.77)] the initial matrix, $U(a)$, can be chosen by inspection (see Appendix K). For complex boundary conditions Scott and Watts [62] have developed a general procedure for generating the initial matrix, $U(a)$.

It often happens that the exact mathematical procedure for obtaining the solution of equations (5.6)-(5.8) leads to poor or even completely incorrect results when applied as a numerical procedure. This occurs when the matrix $F(x)$ has eigenvalues whose real parts are well separated. In this case the various homogeneous solutions and the particular solution all grow at vastly different rates. As a consequence of the finite word length associated with digital computers the rapidly growing solutions eventually swamp all other solutions, making them proportional to these growing solutions or combinations of them. In this case the matrix U will become increasingly ill conditioned such that the vector c determined by equation (5.15) will yield incorrect results. The above mentioned problem arises in the solution of equations (3.13)-(3.17) and (3.72)-(3.77).

Consider equations (3.13) and (3.14) at large y such that the derivatives of the mean velocity profile \bar{U}' and \bar{U}'' are small and the turbulence term, R , is negligible. Then

$$F'''' - (2\alpha^2 + i\alpha\bar{U})F'' + (\alpha^4 + i\alpha^3\bar{U})F - i\alpha^3\bar{U}^2 - \alpha^4\bar{U} = 0 \quad (5.16a)$$

Upon application of the standard method of solution for linear ordinary differential equations with constant coefficients and keeping the two solutions which are bounded at large y there results

$$F = F_{H_1} + F_{H_2} + F_P, \quad (5.16b)$$

$$= A_1 \exp(-\alpha y) + A_2 \exp(-\beta y) + U, \quad (5.16c)$$

where
$$\beta = (\alpha^2 + i\alpha\bar{U})^{1/2} \quad (5.16c)$$

Assuming infinite precision the two homogeneous solutions $\exp(-\alpha y)$ and $\exp(-\beta y)$ could be generated by solving the homogeneous form of (5.16a) subject to the initial conditions

$$F_{H_1} = 1, \quad F_{H_1}^n = (-\alpha)^n \quad y = y_\infty \quad (5.16d)$$

$$F_{H_2} = 1, \quad F_{H_2}^n = (-\beta)^n \quad y = y_\infty \quad (5.16e)$$

where F^n denotes the n th derivative.

In fact these initial conditions will produce the following homogeneous solutions:

$$F_{H_1} = \exp(\alpha y_\infty) \exp(-\alpha y) \quad (5.17a)$$

$$F_{H_2} = \exp(\beta y_\infty) \exp(-\beta y). \quad (5.17b)$$

Since computers do not have infinite precision let the total amount of round off and truncation error, ϵ , (Lightfoot [41]) enter the problem in the initial conditions as follows:

$$F_{H_1} = 1 + \epsilon \quad F_{H_1}^n = (-\alpha)^n \quad \text{at } y_\infty \quad (5.18a)$$

$$F_{H_2} = 1 + \epsilon \quad F_{H_2}^n = (-\beta)^n \quad \text{at } y_\infty \quad (5.18b)$$

The numerical solutions that would be generated using the above boundary conditions are:

$$\begin{aligned} F_{H_1} = & \left[1 + \frac{\beta\epsilon}{2(\beta - \alpha)} - \frac{\alpha\beta\epsilon}{2(\beta^2 - \alpha^2)} \right] e^{\alpha y_\infty} e^{-\alpha y} \\ & + \left[\frac{\alpha\beta\epsilon}{2\alpha(\alpha + \beta)} + \frac{\alpha\beta\epsilon}{(\beta^2 - \alpha^2)} \right] e^{-\alpha y_\infty} e^{\alpha y} \\ & - \frac{\alpha^2\epsilon}{2(\beta^2 - \alpha^2)} e^{\beta y_\infty} e^{-\beta y} - \frac{\alpha^2\epsilon}{2(\beta^2 - \alpha^2)} e^{-\beta y_\infty} e^{\beta y} , \end{aligned} \quad (5.19a)$$

$$\begin{aligned} F_{H_2} = & \left[1 + \frac{\alpha\epsilon}{2(\alpha - \beta)} - \frac{\alpha\beta\epsilon}{2(\alpha^2 - \beta^2)} \right] e^{\beta y_\infty} e^{-\beta y} \\ & \left[\frac{\alpha\beta\epsilon}{2\beta(\alpha + \beta)} + \frac{\alpha\beta\epsilon}{(\alpha^2 - \beta^2)} \right] e^{-\beta y_\infty} e^{\beta y} \\ & - \frac{\beta^2\epsilon}{2(\alpha^2 - \beta^2)} e^{\alpha y_\infty} e^{-\alpha y} - \frac{\beta^2\epsilon}{2(\alpha^2 - \beta^2)} e^{-\alpha y_\infty} e^{\alpha y} . \end{aligned} \quad (5.19b)$$

The behavior of F_{H_1} and F_{H_2} as $y \rightarrow 0$ yields

$$F_{H_1} \rightarrow \frac{-\alpha^2 \epsilon}{2(\beta^2 - \alpha^2)} e^{\beta y_\infty} e^{-\beta y}, \quad (5.20a)$$

$$F_{H_2} \rightarrow e^{\beta y_\infty} e^{-\beta y}, \quad (5.20b)$$

since $|\beta| \gg |\alpha|$.

Hence F_{H_1} and F_{H_2} are no longer independent solutions of the homogeneous form of equation (5.16a). The point at which loss of independence occurs depends on the word size of the computer being used.

Several workers have recognized this difficulty and have proposed methods for maintaining the linear independence of the solutions. These include Kaplan's filtering technique [22], Davey's [17] complete orthonormalization procedure, and the method of compound matrices Ng and Reid [51]. The most widely used and tested method is the Gram-Schmidt orthonormalization procedure.

The use of the Gram-Schmidt orthonormalization procedure was first proposed by Godunov [25] and independently by Bellman and Kalaba [5]. The method has been discussed and used by Conte [14], Gersting [23] and Scott and Watts [63]. Scott and Watts [62] have refined the basic method and incorporated these modifications into an excellent code named Suport [62].

In this thesis the Suport code was used together with an independently written code. The latter was developed to obtain a better understanding of the orthonormalization procedure. The advantage of the Suport code is its extreme efficiency and the modifications which have been added that take advantage of the complex structure of problems like the Orr-Sommerfeld equation (see Watts, Scott and Lord [75]).

(b) Orthonormalization Procedure

The orthonormalization procedure outlined here is the method suggested by Scott and Watts [63], Conte [14] and Godunov [25].

At the points where orthonormalization is necessary the previous independent set of base solutions are converted into a new orthonormal set. The orthonormalization is achieved by employing the "modified" Gram-Schmidt procedure described below. Scott and Watts [62] have suggested that the modified Gram-Schmidt procedure be used since it is (1) more stable (2) easier to code (3) more economical on storage. Thus at any point where orthonormalization is judged necessary

$$U_{old} = P U_{new} \quad (5.21)$$

where U_{old} is the old independent set, U_{new} is the new orthonormal basis and P is an upper triangular matrix (defined in the next section) that is constructed from the columns of U_{old} . At each orthonormalization point the particular solution is turned into the orthogonal complement of the base set

$$v_{new} = v_{old} - U_{new} w_{new} \quad (5.22)$$

where w_{new} is defined in the next section. The terms v_{old} and v_{new} refer to the old and new particular solutions respectively.

Let the points at which orthonormalization has been carried out be denoted by x_1, x_2, \dots, x_n and let $x_0 = a$. Now consider the first interval defined in the range $[x_0, x_1]$. Let the particular solution, homogeneous solutions and overall solution be denoted by $v_0(x)$, $U_0(x)$ and $y_0(x)$ respectively. Then $v_0(x)$ satisfies

$$v'_0(x) = F(x)v_0(x) + g(x), \quad Av(a) = \alpha, \quad (5.23)$$

and $U_0(x)$ satisfies

$$U'_0(x) = F(x)U_0(x), \quad AU_0(a) = 0. \quad (5.24)$$

The general solution on this interval is obtained using the method of superposition. Hence,

$$y_0(x) = v_0(x) + U_0(x)c_0 \quad (5.25)$$

where c_0 is a constant to be determined by matching $y_0(x_1)$ with $y_1(x_1)$.

In using this representation $U_0(x_1)$ and $v_0(x_1)$ are the old independent set of base vectors and the old particular solution at x_1 . The new orthonormal set of base vectors and orthogonal complement to this set at x_1 are denoted by $U_1(x_1)$ and $v_1(x_1)$ respectively. Using $U_1(x_1)$ and $v_1(x_1)$ as initial conditions on the interval (x_1, x_2) the above procedure is repeated by solving

$$v'_1(x) = F(x)v_1(x) + g(x) \quad (5.26)$$

subject to the initial condition

$$v_1(x_1) = v_0(x_1) - U_1(x_1)w_1 \quad (5.27)$$

and by solving the system

$$U'_1(x) = F(x)U_1(x) \quad (5.28)$$

subject to the initial condition

$$U_0(x_1) = U_1(x_1)P_1 . \quad (5.29)$$

The general solution on this interval is

$$y_1(x) = v_1(x) + U_1(x)c_1 , \quad (5.30)$$

where the vector c_1 is determined by matching $y_1(x_2)$ with $y_2(x_2)$,

$$y_1(x_2) = y_2(x_2) . \quad (5.31)$$

Hence, on the interval (x_i, x_{i+1}) the solution is obtained as

$$y_i(x_i) = v_i(x) + U_i(x)c_i , \quad (5.32)$$

provided that the condition of continuity is met

$$y_{i-1}(x_i) = y_i(x_i) . \quad (5.33)$$

Thus from the above condition of continuity

$$v_{i-1}(x_i) + U_{i-1}(x_i)c_{i-1} = v_i(x_i) + U_i(x_i)c_i \quad (5.34)$$

but

$$v_i(x_i) = v_{i-1}(x_i) - U_i(x_i)w_i \quad (5.35)$$

and

$$U_{i-1}(x_i) = U_i(x_i)P_i . \quad (5.36)$$

Therefore equation (5.34) becomes

$$v_{i-1}(x_i) + U_i(x_i)P_i c_{i-1} = v_{i-1}(x_i) + U_i(x_i)(c_i - w_i) . \quad (5.37)$$

This provides the basic recursion formula for the vector c_{i-1} in terms of P_i , w_i and c_i

$$P_i c_{i-1} = (c_i - w_i) \quad (5.38)$$

At the final point, $x = b$, on the interval (x_m, x_b) the solution of the differential equation must satisfy

$$y_m(b) = v_m(b) + U_m(b)c_m . \quad (5.39)$$

Hence, using equation (5.8) the constant c_m can be determined,

$$By_m(b) = Bv_m(b) + BU_m(b)c_m = \beta \quad (5.40)$$

or

$$BU_m(b)c_m = \beta - Bv_m(b) . \quad (5.41)$$

Having determined the constant vector c_m (and providing all the orthonormalization information, such as P_1, P_2, \dots, P_m have been retained) the vectors $c_{m-1}, c_{m-2}, \dots, c_0$ can be found by solving the systems, equation (5.38),

$$P_r c_{r-1} = c_r - w_r \quad r = m, m-1, \dots, 1 \quad (5.38)$$

by back substitution. If the initial values $U_i(x_i), v_i(x_i)$ $i = 0, 1, 2, \dots, m$ have also been retained the solution $y(x)$ can be calculated

at any point $x \in (x_i, x_{i+1})$ by integrating forward from x_i and using the relation

$$y(x) = v_i(x) + U_i(x)c_i \quad (5.42)$$

In the formulation presented above the particular solution is not normalized (i.e. not made into a unit vector). Scott and Watts [62] have shown that the final solution representation with and without normalizing the particular solution are mathematically equivalent. If the particular solution is normalized then the recursion formula equation (5.38) is not valid. Scott and Watts [62] have developed a recursion formula valid for this case. They mention that a possible advantage of normalizing the particular solution is that it is then well scaled.

(c) Gram-Schmidt Orthogonalization Procedure

In this section the modified Gram-Schmidt procedure is outlined together with a set of criteria that must be met to prevent the solution vectors from becoming dependent.

Scott and Watts [62] have suggested that the old independent set of vectors Y_{old} be reorganized such that the vector with the largest norm appears in the first column. This involves postmultiplying the vector Y_{old} by a pivot matrix E such that

$$Y_{old} = Y'_{old} E = U_{new} P \quad (5.43)$$

where Y_{old} is the reorganized matrix. The term Y'_{old} is the matrix obtained directly from integration, E is the permutation matrix, U_{new} is the orthonormalized basis and P is an upper triangular matrix defining

the transformation. If the permutation matrix is included in the algorithm then the recursion formula equation (5.38) must be modified.

Consider the interval (x_{i-1}, x_i) .

$$y_{i-1}(x_i) = v_{i-1}(x_i) + U_{i-1}(x_i) E_{i-1} \tilde{c}_{i-1} \quad (5.44)$$

where

$$U_{i-1}(x_i) E_{i-1} = U_i(x_i) P . \quad (5.45)$$

Also

$$y_i(x_i) = v_i(x_i) + U_i(x_i) E_i \tilde{c}_i , \quad (5.46)$$

$$= v_i(x_i) + U_i(x_i) c_i . \quad (5.47)$$

Equating (5.44) and (5.47) at, x_i , yields

$$v_{i-1}(x_i) + U_{i-1}(x_i) E_{i-1} \tilde{c}_{i-1} = v_i(x_i) + U_i(x_i) c_i \quad (5.48)$$

Eliminating $v_{i-1}(x_i)$ and $v_i(x_i)$, the following recursion relation is obtained:

$$P_i \tilde{c}_{i-1} = (c_i - w_i) , \quad (5.49)$$

where

$$c_{i-1} = E_{i-1} \tilde{c}_{i-1} \quad (5.50)$$

The modified Gram-Schmidt procedure defines the matrix P (see Stewart [67]) as,

$$P = \begin{bmatrix} \|u_1^{(0)}\| & (u_2^{(0)}, u_1) & (u_3^{(0)}, u_1) \cdots (u_k^{(0)}, u_1) \\ & \|u_2^{(1)}\| & (u_3^{(1)}, u_2) \cdots (u_k^{(1)}, u_2) \\ & & \|u_3^{(2)}\| \cdots (u_k^{(2)}, u_3) \\ & & & \|u_k^{(k-1)}\| \end{bmatrix} \quad (5.51)$$

and the matrix U by

$$\begin{aligned} u_j^{(0)} &= y_j, \quad j = 1, \dots, k \\ u_1 &= u_1^{(0)} / \|u_1^{(0)}\| \\ \left. \begin{aligned} u_j^{(i)} &= u_j^{(i-1)} - (u_j^{(i-1)}, u_i) u_i \\ & \qquad \qquad \qquad i = 1, \dots, k-1 \\ & \qquad \qquad \qquad j = i+1, \dots, k \\ u_j &= u_j^{(j-1)} / \|u_j^{(j-1)}\| \end{aligned} \right\} \quad (5.52) \end{aligned}$$

The subscript notation refers to the corresponding column vectors in Y_{old} and U_{new} [see equation (5.43)].

The particular solution v_{old} is turned into the orthogonal complement of the new base set U_{new} (i.e. the vector, v_{old} , is converted into a vector v_{new} such that v_{new} is orthogonal to all the components of U_{new})

$$v_{new} = v_{old} - U_{new} w_{new}, \quad (5.53a)$$

where w_i the i -th component of the vector w is defined to be

$$w_i = v_{\text{old}}^T u_i . \quad (5.53b)$$

Here v_{old}^T is the transpose of v_{old} and u_i is the i -th column of U_{new} .

It should be noted that the above operation simply makes use of the Gram-Schmidt procedure.

Several tests have appeared in the literature to determine whether an orthonormalization is necessary (Scott and Watts [62] Gersting and Jankowski [22]). Scott and Watts have suggested a check which is described below. The algorithm has been implemented in the code developed for this thesis. A slightly different version is used in the Suport code [62]. The basic idea is to avoid using solutions that violate a condition which implies that linear dependence may not be present.

The conditions chosen are,

$$\| u_j^{j-1} \| < \epsilon \| y_j \| \quad j = 1, 2, \dots k \quad (5.54)$$

and

$$\| v_{\text{new}} \| < \epsilon \| v_{\text{old}} \| \quad (5.55)$$

where $\epsilon = 10^{-L}$ and L is about three-fourths of the number of significant decimal digits available in the computer wordlength. Scott and Watts [62] present the following justification of the above criteria. Suppose that a vector in the old set is dependent, then the orthonormalization procedure will turn it into a null vector. This provides the motivation for comparing the size of P_{jj} with that of P_{11} , where $P_{11} = \| u_1^0 \|^2$ is

used since the vector u_1^0 has the largest magnitude of the vectors in the old set as a result of the pivoting process.

Since the magnitude of the vectors in the original set may vary these vectors are appropriately scaled by producing a set of unit vectors, Y_S . Hence

$$Y_S = U P S = U \bar{P} \quad (5.56)$$

where $S = \text{diag} \{ 1/\|y_1\|, \dots, 1/\|y_k\| \}$

and

$$\bar{P}_{jj} = \frac{P_{jj}}{\|y_j\|} \quad (5.57)$$

The linear dependence test on the diagonal now requires that

$$\frac{P_{jj}}{\|y_j\|} < \epsilon \frac{P_{11}}{\|y_1\|} = \epsilon \quad (5.58)$$

The above expression is the required linear dependence test.

(d) Numerical Solution of the Mean Energy and Mean Dissipation Equations

The system of equations (3.67)-(3.71) describing the mean energy and mean dissipation can be written in the form

$$\frac{d}{dy} \left[\left(1 + \frac{\bar{v}_t}{v_\epsilon} \right) \frac{d\bar{K}}{dy} \right] + \bar{G}_{\bar{K}}(\bar{K}, \bar{\epsilon}, y) = 0 \quad (5.59)$$

$$\frac{d}{dy} \left[\left(1 + \frac{\bar{v}_t}{v\sigma_\epsilon} \right) \frac{d\bar{\epsilon}}{dy} \right] + \bar{G}_{\bar{\epsilon}}(\bar{K}, \bar{\epsilon}, y) = 0 \quad (5.60)$$

These differential equations are subject to the boundary conditions

$$\overline{K} = 0, \overline{\varepsilon} = 0 \text{ at } y = 0 \quad (5.61a)$$

$$\overline{K} = \frac{1}{C_{\mu}^{1/2}}, \overline{\varepsilon} = \frac{1}{\kappa y} \text{ for large } y \quad (5.61b)$$

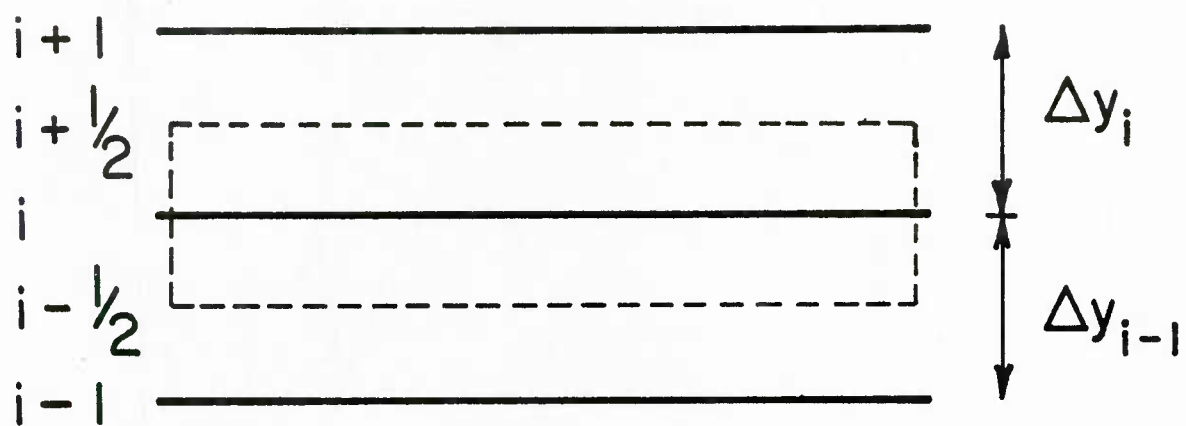
where κ is the Von Karman constant. The boundary conditions at large y are simply that the mean flow is described by a constant stress layer. In the above equations $G_{\overline{K}}$ and $G_{\overline{\varepsilon}}$ appear as source terms and represent the combined effects of production and dissipation.

These highly nonlinear equations are solved using finite difference techniques and Newton's method. In order to derive the discretization equations a control volume is set up on a variable step grid such that the boundaries are midway between the grid points (see Figure 5.1). Equations (5.59) and (5.60) can then be integrated across the control volume to yield

$$\left(1 + \frac{\overline{v}_t}{v}\right)_{i+1/2} \frac{d\overline{K}}{dy} \Big|_{i+1/2} - \left(1 + \frac{\overline{v}_t}{v}\right)_{i-1/2} \frac{d\overline{K}}{dy} \Big|_{i-1/2} + \int_{i-1/2}^{i+1/2} \frac{G_{\overline{K}}}{K} dy = 0, \quad (5.62)$$

$$\left(1 + \frac{\overline{v}_t}{v\sigma_{\varepsilon}}\right)_{i+1/2} \frac{d\overline{\varepsilon}}{dy} \Big|_{i+1/2} - \left(1 + \frac{\overline{v}_t}{v\sigma_{\varepsilon}}\right)_{i-1/2} \frac{d\overline{\varepsilon}}{dy} \Big|_{i-1/2} + \int_{i-1/2}^{i+1/2} \frac{G_{\overline{\varepsilon}}}{\varepsilon} dy = 0. \quad (5.63)$$

The derivatives in equations (5.62) and (5.63) are approximated by using a piecewise linear profile. The integral terms are estimated by using the average value of the functions $G_{\overline{K}}$ and $G_{\overline{\varepsilon}}$ respectively.



Typical Control Volume

Figure 5.1. Grid Used for Integrating Mean K- ϵ Model Equations

Since the grid consists of $m + 2$ levels and since the energy and dissipation are known at both boundaries, finite difference equations need only be written for the grid points $2 \leq i \leq m + 1$,

$$\left(1 + \frac{\bar{v}_t}{v}\right)_{i+\frac{1}{2}} \frac{(\bar{K}_{i+1} - \bar{K}_i)}{\Delta y_i} - \left(1 + \frac{\bar{v}_t}{v}\right)_{i-\frac{1}{2}} \frac{(\bar{K}_i - \bar{K}_{i-1})}{\Delta y_{i-1}} + G_{\bar{K}_i} \frac{(\Delta y_i + \Delta y_{i-1})}{2} = 0, \quad (5.63a)$$

$$\left(1 + \frac{\bar{v}_t}{v\sigma_\epsilon}\right)_{i+\frac{1}{2}} \frac{(\bar{\epsilon}_{i+1} - \bar{\epsilon}_i)}{\Delta y_i} - \left(1 + \frac{\bar{v}_t}{v\sigma_\epsilon}\right)_{i-\frac{1}{2}} \frac{(\bar{\epsilon}_i - \bar{\epsilon}_{i-1})}{\Delta y_{i-1}} + G_{\bar{\epsilon}_i} \frac{(\Delta y_i + \Delta y_{i-1})}{2} = 0, \quad (5.63b)$$

$$\bar{K}_1 = 0, \quad \bar{\epsilon}_1 = 0, \quad (5.63c)$$

$$\bar{K}_{m+2} = \frac{1}{C \frac{1}{2}}, \quad \bar{\epsilon}_{m+2} = \frac{1}{\kappa} y_{m+2}. \quad (5.63d)$$

The above system represents $2m$ nonlinear algebraic equations in $2m$ unknowns $\bar{K}_2, \epsilon_2, \bar{K}_3, \epsilon_3, \dots, \bar{K}_{m+2}, \epsilon_{m+2}$. The algebraic equations were solved using Newton's method, Abrams [1]. The solution procedure was to linearize the source terms $G_{\bar{K}_i}$ and $G_{\bar{\epsilon}_i}$ as follows

$$\frac{G_{\bar{K}_i}^n}{\bar{K}_i} = \frac{G_{\bar{K}_i}^{n-1}}{\bar{K}_i} + \frac{dG_{\bar{K}_i}}{d\bar{K}_i} \Big|^{n-1} (\bar{K}_i^{n+1} - \bar{K}_i^n) + \frac{dG_{\bar{K}_i}}{d\bar{\epsilon}_i} \Big|^{n-1} (\bar{\epsilon}_i^n - \bar{\epsilon}_i^{n-1}), \quad (5.64a)$$

$$G_{\bar{\epsilon}_i}^n = G_{\bar{\epsilon}_i}^{n-1} + \frac{dG_{\bar{\epsilon}_i}}{d\bar{K}_i} \Big|^{n-1} (\bar{K}_i^n - \bar{K}_i^{n-1}) + \frac{dG_{\bar{\epsilon}_i}}{d\bar{\epsilon}_i} \Big|^{n-1} (\bar{\epsilon}_i^n - \bar{\epsilon}_i^{n-1}) \quad (5.64b)$$

and to linearize the diffusion terms as follows,

$$\begin{aligned} \left(1 + \frac{\bar{v}_t}{v}\right)_{i+\frac{1}{2}}^n (\bar{K}_{i+1}^n - \bar{K}_i^n) &= \left(1 + \frac{\bar{v}_t}{v}\right)_{i+\frac{1}{2}}^{n-1} (\bar{K}_{i+1}^{n-1} - \bar{K}_i^{n-1}) \\ &+ \left(1 + \frac{\bar{v}_t}{v}\right)_{i+\frac{1}{2}}^{n-1} (\bar{K}_{i+1}^n - \bar{K}_{i+1}^{n-1}) + \left(1 + \frac{\bar{v}_t}{v}\right)_{i+\frac{1}{2}}^{n-1} (\bar{K}_i^n - \bar{K}_i^{n-1}), \end{aligned} \quad (5.65a)$$

$$\begin{aligned} \left(1 + \frac{\bar{v}_t}{v\sigma_\epsilon}\right)_{i+\frac{1}{2}}^n (\bar{\epsilon}_{i+1}^n - \bar{\epsilon}_i^n) &= \left(1 + \frac{\bar{v}_t}{v\sigma_\epsilon}\right)_{i+\frac{1}{2}}^{n-1} (\bar{\epsilon}_{i+1}^{n-1} - \bar{\epsilon}_i^{n-1}) \\ &+ \left(1 + \frac{\bar{v}_t}{v\sigma_\epsilon}\right)_{i+\frac{1}{2}}^{n-1} (\bar{\epsilon}_{i+1}^n - \bar{\epsilon}_{i+1}^{n-1}) + \left(1 + \frac{\bar{v}_t}{v\sigma_\epsilon}\right)_{i+\frac{1}{2}}^{n-1} (\bar{\epsilon}_i^n - \bar{\epsilon}_i^{n-1}). \end{aligned} \quad (5.65b)$$

Similar expressions to (5.65a) and (5.65b) can be derived for the diffusion terms $(1 + \bar{v}_t/v)_{i-\frac{1}{2}}^n (\bar{K}_i^n - \bar{K}_{i-1}^n)$ and $(1 + \bar{v}_t/\sigma_\epsilon v)_{i-\frac{1}{2}}^n (\bar{\epsilon}_i^n - \bar{\epsilon}_{i-1}^n)$.

In the above equations the superscript, n, refers to the nth iterate while the superscript, n-1, refers to the previously known iterate. For convenience the following notation is introduced

$$\delta_{\bar{K}_i} = \bar{K}_i^n - \bar{K}_i^{n-1} \quad 2 \leq i \leq m+1, \quad (5.66a)$$

$$\delta_{\bar{\epsilon}_i} = \bar{\epsilon}_i^n - \bar{\epsilon}_i^{n-1} \quad 2 \leq i \leq m+1, \quad (5.66b)$$

$$\delta_{\bar{K}_1} = \delta_{\bar{\epsilon}_1} = 0, \quad (5.66c)$$

$$\delta_{\bar{K}_{m+2}} = \delta_{\bar{\epsilon}_{m+2}} = 0. \quad (5.66d)$$

If equations (5.66a)-(5.66d) are substituted into equations (5.64a)-(5.65b) and the resulting equations substituted into equations (5.63a)-(5.63d) a linear system of $2m$ equations for the unknown iterates $\delta_{\bar{K}_2}, \delta_{\bar{\epsilon}_2}, \dots, \delta_{\bar{K}_{m+1}}, \delta_{\bar{\epsilon}_{m+1}}$, is obtained. These iterates are then used to update the values of $\bar{K}_2^{n-1}, \bar{\epsilon}_2^{n-1}, \dots, \bar{K}_{m+1}^{n-1}, \bar{\epsilon}_{m+1}^{n-1}$.

This procedure is repeated until a satisfactory level of convergence is obtained.

CHAPTER 6

RESULTS

In this chapter the results of the calculations made with the various models developed in Chapter 3 are presented. An interpretation and discussion of the results is made in the final chapter of this thesis.

The solution of equation (3.13) provides detailed information on the velocity, shear stress and pressure fields. It is found that the flow field in the immediate vicinity of the wave surface and the wave induced surface shear stress are particularly sensitive to the type of turbulence model employed. Therefore, emphasis will be placed on the prediction of the measured surface shear stress profiles presented in Chapter 4. These profiles are characterized by a dimensionless amplitude $a |\hat{\tau}(0)|$ and phase angle θ such that $\text{Real} (a \hat{\tau}(0) e^{i\alpha x}) = a |\hat{\tau}(0)| \cos(\alpha x + \theta)$. For thick boundary layers both $|\hat{\tau}(0)|$ and θ are functions of a single parameter, α , the dimensionless wave number.

Where possible the predicted wave induced surface pressure is also compared with the available measurements. However, the considerable scatter in the pressure measurements makes the comparison difficult. The wave induced pressure is also characterized by a dimensionless amplitude $a |\hat{p}(0)|$ and a phase angle θ_p such that $\text{Real} (a \hat{p}(0) e^{i\alpha x}) = a |\hat{p}(0)| \cos(\alpha x + \theta_p)$.

(a) Quasi-Laminar Model: Model A

The simplest model developed in Chapter 3 is the Quasi-Laminar Model (Model A), for which the effects of turbulence enter the problem

only in the specification of the mean velocity profile. Thorsness [70] has examined several velocity profile relations and concluded that the calculations are insensitive to the choice of a velocity profile function provided it gives a reasonable fit to the experimental measurements. Consequently the calculations were carried out using the Van Driest velocity profile with the Von Karman constant, $\kappa = 0.41$, and the viscous thickness parameter, $A = 26$. Figures 6.1 and 6.2 compare the predicted values of the magnitude and phase angle of the wave induced shear stress with measurements as a function of α . For large values of α , corresponding to small wavelengths, experiment and theory are in fair agreement; however, as the wave number decreases the deviations between experiment and theory increase. This is expected since the influence of the wave surface extends further into the flow as the wavelength increases (decreasing α). For large values of α the effects of the wave surface are confined to the viscous wall region. Since the fully turbulent part of the boundary layer is undisturbed the effect of turbulence on the wave induced flow is not important. Figures 6.3, 6.4, 6.5 and 6.6 show the wave induced velocity profile function, $\text{Real}(\hat{u}(y) e^{i\alpha x})$, for $\alpha = 0.1, 0.01, 0.0045$ and 0.001 respectively. These show how the disturbance caused by the wave is confined closer to the surface as α increases.

Figures 6.7 and 6.8 compare the predicted magnitude and phase angle of the surface pressure with the available data.

(b) Model C*

The first turbulence model tested, Model C*, employs the Van Driest mixing length hypothesis to estimate a turbulent viscosity and ultimately a turbulent shear stress. The model uses the flat plate value of $A = 26$ for the viscous sublayer parameter. To account for the effects of pressure

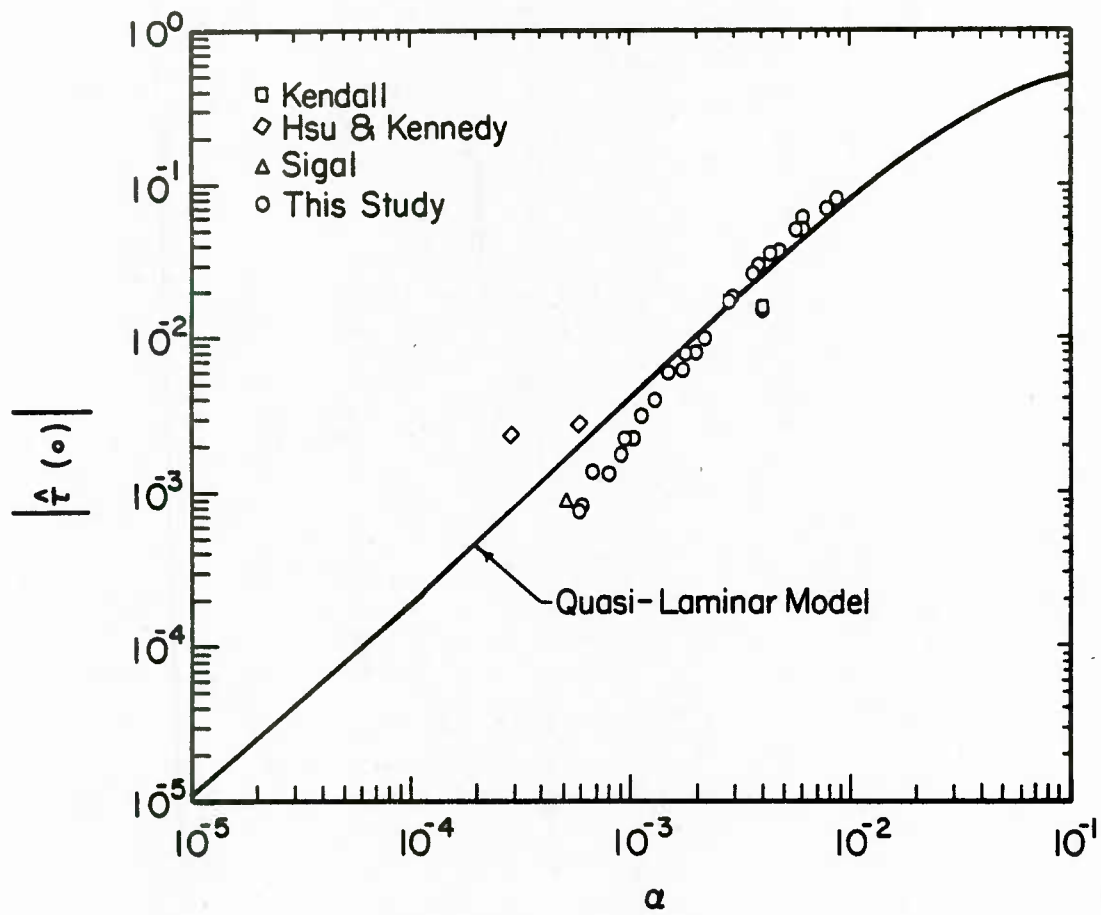


Figure 6.1. $|\hat{\tau}(\alpha)|$ for Quasi-Laminar Model

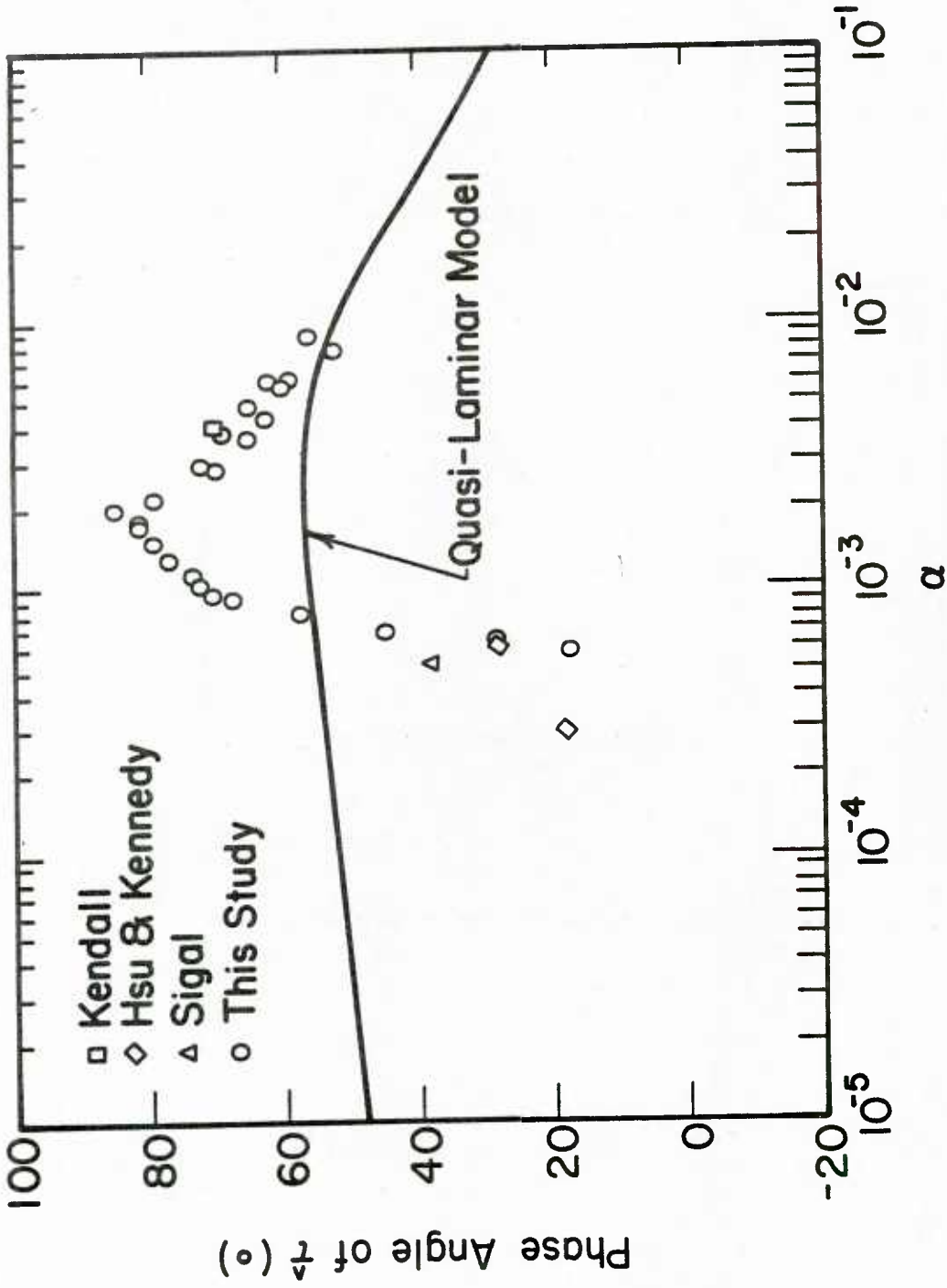


Figure 6.2. $\hat{\tau}(\alpha)$ Phase Angle for Quasi-Laminar Model

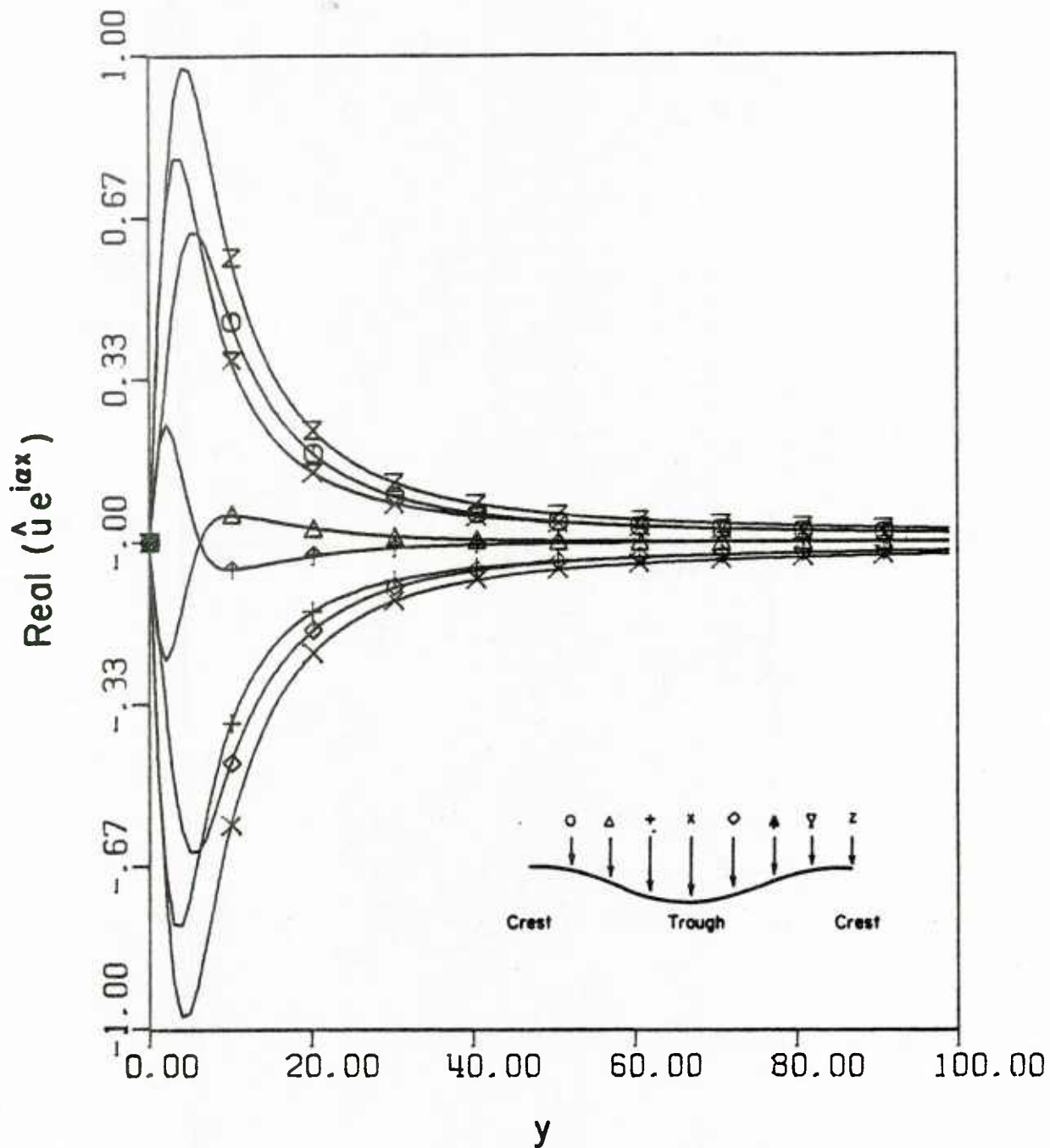


Figure 6.3. $\text{Real}(\hat{u} e^{i\alpha x})$ for Quasi-Laminar Model $\alpha = 0.1$

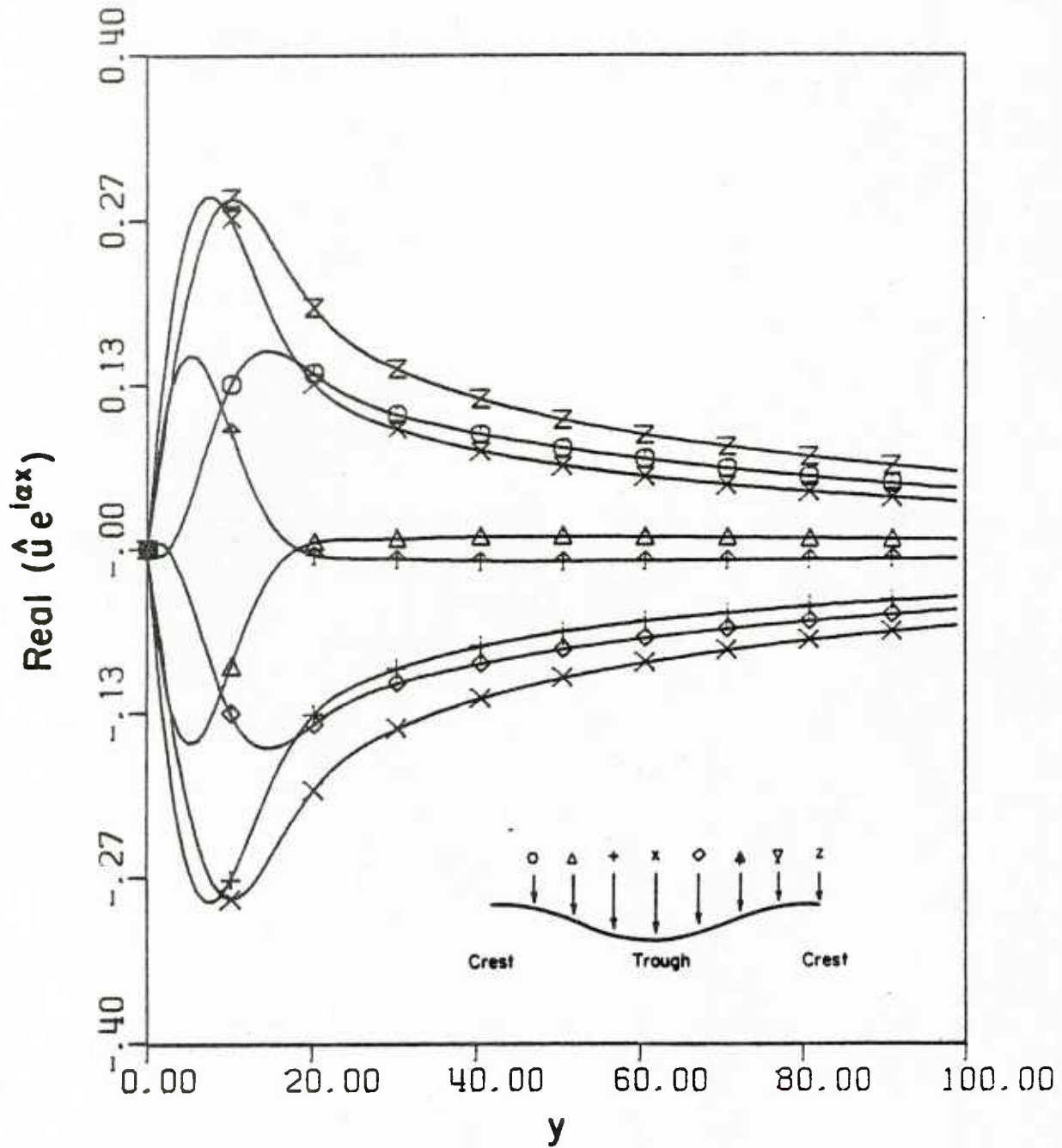


Figure 6.4. $\text{Real}(\hat{u} e^{i\alpha x})$ for Quasi-Laminar Model $\alpha = 0.01$

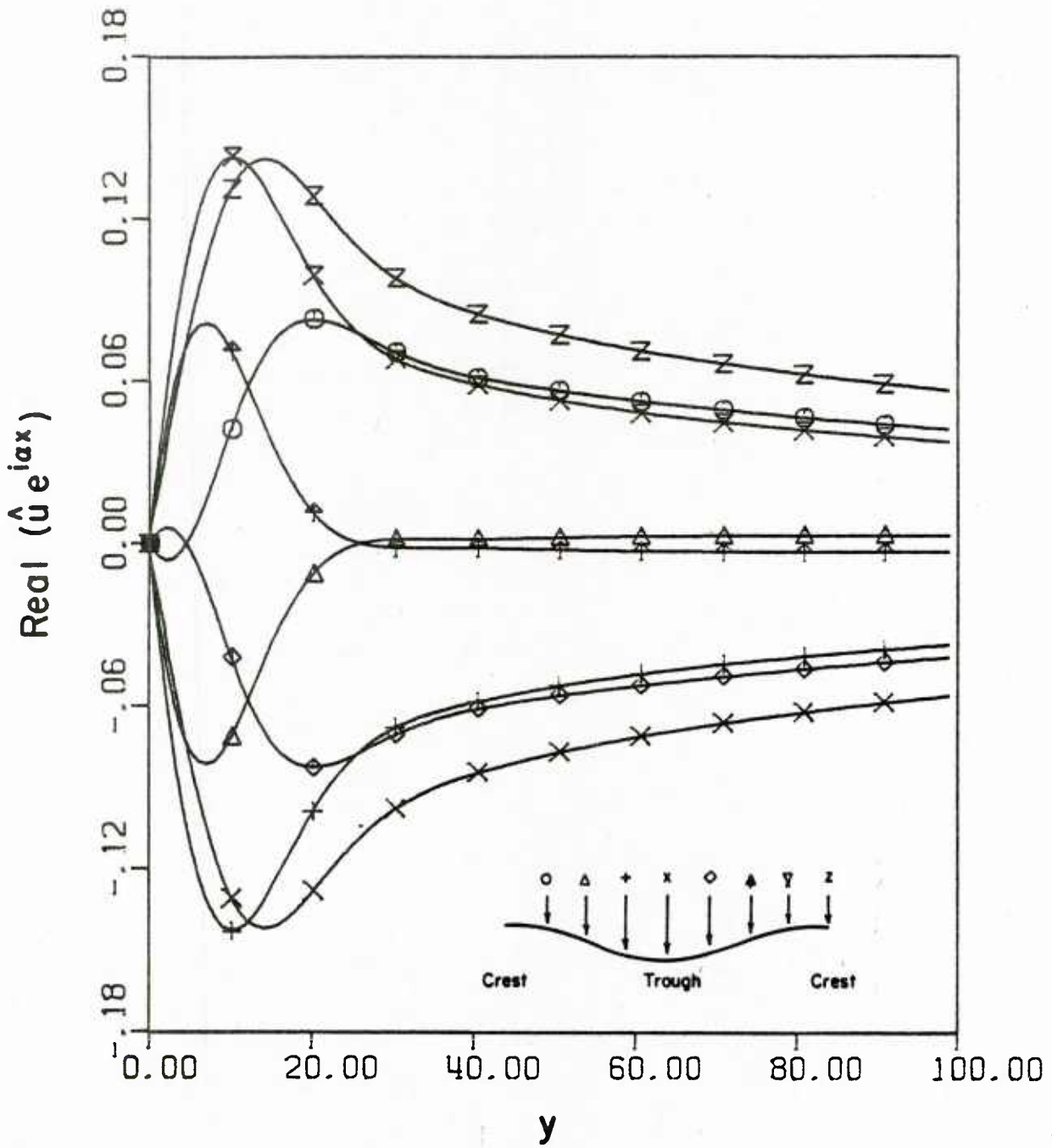


Figure 6.5. $\text{Re}(\hat{u} e^{i\alpha x})$ for Quasi-Laminar Model $\alpha = 0.0045$

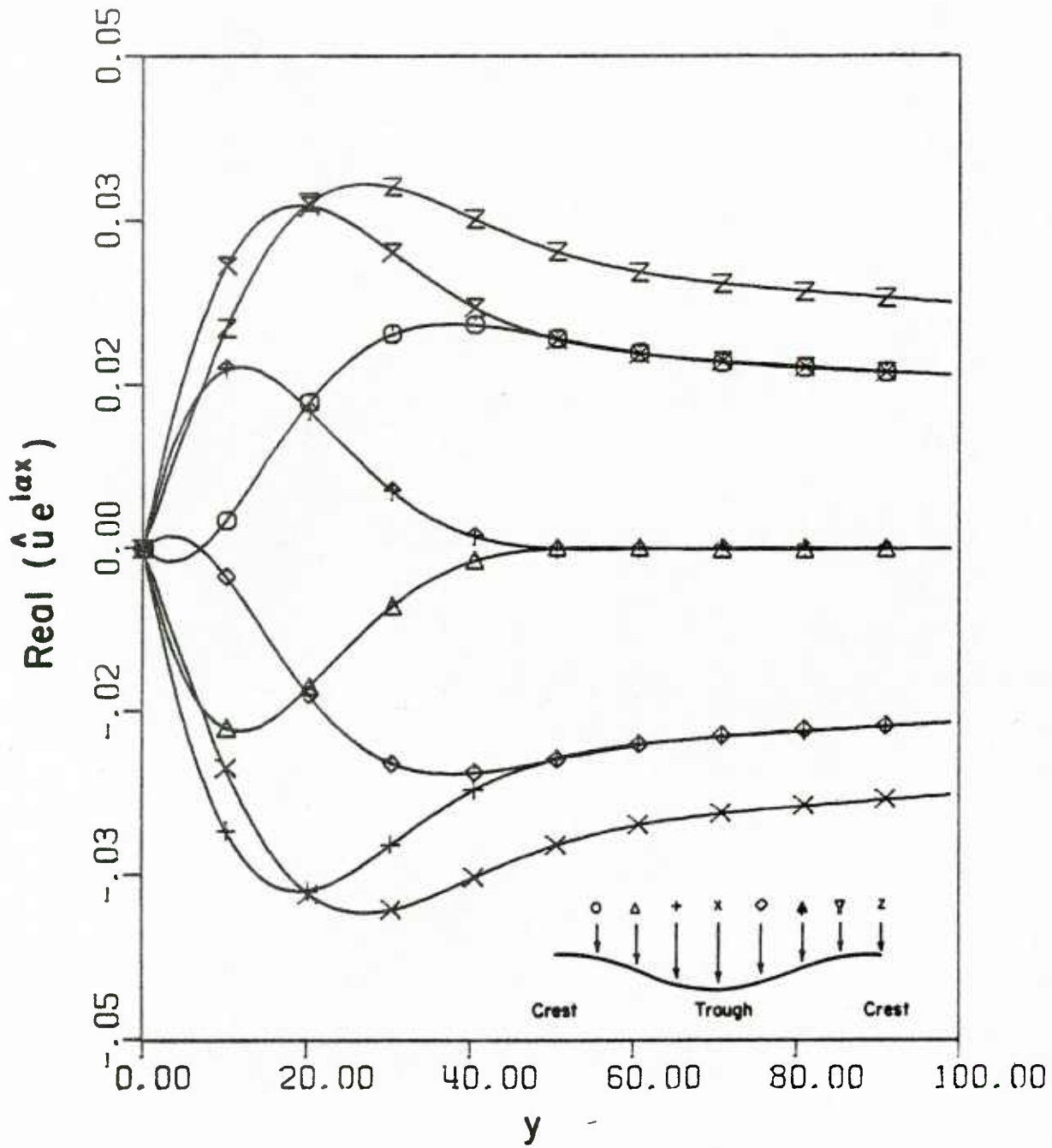
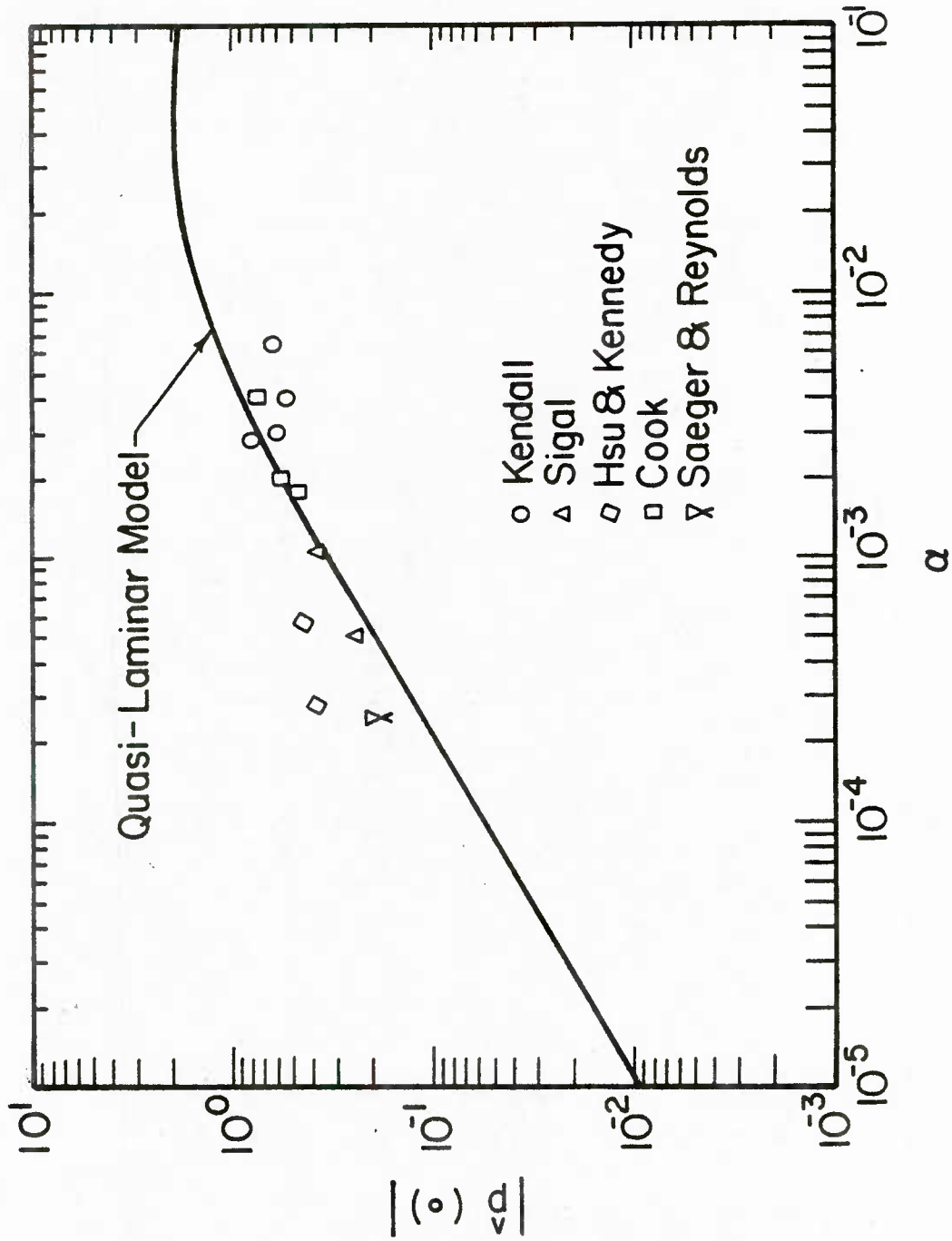


Figure 6.6. Real ($\hat{u} e^{i\alpha x}$) for Quasi-Laminar Model $\alpha = 0.001$

Figure 6.7. $|\hat{p}(\alpha)|$ for Quasi-Laminar Model

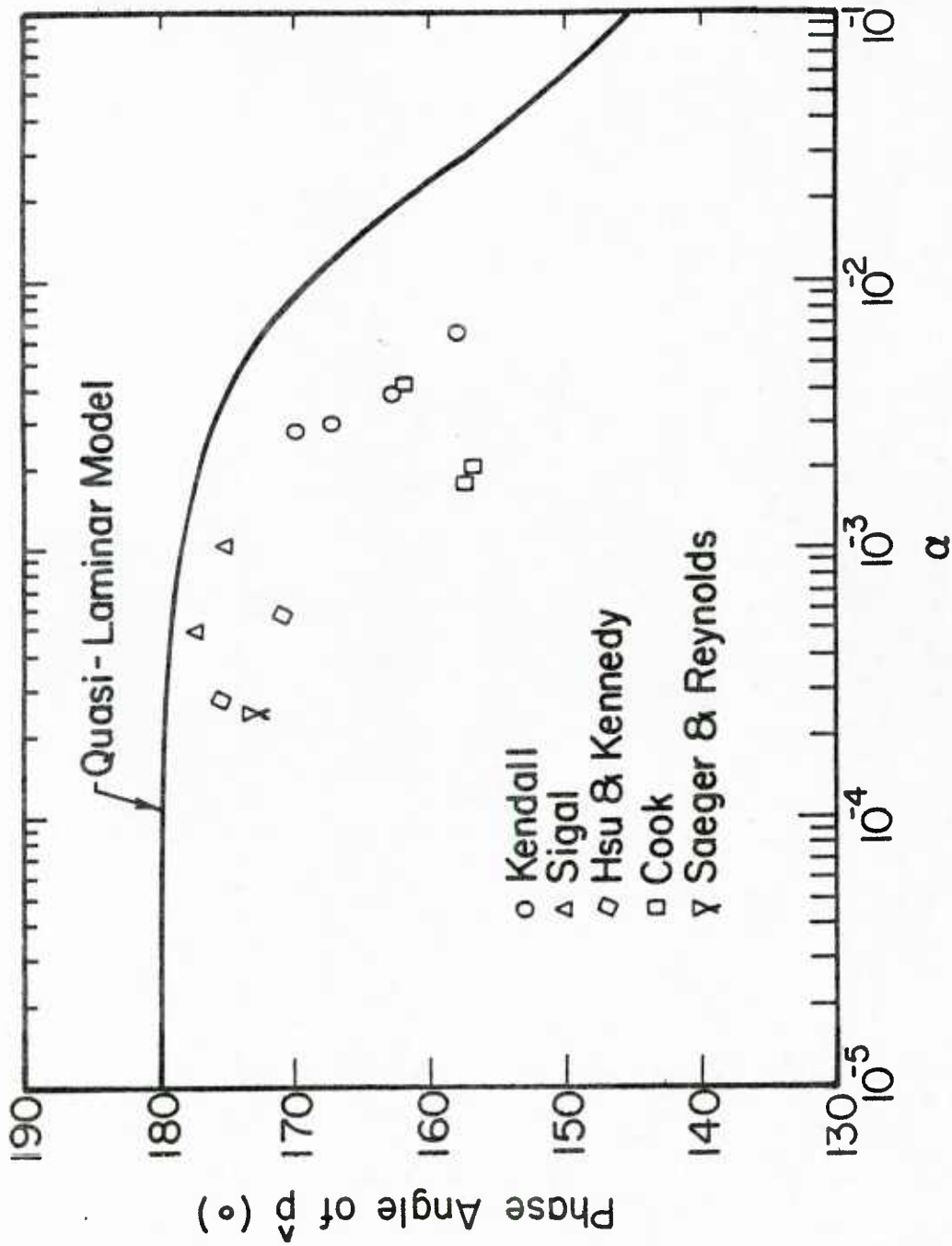


Figure 6.8. $\hat{p}(\alpha)$ Phase Angle for Quasi-Laminar Model

gradient on the thickness of the viscosity dominated sublayer the local value of the wall shear stress is used in the Van Driest damping function. Figures 6.9 and 6.10 compare the amplitude and phase angle of the shear stress with measured values. The model predicts a maximum in the phase angle of the shear stress at $\alpha = 0.007$ which is not what is observed experimentally. The model also fails to predict the sharp decrease in the phase angle of the wave induced shear stress.

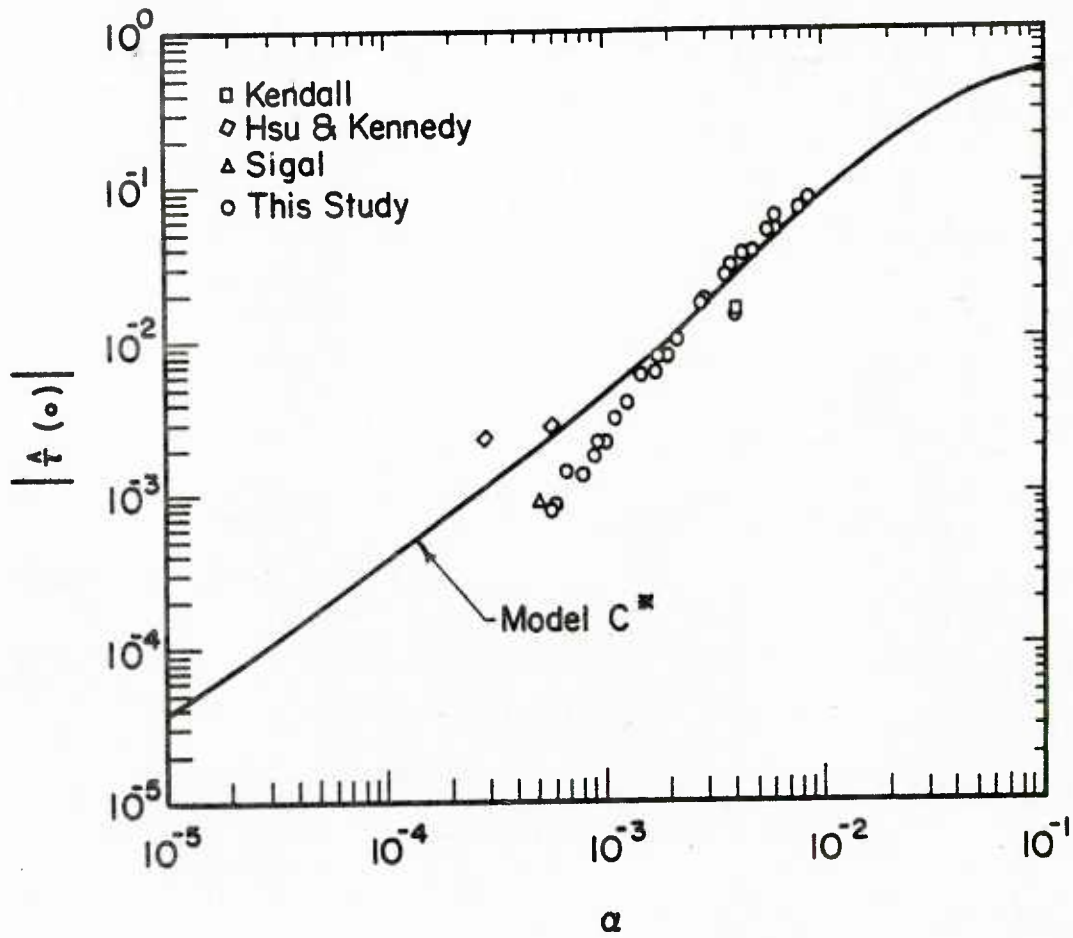
The phase angle and amplitude of the wave induced surface pressure are shown in Figures 6.11 and 6.12. Figures 6.13, 6.14 and 6.15 show the wave induced velocity profiles for $\alpha = 0.01$, 0.0045 and 0.001 respectively.

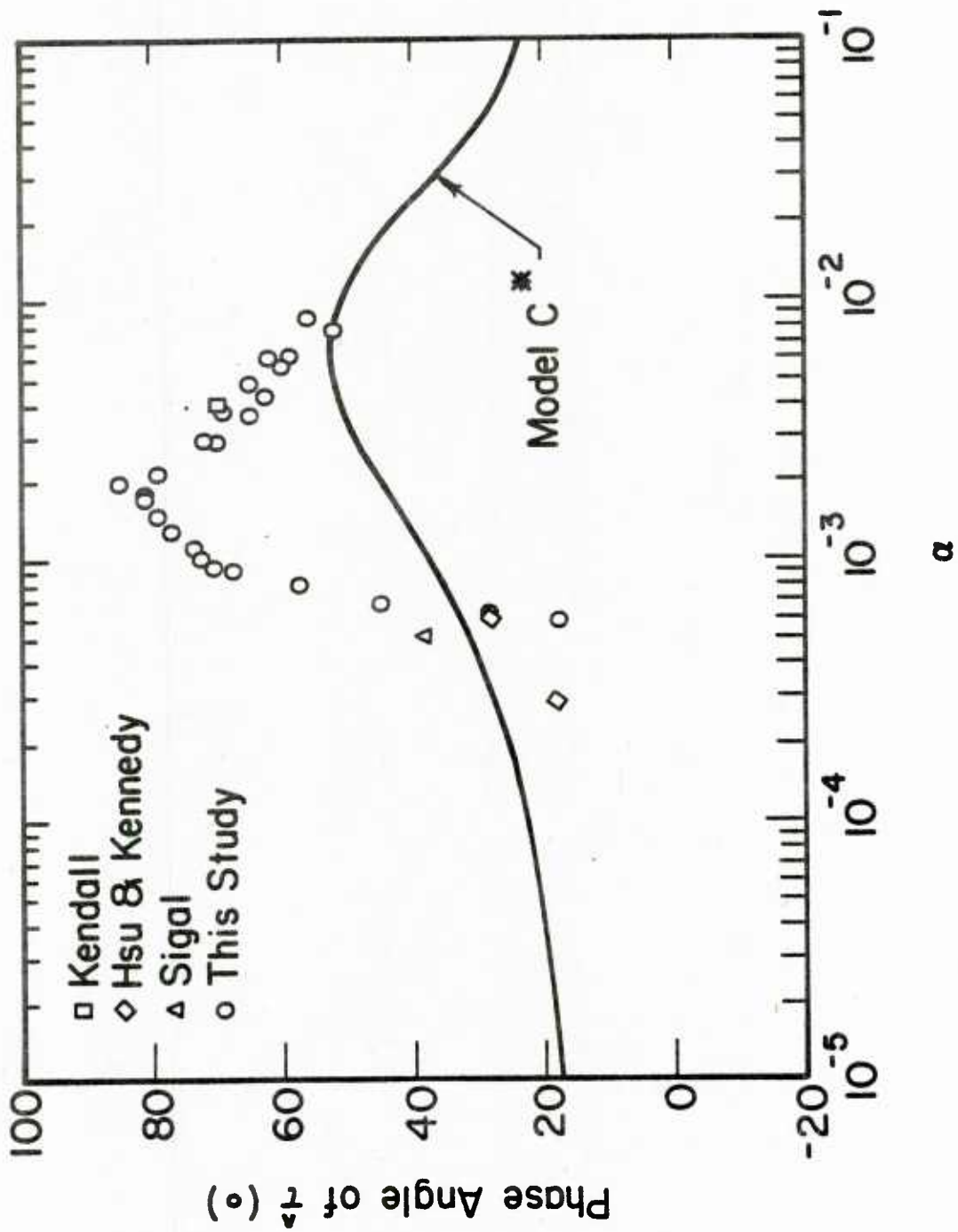
(c) Equilibrium Turbulence Model

The next model tested is similar to Model C* except that the effect of pressure gradient on the viscous sublayer is accounted for by allowing the sublayer parameter, A, to be composed of a mean value and a wave induced value, $\hat{A} e^{i\alpha x}$, which is a function of the pressure gradient. This formulation is referred to as the Equilibrium Turbulence Model since the model assumes that the turbulence adjusts instantaneously to changes in the pressure gradient.

The implementation of this model requires the specification of a single constant, k_1 , defined in equation 3.47. Kays et al. suggest a value of $-30 < k_1 < -20$ be used. Figure 6.16 shows the effect of this constant on the calculated phase angle of the wave induced shear stress.

For an equilibrium situation the pressure gradient would tend to shift the maximum in the wall shear stress in the downstream direction because an adverse pressure gradient which tends to enhance turbulence exists on the downstream side of the wave. Therefore for small values

Figure 6.9. $|\hat{t}(o)|$ for Model C*

Figure 6.10. $\hat{\tau}(\alpha)$ Phase Angle for Model C*

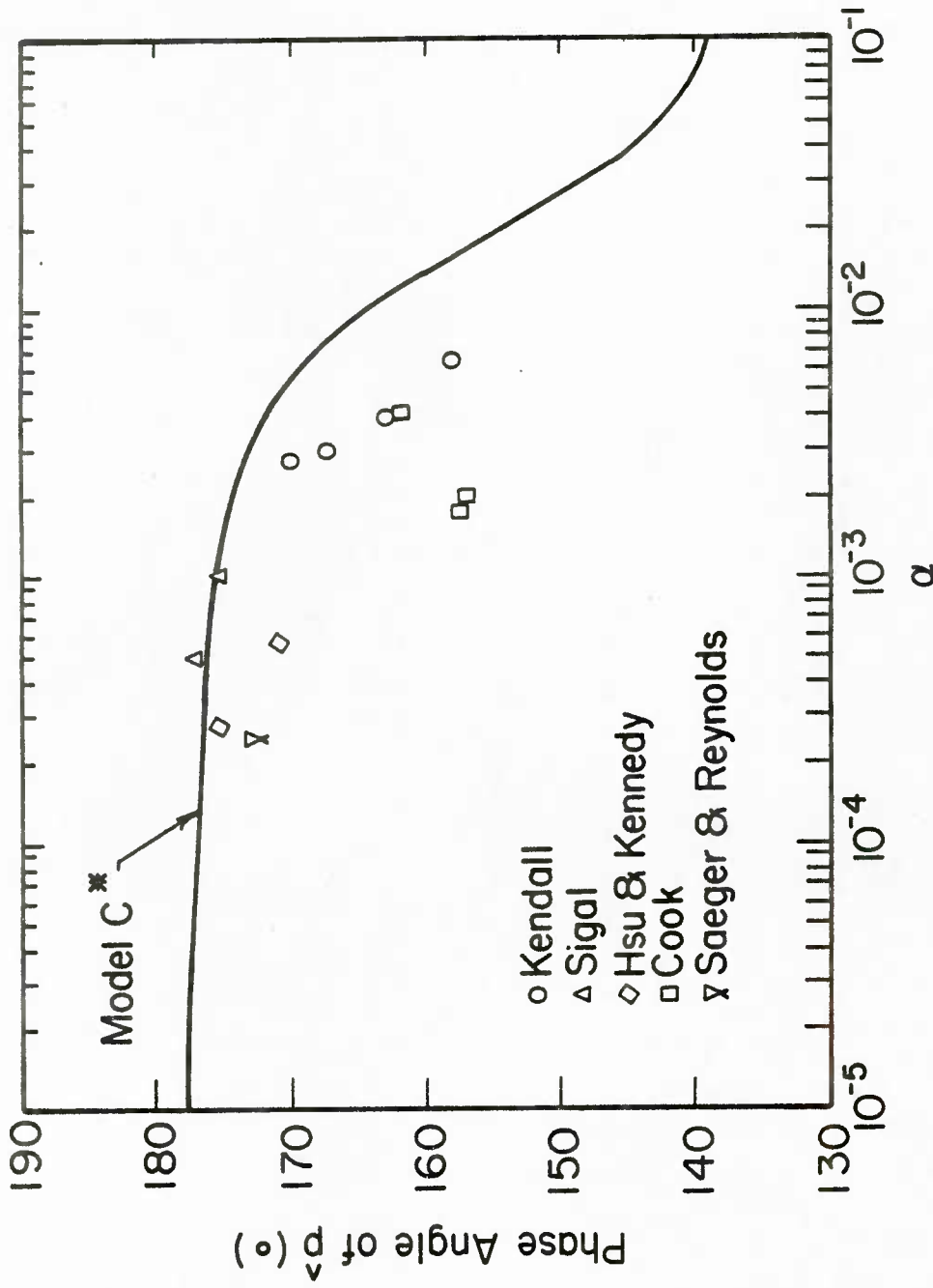


Figure 6.11. $\hat{p}(\alpha)$ Phase Angle for Model C*

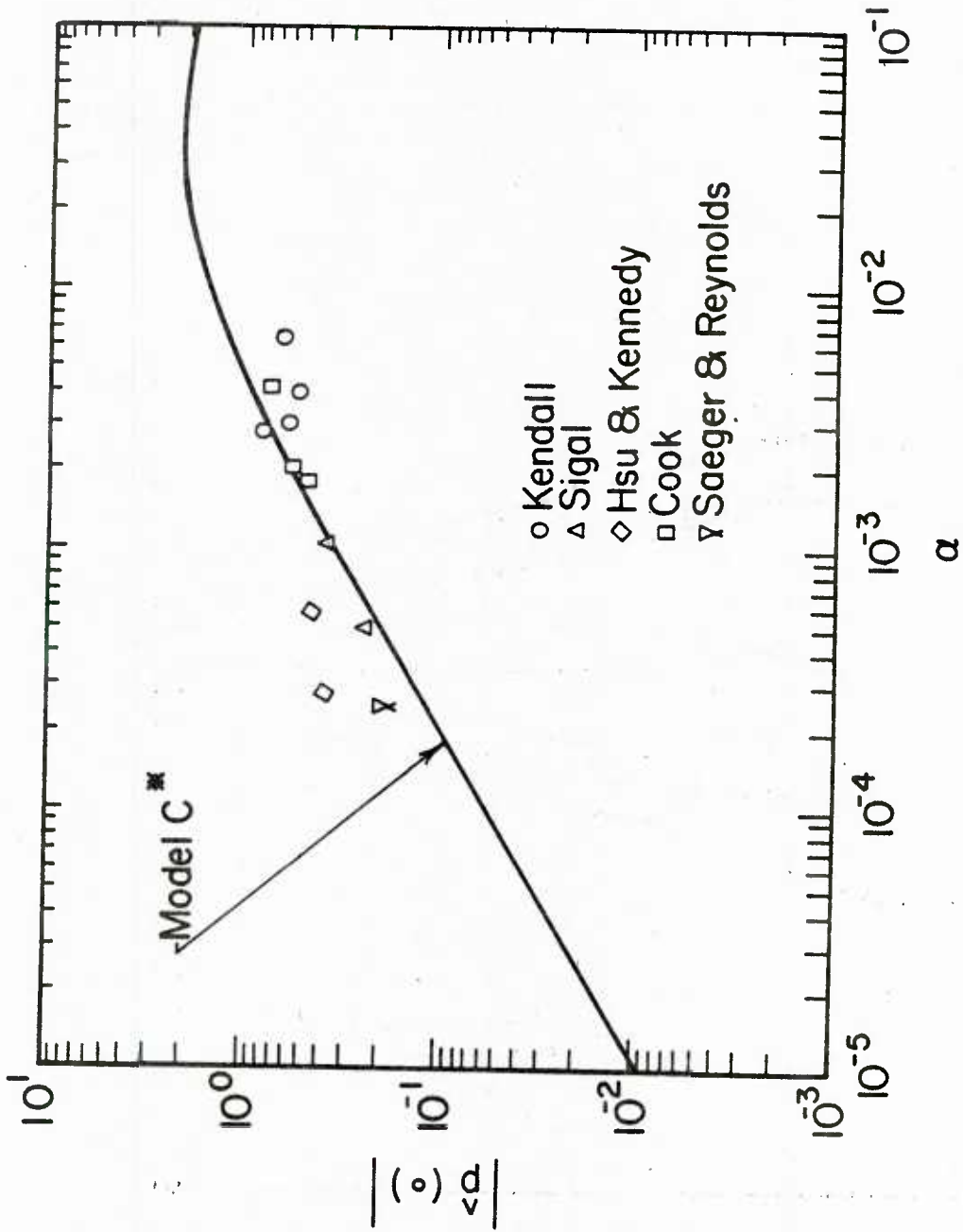


Figure 6.12. $|\hat{p}(\alpha)|$ for Model C^*

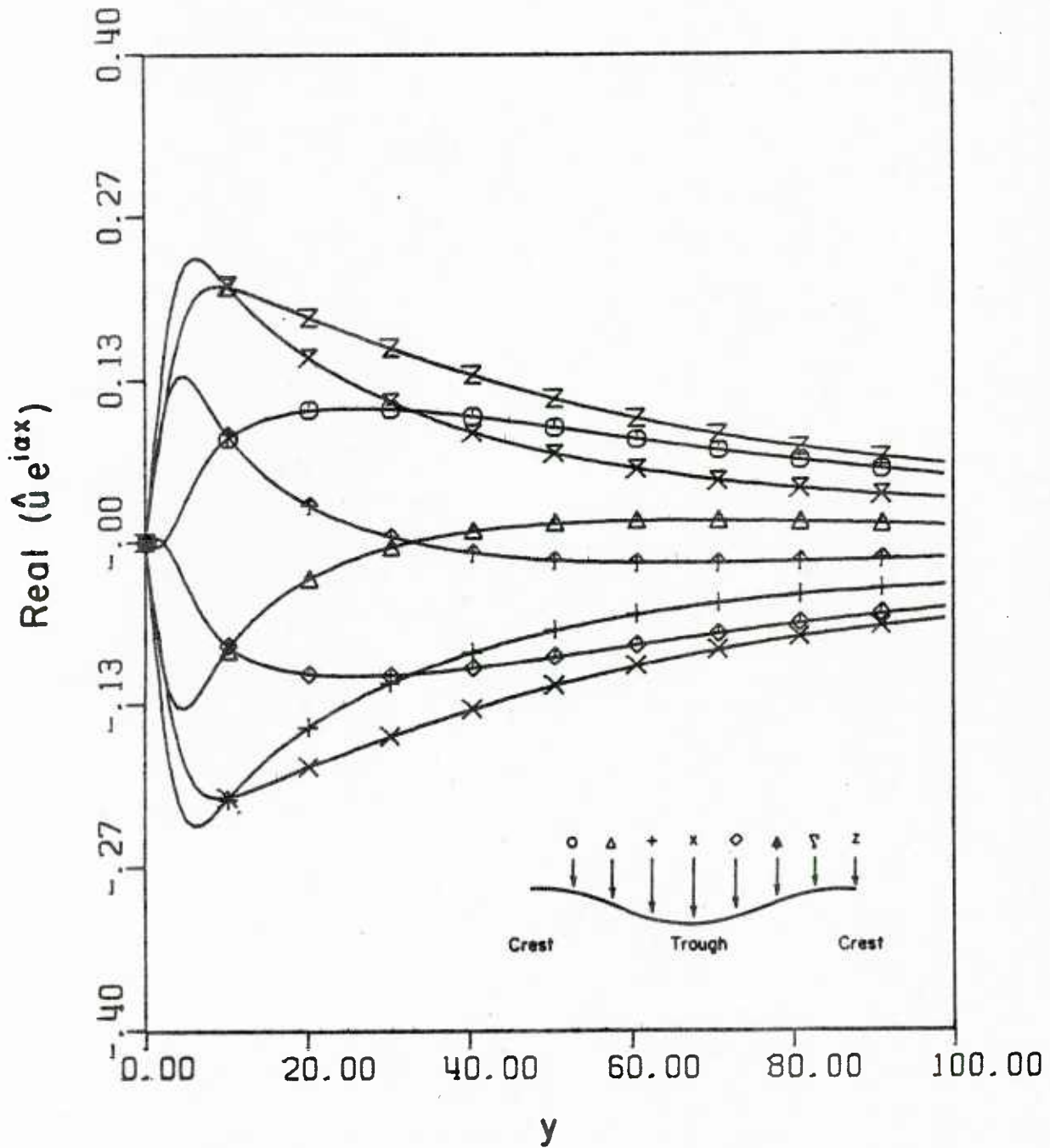


Figure 6.13. $\text{Re}(\hat{u} e^{i\alpha x})$ for Model C* $\alpha = 0.01$

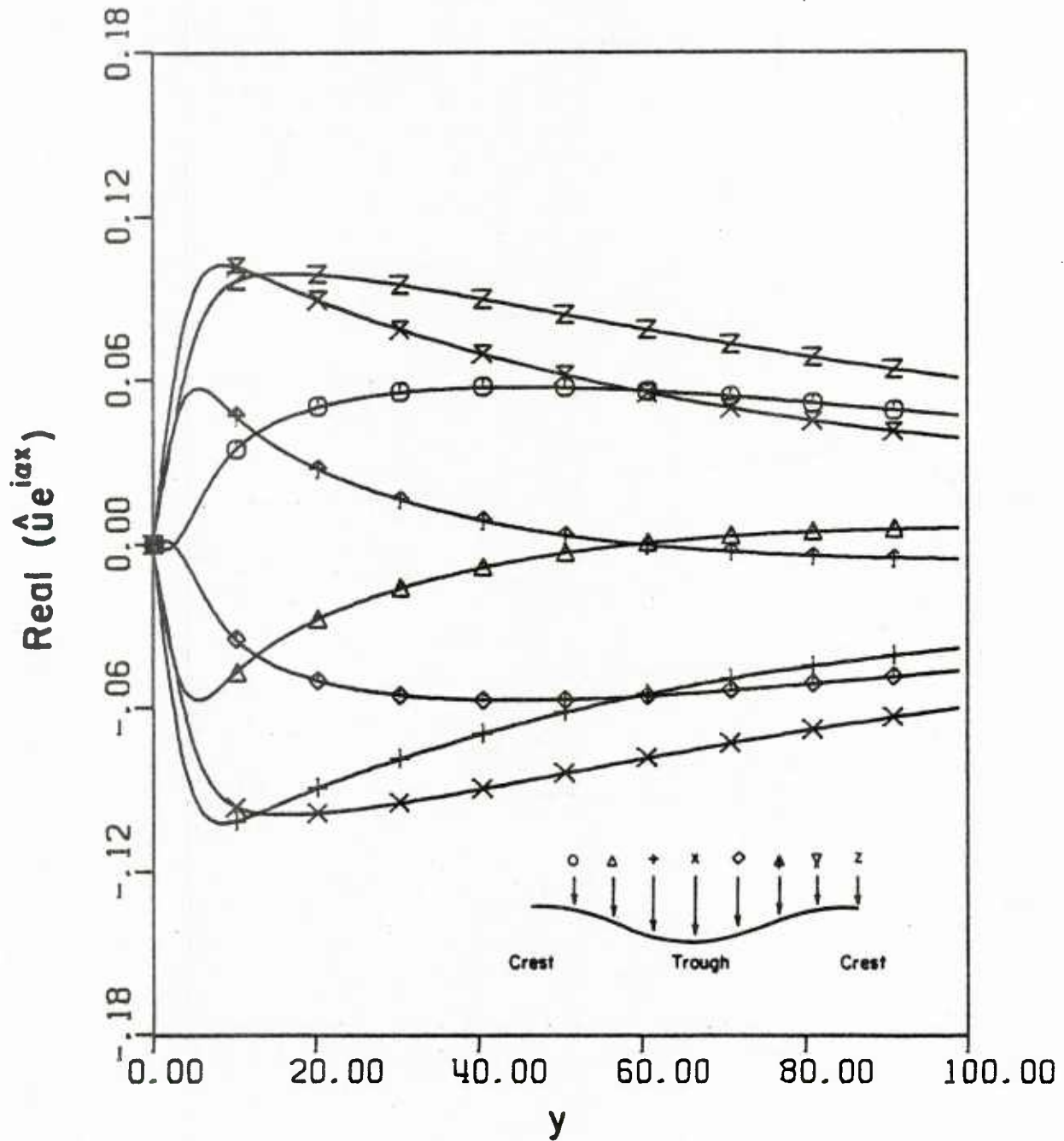


Figure 6.14. $\text{Real}(\hat{u} e^{i\alpha x})$ for Model C* $\alpha = 0.0045$

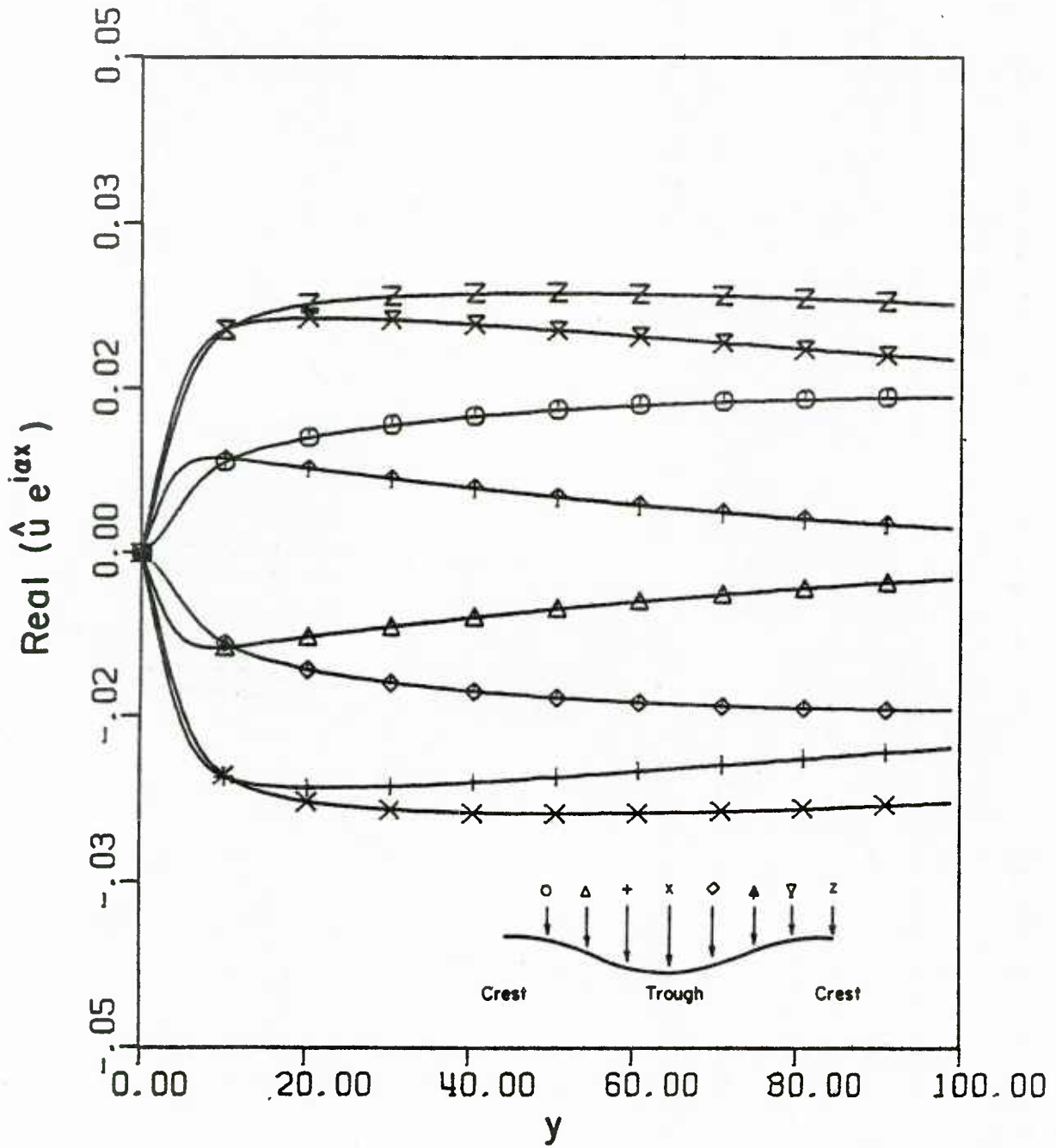


Figure 6.15. Real ($\hat{u} e^{i\alpha x}$) for Model C* $\alpha = 0.001$

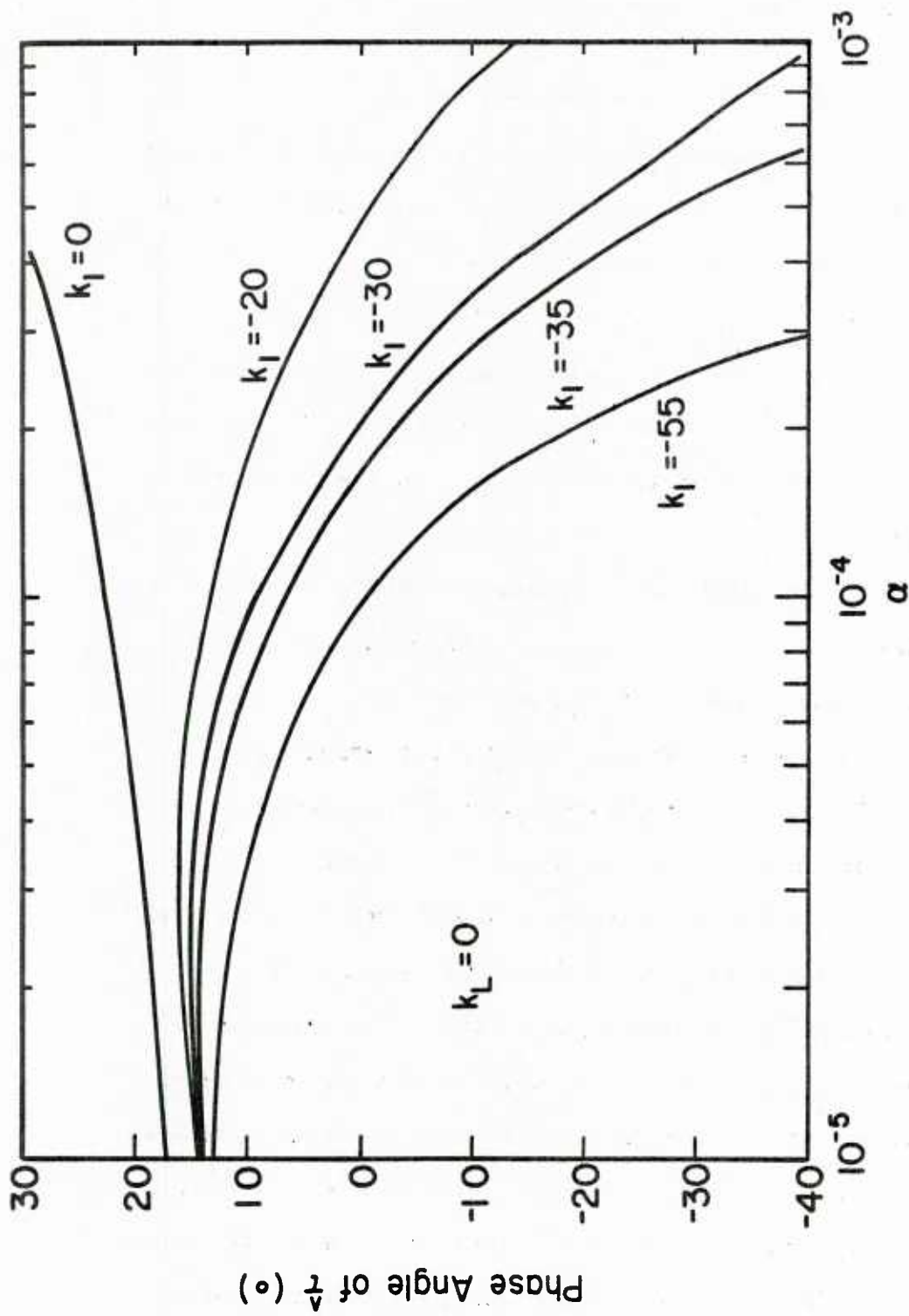


Figure 6.16. $\hat{\tau}(o)$ Phase Angle for Equilibrium Turbulence Model for Different Values of k_I

of α the consequence of including pressure gradient effects in an equilibrium model is to give lower values of the phase shift than would be obtained with Model C* ($k_L = 0$), Figure 6.16.

(d) Model D* and Relaxation Turbulence Model

The turbulence is not expected to be in a state of equilibrium with the local pressure gradient. Two approaches which are extensions of the Equilibrium Turbulence Model are explored.

The first assumes that the turbulence only in the viscous wall region is not in equilibrium with the local pressure gradient. To account for this an effective wave induced sublayer parameter, $\hat{A}_{eff} e^{i\alpha x}$, defined in equation (3.55) is used. This formulation has been designated as Model D* (see Chapter 3).

The implementation of this model requires the specification of an additional constant, k_L , defined in equation (3.53). Figures 6.17 and 6.18 compare the predicted phase angle and amplitude of the wave induced shear stress with measurements. Figures 6.19 and 6.20 compare the predicted phase angle and amplitude of the pressure with measurements. The constants used in these calculations are $k_L = -35$ and $k_L = 1800$. Figures 6.21-6.24 show the effect of α on the wave induced velocity field. The values of α are 0.01, 0.0045, 0.001 and 0.0006 respectively.

The second approach differs from Model D* in that the turbulence throughout the boundary layer is not considered to be in equilibrium with the pressure gradient. To account for this the complete Reynolds stress term defined in equation (3.33) is relaxed, rather than only $\hat{A} e^{i\alpha x}$. The implementation of this model, previously referred to as the Relaxation Model, also requires the specification of a second constant, k_R , defined in equation (3.14).

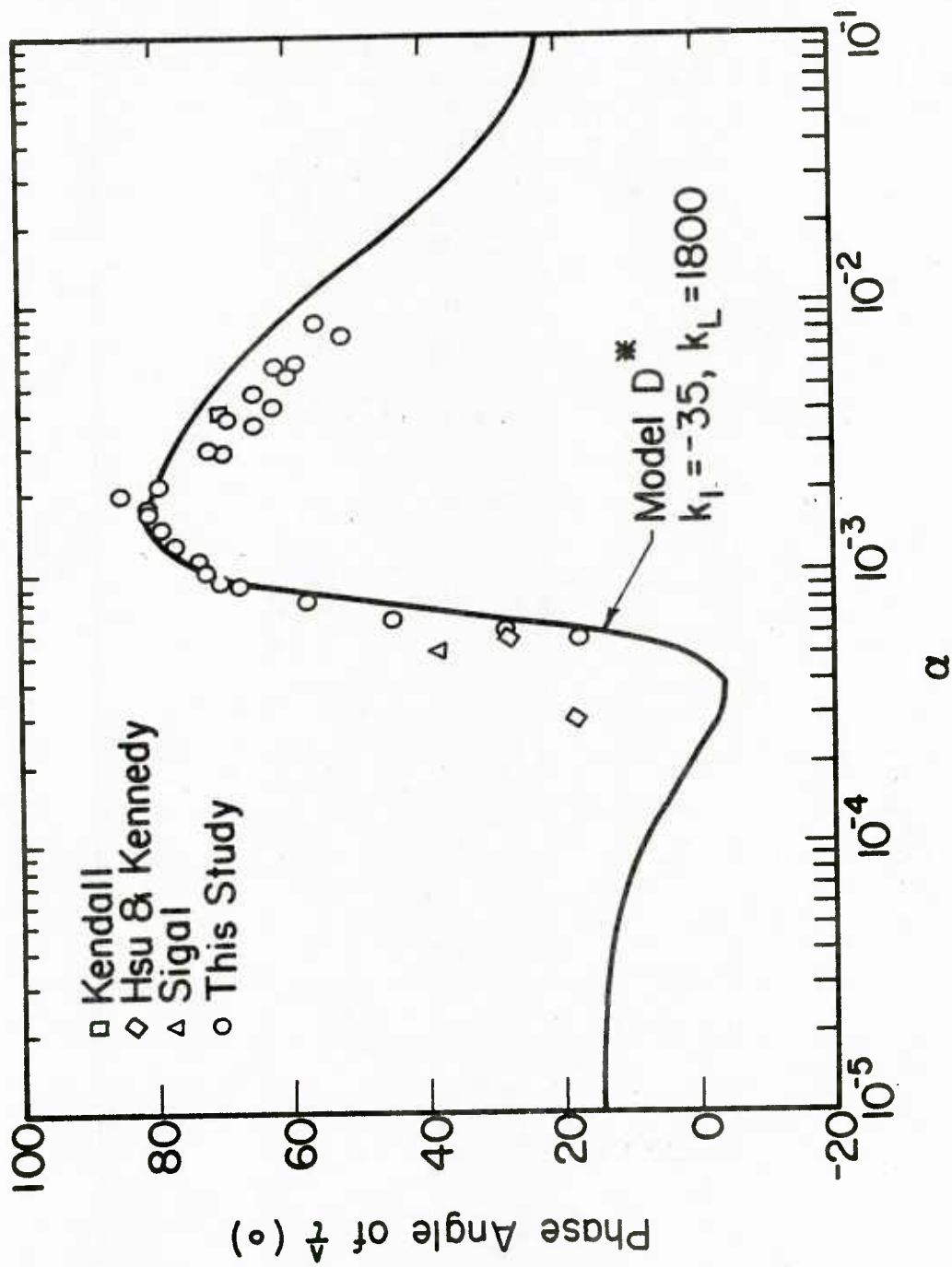


Figure 6.17. $\hat{f}(\alpha)$ Phase Angle for Model D* for $k_I = -35$ and $k_L = 1800$

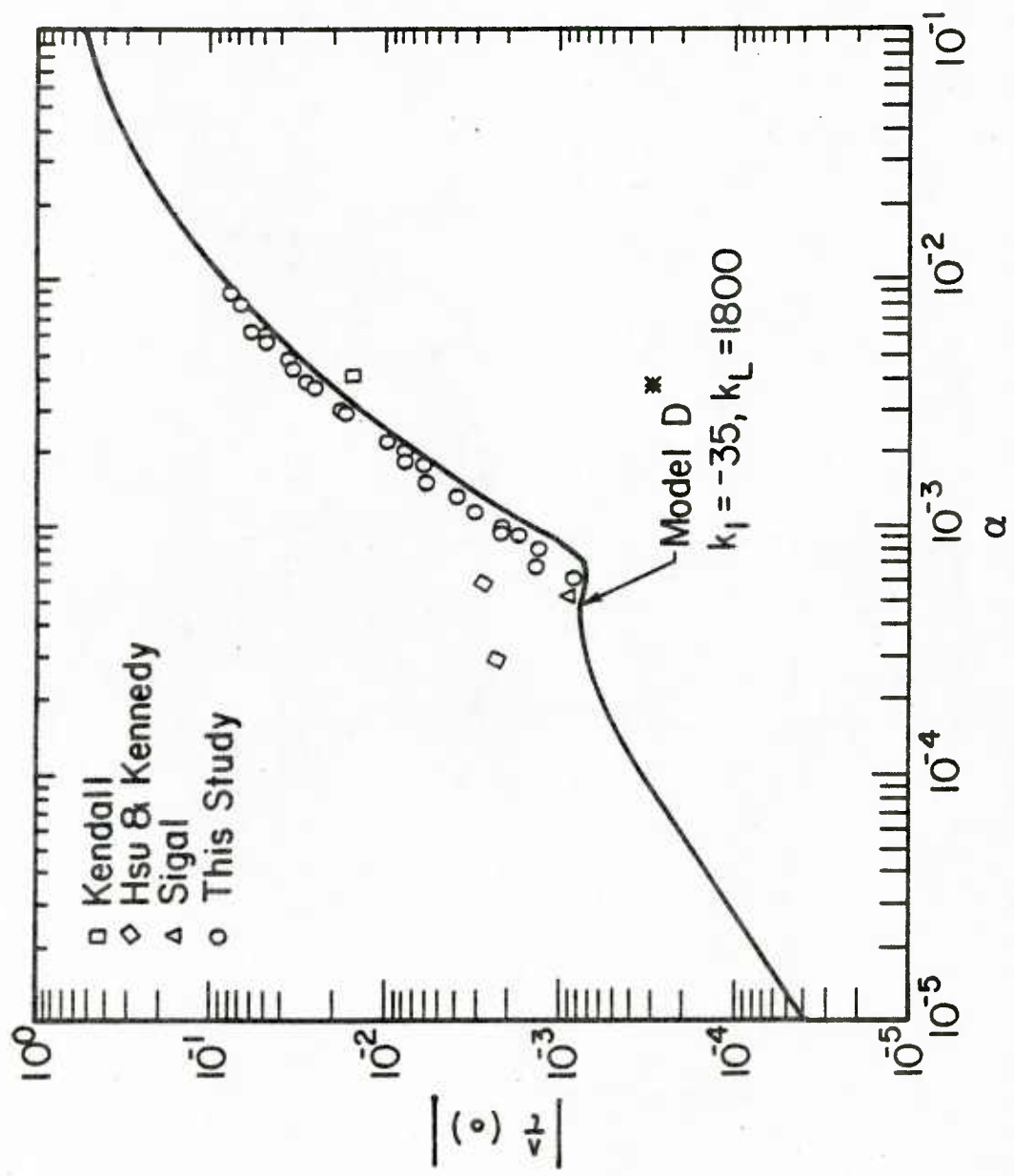


Figure 6.18. $|\hat{\tau}(\alpha)|$ for Model D* for $k_1 = -35$ and $k_L = 1800$

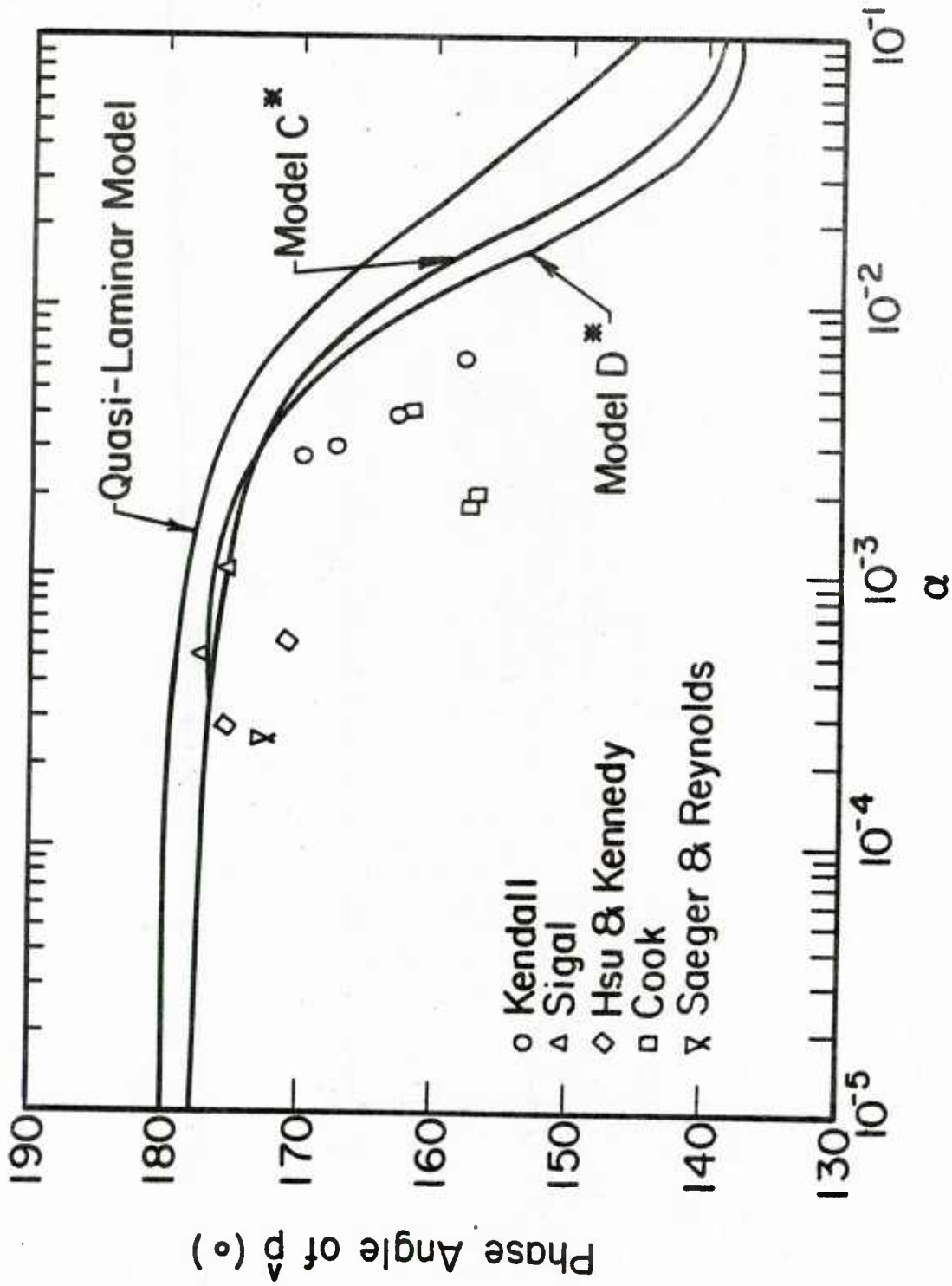


Figure 6.19. $\hat{p}(\alpha)$ Phase Angle for Model D* for $k_1 = \sim 0.5$ and $k_L = 1800$

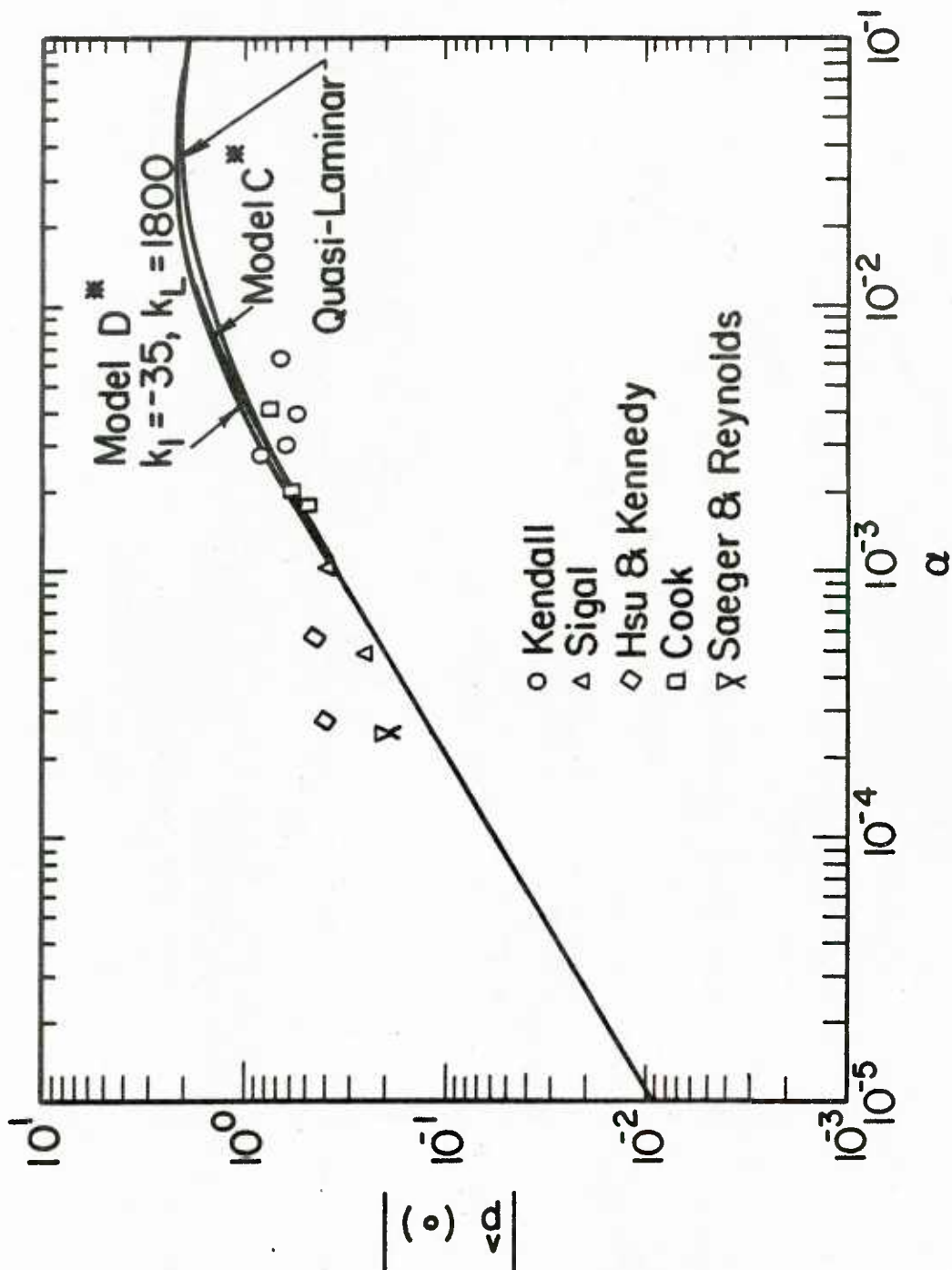


Figure 6.20. $|\hat{p}(o)|$ for Model D* for $k_1 = -35$ and $k_L = 1800$

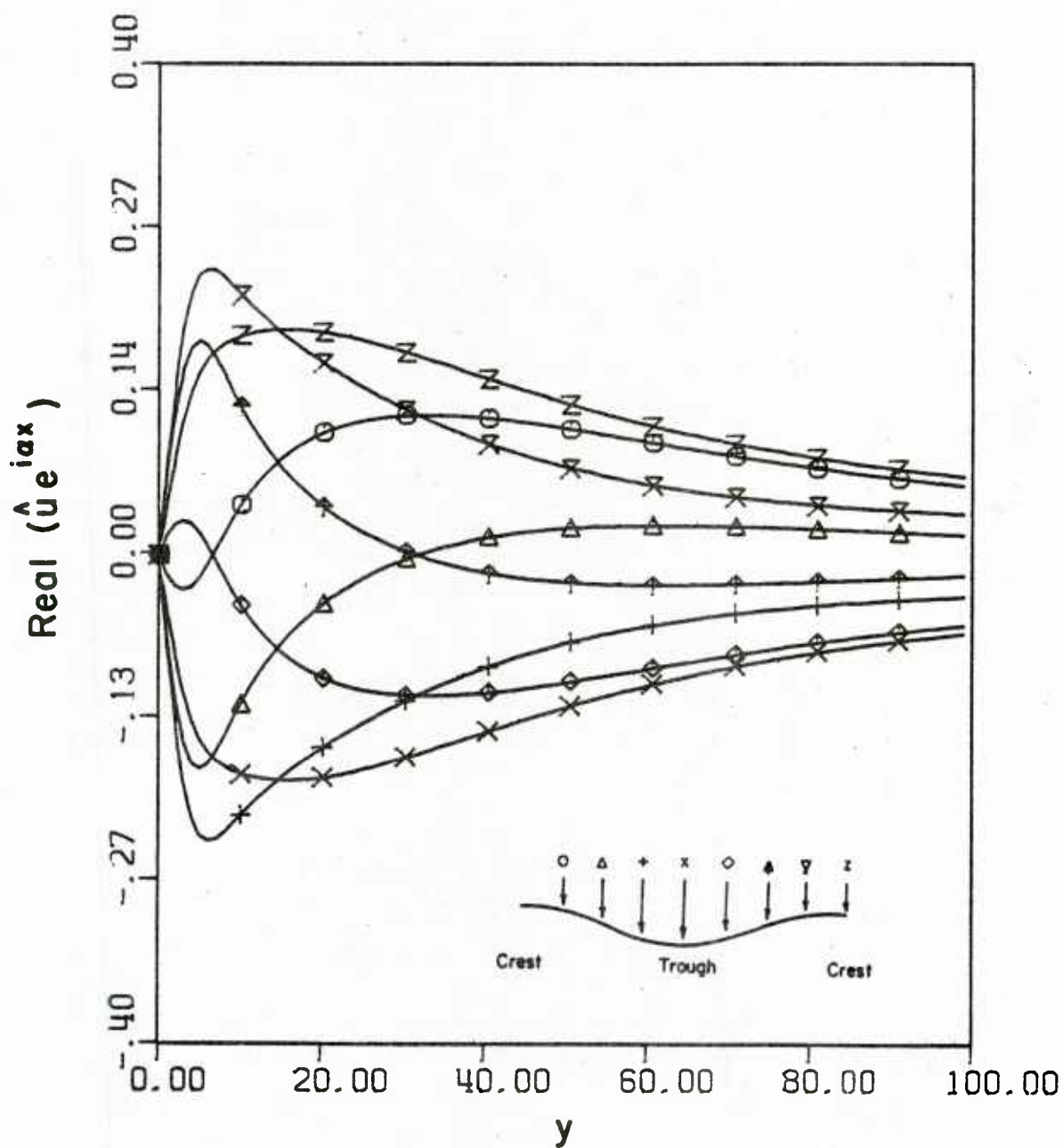


Figure 6.21. $\text{Re}(\hat{u}_e^{i\alpha x})$ for Model D* for $k_L = -35$, $k_L = 1800$ and $\alpha = 0.01$

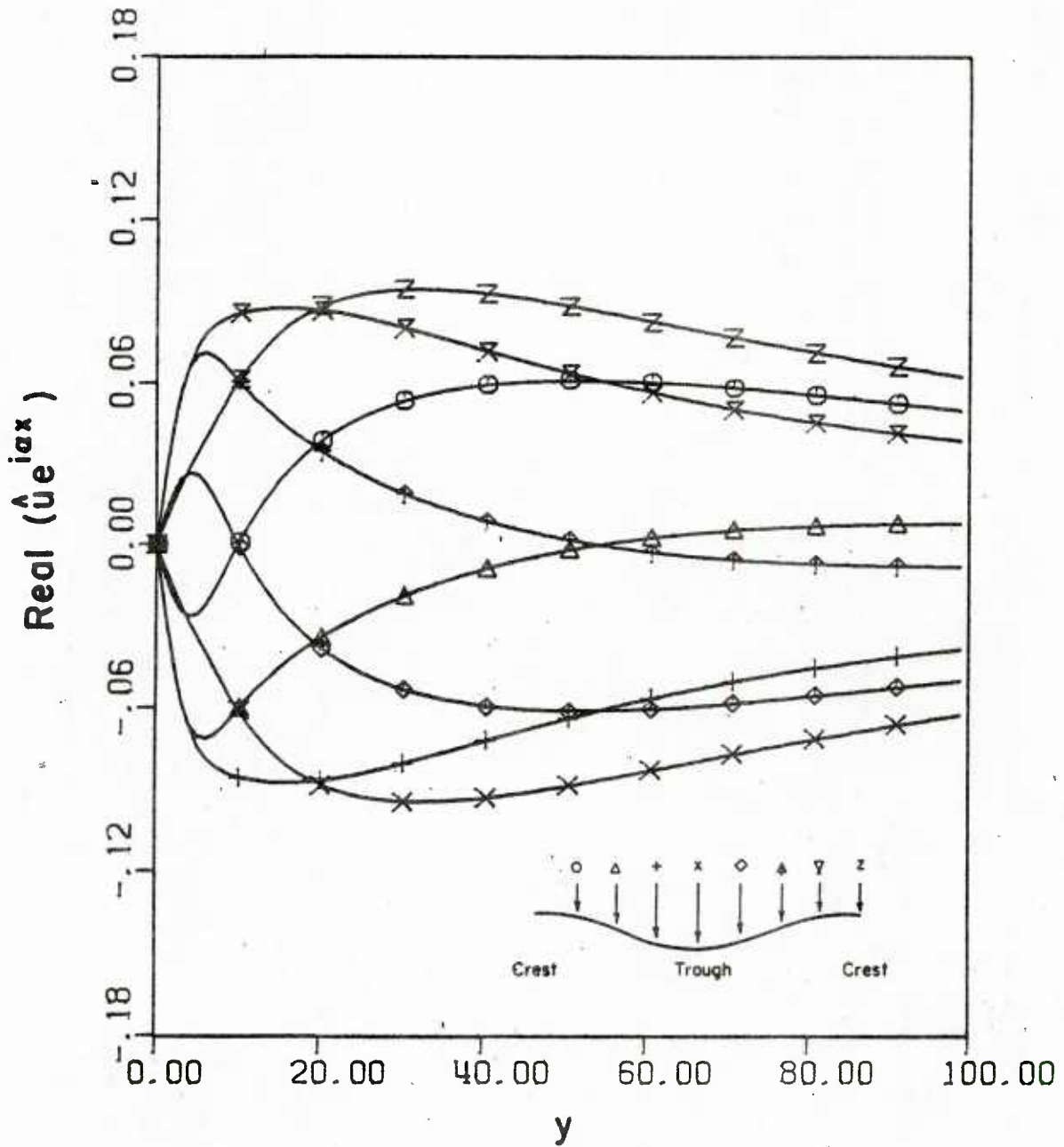


Figure 6.22. $\text{Real}(\hat{u} e^{i\alpha x})$ for Model D* for $k_1 = -35$, $k_L = 1800$ and $\alpha = 0.0045$

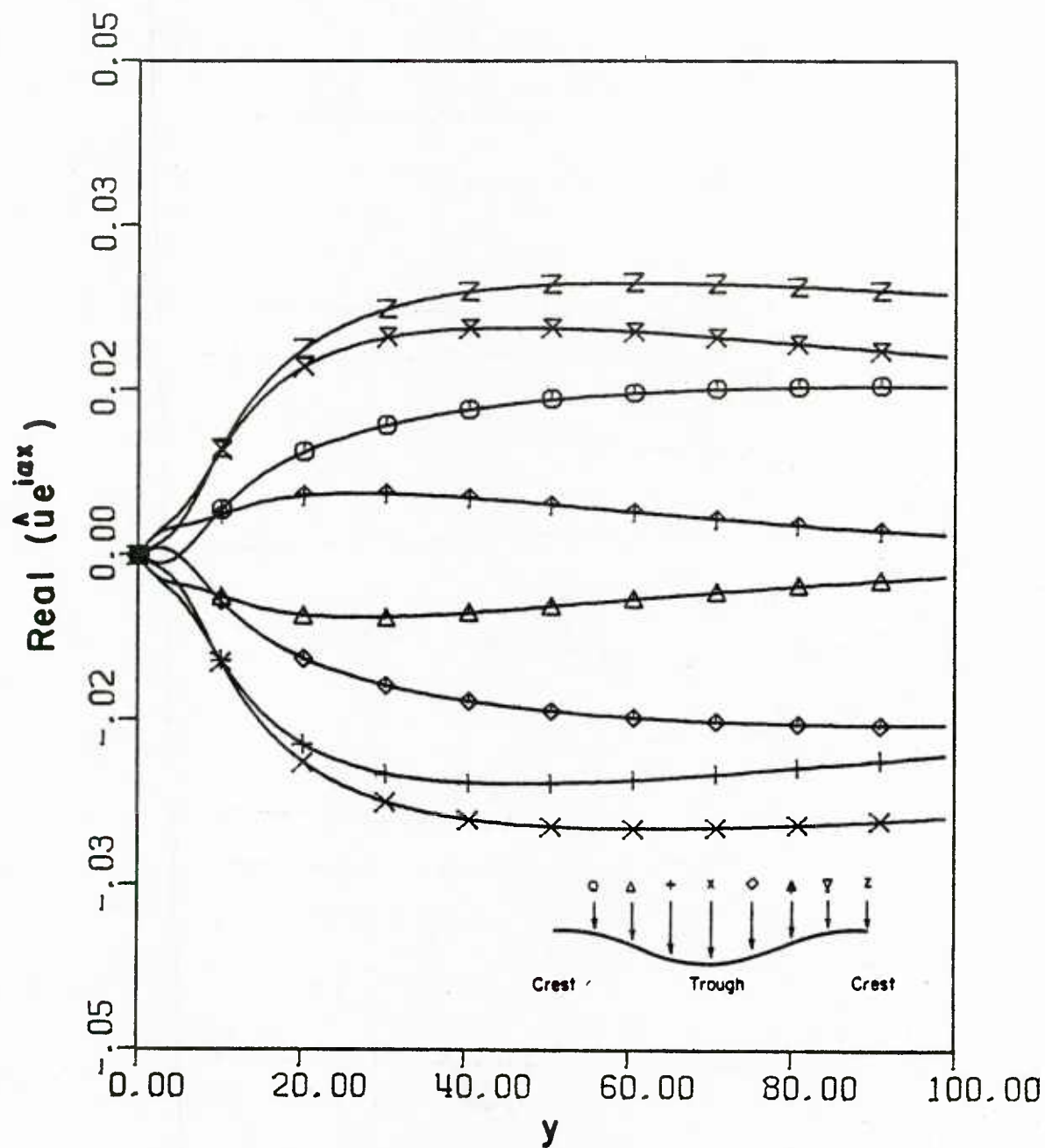


Figure 6.23. $\text{Re}(\hat{u} e^{i\alpha x})$ for Model D* for
 $k_1 = -35$, $k_L = 1800$ and $\alpha = 0.001$

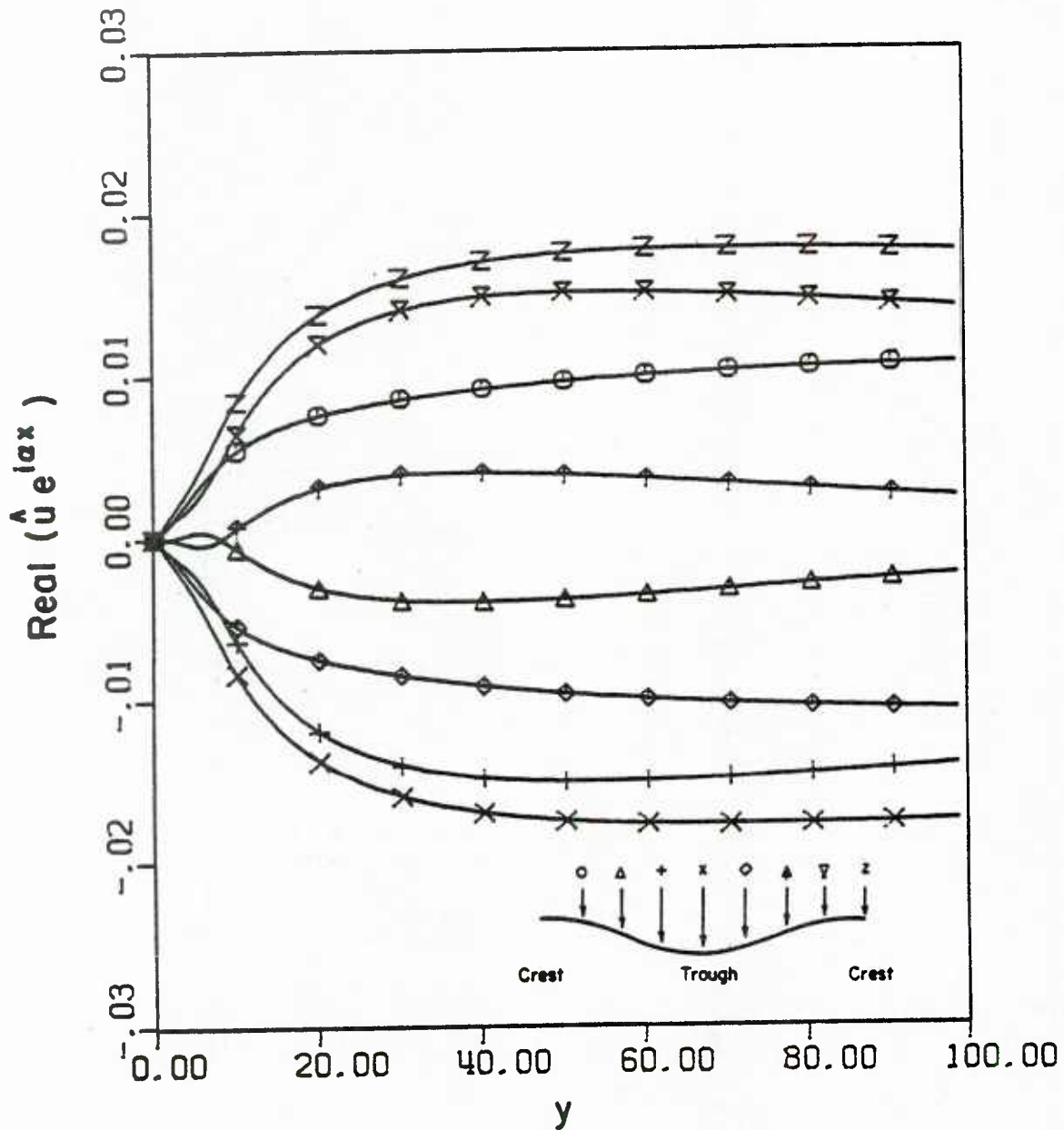


Figure 6.24. $\text{Real}(\hat{u} e^{i\alpha x})$ for Model D* for $k_L = -35$, $k_L = 1800$ and $\alpha = 0.0006$

An excellent fit of the measurements of the phase angle and amplitude of the wave induced shear stress Figures 6.25 and 6.26 is obtained with $k_1 = -20$ and $k_R = 4200$. Figures 6.27 and 6.28 show the effect of the constants k_1 and k_R on the model by comparing the predicted values of the fluctuating wall shear stress with measurements for three sets of values of the constants. Figures 6.29 and 6.30 compare the predicted phase angle and amplitude of the wave induced pressure with measurements. The effect of α on the wave induced velocity field is shown in Figures 6.31-6.34 for $\alpha = 0.01, 0.0045, 0.001$ and 0.0006 respectively.

(e) K- ϵ Model

The last model to be tested is the K- ϵ Model. In this model the effects of pressure gradient and relaxation are accounted for in a natural way through the defining differential equations. The mean velocity profile used in calculating the wave induced flow is not the Van Driest profile, but rather one generated using the mean momentum, mean energy and mean dissipation equations. The profiles of these quantities are shown in Figures 6.35-6.37 respectively.

Figures 6.38 and 6.39 compare the calculated phase angle and amplitude of the wave induced shear stress predicted by the K- ϵ Model. The calculated maximum in the phase angle occurs at $\alpha \approx 8 \times 10^{-5}$. The sharp decrease in the phase angle as a function of α is not as apparent as that predicted by either Model D* or the Relaxation Model. The K- ϵ Model also under-predicts the magnitude of the maximum phase shift of the shear stress. Figures 6.40 and 6.41 compare the predicted phase angle and amplitude of the wave induced pressure with measurements.

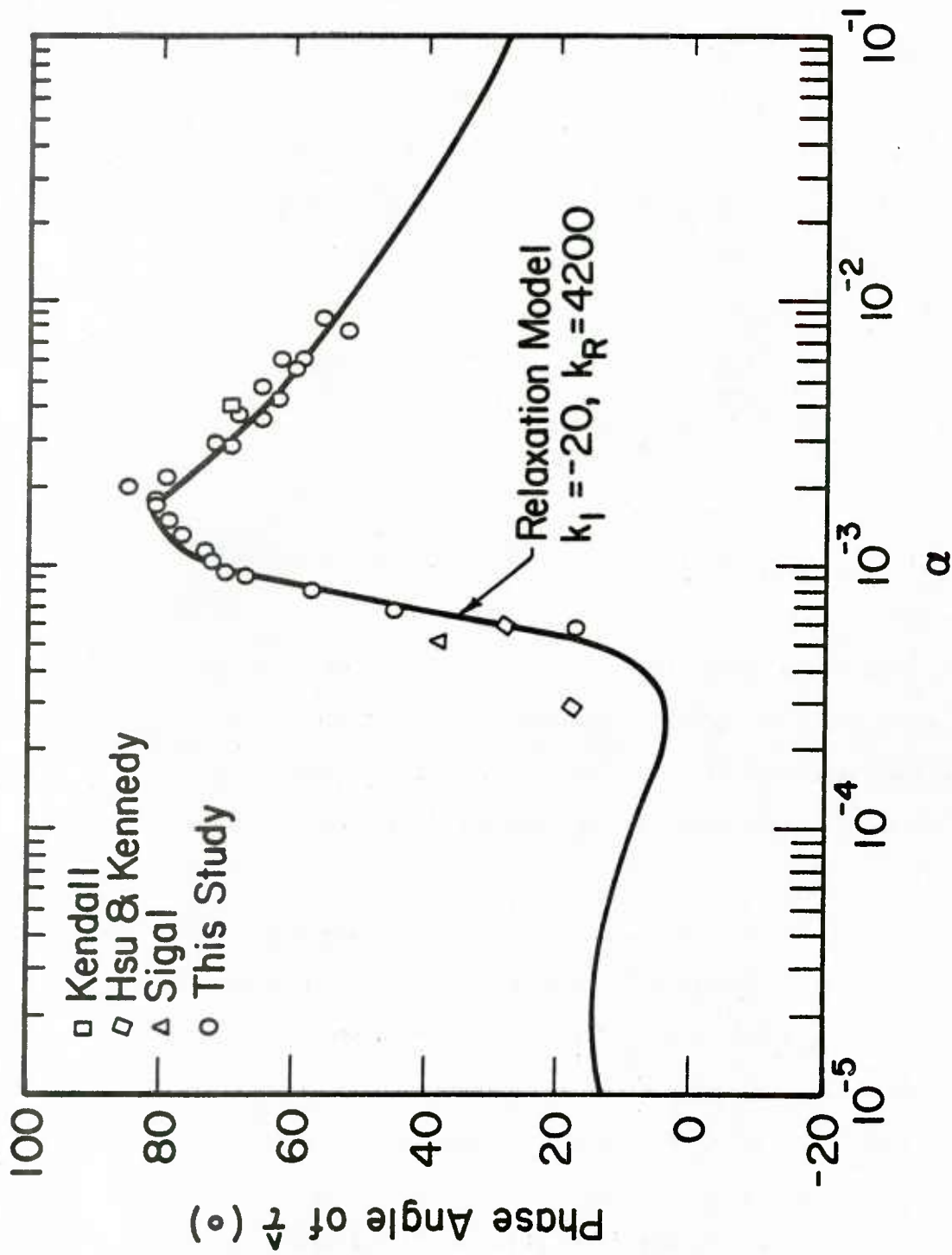


Figure 6.25. $\hat{\tau}(\circ)$ Phase Angle for Relaxation Model for $k_1 = -20$ and $k_R = 4200$

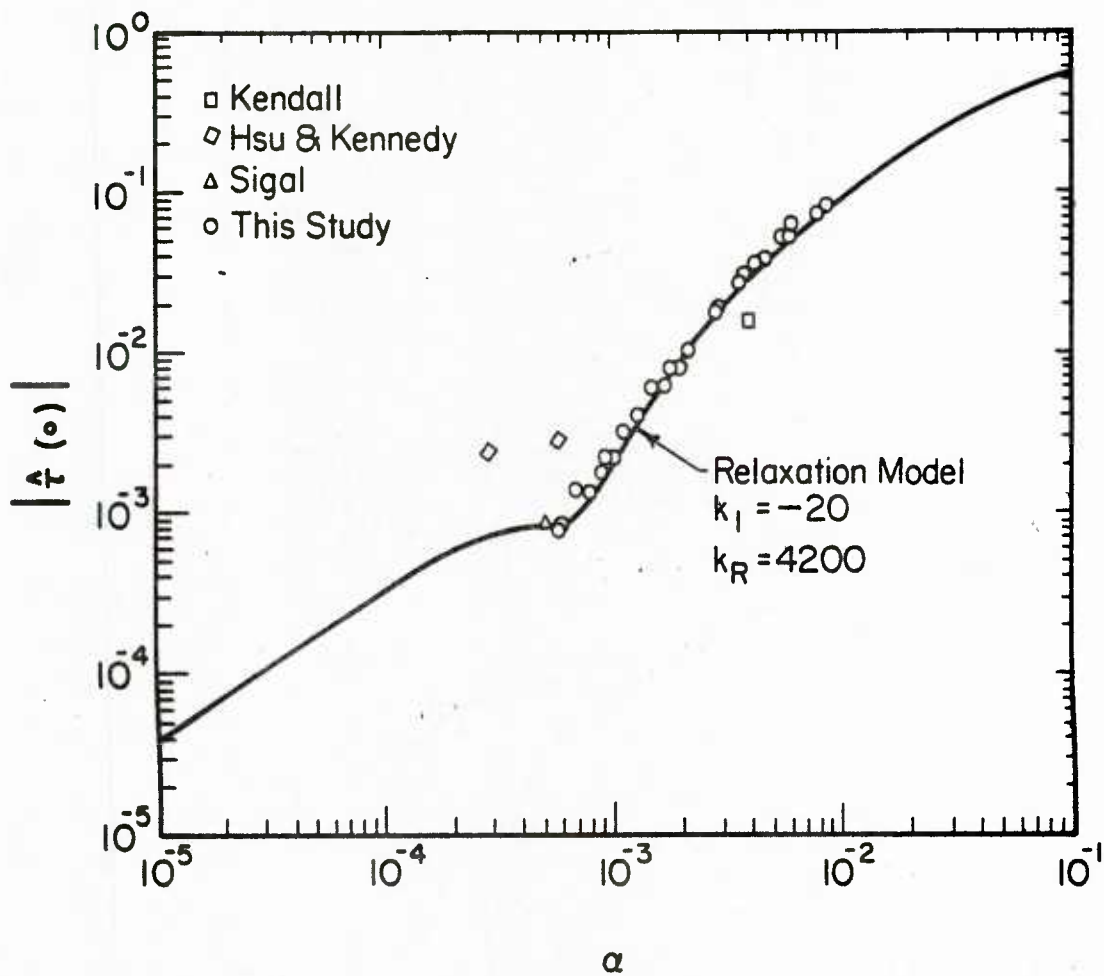


Figure 6.26. $|\hat{\tau}(\omega)|$ for Relaxation Model for $k_1 = -20$ and $k_L = 4200$

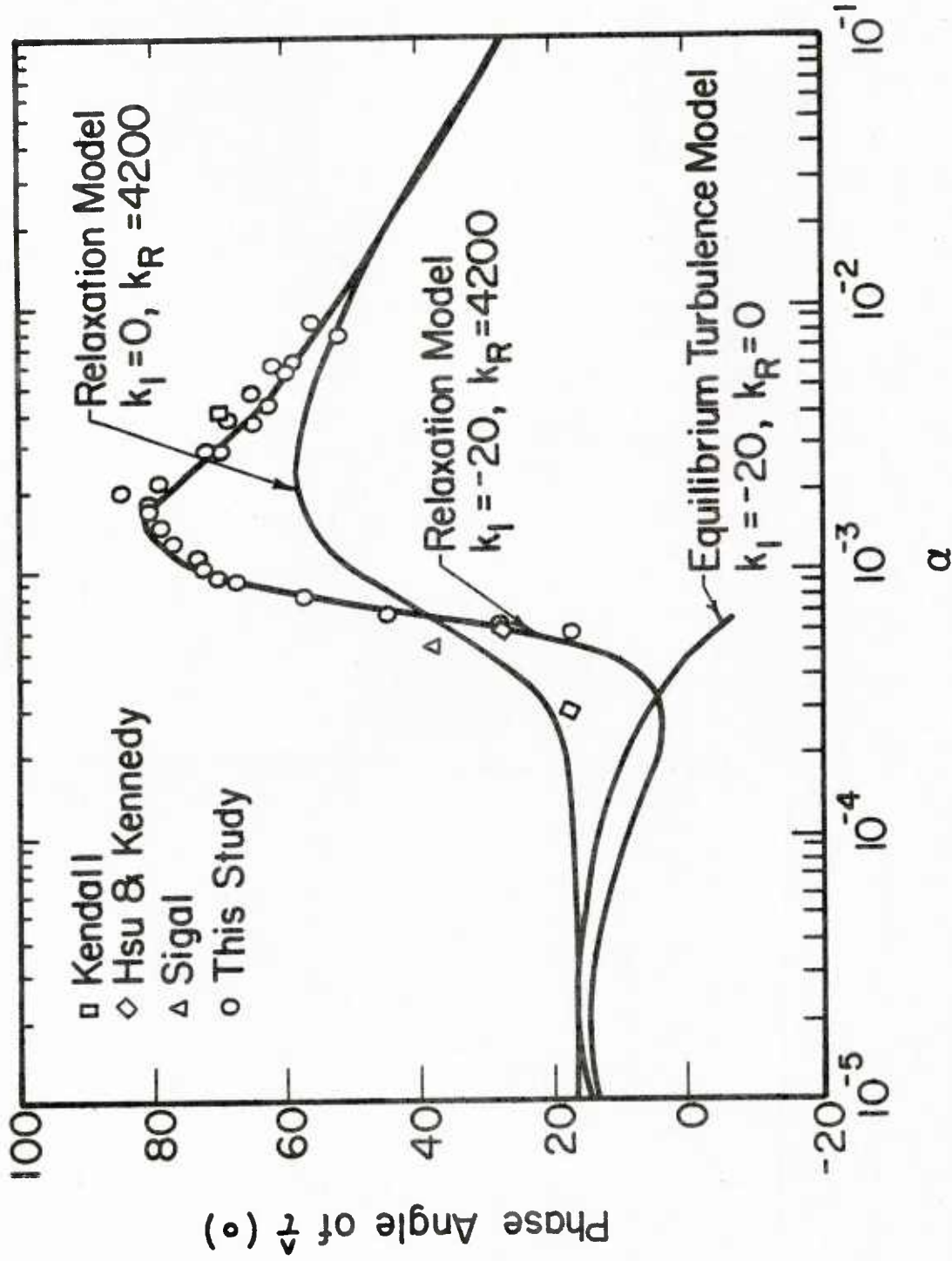


Figure 6.27. Effect of k_I and k_R on $\hat{\tau}$ (\circ) Phase Angle for Relaxation Model

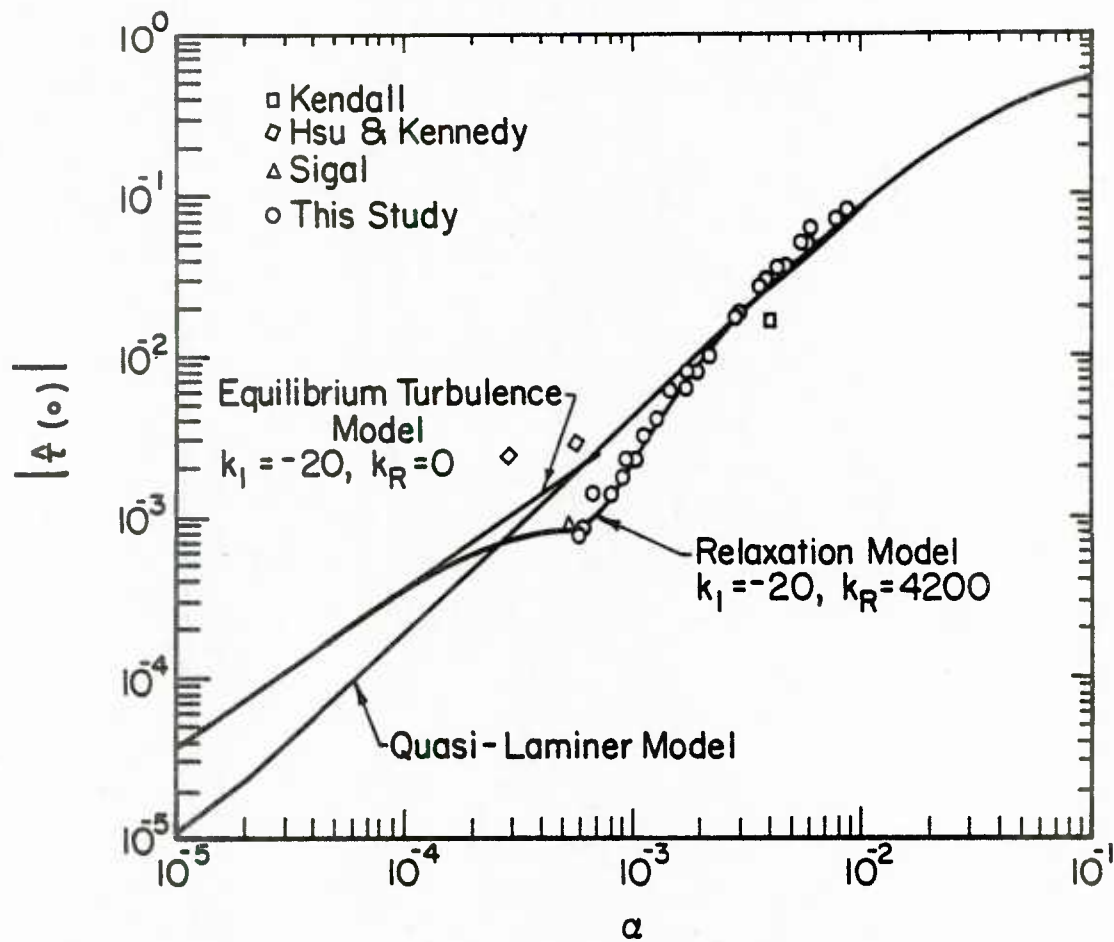


Figure 6.28. Effect of k_1 and k_R on $|\hat{\tau}(\alpha)|$ for Relaxation Model

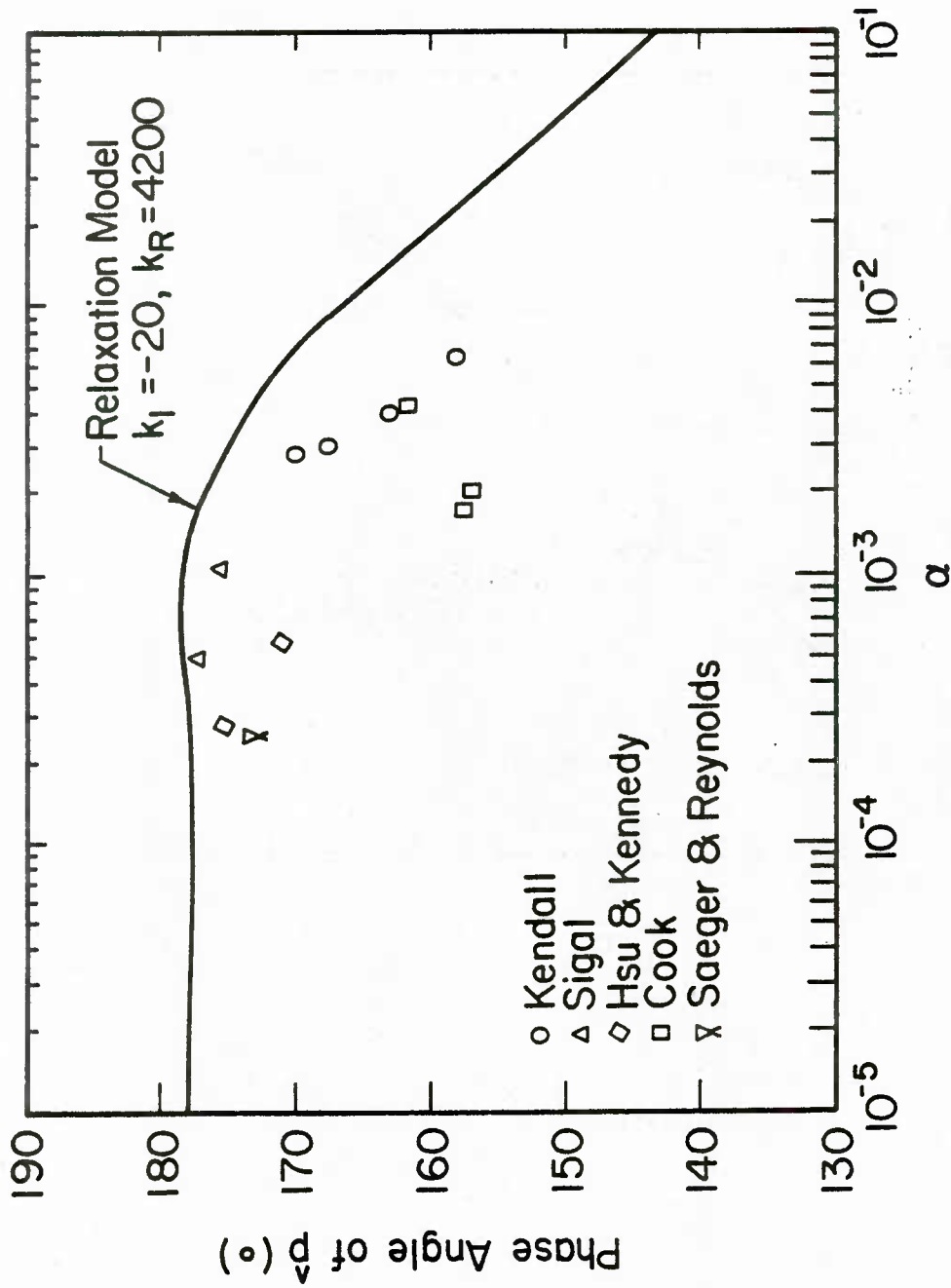


Figure 6.29. $\hat{p}(\alpha)$ Phase Angle for Relaxation Model for $k_1 = -20$ and $k_R = 4200$

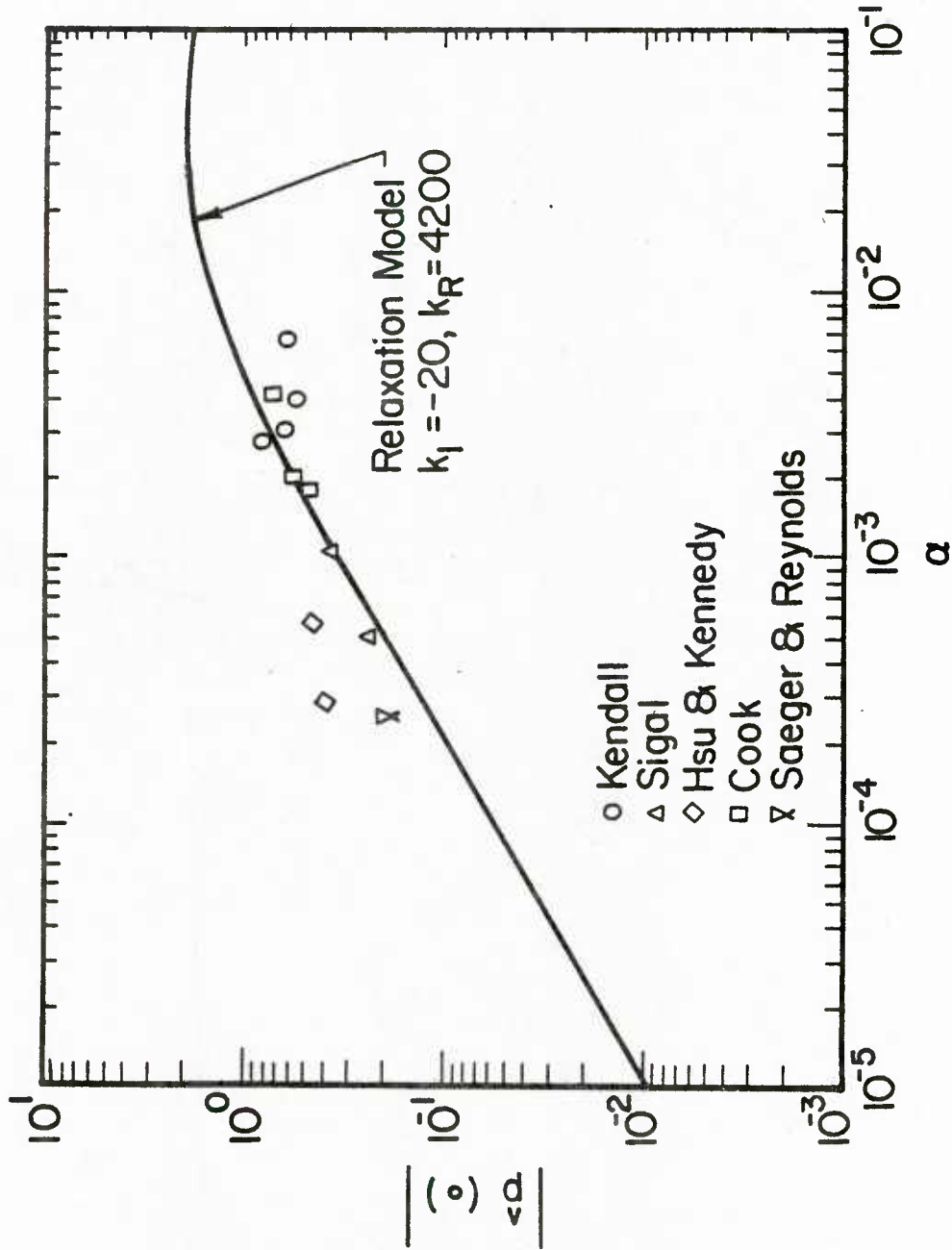


Figure 6.30. $|\hat{p}(\alpha)|$ for Relaxation Model for $k_I = -20$ and $k_R = 4200$

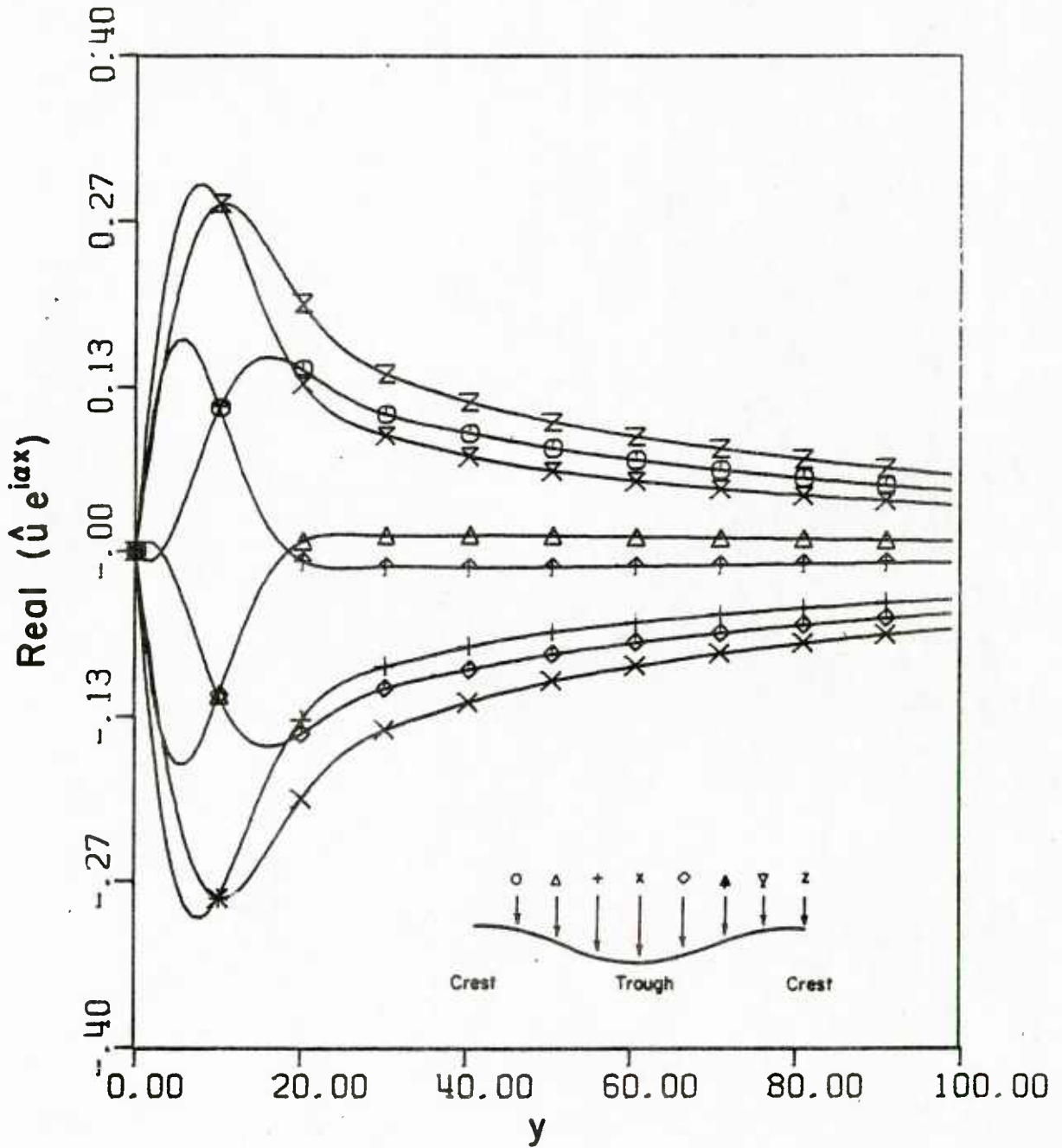


Figure 6.31. $\text{Real}(\hat{u} e^{i\alpha x})$ for Relaxation Model for $K_1 = -20$, $k_R = 4200$ and $\alpha = 0.01$

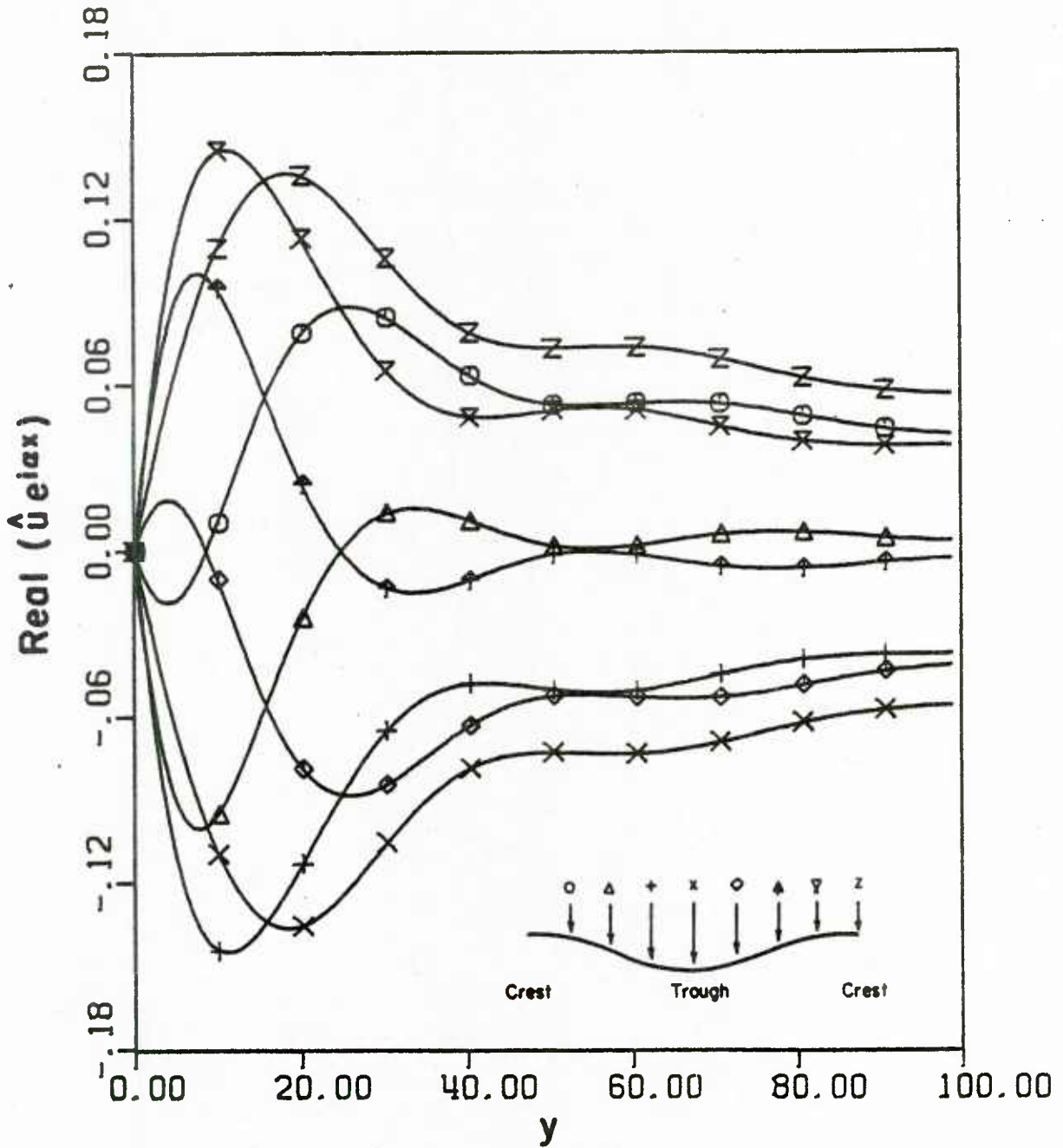


Figure 6.32. $\text{Real}(\hat{u} e^{i\alpha x})$ for Relaxation Model for $k_1 = -20$, $k_R = 4200$ and $\alpha = 0.0045$

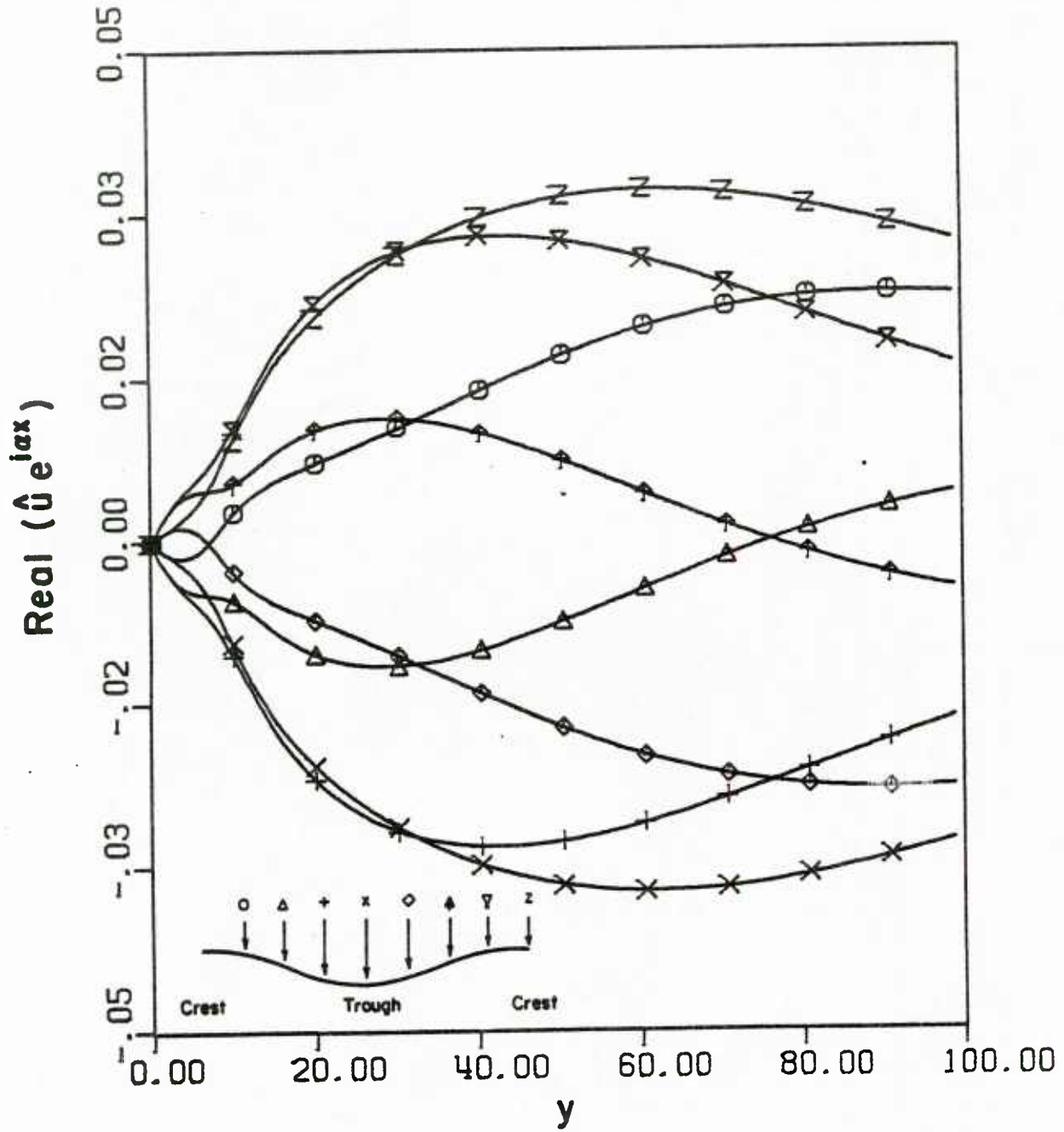


Figure 6.33. $\text{Real}(\hat{u} e^{i\alpha x})$ for Relaxation Model for $k_1 = -20$, $k_R = 4200$ and $\alpha = 0.001$

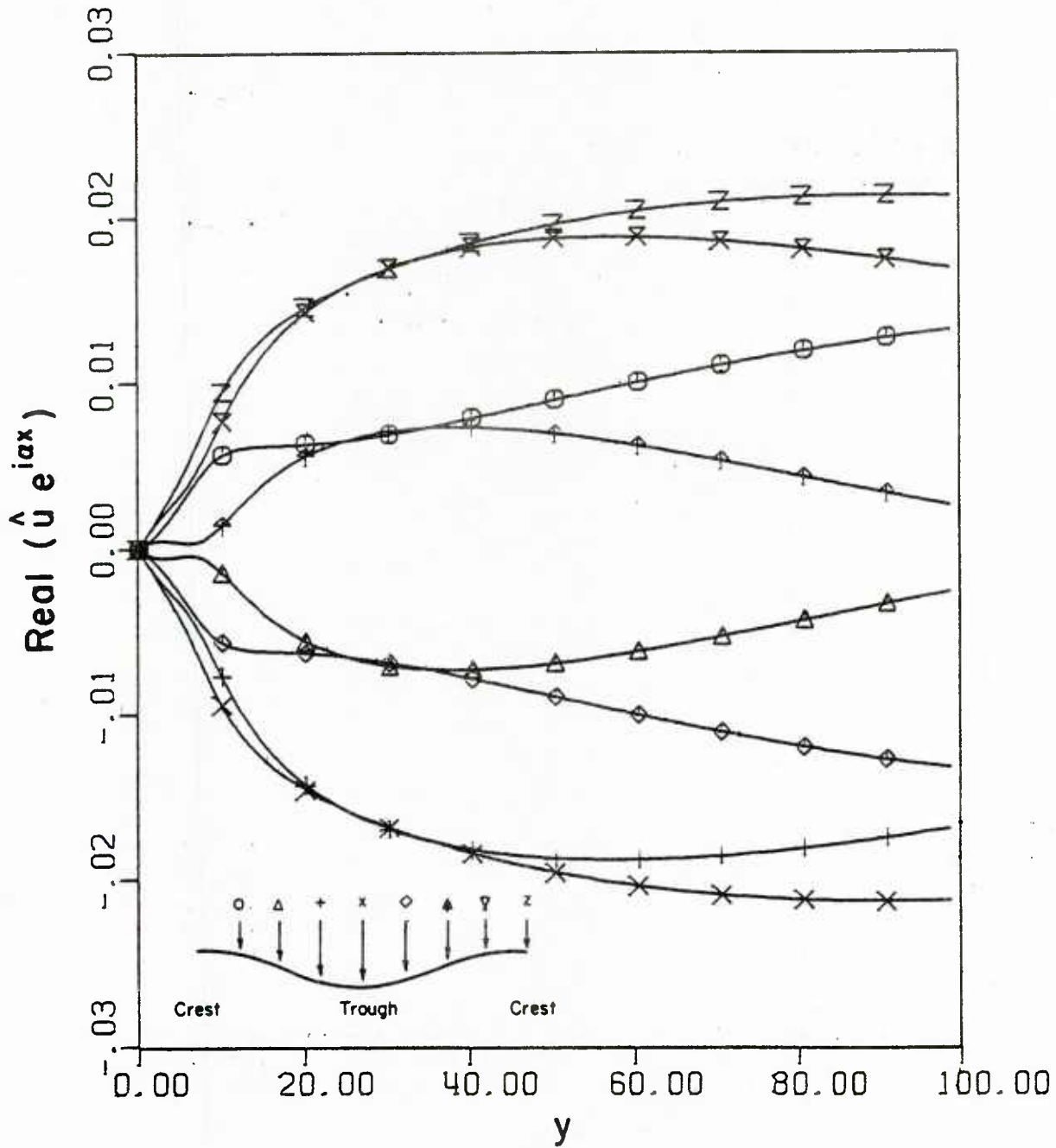


Figure 6.34. $\text{Real}(\hat{u} e^{i\alpha x})$ for Relaxation Model for $k_1 = -20$, $k_R = 4200$ and $\alpha = 0.0006$

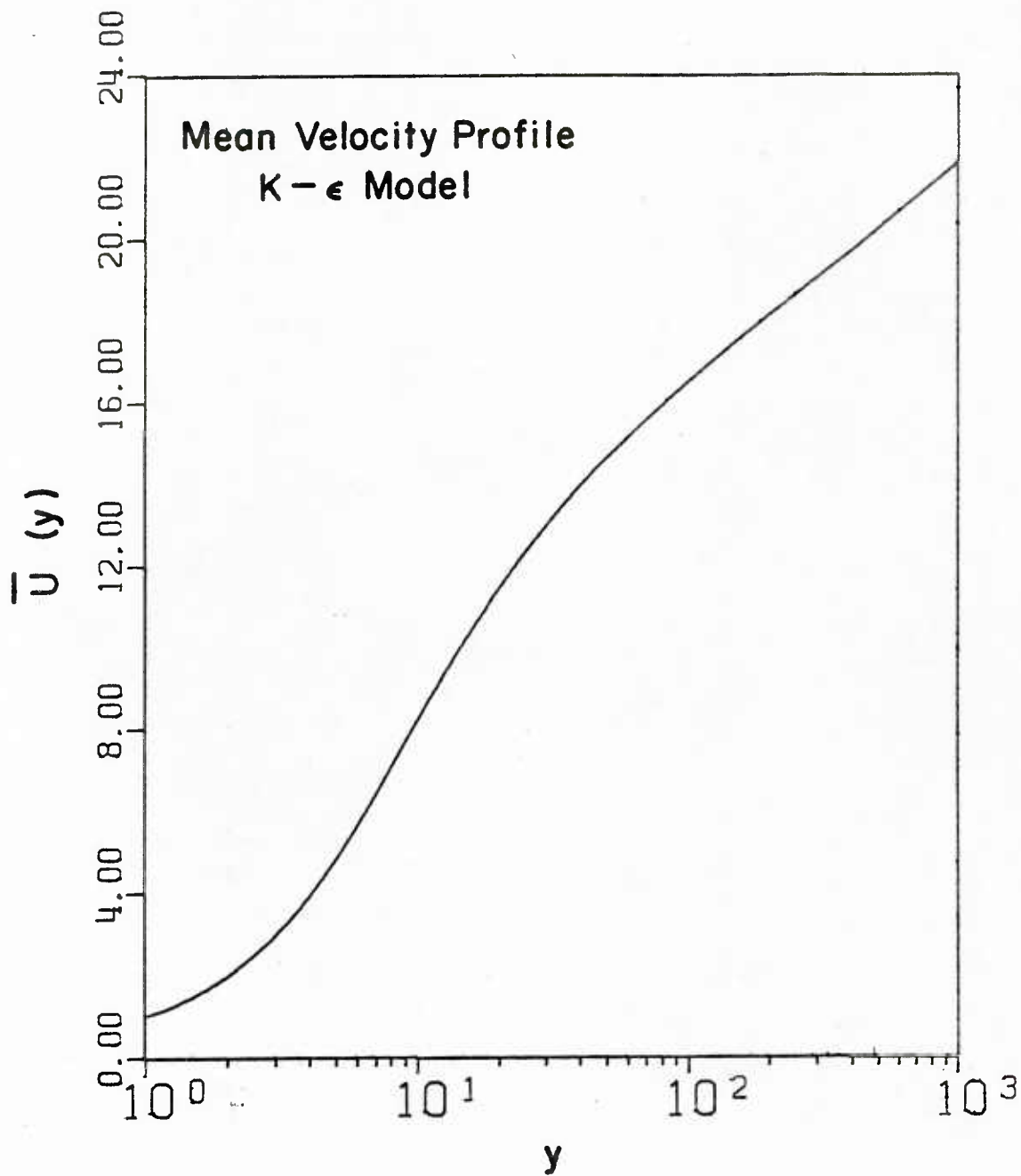


Figure 6.35. Mean Velocity Profile for K- ϵ Model

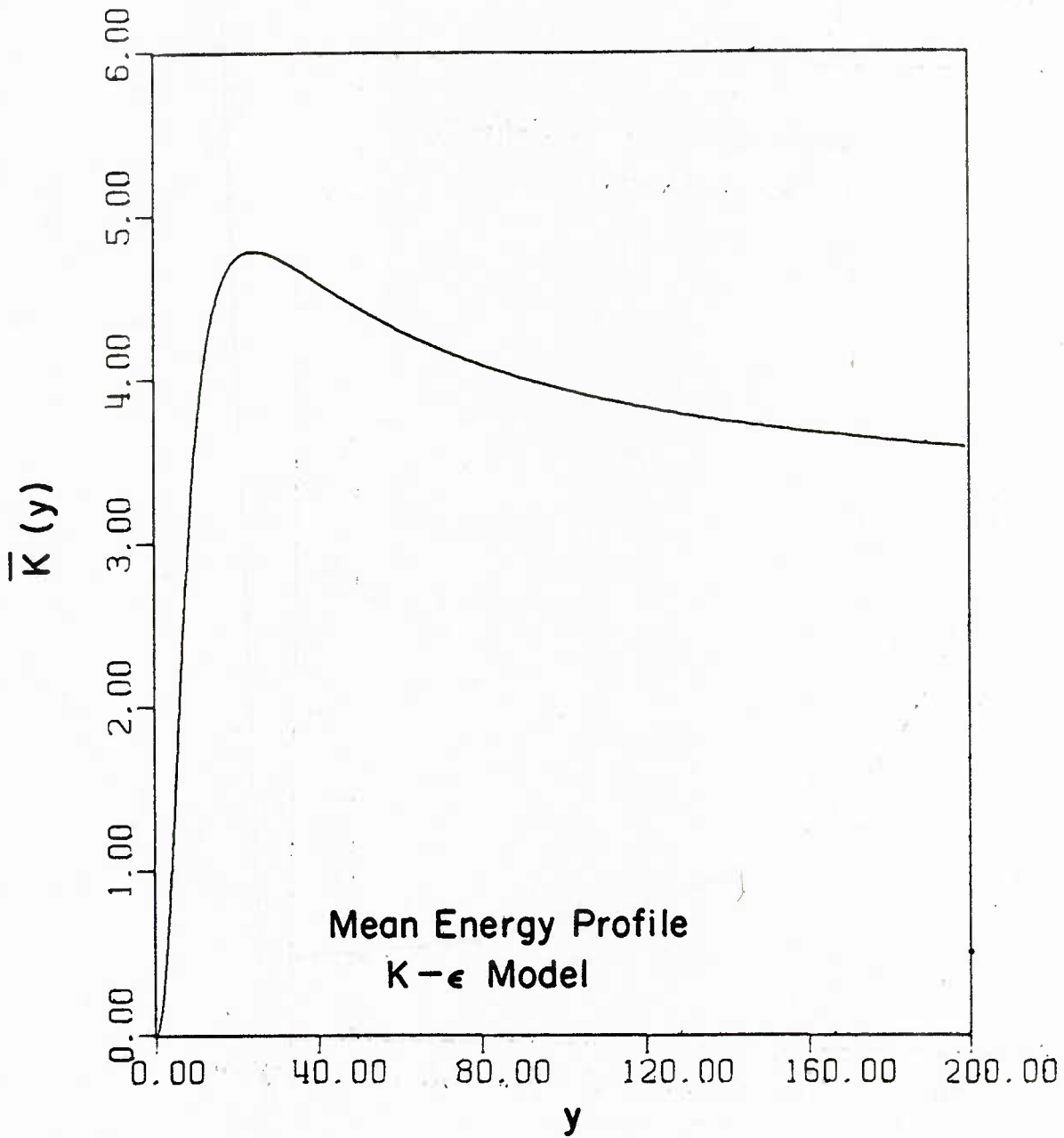


Figure 6.36. Mean Energy Profile for K- ϵ Model

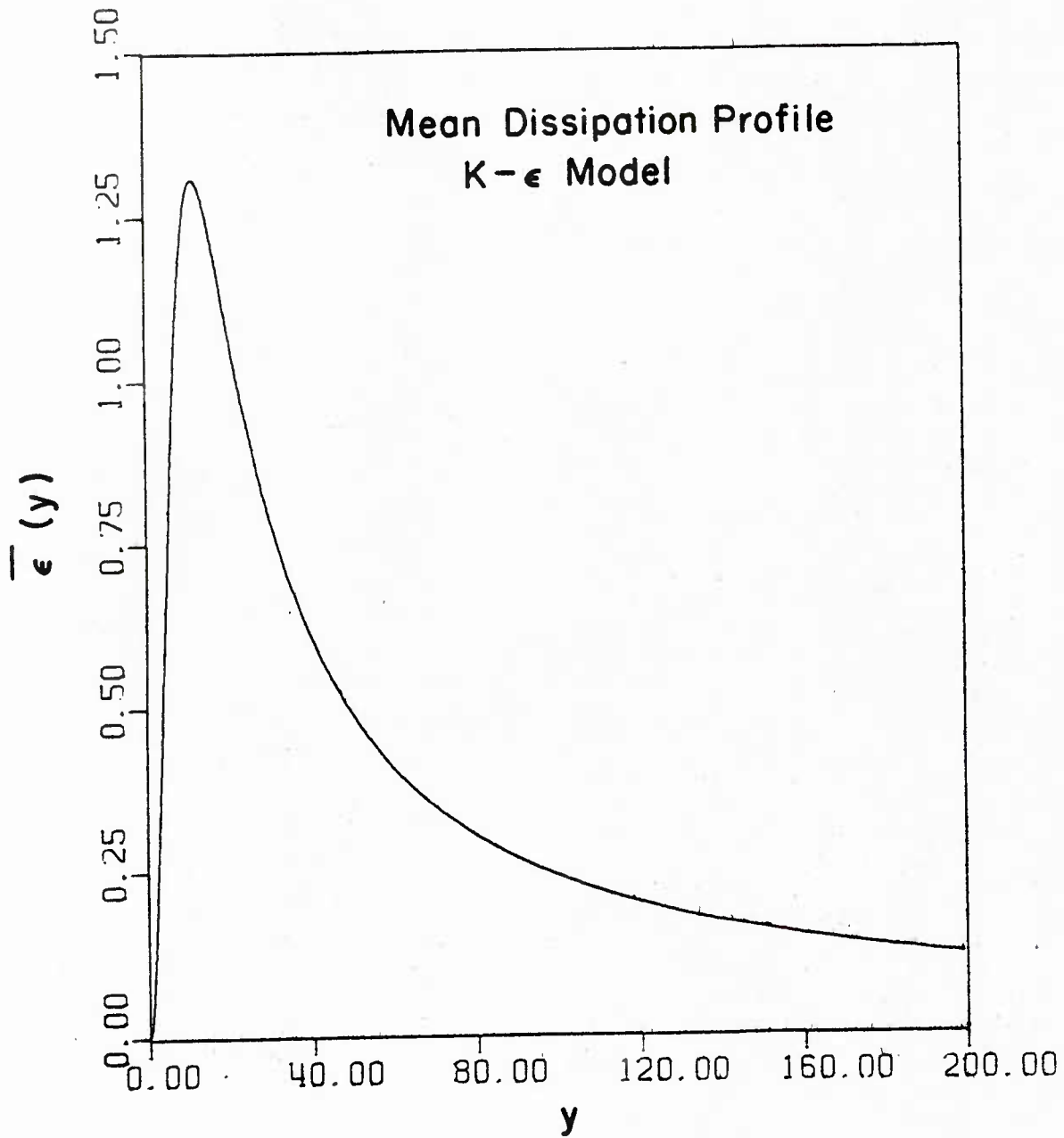


Figure 6.37. Mean Dissipation Profile for K- ϵ Model

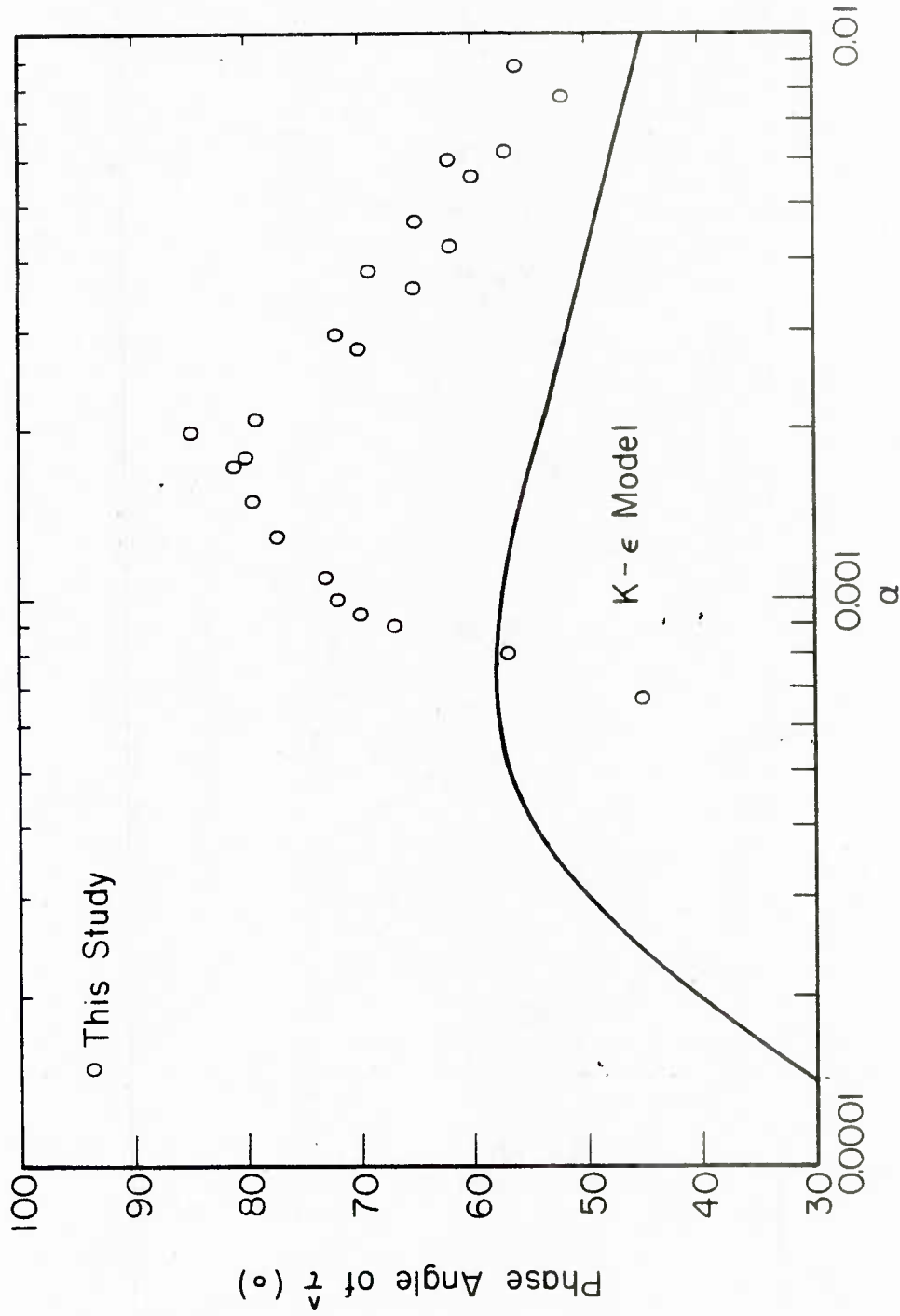


Figure 6.38. $\hat{\tau}(\alpha)$ Phase Angle for K- ϵ Model

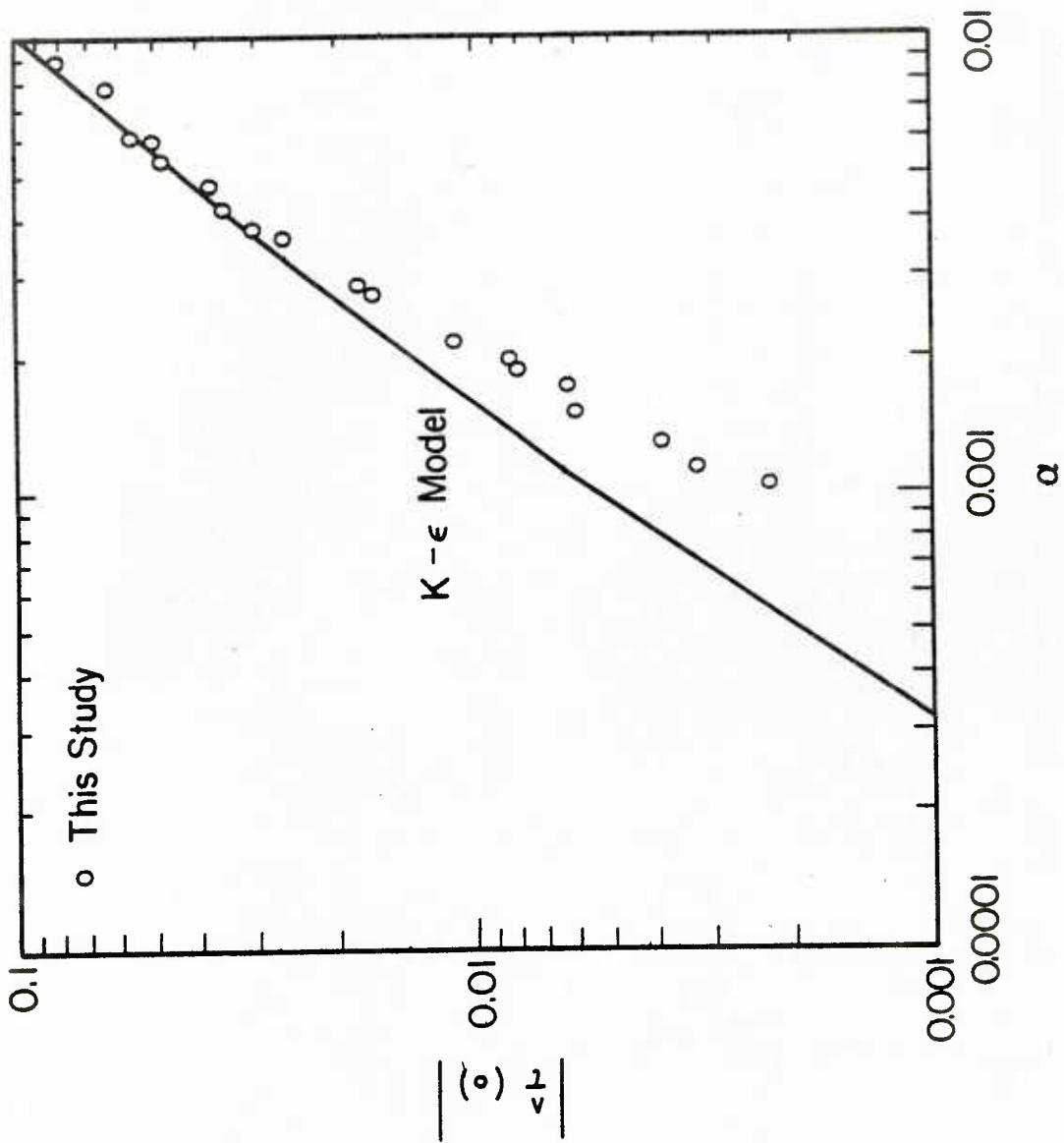


Figure 6.39. $|\hat{\tau}(o)|$ for K- ϵ Model

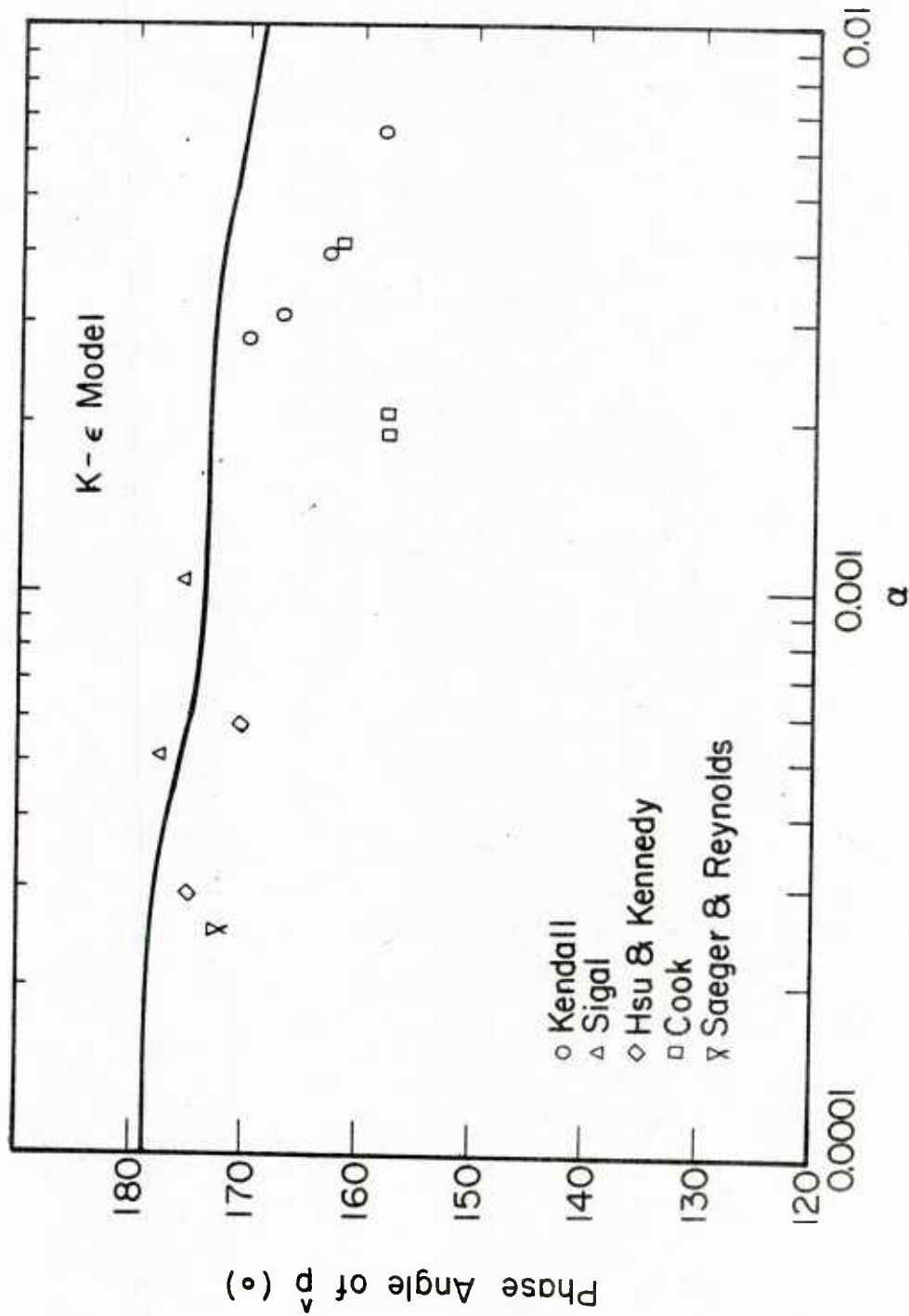


Figure 6.40. $\hat{p}(\alpha)$ Phase Angle for K- ϵ Model

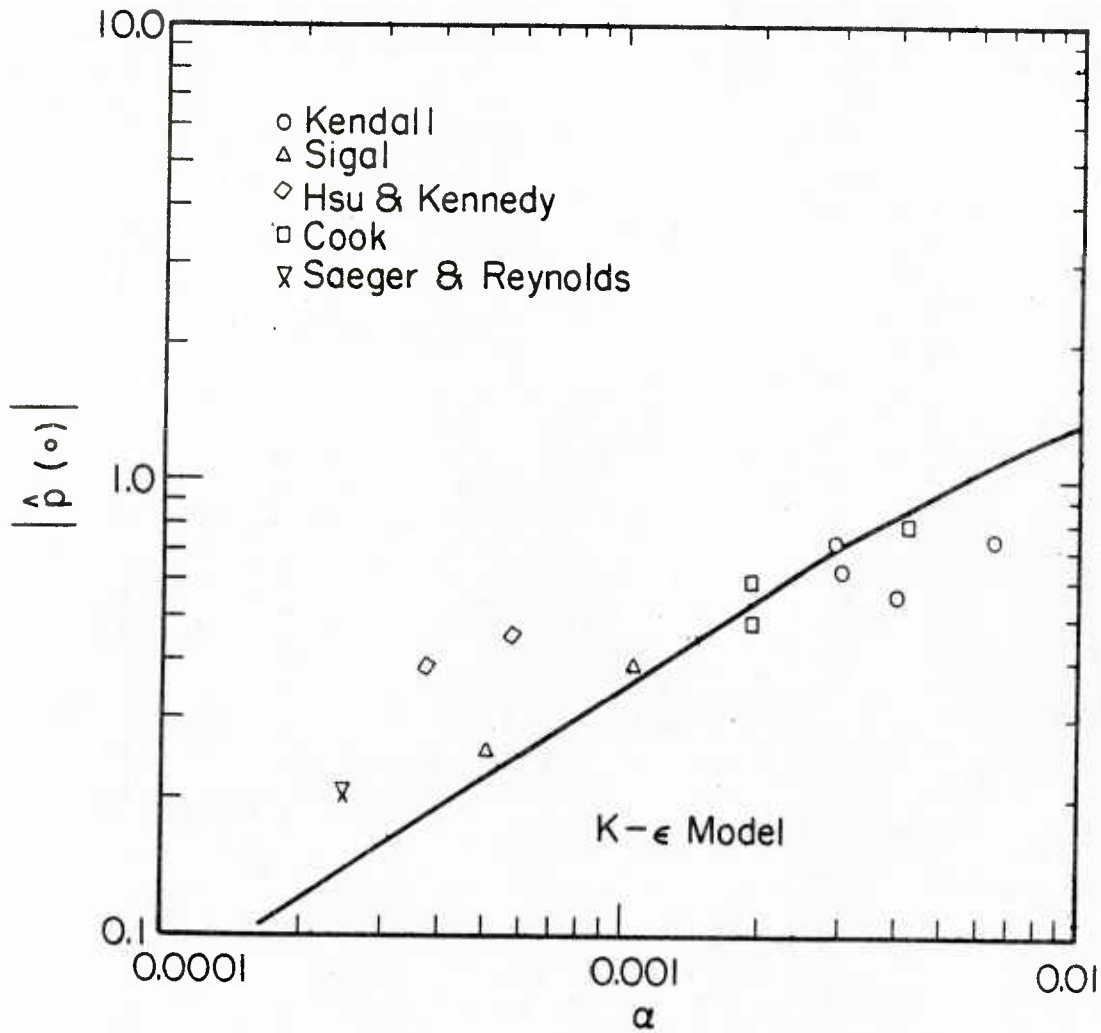


Figure 6.41. $|\hat{p}(o)|$ for K- ϵ Model

In Appendix L it is shown how the wave induced turbulent kinetic energy, $a \hat{k}(y) e^{i\alpha x}$, is related to the wave induced variation of the root mean square level of the fluctuating velocity gradient, $\sqrt{\overline{s_x'^2} / \overline{S_x}}$. Figures 6.42 and 6.43 compare the phase angle and amplitude of the predicted wave induced kinetic energy with the experimentally determined values. In the range of the experiments the predicted amplitude is in fair agreement with the data. Poor agreement between the measured and predicted phase shifts of $a \hat{k}(y) e^{i\alpha x}$ is obtained. However both theory and experiment predict a phase shift such that the maximum occurs on the upstream side of the wave.

(f) Curvature Effects

Model C* was modified to include curvature effects by multiplying the plane flow mixing length expression equation (3.35) by a curvature correction equation (3.79). This model was chosen as opposed to either the Relaxation Model or Model D* in order to isolate the effect of curvature on the turbulence. The straightforward application of the curvature correction requires the specification of one constant, β_c , and assumes that the local turbulence is always in equilibrium with the streamline curvature.

Figures 6.44, 6.45, 6.46 and 6.47 show the phase angle and amplitude of the wave induced pressure and shear stress for different values of β_c respectively. For small values of α the effect of curvature is to shift the phase angle of the shear stress in the upstream direction. This may be explained since the effect of the wave on the turbulence (from curvature considerations) is to enhance the turbulence at the trough and suppress the turbulence at the crest. For large values of

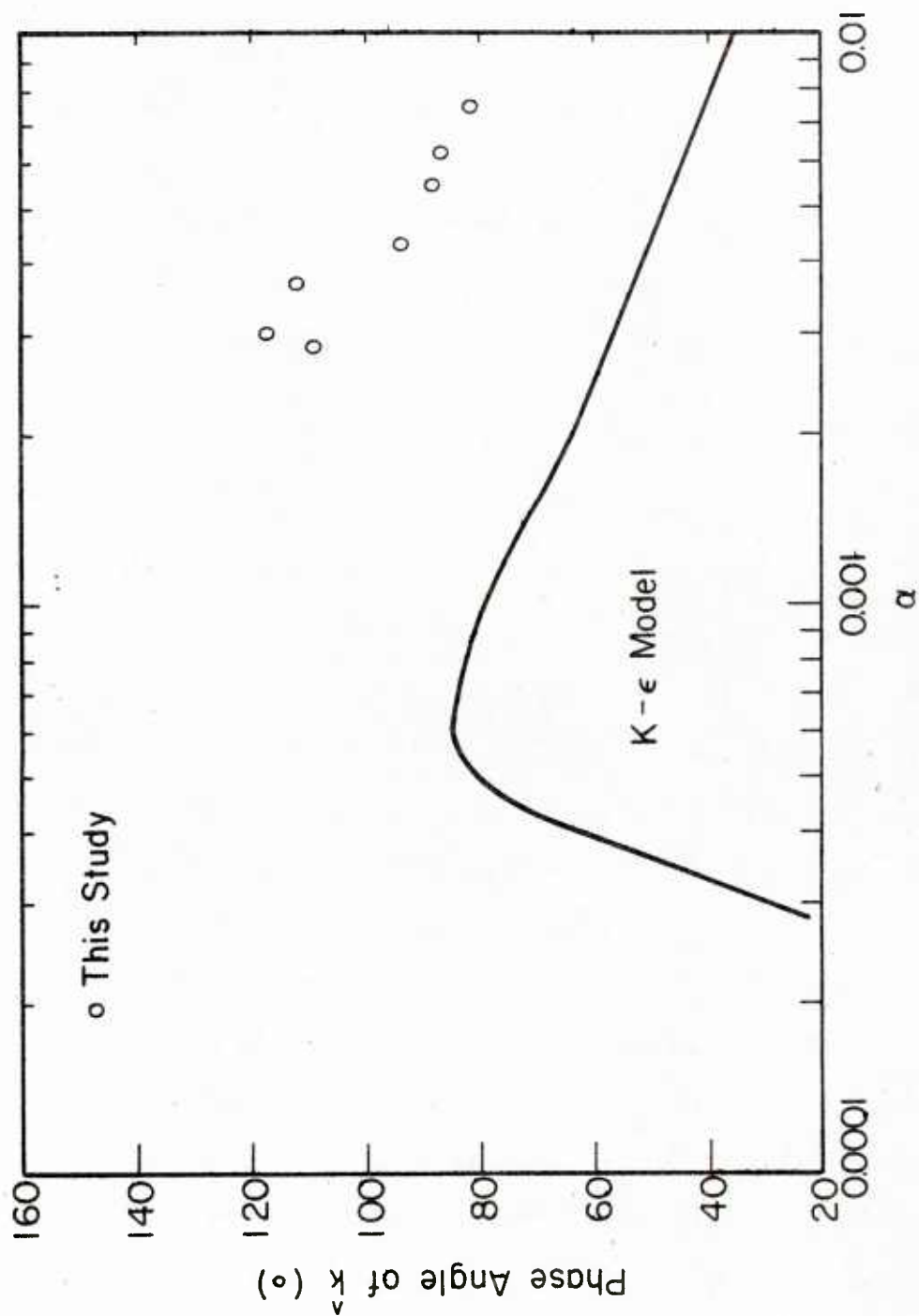


Figure 6.42. $\hat{k}(\alpha)$ Phase Angle for K- ϵ Model

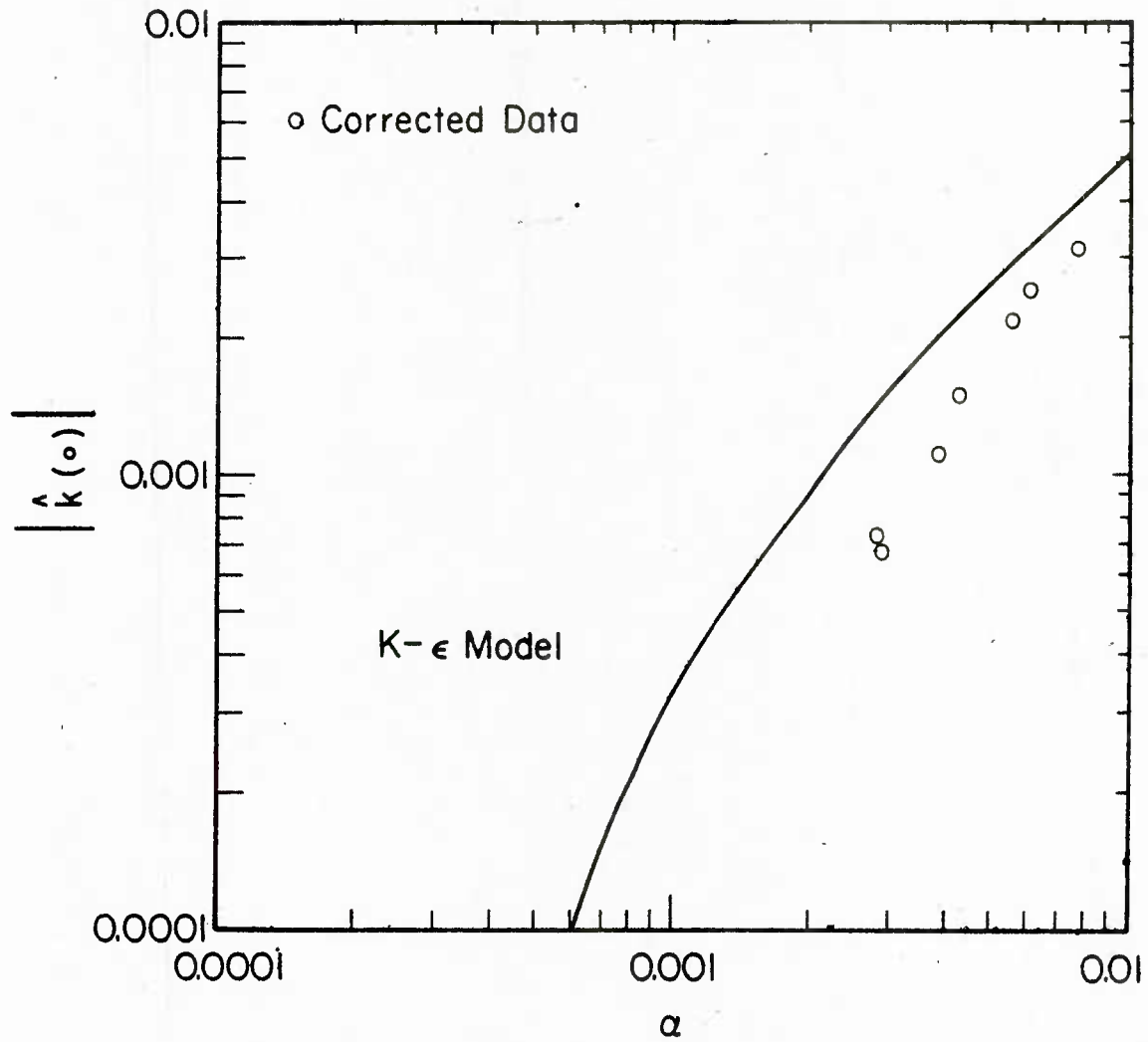


Figure 6.43. $|\hat{k}(o)|$ for K- ϵ Model

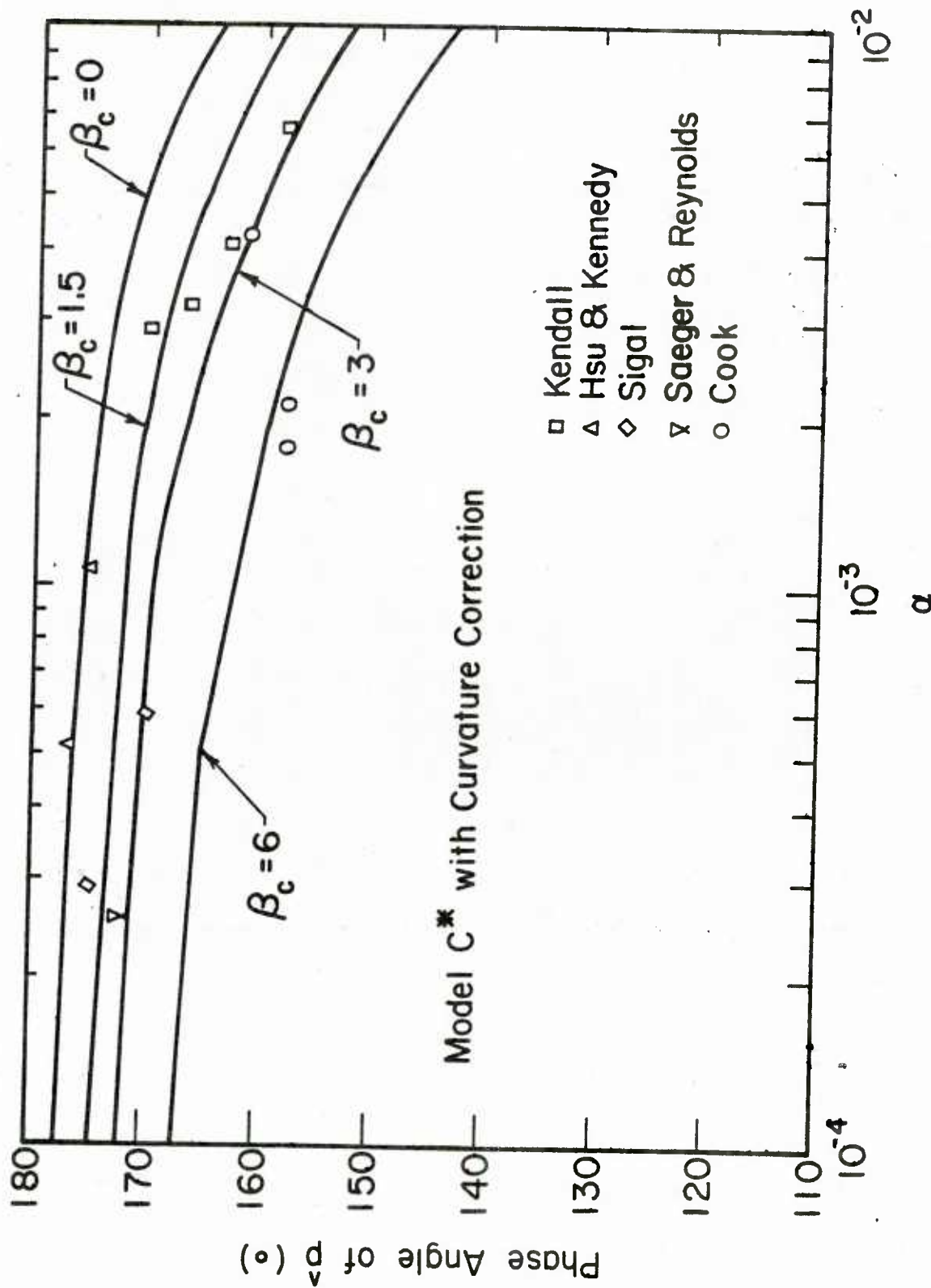


Figure 6.44. $\hat{p}(\alpha)$ Phase Angle for Model C* for Different Values of β_c

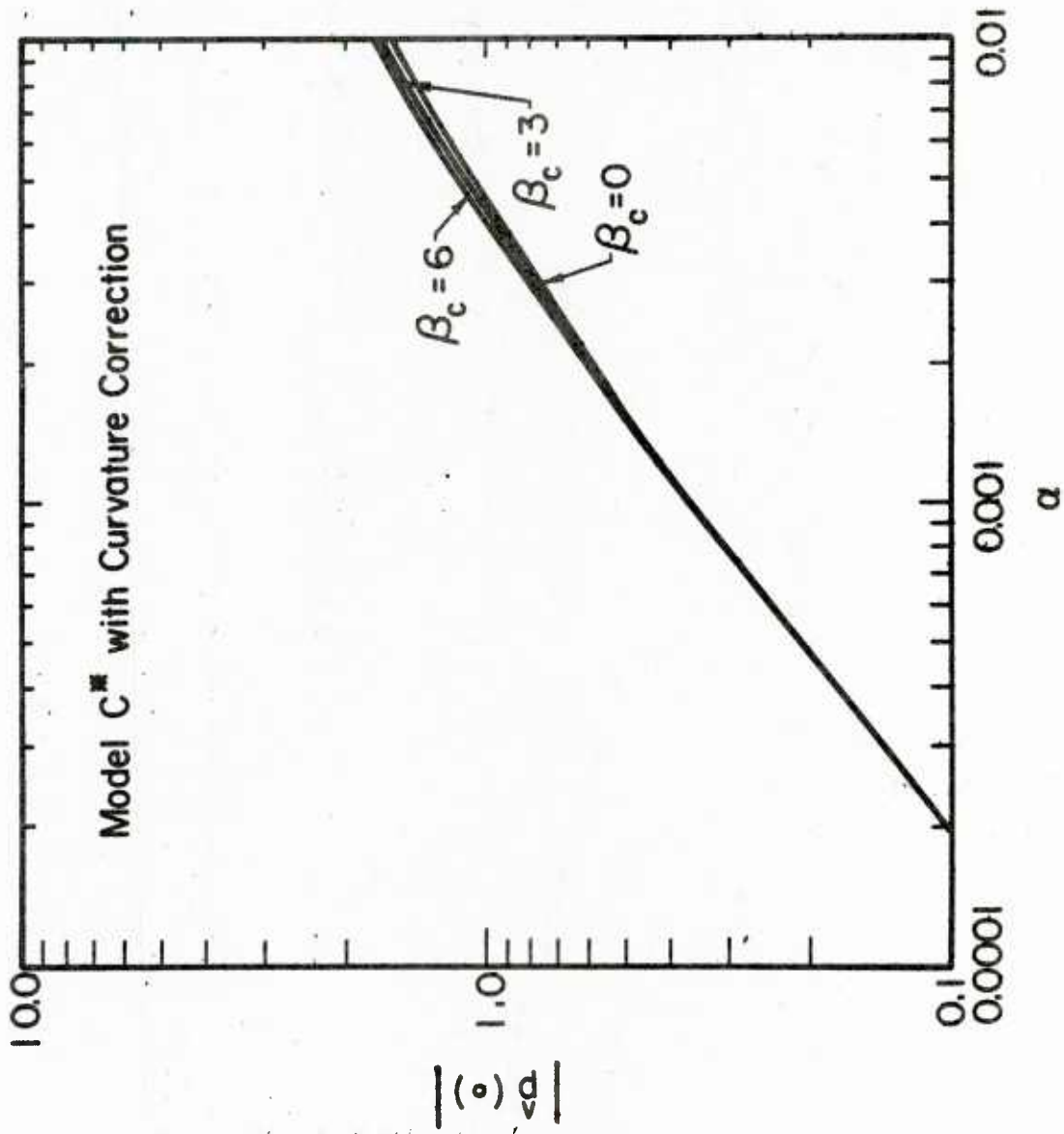


Figure 6.45. $|\hat{p}(0)|$ for Model C* for Different Values of β_c

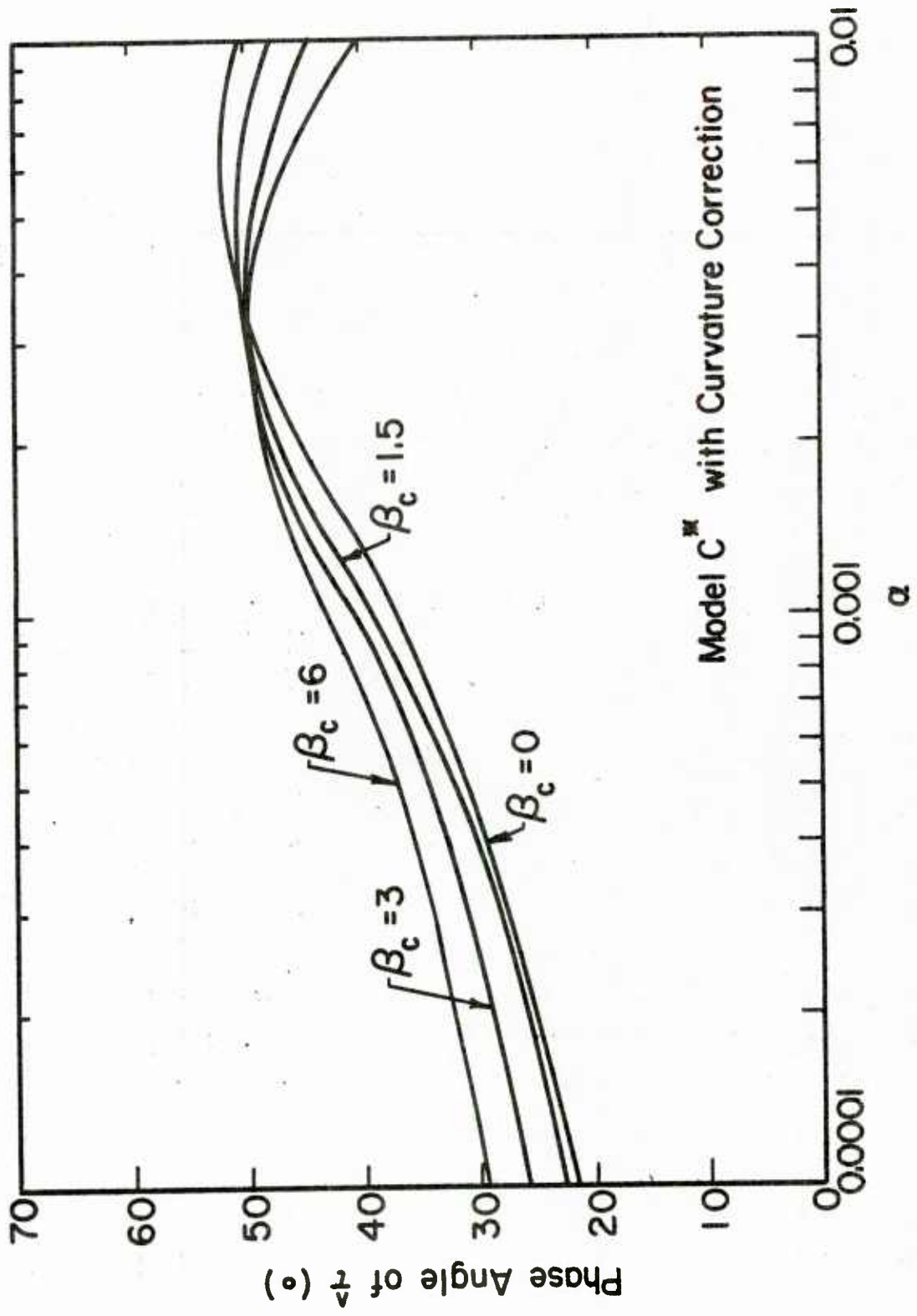


Figure 6.46. $\hat{\tau}(o)$ Phase Angle for Model C^* for Different Values of β_c

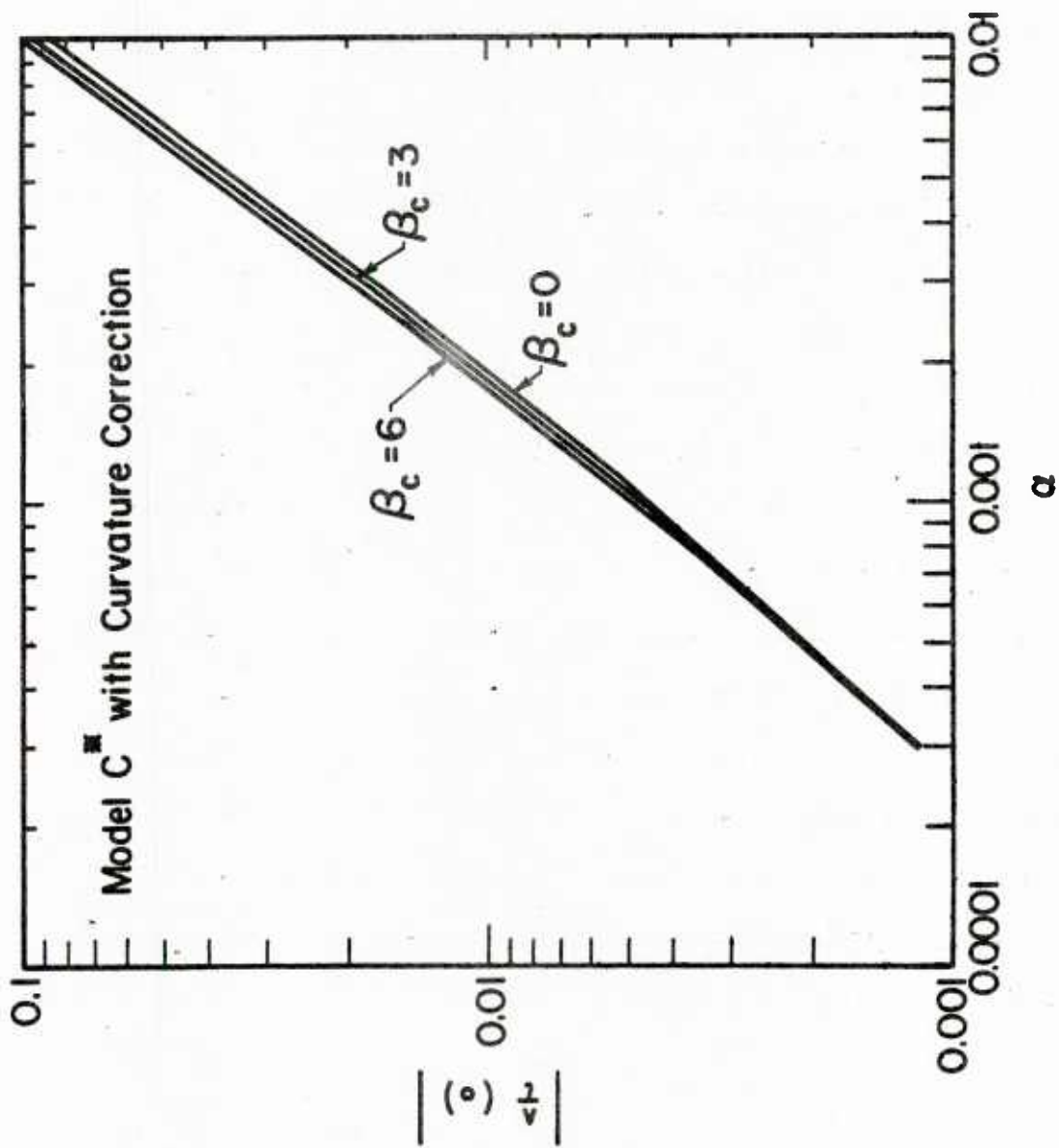


Figure 6.47. $|\hat{t}(o)|$ for Model C^* for Different Values of β_c

α the effect of curvature is to shift the maximum in the pressure and hence the minimum in the pressure gradient in the downstream direction. This in turn (from laminarization arguments) causes the shear stress to move in the downstream direction.

Since the turbulence is not expected to respond instantaneously to changes in the streamline curvature Bradshaw suggests that an effective radius of curvature defined in equation (3.82) be used. This requires the specification of a curvature lag constant, k_c . Figures 6.48, 6.49, 6.50 and 6.51 show the effect of this constant on the phase angle and amplitude of the wave induced pressure and shear stress respectively.

Recent pressure measurements from Langley Field [35] not included in this thesis indicate that the phase angle measurements of Kendall are the most reliable. It is concluded (see Figure 6.48) that inclusion of curvature with $\beta_c \approx 1.5$ provides the best fit of the available pressure data. Consequently calculations were made using Model D* with a curvature correction. This model was chosen since it allows the turbulence to adjust at different rates to the effect of pressure gradient and streamline curvature. Figures 6.52, 6.53, 6.54 and 6.55 compare the wave induced phase angle and amplitude of the shear stress and pressure with measurements. The constants used in these calculations are $k_L = -30$, $k_L = 1550$, $\beta_c = 2$ and $k_c = 0$.

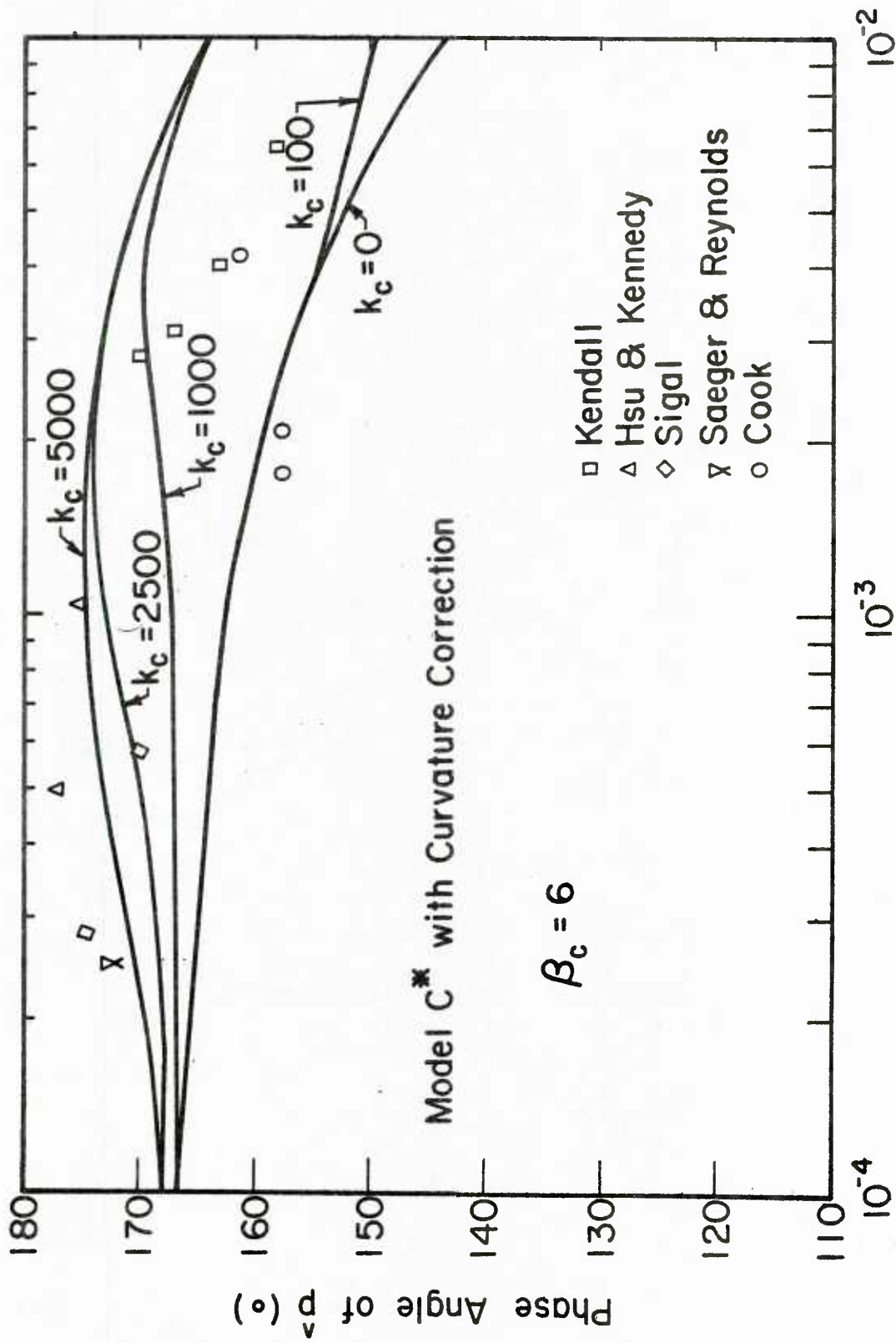


Figure 6.48. $\hat{p}(\alpha)$ for Model C* for $\beta_c = 6$ and Different Values of k_c

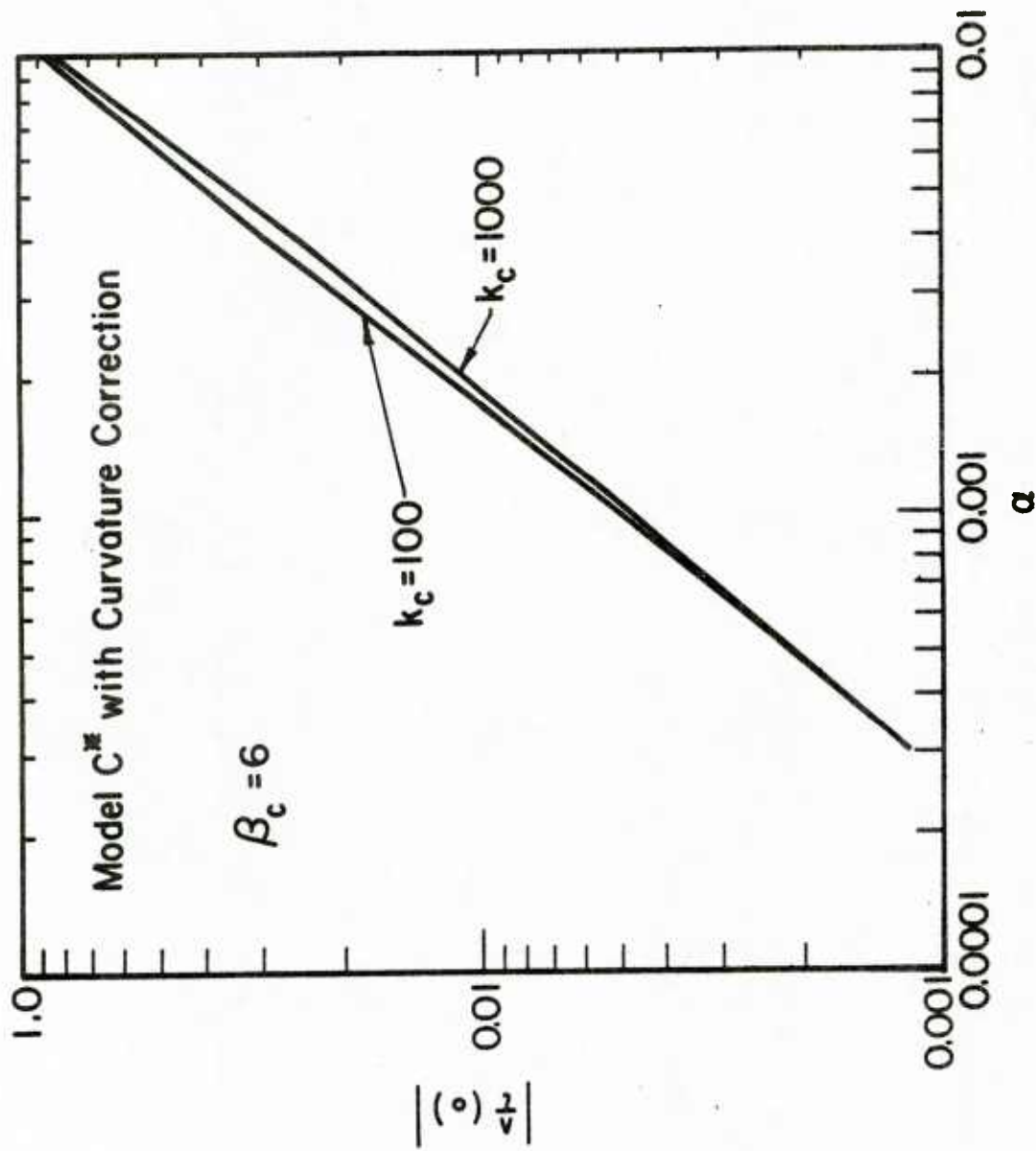


Figure 6.49. $|\hat{p}(o)|$ for Model C* for $\beta_c = 6$ and Different Values k_c

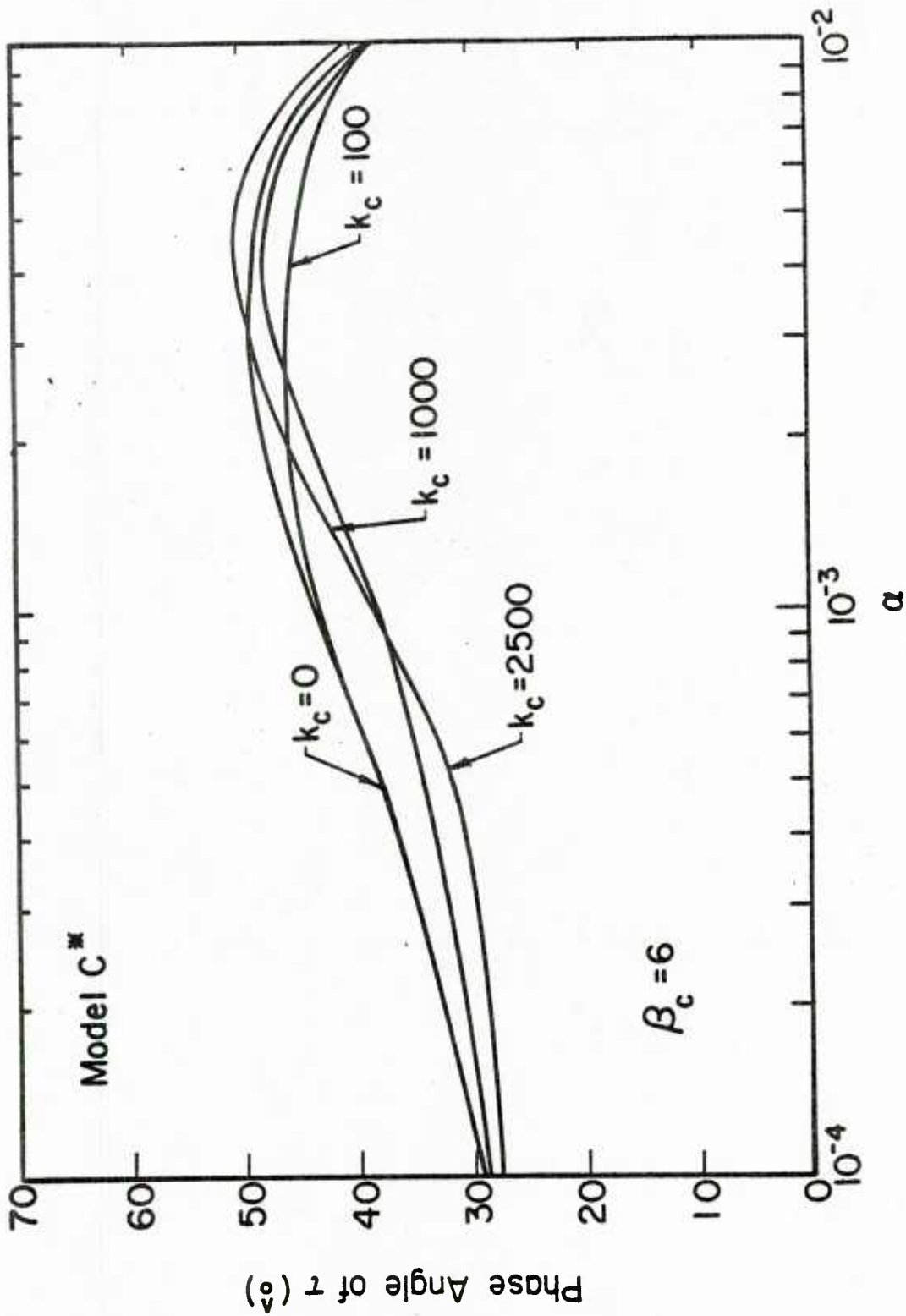


Figure 6.50 $\hat{\tau}(\alpha)$ Phase Angle for Model C* for $\beta_c = 6$ and Different Values of k_c

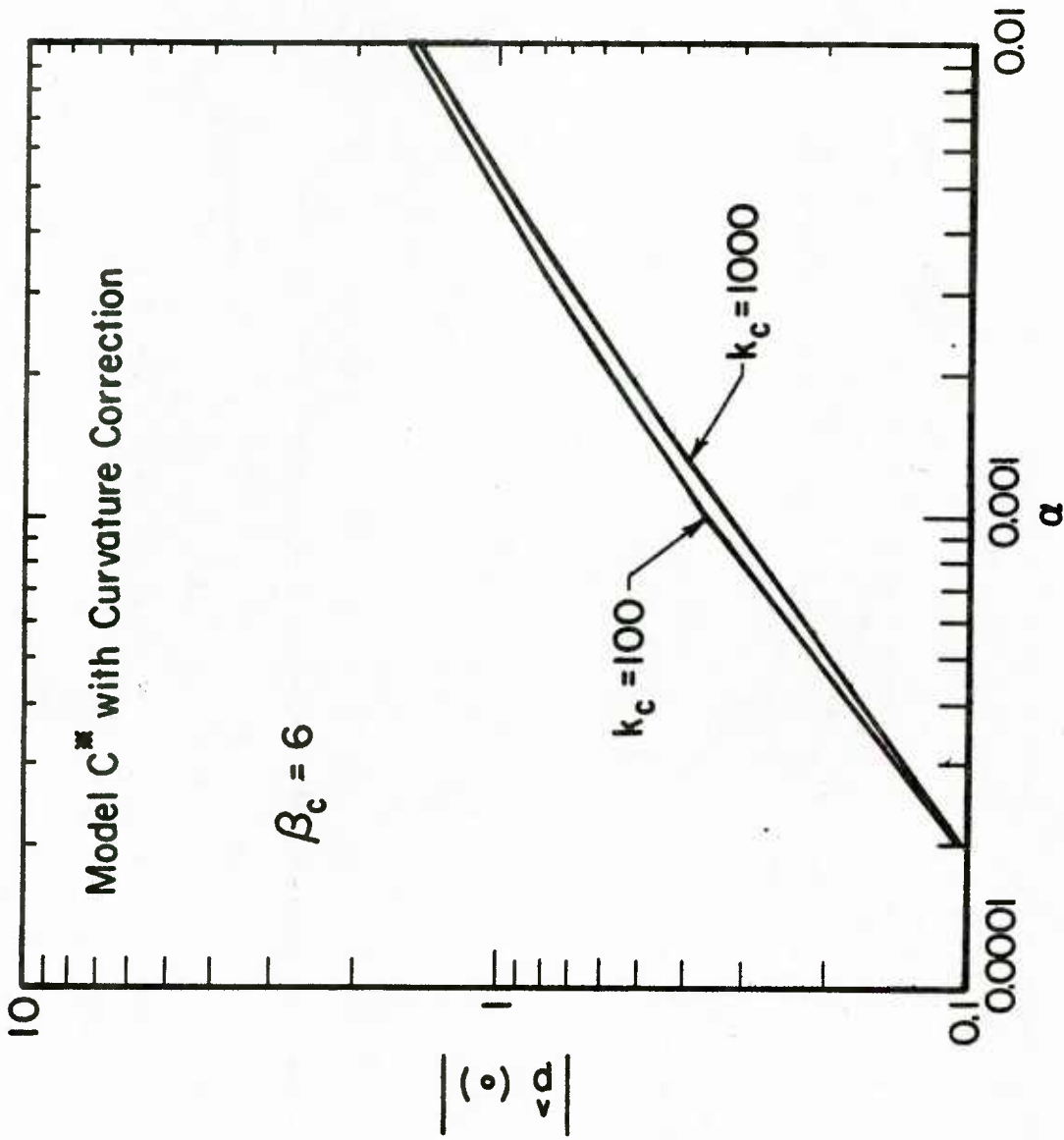


Figure 6.51. $|\hat{v}(0)|$ for Model C* for $\beta_c = 6$ and Different Values of k_c

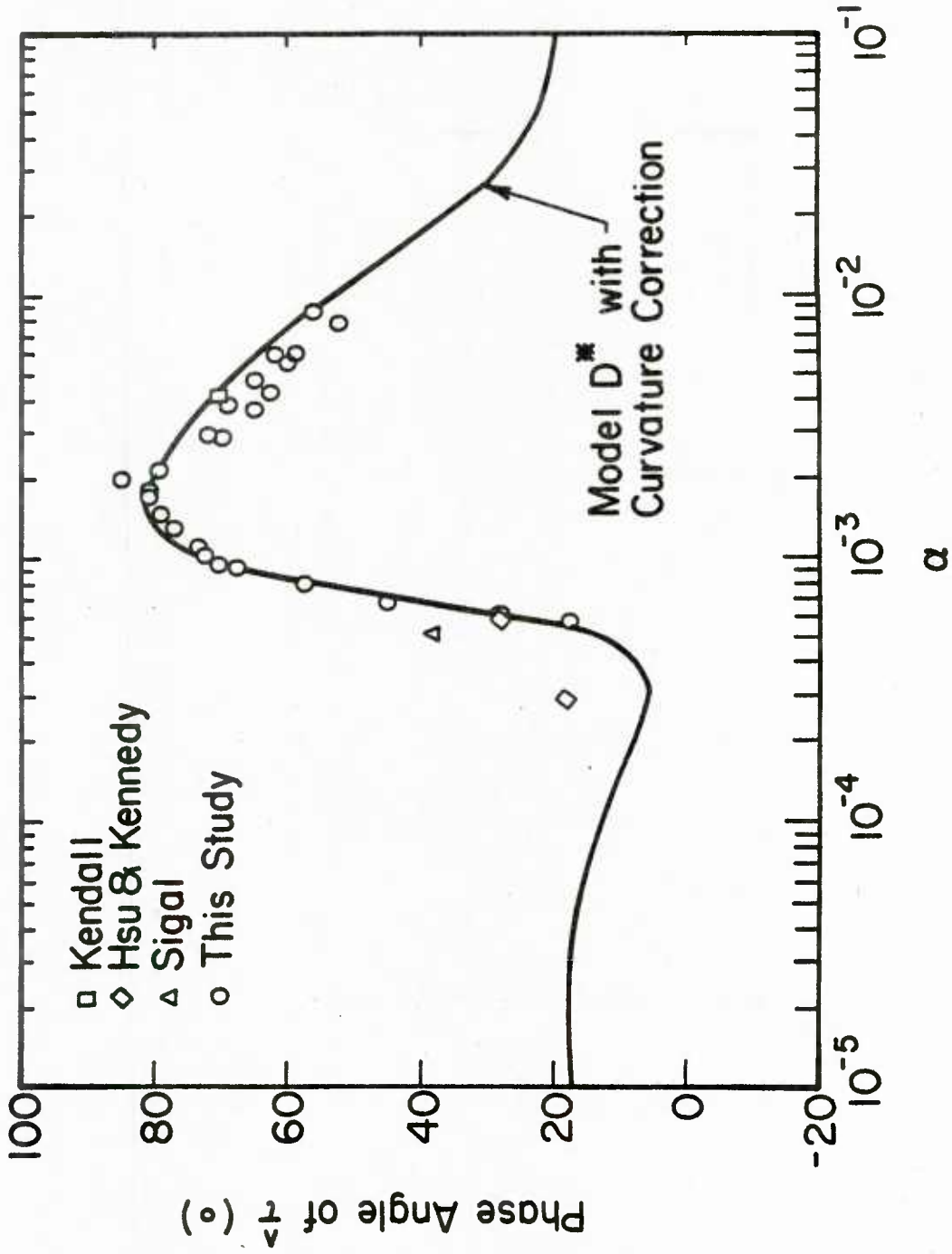


Figure 6.52. $\hat{\tau}(\alpha)$ Phase Angle for Model D^{**} for $k_1 = -30$,
 $k_L = 1550$, $\beta_c = 2$ and $k_c = 0$

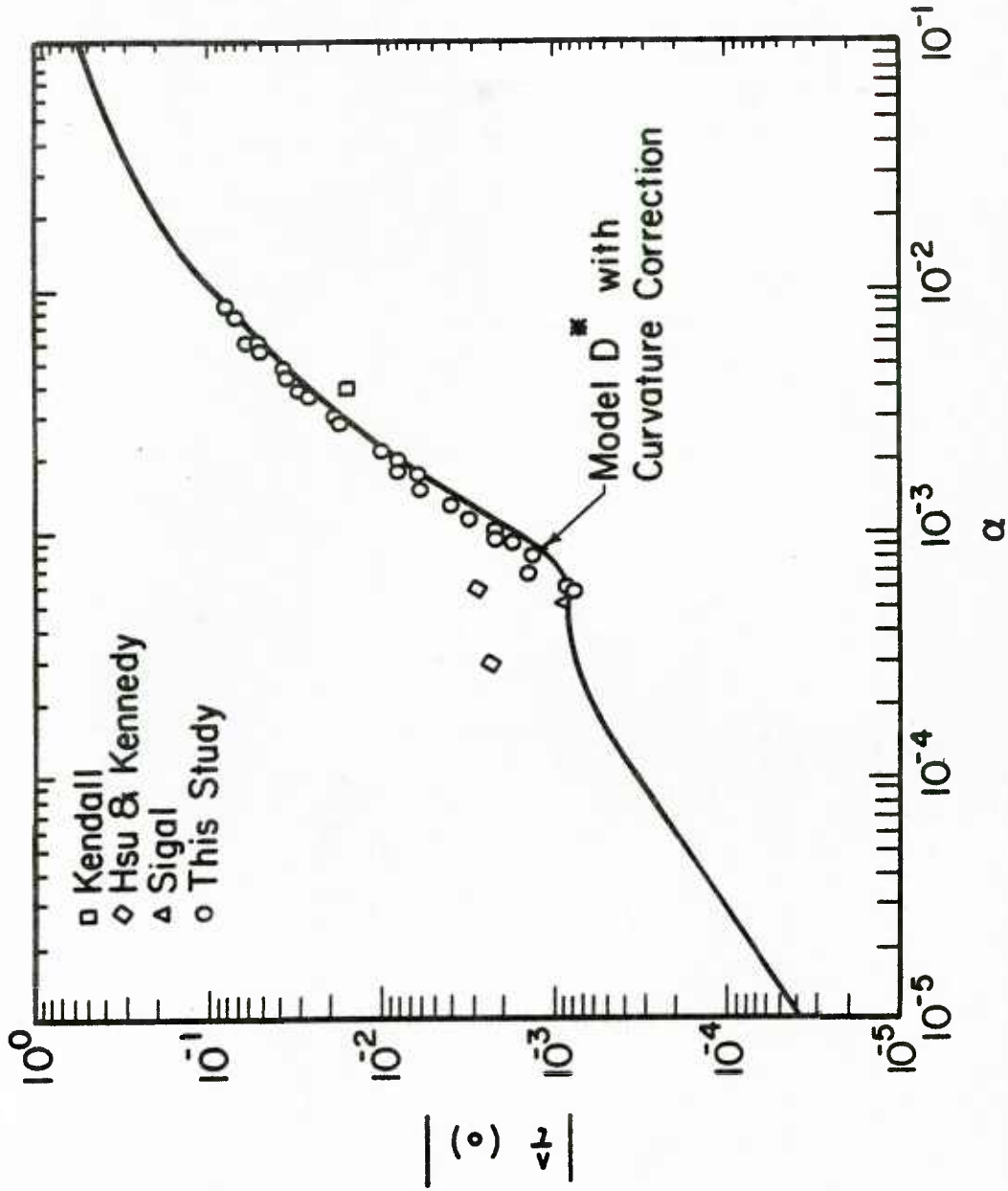


Figure 6.53. $|\hat{\tau}(o)|$ for Model D* for $k_1 = -30, k_L = 1550, \beta_c = 2$ and $k_c = 0$

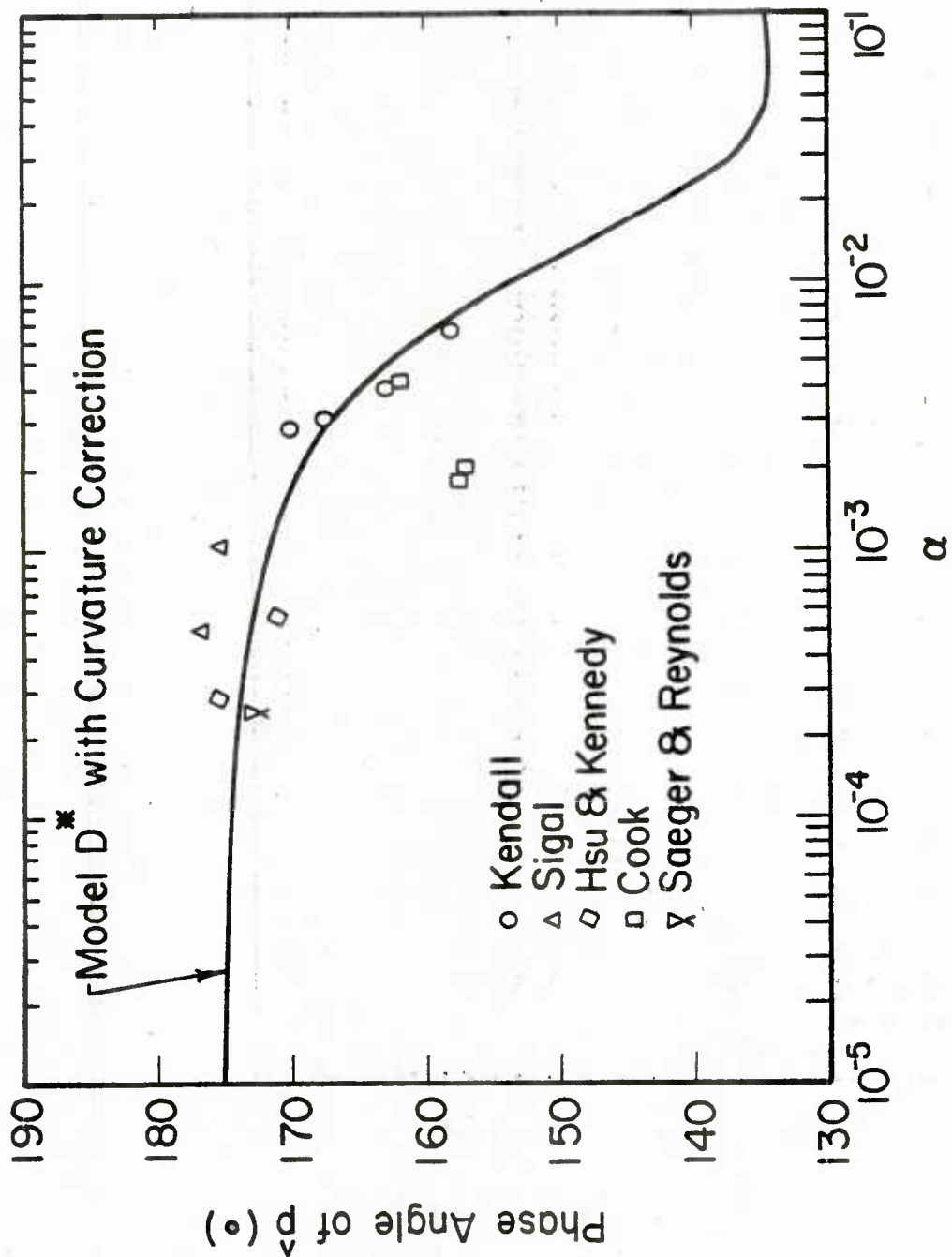


Figure 6.54. $\hat{p}(\alpha)$ Phase Angle for Model D* for $k_1 = -30$, $k_L = 1550$, $\beta_c = 2$ and $k_c = 0$

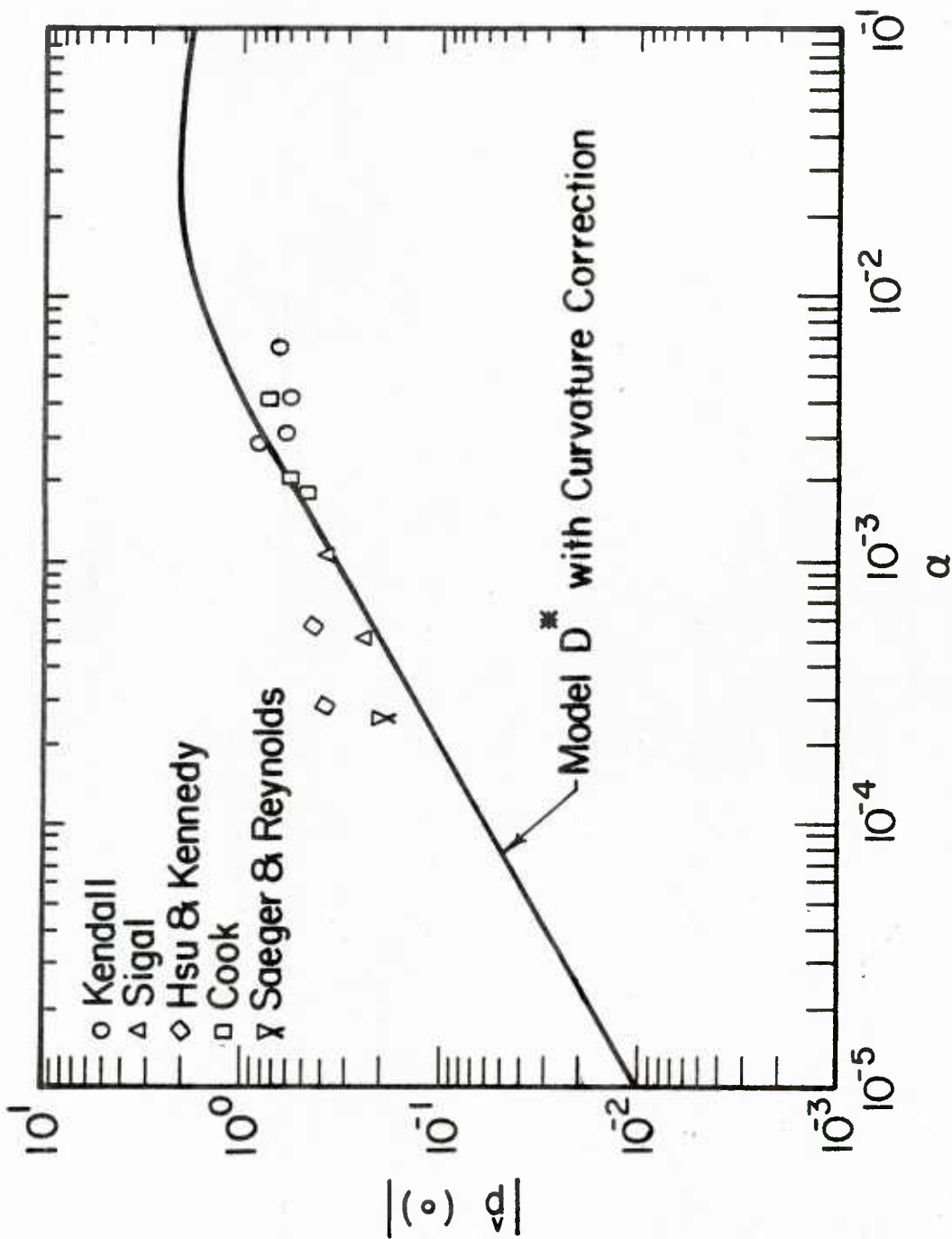


Figure 6.55. $|\hat{p}'(\alpha)|$ for Model D* for $k_1 = -30$, $k_L = 1550$, $\beta_c = 2$ and $k_c = 0$

CHAPTER 7

DISCUSSION OF RESULTS

In this chapter the major points which have emerged from the experiments and the calculations are presented.

The measurements of wall shear stress have been shown to provide an extremely sensitive test for turbulence models. Consequently the reliability of any theory should be tested by examining its ability to predict the variation of the wall shear stress over a wide range of conditions rather than its ability to predict the shear stress profiles for some fixed flow condition.

Figures 7.1 and 7.2 compare the calculated values of the amplitude and phase angle of the wave induced shear stress of the Quasi-Laminar Model with those of several turbulence models. For $\alpha > 0.07$, the Quasi-Laminar Model and all turbulence models yield similar results since the disturbance field introduced by the wave surface is contained in a region where the effects of turbulence on the wave induced flow are small. For $\alpha < 3 \times 10^{-5}$ all turbulence models predict similar variations of the shear stress. In this range the effect of pressure gradient on the flow is small. The flow can be visualized as one over a surface with radius of curvature $1/R = -a \alpha^2 \cos(\alpha x)$, an external velocity $U = U_\infty(1 + a \cos(\alpha x))$ and a pressure gradient, $\partial P/\partial x = -a \alpha^2 U_\infty^2 \sin(\alpha x)$. In the range $3 \times 10^{-5} < \alpha < 0.03$ the Equilibrium Turbulence Model over predicts the effect of pressure gradient and the only models which reliably predict both the magnitude and phase angle of the shear stress are Model D* and the Relaxation Model (not shown in Figures 7.1 and 7.2). Therefore this rise is associated with relaxation effects. In fact for $\alpha > 7 \times 10^{-4}$ relaxation effects are such that the calculated effective pressure gradient can be

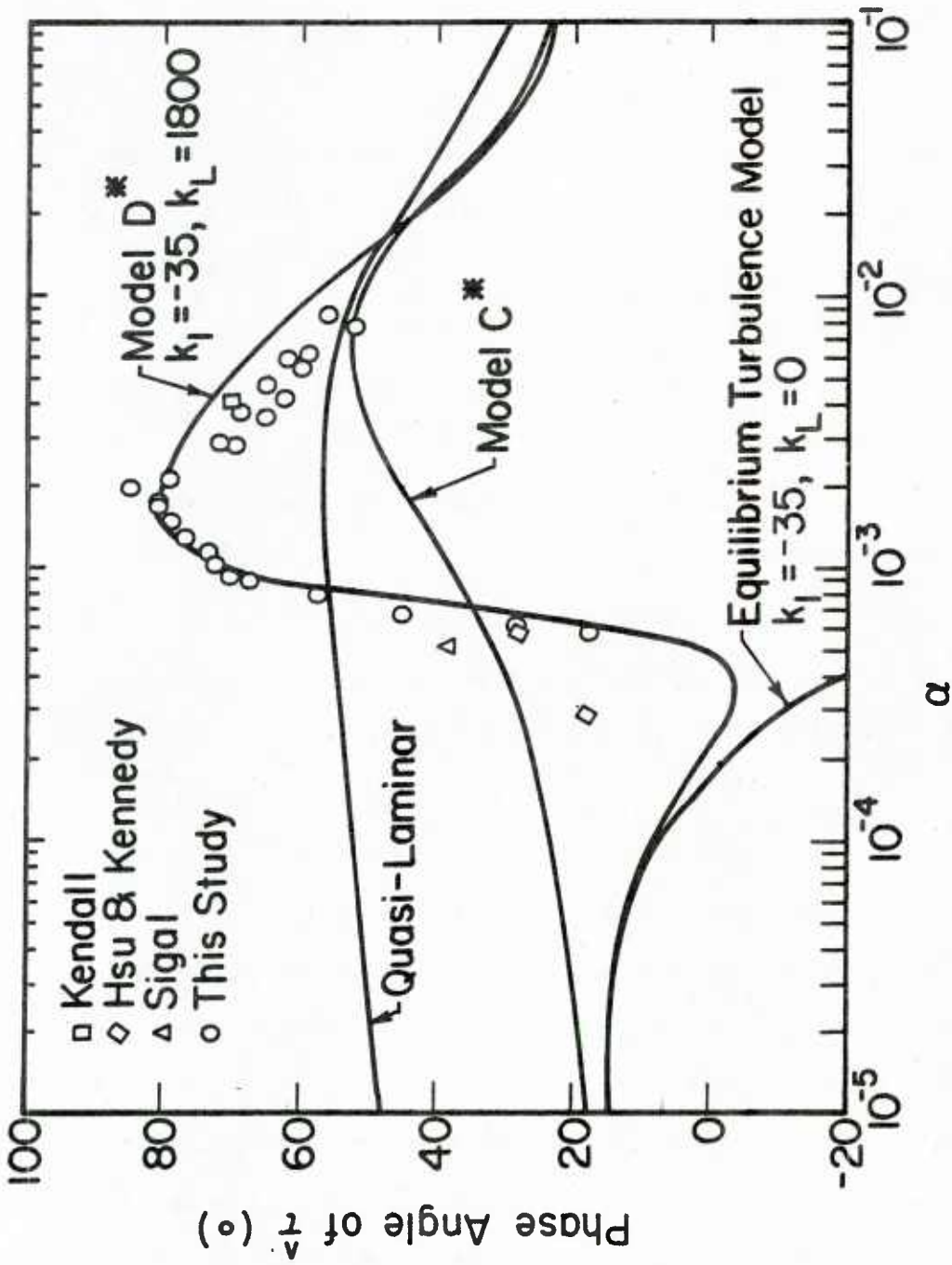


Figure 7.1. Comparison of Several Calculation Models with the Data for Shear Stress Phase Angle

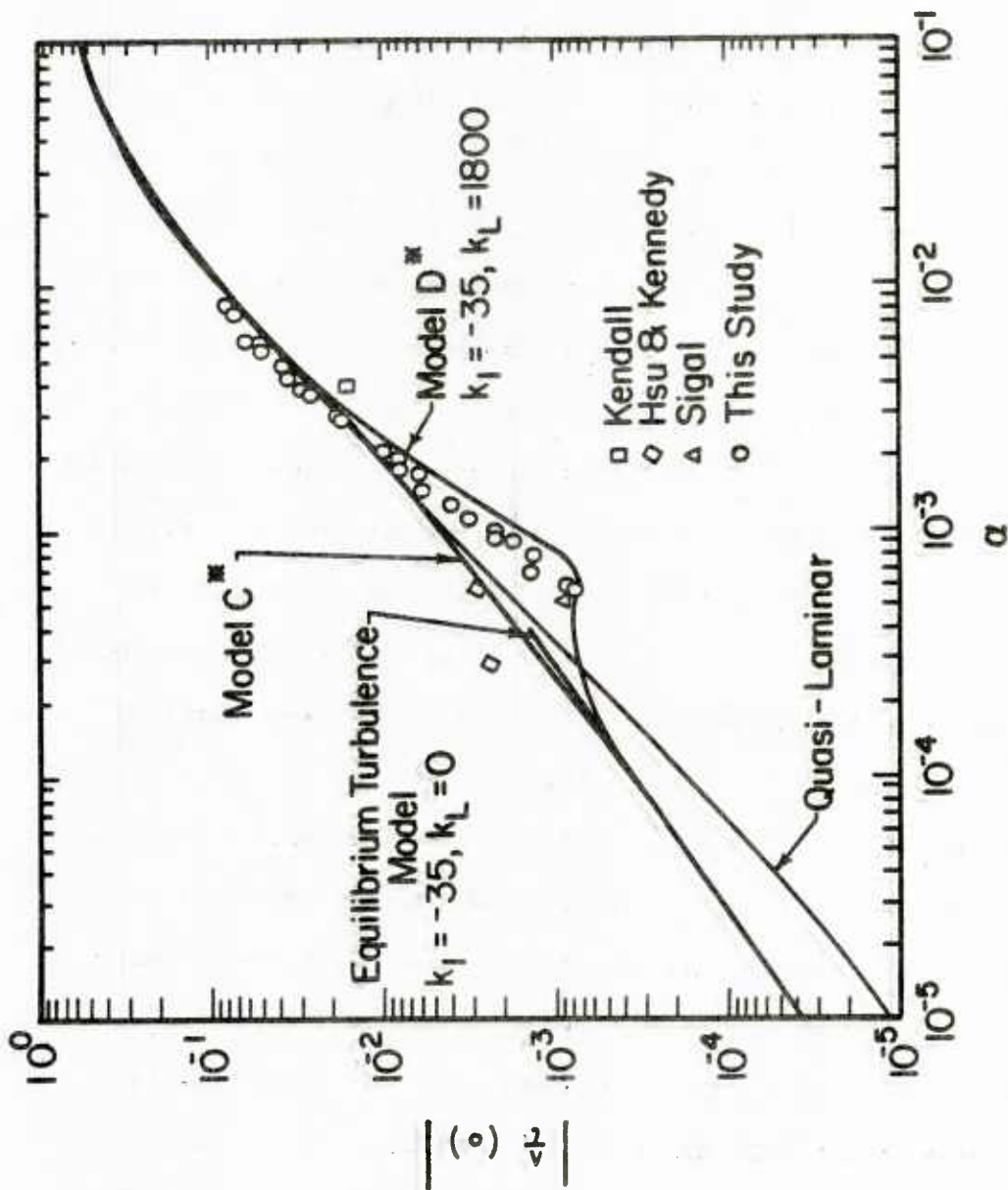


Figure 7.2. Comparison of Several Calculation Models with the Data for Shear Stress Amplitude

as much as 90° out of phase with the calculated local pressure gradient (Figure 7.3) causing the maximum in the wall shear stress to shift in the upstream direction.

Measurements of the streamwise component of the turbulent kinetic energy (see Figure 6.42) show that the kinetic energy close to the wave surface reaches a maximum on the upstream side of the wave. This finding provides further evidence that the turbulence close to the wall in the range $3 \times 10^{-5} < \alpha < 0.02$ is not in equilibrium with the local pressure gradient, since (from laminarization arguments) it is expected that the turbulent energy would reach a maximum on the downstream side of the wave due to flow deceleration in this region.

The inclusion of curvature effects in Model D* causes a significant improvement in the calculated phase angle of the wave induced pressure (Figure 7.4 in the range $1 \times 10^{-4} < \alpha < 0.5$). These results are of particular importance in the prediction of instabilities at a gas liquid interface where recent calculations of Frederick [21] have indicated that Model D* may be underpredicting the pressure.

In summary the presence of waves introduces two complications that would not be present at a flat surface: Wave induced variations of the pressure gradient along the wave surface can cause a thickening and thinning of the viscous wall region. Wave induced curvature of the streamlines can cause a change in turbulent transport which results in a periodic enhancement and damping of the turbulence. Calculations have shown that the wall shear stress measurements and in particular the sharp change in the measured phase angle of, $\hat{\tau}(0) e^{i\alpha x}$, at $\alpha = 0.0015$ provide an excellent test of turbulence models. Significant

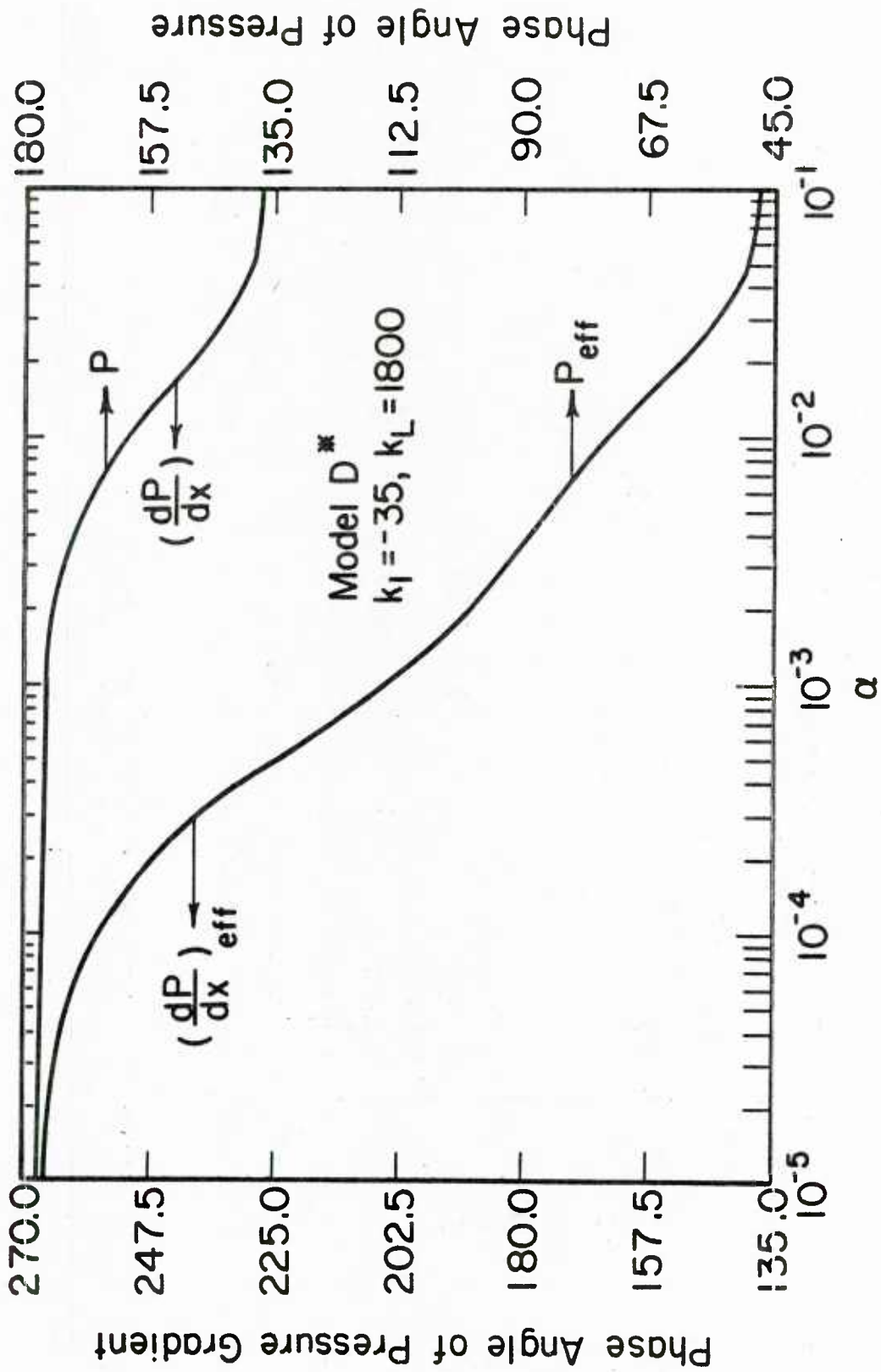


Figure 7.3. Comparison of Phase Angle of Pressure Gradient and Effective Pressure Gradient for Model D*

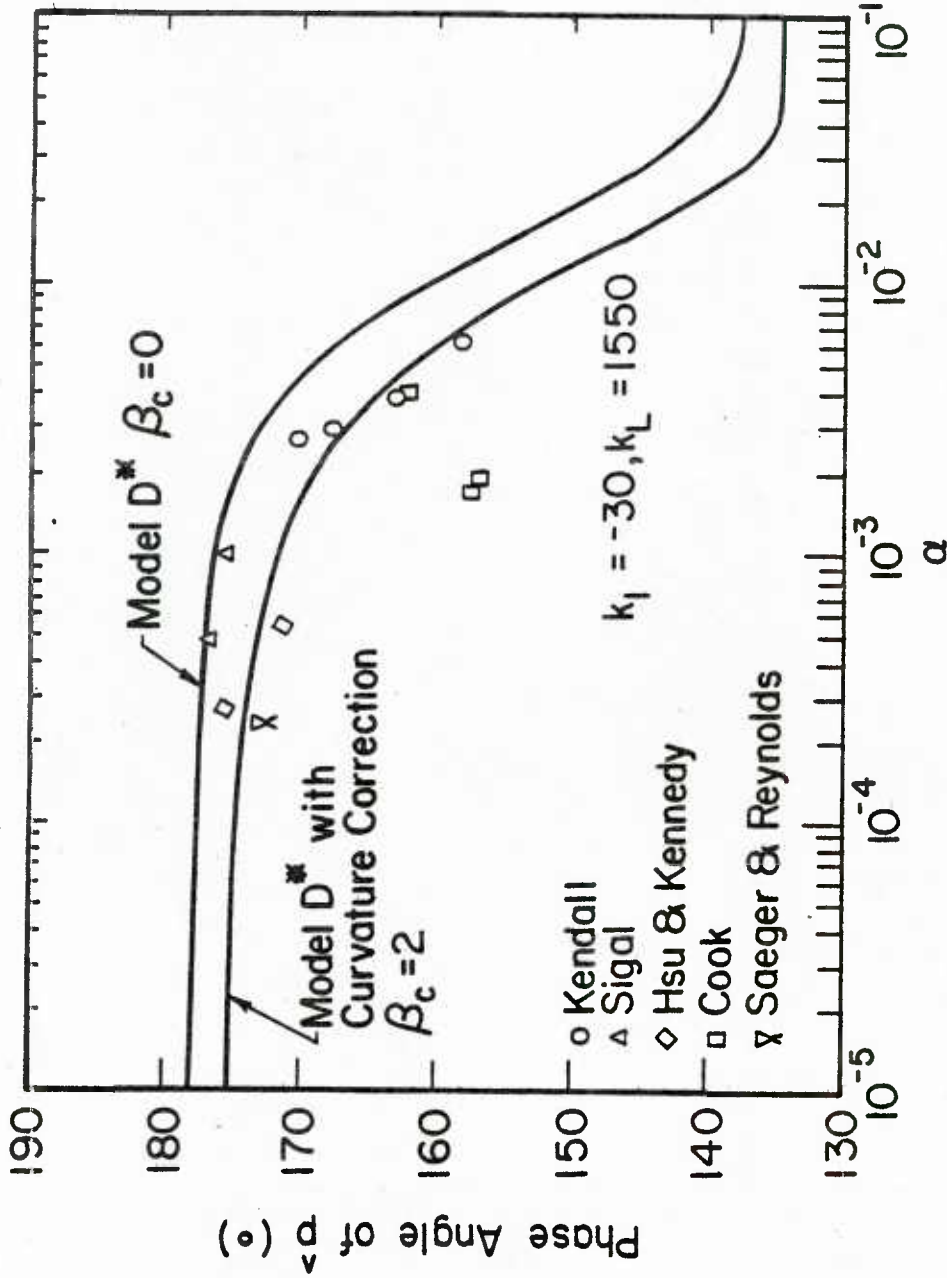


Figure 7.4. Comparison of Predicted Phase Angle of $\hat{p}(\alpha)$ for Model D* With and Without Curvature Correction

errors are obtained in predicting the wall shear stress if the influence of the wave induced pressure gradient is ignored.

The sensitivity of Model D* to the value of the relaxation parameter, k_L , points out the need to introduce relaxation effects in a more fundamental way. Work along these lines using the K- ϵ Model reveals qualitatively the same behavior as Model D*. However Model D*, modified to include the effect of streamline curvature on turbulence, provides the best overall fit of the available pressure and shear stress measurements to date.

APPENDIX A
CONDITIONS FOR LINEARITY

The necessary conditions for flow over a wavy surface to be described by a linear form of the Navier Stokes equations are developed.

The flow field is considered as the sum of a mean and a wave induced quantity.

$$U(x, y) = \bar{U}(y) + \tilde{u}(x, y) \quad (\text{A.1})$$

$$V(x, y) = \tilde{v}(x, y) \quad (\text{A.2})$$

where the over bar and tilda represent a mean and a wave induced quantity respectively. The wave induced streamwise velocity and velocity gradient scale as

$$\tilde{u} \sim a \frac{d\bar{U}}{dy}, \quad \frac{d\tilde{u}}{dx} \sim a \alpha \frac{d\bar{U}}{dy}, \quad (\text{A.3})$$

since the presence of the wave surface with amplitude, a , displaces the mean flow by an amount, $a \frac{d\bar{U}}{dy}$, to a first order of approximation. From continuity

$$\frac{\partial \tilde{v}}{\partial y} \sim a \alpha \frac{d\bar{U}}{dy}. \quad (\text{A.4})$$

On integrating (A.4) from 0 to δ , where δ is a boundary layer thickness

$$\tilde{v} \sim a \alpha \delta \frac{d\bar{U}}{dy}. \quad (\text{A.5})$$

If $\tilde{v} \frac{d\bar{U}}{dy}$ is taken as a typical linear term, a comparison of the ratio of nonlinear to linear terms yields

$$\frac{\tilde{v} \frac{\partial \tilde{u}}{\partial y}}{\tilde{v} \frac{d\bar{U}}{dy}} \sim \frac{a}{\delta} \quad (\text{A.6})$$

$$\frac{\tilde{u} \frac{\partial \tilde{u}}{\partial x}}{\tilde{v} \frac{d\bar{U}}{dy}} \sim \frac{a}{\delta} \quad (\text{A.7})$$

Therefore in addition to α being small, the additional requirement that $a/\delta < 1$ is necessary for the flow field to be described by linear equations.

APPENDIX B

FORMULATION OF OUTER BOUNDARY CONDITION

The outer boundary condition is such that the flow field far from the surface is just that which would be present over a flat surface. This requires that the velocity field in boundary layer coordinates at y_m , see Figure (B.1) be equated to the undisturbed flow in cartesian coordinates.

For a small α the velocity field in boundary layer coordinates at y_m can be transformed into cartesian coordinates as follows:

$$U_o(x, y_m) = U(x, y_m) - V(x, y_m) i\alpha a e^{i\alpha x} \quad (B.1)$$

$$V_o(x, y_m) = U(x, y_m) i\alpha a e^{i\alpha x} + V(x, y_m) \quad (B.2)$$

where the subscript, o , denotes cartesian coordinates. If U and V are written in terms of average and wave induced quantities, equations (B.1) and (B.2) neglecting $o(a^2)$ terms become

$$U_o(x, y_m) = \bar{U}(y_m) + a\hat{u}e^{i\alpha x} \quad (B.3)$$

$$V_o(x, y_m) = \bar{U}(y_m) i\alpha a e^{i\alpha x} + \hat{v}a e^{i\alpha x} \quad (B.4)$$

The cartesian description of the flow at $(Y_m + a e^{i\alpha x})$ is obtained by a Taylor series expansion at Y_m as follows

$$U_o(x, y_m) = U_o(x, Y_m) + \left. \frac{\partial U_o(x, y)}{\partial y} \right|_{Y_m} a e^{i\alpha x} \quad (B.5)$$

$$V_o(x, y_m) = V_o(x, Y_m) + \frac{\partial V_o(x, y)}{\partial y} \Big|_{Y_m} a e^{i\alpha x} . \quad (B.6)$$

Since the flow at Y_m is considered undisturbed

$$U_o(x, Y_m) = \bar{U}(Y_m) \quad (B.7)$$

$$V_o(x, Y_m) = 0 . \quad (B.8)$$

Equations (B.3) and (B.4) can now be equated to (B.5) and (B.6) respectively to yield

$$\bar{U}(y_m) + a \hat{u}(y_m) e^{i\alpha x} = \bar{U}(Y_m) + \frac{d\bar{U}}{dy}(Y_m) a e^{i\alpha x} \quad (B.9)$$

and

$$\bar{U}(y_m) i \alpha a e^{i\alpha x} + \hat{v} a e^{i\alpha x} = 0 . \quad (B.10)$$

On equating terms of similar order and introducing the stream function, $a F e^{i\alpha x}$, the following relations are obtained,

$$\bar{U}(y_m) = \bar{U}(Y_m) \quad (B.11)$$

$$F'(y_m) = \frac{d\bar{U}}{dy}(y_m) \quad (B.12)$$

$$F(y_m) = \bar{U}(y_m) . \quad (B.13)$$

Equation (B.11) implies that the average flow field is not disturbed by the presence of the wave surface and equations (B.12) and (B.13) are the required boundary conditions for the wave induced flow for large values of y .

APPENDIX C

DERIVATION OF TURBULENT ENERGY AND DISSIPATION EQUATIONS

Consider a flow over a two dimensional curved surface. Use general orthogonal coordinates with x measured along the surface, y normal to the surface and z at right angles to the x - y plane which is the plane of motion. The curvature of the surface $\kappa(x) = 1/R(x)$, is taken as positive for convex curvature and negative for concave curvature where, $R(x)$, is the radius of curvature of the surface. The elements of length along the parallel curves and along the normal are $h_1 = 1 + \kappa y$ and $h_2 = 1$. The element of length along the z direction is $h_3 = 1$. If u , v , and w are the velocity components along the x , y , and z directions respectively the following equations for u , v , and w are obtained (see Bradshaw [8]).

continuity

$$\frac{\partial u}{\partial x} + \frac{\partial}{\partial y} \{ (1 + \kappa y)v \} + \frac{\partial}{\partial z} \{ (1 + \kappa y)w \} = 0 \quad (C.1)$$

x momentum

$$\begin{aligned} \frac{\partial u}{\partial t} + \frac{1}{(1 + \kappa y)} u \frac{\partial u}{\partial x} + v \frac{\partial u}{\partial y} + w \frac{\partial u}{\partial z} + \frac{\kappa uv}{(1 + \kappa y)} = - \frac{1}{(1 + \kappa y)} \frac{\partial p}{\partial x} \\ + \frac{1}{(1 + \kappa y)} \frac{\partial \tau_{xx}}{\partial x} + \frac{\partial \tau_{xy}}{\partial y} + \frac{\partial \tau_{xz}}{\partial z} + \frac{2 \kappa \tau_{xz}}{(1 + \kappa y)} \end{aligned} \quad (C.2)$$

y momentum

$$\begin{aligned} \frac{\partial v}{\partial t} + \frac{1}{(1 + \kappa y)} u \frac{\partial v}{\partial x} + v \frac{\partial v}{\partial y} + w \frac{\partial v}{\partial z} - \frac{\kappa u^2}{(1 + \kappa y)} = - \frac{\partial p}{\partial y} \\ + \frac{1}{(1 + \kappa y)} \frac{\partial \tau_{xy}}{\partial x} + \frac{\partial \tau_{yy}}{\partial y} + \frac{\partial \tau_{yz}}{\partial z} - \frac{1}{(1 + \kappa y)} (\tau_{xx} - \tau_{yy}) \end{aligned} \quad (C.3)$$

z momentum

$$\begin{aligned} \frac{\partial w}{\partial t} + \frac{1}{(1 + \kappa y)} u \frac{\partial w}{\partial x} + v \frac{\partial w}{\partial y} + w \frac{\partial w}{\partial z} = - \frac{\partial p}{\partial z} \\ + \frac{1}{(1 + \kappa y)} \frac{\partial \tau_{xy}}{\partial x} + \frac{\partial \tau_{yz}}{\partial y} + \frac{\partial \tau_{zz}}{\partial z} - \frac{\kappa \tau_{yz}}{(1 + \kappa y)} \end{aligned} \quad (C.4)$$

where

$$\tau_{xx} = 2S_{xx} = 2 \left[\frac{1}{(1 + \kappa y)} \frac{\partial u}{\partial x} + \frac{\kappa v}{(1 + \kappa y)} \right] \quad (C.5)$$

$$\tau_{yy} = 2S_{yy} = 2 \frac{\partial v}{\partial y} \quad (C.6)$$

$$\tau_{zz} = 2S_{zz} = 2 \frac{\partial w}{\partial z} \quad (C.7)$$

$$\tau_{xy} = 2S_{xy} = (1 + \kappa y) \left[\frac{\partial}{\partial y} \left(\frac{u}{(1 + \kappa y)} \right) + \frac{1}{(1 + \kappa y)} \frac{\partial v}{\partial x} \right] \quad (C.8)$$

$$\tau_{yz} = 2S_{yz} = \left(\frac{\partial v}{\partial z} + \frac{\partial w}{\partial y} \right) \quad (C.9)$$

$$\tau_{xz} = 2S_{xz} = \left(\frac{\partial u}{\partial z} + \frac{1}{(1 + \kappa y)} \frac{\partial w}{\partial x} \right) \quad (C.10)$$

Consider a turbulent flow that is two dimensional in the mean. Therefore, the mean flow in the z direction is zero and all $\frac{\partial}{\partial z}$ of the mean flow quantities vanish. If the equations of motion are decomposed into mean velocities U, V plus fluctuating velocities u', v', w' and their corresponding pressures P and p' the following equation for the turbulent kinetic energy can be derived (see Bradshaw [8]).

$$\begin{aligned}
 & \text{I} \\
 & \frac{\partial K}{\partial t} + \frac{U}{(1 + \kappa y)} \frac{\partial K}{\partial x} + V \frac{\partial K}{\partial y} \\
 & \text{II} \qquad \qquad \qquad \text{III} \\
 = & - \frac{1}{(1 + \kappa y)} \frac{\partial}{\partial x} \left(\frac{\overline{u'^3} + \overline{u'v'^2} + \overline{u'w'^2}}{2} + \overline{u'p'} - \overline{u'\tau'_{xx}} - \overline{v'\tau'_{xy}} - \overline{w'\tau'_{xz}} \right) \\
 & \text{IV} \qquad \qquad \qquad \text{V} \\
 & - \frac{\partial}{\partial y} \left(\frac{\overline{v'u'^2} + \overline{v'^3} + \overline{v'w'^2}}{2} + \overline{v'p'} - \overline{u'\tau'_{xy}} - \overline{v'\tau'_{yy}} - \overline{w'\tau'_{yz}} \right) \\
 & \text{VI} \qquad \qquad \qquad \text{VII} \\
 & - \frac{\kappa}{(1 + \kappa y)} \left(\frac{\overline{v'u'^2} + \overline{v'^3} + \overline{v'w'^2}}{2} + \overline{v'p'} - \overline{u'\tau'_{xy}} - \overline{v'\tau'_{yy}} - \overline{w'\tau'_{yz}} \right) \\
 & \text{VIII} \\
 & - \overline{u'v'} \left[\frac{\partial U}{\partial y} - \frac{\kappa U}{(1 + \kappa y)} + \frac{1}{(1 + \kappa y)} \frac{\partial V}{\partial x} \right] \\
 & \text{VIII} \qquad \qquad \qquad \text{VIII} \\
 & - \overline{u'^2} \left[\frac{1}{(1 + \kappa y)} \frac{\partial U}{\partial x} + \frac{2\kappa V}{(1 + \kappa y)} \right] - \overline{v'^2} \frac{\partial V}{\partial y}
 \end{aligned}$$

IX

$$- \left[\frac{\overline{\tau'_{xx}}}{(1 + \kappa y)} \frac{\partial u'}{\partial x} + \overline{\tau'_{xy}} \frac{\partial u'}{\partial y} + \frac{1}{(1 + \kappa y)} \overline{\tau'_{xy}} \frac{\partial v'}{\partial x} \right.$$

IX

$$\left. + \overline{\tau'_{yy}} \frac{\partial v'}{\partial y} + \frac{\kappa}{(1 + \kappa y)} \overline{v' \tau'_{xx}} - \frac{\kappa}{(1 + \kappa y)} \overline{u' \tau'_{xy}} \right.$$

IX

$$\left. - \frac{\overline{\tau'_{xz}} \frac{\partial w'}{\partial x}}{(1 + \kappa y)} - \overline{\tau'_{yz}} \frac{\partial w'}{\partial y} + \frac{\kappa}{(1 + \kappa y)} \overline{w' \tau'_{yz}} - \overline{\tau'_{zz}} \frac{\partial w'}{\partial z} \right] \quad (\text{C.11})$$

Jones and Launder [29] and Chien [13] have suggested the following assumptions

$$\frac{\overline{u'^3} + \overline{u'v'^2} + \overline{u'w'^2}}{2} + \overline{u'p'} = - \frac{1}{(1 + \kappa y)} \frac{v_t}{\nu \sigma_K} \frac{\partial K}{\partial x} \quad (\text{C.12})$$

$$\frac{\overline{v'u'^2} + \overline{v'^3} + \overline{v'w'^2}}{2} + \overline{v'p'} = - \frac{v_t}{\nu \sigma_K} \frac{\partial K}{\partial y} \quad (\text{C.13})$$

The terms involving the fluctuating shear stress, τ'_{ij} , are generally written as the sum of a term representing viscous diffusion of kinetic energy and a term representing the isotropic dissipation of kinetic energy, Tennekes and Lumley [69].

$$\begin{aligned} \text{III} + \text{V} + \text{VII} + \text{IX} &= \frac{1}{(1 + \kappa y)} \frac{\partial}{\partial x} \left(\frac{1}{(1 + \kappa y)} \frac{\partial K}{\partial x} \right) + \frac{\partial}{\partial y} \left(\frac{\partial K}{\partial y} \right) \\ &+ \frac{\kappa}{(1 + \kappa y)} K - \epsilon - \frac{2K}{y} \quad , \end{aligned} \quad (\text{C.14})$$

where the term $\frac{2K}{y^2}$ is included in order to balance the viscous diffusion of turbulent kinetic energy y at the wall.

Equations for the velocity fluctuations u' , v' and w' can be written in cartesian tensor notation as follows (Tennekes and Lumley [69]).

$$\frac{\partial U_i}{\partial t} + u'_k \frac{\partial U_i}{\partial x_k} + u'_k \frac{\partial U_i}{\partial x_k} + u'_k \frac{\partial u'_i}{\partial x_k} - u'_k \frac{\partial u'_i}{\partial x_k} - u'_k \frac{\partial u'_i}{\partial x_k} = - \frac{\partial p'}{\partial x_i} + \frac{\partial^2 u'_i}{\partial x_k^2} \quad (\text{C.15})$$

An equation for the isotropic dissipation rate $\overline{\frac{\partial u'_i}{\partial x_j} \frac{\partial u'_i}{\partial x_j}}$ can be obtained by differentiating (C.15) with respect to x_n , multiplying the resulting equation by $\frac{\partial u'_i}{\partial x_n}$ and taking the time average

$$\begin{aligned} & \text{I} \qquad \qquad \qquad \text{II} \qquad \qquad \qquad \text{III} \\ & \frac{\partial \epsilon}{\partial t} + U_k \frac{\partial \epsilon}{\partial x_k} = \frac{\partial}{\partial x_k} \left[\frac{\partial \epsilon}{\partial x_k} - \overline{u'_k \epsilon} - \frac{\partial p'}{\partial x_n} \frac{\partial u'_k}{\partial x_n} \right] \\ & \qquad \text{IV} \\ & \qquad - 2 \frac{\partial U_i}{\partial x_k} \left[\frac{\partial u'_i}{\partial x_n} \frac{\partial u'_k}{\partial x_n} + \frac{\partial u'_n}{\partial x_i} \frac{\partial u'_n}{\partial x_k} \right] \\ & \qquad \text{V} \qquad \qquad \qquad \text{VI} \qquad \qquad \qquad \text{VII} \\ & \qquad - 2 \frac{\partial^2 U_i}{\partial x_k \partial x_n} \overline{u'_n \frac{\partial u'_i}{\partial x_n}} - 2 \frac{\partial u'_i}{\partial x_k} \frac{\partial u'_k}{\partial y_n} \frac{\partial u'_i}{\partial x_n} - 2 \left[\frac{\partial^2 u'_i}{\partial x_k \partial x_n} \right]^2 \end{aligned} \quad (\text{C.16})$$

Jones and Launder [29] and Chien [13] have suggested the following closure assumptions,

Term III: Turbulent diffusion by velocity and pressure fluctuations,

$$\text{III} = \frac{\partial}{\partial x_K} \frac{v_t}{\nu \sigma_\epsilon} \frac{\partial \epsilon}{\partial x_K}, \quad (\text{C.17})$$

Terms V and VI: Generation by mean motion,

$$\text{V} + \text{VI} = \frac{C_1 \epsilon P_K}{K}, \quad (\text{C.18})$$

where P_K is the production of turbulent kinetic energy,

Term VII: Dissipation of ϵ ,

$$\text{VII} = C_2 f_0 \frac{\epsilon^2}{K} - \frac{2\epsilon}{y} f_d, \quad (\text{C.19})$$

where the second term is included to balance viscous diffusion of ϵ at the wall. The functions f_0 and f_d are defined in Chapter 3 [see equations (3.63.1) and (3.63.2)].

Term VI: Generation by self stretching action of turbulence. The effect of this term is accounted for in the modeling of term IV (see Reynolds [59]).

The dissipation equation with closure assumptions is then transformed into boundary layer coordinates, equation (3.62).

APPENDIX D

DERIVATION OF STREAMLINE CURVATURE

In this appendix an expression for the curvature of the streamlines in boundary layer coordinates is derived. Let $\vec{b}(x)$ be a position vector describing the streamline $\psi(x, y) = C$ where

$$\psi(x, y) = \int_0^y \bar{U}(y) dy + F a e^{i\alpha x} \quad (D.1)$$

$$\vec{b}(s) = (x(s), y(s)) \quad (D.2)$$

If s is a measure of the arc length, then $\frac{d\vec{b}(s)}{ds}$ is a unit vector and the magnitude of the curvature of the streamlines $\psi(x, y) = C$ is given by

$$\left| \frac{d^2 \vec{b}(s)}{ds^2} \right|.$$

In boundary layer coordinates

$$\frac{d\vec{b}}{ds} = h_x x' \vec{i}_x + h_y y' \vec{i}_y, \quad (D.3)$$

where \vec{i}_x and \vec{i}_y are unit vectors along and perpendicular to the wave surface respectively. The metrics h_x and h_y are defined as

$$h_x = 1 + \kappa y \quad (D.4.1)$$

and

$$h_y = 1 \quad (D.4.2)$$

where κ is the curvature of the wave surface. The primes denote differentiation with respect to s , such that

$$x' = \frac{dx(s)}{ds} \quad (D.5.1)$$

and

$$y' = \frac{dy(s)}{ds} . \quad (D.5.2)$$

Therefore

$$\frac{d^2 \vec{b}}{ds^2} = h'_x x' \vec{i}_x + h_x x'' \vec{i}_x + h_x x' \vec{i}'_x + h'_y y' \vec{i}_y + h_y y'' \vec{i}_y + h_y y' \vec{i}'_y . \quad (D.6)$$

Also

$$\vec{i}'_x = x' \frac{\partial \vec{i}_x}{\partial x} + y' \frac{\partial \vec{i}_x}{\partial y} \quad (D.7.1)$$

$$\vec{i}'_y = x' \frac{\partial \vec{i}_y}{\partial x} + y' \frac{\partial \vec{i}_y}{\partial y} \quad (D.7.2)$$

$$\frac{\partial \vec{i}_x}{\partial x} = -\kappa \vec{i}_y ; \quad \frac{\partial \vec{i}_x}{\partial y} = 0 \quad (D.8.1)$$

$$\frac{\partial \vec{i}_y}{\partial x} = \kappa \vec{i}_x ; \quad \frac{\partial \vec{i}_y}{\partial y} = 0 \quad (D.8.2)$$

Hence (D.7.1) and (D.7.2) become

$$\vec{i}'_x = -\kappa x' \vec{i}_y \quad (D.9.1)$$

$$\vec{i}'_y = \kappa x' \vec{i}_x . \quad (D.9.2)$$

Equation (D.6) can now be written as

$$\frac{d^2 \vec{b}}{ds^2} = (h_x x'' + h'_x x' + h_y y' \kappa) \vec{i}_x + (h_y y'' - h_x \kappa (x')^2) \vec{i}_y \quad (D.10)$$

where to 0(a)

$$h'_x = a\alpha^3 y e^{i\alpha x} x' + a\alpha^2 y e^{i\alpha x} y' \quad (\text{D.11.1})$$

and

$$h'_y = 0 \quad (\text{D.11.2})$$

Since $\psi(x, y) = C$

$$\frac{d\psi}{ds} = \psi_x x' + \psi_y y' = 0. \quad (\text{D.12})$$

On differentiating (D.12) with respect to s and rearranging, x'' and y'' can be written explicitly in terms of x' and y'

$$\psi_x x'' + \psi_y y'' = -\psi_{xx} (x')^2 - \psi_{yy} (y')^2 - 2\psi_{xy} x' y', \quad (\text{D.13.1})$$

$$= G. \quad (\text{D.13.2})$$

Since $\left| \frac{d\vec{b}}{ds} \right| = 1$ and using equation (D.3)

$$(h'_x x')^2 + (y')^2 = 1. \quad (\text{D.14})$$

Now on differentiating (D.14) with respect to s

$$h''_x x' x'' + y' y'' = -h'_x x' \quad (\text{D.15})$$

(D.13.2) and (D.15) can now be solved simultaneously for x'' and y'' .

$$x'' = \frac{Gy' - \psi_y (-h'_x x')}{\psi_x y' - \psi_y h'_x x'} \quad (D.16)$$

$$y'' = \frac{\psi_x h'_x x' - Gx'}{\psi_x y' - \psi_y h'_x y'} \quad (D.17)$$

Now to $O(a)$

$$\psi_x = Fiaae^{iax} \quad (D.18)$$

$$\psi_{xx} = -Fa^2 ae^{iax} \quad (D.19)$$

$$\psi_y = \bar{U} + F' ae^{iax} \quad (D.20)$$

$$\psi_{yy} = \bar{U}' + F'' ae^{iax} \quad (D.21)$$

$$\psi_{xy} = iaF' ae^{iax} \quad (D.22)$$

$$\psi_x / \psi_y = \frac{F}{\bar{U}} iaae^{iax} \quad (D.22)$$

Substituting (D.18)-(D.23) into (D.12) and (D.14) and neglecting terms of $O(a^2)$ x' and y' can be expressed in terms of the stream function, $aF e^{iax}$, as follows:

$$x' = (1 - aa^2 y e^{iax}) \quad (D.24)$$

$$y' = \frac{F}{\bar{U}} iaae^{iax} \quad (D.25)$$

Substituting (D.18)-(D.23) into (D.16) and (D.17) and neglecting terms of $O(a^2)$,

$$x'' = i\alpha y a e^{i\alpha x} \quad (D.26)$$

$$y'' = \frac{F}{U} \alpha^2 a e^{i\alpha x} \quad (D.27)$$

Substituting (D.24)-(D.27) into the expression for $\frac{d^2 \vec{b}}{ds^2}$ and keeping terms of $O(a)$ the following equation for the magnitude of the curvature is obtained

$$\left| \frac{d^2 \vec{b}}{ds^2} \right| = \left| \left(\frac{F - \bar{U}}{\bar{U}} \right) a \alpha^2 e^{i\alpha x} \right| \quad (D.28)$$

In this study the sign of the curvature is defined such that a convex surface has a positive radius of curvature and a concave surface has a negative radius of curvature. With this convention

$$\frac{1}{R_c} = - \frac{(F - \bar{U})}{\bar{U}} a \alpha^2 e^{i\alpha x} \quad (D.29)$$

At the wave surface $F \rightarrow 0$ and therefore

$$\frac{1}{R_c} = a \alpha^2 e^{i\alpha x}, \quad (D.30)$$

which is simply the curvature of the wave surface. For large y $F \rightarrow U$ and here $\frac{1}{R_c} \rightarrow 0$

APPENDIX E

FINITE BOUNDARY LAYER CALCULATION

In this appendix the details of the finite boundary layer calculation are presented. As explained in Chapter 3 a finite boundary layer consists of two layers. In the inner layer the mixing length is given by equation (3.35) and in the outer layer the mixing length is given by equation (3.90). In order to provide for a smooth transition between these two layers the following composite expression is used across the entire boundary layer

$$l_o = \gamma\delta \tanh(\kappa y/\gamma\delta) (1 - \exp(-y\tau^{1/2}/\bar{A})), \quad (\text{E.1})$$

The expression for l_o has the correct asymptotic behavior since

$$\gamma\delta \tanh(\kappa y/\gamma\delta) \rightarrow \kappa y \quad y < \frac{\gamma\delta}{\kappa} \quad (\text{E.2})$$

and

$$\gamma\delta \tanh(\kappa y/\gamma\delta) \rightarrow \gamma\delta \quad y > \frac{\gamma\delta}{\kappa}. \quad (\text{E.3})$$

The wave induced components of l_o , v_t and τ , using equations (E.1), (3.34) and (3.36), are found to be respectively

$$a\hat{l}_o e^{i\alpha x} = a\gamma\delta \tanh(\kappa y/\gamma\delta) \exp(-y/\bar{A}) \left[\frac{\hat{\tau}}{2} - \frac{\hat{A}}{\bar{A}} \right] e^{i\alpha x}, \quad (\text{E.4})$$

$$a\hat{v}_t e^{i\alpha x} = a \left[\frac{\hat{s}_{xy}}{s_{xy}} + \frac{2 \exp(-y/\bar{A})}{[1 - \exp(-y/\bar{A})]} \left[\frac{y}{\bar{A}} \right] \left[\frac{\hat{\tau}}{2} - \frac{\hat{A}}{\bar{A}} \right] \right] \frac{\bar{v}_t}{v} e^{i\alpha x} \quad (\text{E.5})$$

$$\hat{a} e^{i\alpha x} = a \frac{\left[\left(2 \frac{v}{v} + 1 \right) 2 \hat{s}_{xy} - \frac{2 \frac{v}{v} \bar{U}' \exp(-y/\bar{A})}{[1 - \exp(-y/\bar{A})]} \left(\frac{y}{\bar{A}} \right) \frac{\hat{A}}{\bar{A}} \right]}{\left[1 - \frac{\frac{v}{v} \bar{U}' \exp(-y/\bar{A}) y}{[1 - \exp(-y/\bar{A})] \bar{A}} \right]} e^{i\alpha x}. \quad (\text{E.6})$$

For large values of y equations (E.4) - (E.6) are respectively

$$a \hat{a}_0 e^{i\alpha x} = 0 \quad (\text{E.7})$$

$$a \frac{\hat{v}}{v} e^{i\alpha x} = a \gamma^2 \delta^2 2 \hat{s}_{xy} e^{i\alpha x} \quad (\text{E.8})$$

$$\hat{a} e^{i\alpha x} = a 2 \gamma^2 \delta^2 \bar{U}' (2 \hat{s}_{xy}) e^{i\alpha x} \quad (\text{E.9})$$

Calculations were made using the finite boundary layer form of Model D*, equations (E.4)-(E.6). For boundary layer thicknesses $\delta < 500$, it is not possible to sustain a turbulent boundary layer (see Cebeci and Smith [12]). Therefore, this was the smallest value of δ considered.

The calculations show that the effect of δ on the wave induced phase angle and amplitude of the shear stress and pressure is small for any realistic boundary layer thickness, Figures (E.1), (E.2), (E.3) and (E.4) respectively.

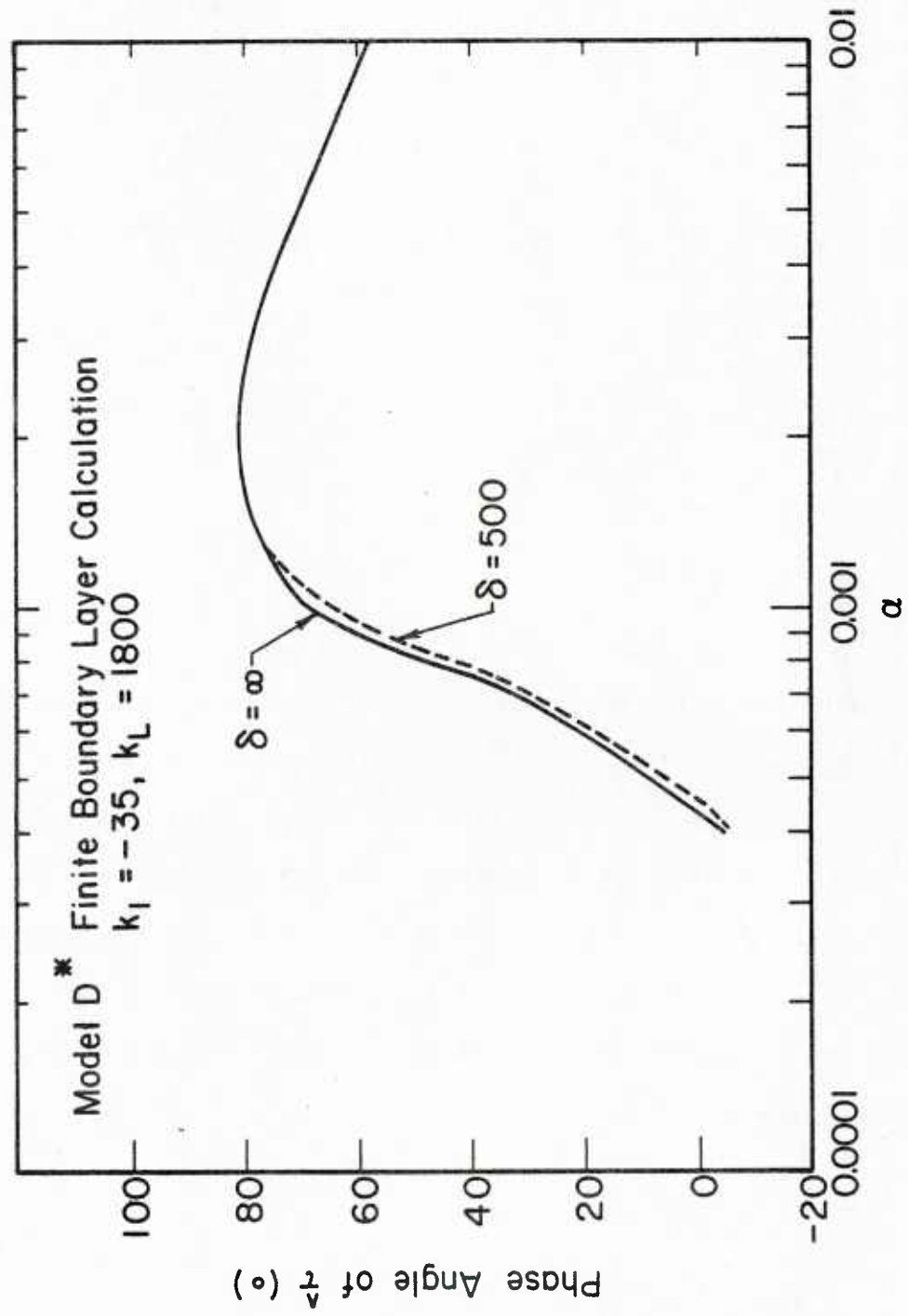


Figure E.1. Effect of Finite Boundary Layer Thickness on $\hat{\tau}(\alpha)$
Phase Angle for Model D* $k_I = -35$ and $k_L = 1800$

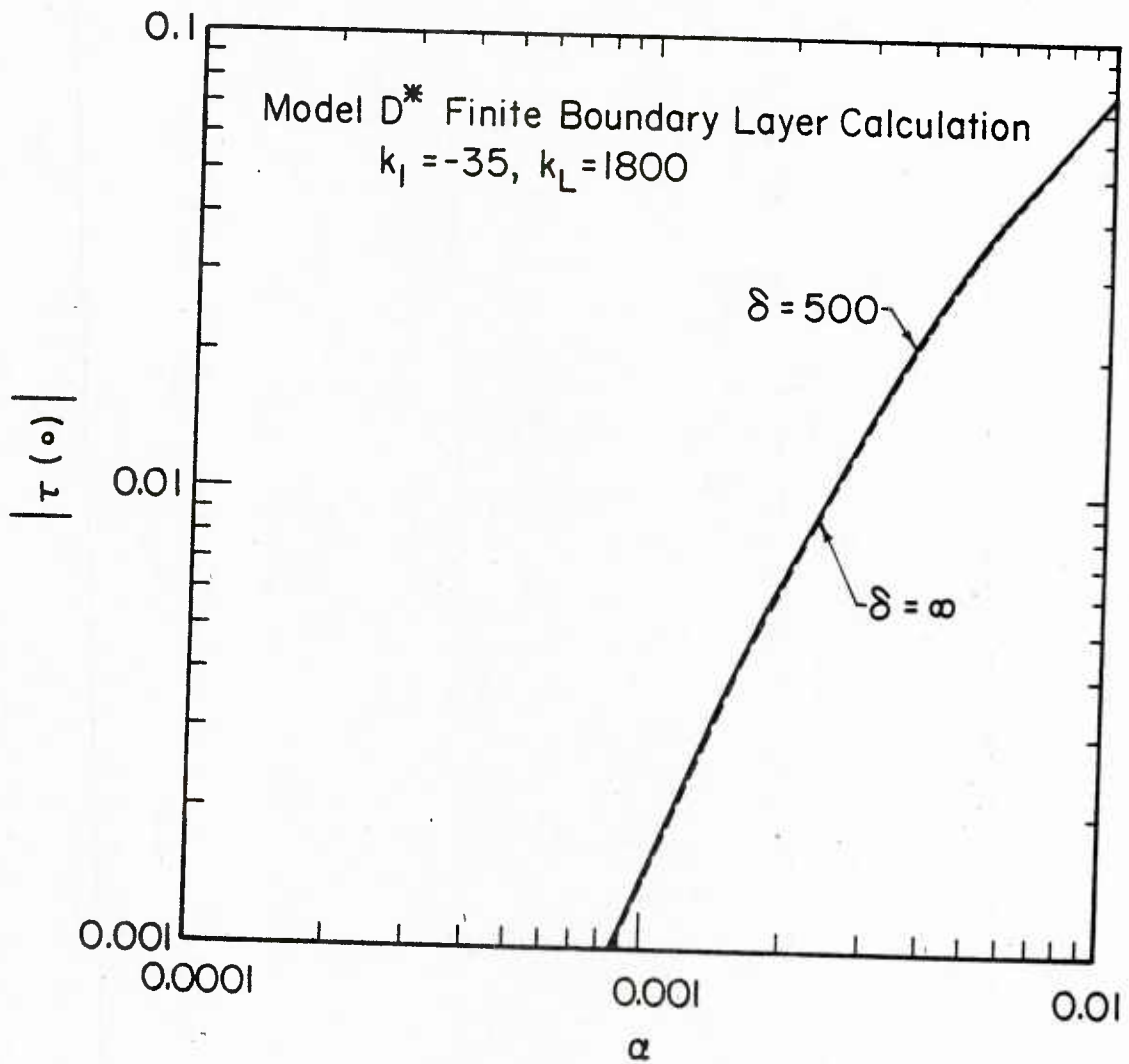


Figure E.2. Effect of Finite Boundary Layer Thickness on $|\hat{\tau}(o)|$ for Model D* $k_1 = -35$ and $k_L = 1800$

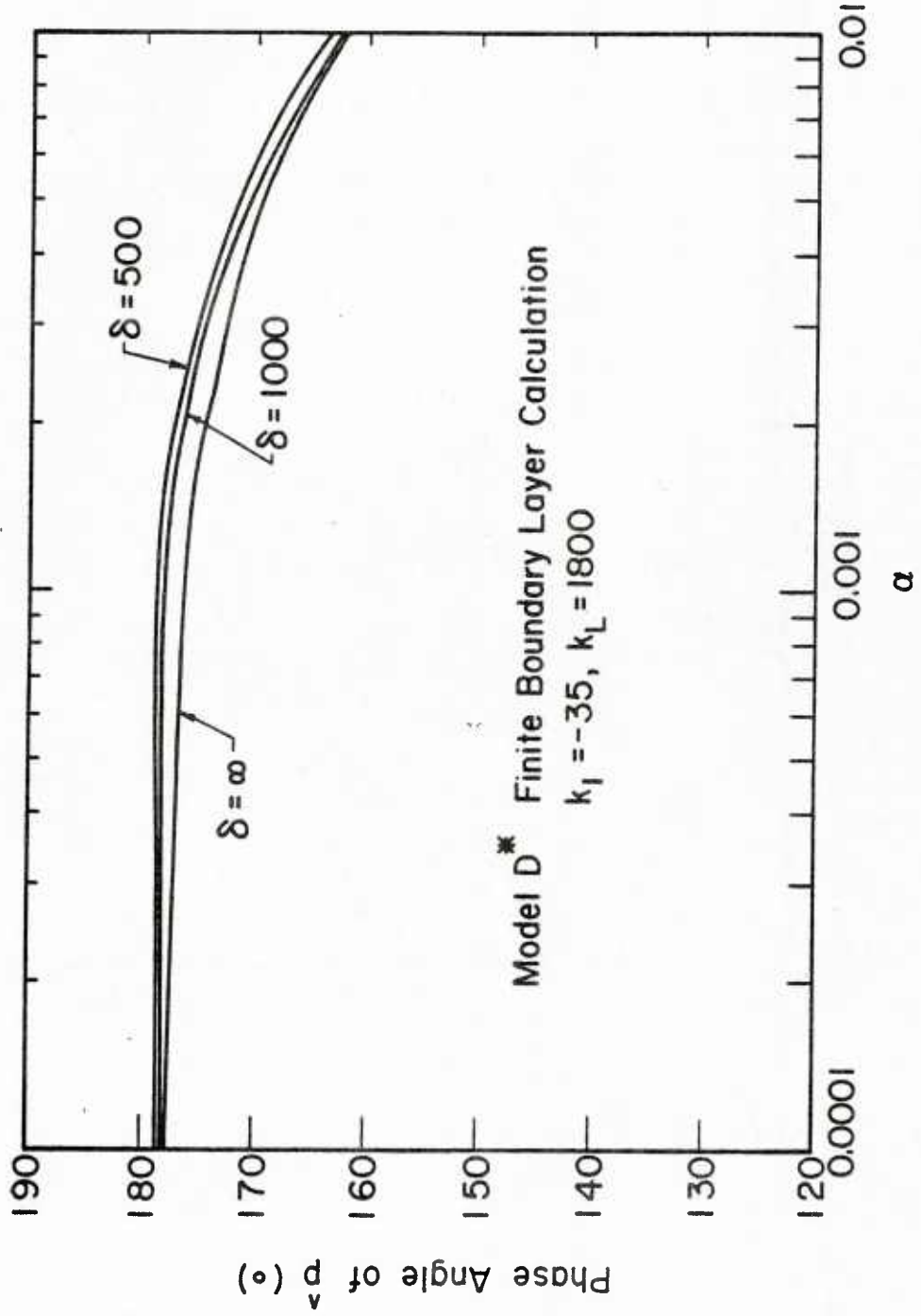


Figure E.3. Effect of Finite Boundary Layer Thickness on $\hat{p}(\alpha)$ Phase Angle for Model D* $k_1 = -35$ and $k_L = 1800$

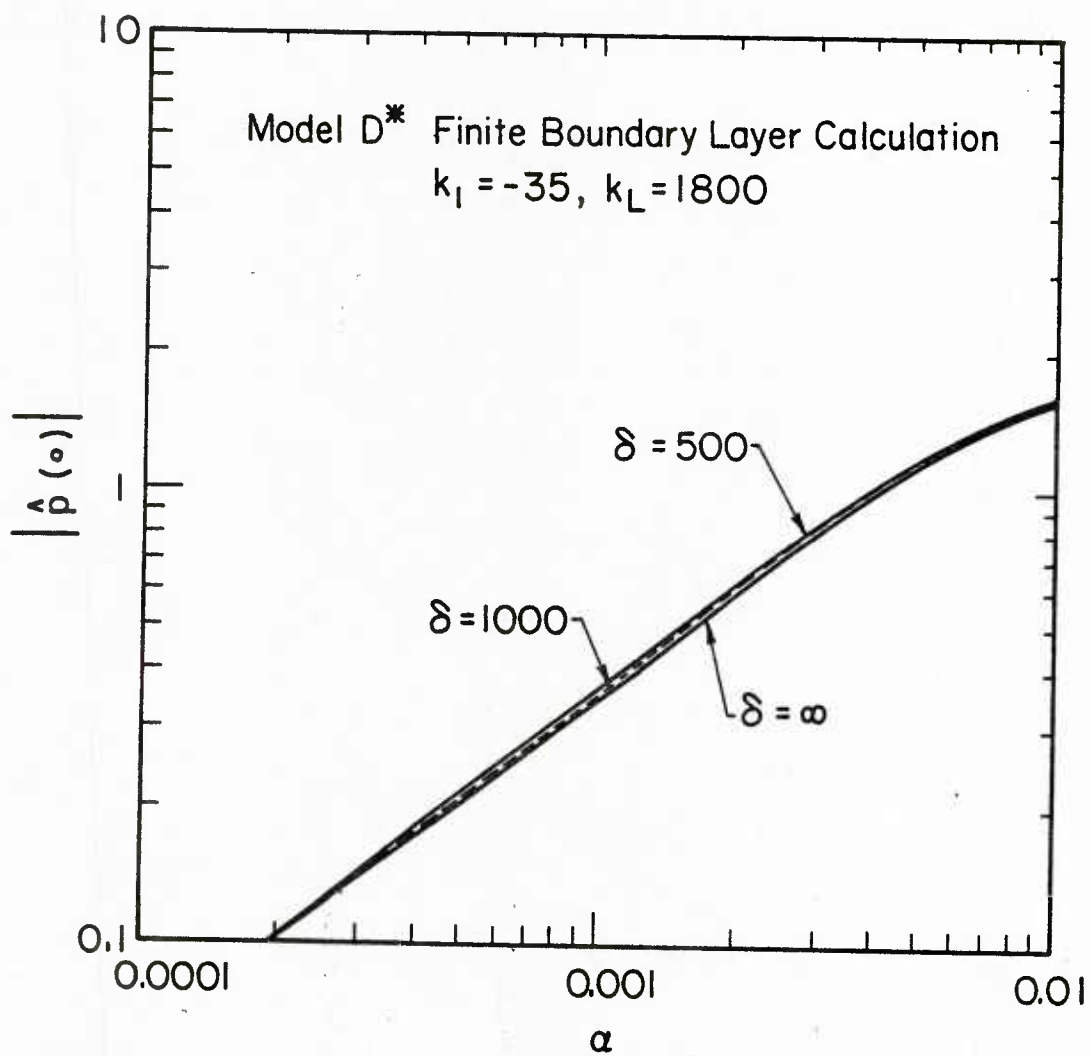


Figure E.4. Effect of Finite Boundary Layer Thickness on $|\hat{p}(o)|$ for Model D* $k_1 = -35$ and $k_L = 1800$

APPENDIX F
TABULATED DATA

This appendix presents in tabulated form the wave profile, average shear stress and fluctuating shear stress distributions reported in this work.

The wave profile data are reported in inches. The shear stress and fluctuating shear stress data are reported in the dimensionless form as discussed in Chapter 4.

Table F.1 Wave Profile Measurements

$\frac{x}{\lambda}$	Wave 9 in. $\times 10^3$	Wave 8 in. $\times 10^3$	Wave 6 in. $\times 10^3$
0.00	29.00	30.00	30.00
0.05	28.00	29.00	28.50
0.10	26.00	28.00	28.00
0.15	24.00	22.50	22.50
0.20	20.00	22.00	22.00
0.25	16.00	17.00	17.00
0.30	12.00	13.00	13.00
0.35	8.00	9.50	9.50
0.40	5.00	6.00	6.00
0.45	1.50	3.00	3.00
0.50	0.00	0.00	0.00
0.55	0.50	0.50	0.50
0.60	2.00	3.00	3.00
0.65	6.00	6.50	6.50
0.70	10.00	10.00	10.50
0.75	14.00	15.00	15.00
0.80	18.50	19.00	19.00
0.85	23.00	23.00	23.50
0.90	26.00	27.00	27.00
0.95	28.00	29.00	29.00
1.00	29.00	30.00	30.00

Table F.2. Summary of Average Shear Stress Measurements

Run No.	$\frac{U_b h/2}{\nu}$	$\frac{2 \Pi \nu}{\lambda u^*}$	θ_τ	$\frac{\tau_w - \bar{\tau}_w}{\bar{\tau}_w}$
1	5970.00	.00871	56.82	0.40
2	5970.00	.00871	56.00	0.40
3	5970.00	.00871	56.70	0.43
4	6680.00	.00787	50.00	0.38
5	6680.00	.00787	54.50	0.43
6	6680.00	.00787	52.00	0.39
7	8450.00	.00621	57.20	0.38
8	8450.00	.00621	59.00	0.42
9	8450.00	.00621	60.00	0.39
10	8950.00	.00607	60.00	0.36
11	8950.00	.00607	63.40	0.39
12	8950.00	.00607	63.12	0.36
13	9650.00	.00566	60.30	0.41
14	9650.00	.00566	63.00	0.41
15	9650.00	.00566	56.50	0.36
16	11400.00	.00489	65.00	0.32
17	11400.00	.00489	65.50	0.35
18	11400.00	.00489	65.70	0.34
19	13000.00	.00435	55.46	0.29
20	13000.00	.00435	61.00	0.34
21	13000.00	.00435	64.14	0.37

Table F.3. Summary of Average Shear Stress Measurements

Run No.	$\frac{U_b h/2}{\nu}$	$\frac{2 \Pi \nu}{\lambda u^*}$	θ_τ	$\frac{\overline{\tau_w} - \overline{\tau_w}}{\overline{\tau_w}}$
22	14600.00	.00389	69.80	0.31
23	14600.00	.00389	71.47	0.34
24	14600.00	.00389	65.00	0.36
25	15700.00	.00367	70.00	0.31
26	15700.00	.00367	76.50	0.33
27	15700.00	.00367	69.00	0.32
28	19800.00	.00297	73.40	0.27
29	19800.00	.00297	76.00	0.27
30	19800.00	.00297	76.00	0.25
31	19800.00	.00297	67.00	0.29
32	19800.00	.00297	76.00	0.29
33	19800.00	.00297	69.00	0.24
34	20600.00	.00287	74.00	0.23
35	20600.00	.00287	66.00	0.29
36	20600.00	.00287	71.00	0.27
37	27950.00	.00218	78.50	0.20
38	27950.00	.00218	80.60	0.21
39	27950.00	.00218	78.30	0.20
40	30620.00	.00201	86.40	0.16
41	30620.00	.00201	84.80	0.18
42	30620.00	.00201	86.00	0.17

Table F.4. Summary of Average Shear Stress Measurements

Run No.	$\frac{U_b h/2}{\nu}$	$\frac{2 \Pi \nu}{\lambda u^*}$	θ_τ	$\frac{\overline{\tau_w} - \overline{\tau_w}}{\overline{\tau_w}}$
43	34700.00	.00181	84.90	0.19
44	34700.00	.00181	77.38	0.20
45	36000.00	.00174	81.65	0.16
46	36000.00	.00174	81.00	0.14
47	36000.00	.00174	80.00	0.16
48	36000.00	.00174	81.20	0.17
49	36000.00	.00174	83.00	0.16
50	58000.00	.00135	78.35	0.13
51	58000.00	.00135	73.27	0.15
52	58000.00	.00135	70.00	0.12
53	58000.00	.00135	73.00	0.11
54	64000.00	.00139	72.00	0.23
55	64000.00	.00139	73.00	0.11
56	71000.00	.000951	76.20	0.11
57	71000.00	.000951	67.00	0.13
58	71000.00	.000951	69.00	0.09
59	73500.00	.000912	71.00	0.10
60	73500.00	.000912	65.70	0.08
61	73500.00	.000912	68.50	0.09
62	73500.00	.000912	68.15	0.08
63	84500.00	.000813	58.65	0.08

Table F.5. Summary of Average Shear Stress Measurements

Run No.	$\frac{U_b h/2}{\nu}$	$\frac{2 \Pi \nu}{\lambda u^*}$	θ_τ	$\frac{\tau_w - \tau_w}{\tau_w}$
64	84500.00	.000813	54.10	0.07
65	84500.00	.000813	57.00	0.06
66	102500.00	.000683	45.00	0.09
67	114500.00	.000618	28.00	0.06
68	122500.00	.000582	17.00	0.06
69	42500.00	.00151	79.00	0.17
70	50000.00	.00129	77.00	0.13

Table F.6. Summary of Fluctuating Shear Stress Measurements

Run No.	$\frac{U_b h/2}{\nu}$	$\frac{2 \Pi \nu}{\lambda u^*}$	θ	$\sqrt{s_x'^2} / \bar{s}_x$
5	6680.00	.00787	77.00	.0523
6	6680.00	.00787	86.00	.0402
7	8450.00	.00621	80.86	.0448
8	8450.00	.00621	91.40	.0497
9	8450.00	.00621	90.00	.0501
13	9650.00	.00566	84.00	.0502
14	9650.00	.00566	91.00	.0560
15	9650.00	.00566	90.00	.0351
20	13000.00	.00435	96.00	.0316
21	13000.00	.00435	92.00	.0416
25	15700.00	.00367	109.00	.0300
26	15700.00	.00367	119.00	.0347
27	15700.00	.00367	108.00	.0267
32	19800.00	.00297	117.00	.0211
35	20600.00	.00287	100.00	.0196
36	20600.00	.00287	119.00	.0264

Table F.7. Average Shear Stress Measurements

$\frac{x}{\lambda}$	$\tau_w/\bar{\tau}_w$					
	Run 1	Run 2	Run 3	Run 4	Run 5	Run 6
0.00	1.31	1.20	1.10	1.17	1.15	1.21
0.05	1.12	1.02	1.21	1.12	1.11	1.14
0.10	0.91	0.99	0.97	1.05	0.96	1.00
0.15	0.82	0.86	0.87	1.04	0.92	0.94
0.20	0.77	0.75	0.78	0.76	0.75	0.78
0.25	0.66	0.70	0.68	0.76	0.71	0.70
0.30	0.62	0.62	0.62	0.61	0.64	0.62
0.35	0.61	0.61	0.61	0.66	0.60	0.65
0.40	0.63	0.63	0.59	0.59	0.55	0.60
0.45	0.65	0.68	0.63	0.65	0.61	0.66
0.50	0.68	0.77	0.72	0.68	0.66	0.72
0.55	0.85	0.82	0.79	0.78	0.78	0.79
0.60	0.99	0.93	1.07	0.94	0.99	0.88
0.65	1.15	1.15	1.12	1.11	1.18	1.19
0.70	1.27	1.28	1.31	1.20	1.31	1.24
0.75	1.35	1.34	1.32	1.33	1.42	1.34
0.80	1.35	1.40	1.45	1.34	1.35	1.39
0.85	1.40	1.42	1.32	1.44	1.42	1.40
0.90	1.37	1.34	1.46	1.35	1.42	1.29
0.95	1.31	1.31	1.23	1.28	1.32	1.27
1.00	1.18	1.22	1.12	1.14	1.15	1.21

Table F.8. Average Shear Stress Measurements

$$\tau_w / \bar{\tau}_w$$

$\frac{x}{\lambda}$	Run 7	Run 8	Run 9	Run 10	Run 11	Run 12
0.00	1.26	1.13	1.10	1.24	1.14	1.14
0.05	1.08	1.08	1.06	1.10	1.05	1.07
0.10	0.95	0.92	0.91	0.97	0.92	0.95
0.15	0.83	0.85	0.85	0.85	0.84	0.85
0.20	0.70	0.73	0.76	0.73	0.74	0.71
0.25	0.69	0.65	0.69	0.70	0.66	0.66
0.30	0.61	0.60	0.69	0.62	0.63	0.64
0.35	0.62	0.64	0.63	0.67	0.63	0.66
0.40	0.65	0.67	0.66	0.65	0.62	0.68
0.45	0.68	0.70	0.69	0.70	0.68	0.72
0.50	0.76	0.74	0.72	0.76	0.77	0.81
0.55	0.89	0.81	0.74	0.91	0.88	0.88
0.60	1.03	1.14	0.98	1.05	1.10	1.01
0.65	1.13	1.09	1.21	1.20	1.20	1.20
0.70	1.25	1.34	1.34	1.25	1.32	1.32
0.75	1.35	1.41	1.39	1.33	1.33	1.34
0.80	1.35	1.30	1.46	1.30	1.39	1.35
0.85	1.26	1.41	1.39	1.33	1.35	1.33
0.90	1.38	1.46	1.34	1.31	1.36	1.27
0.95	1.33	1.15	1.26	1.21	1.23	1.24
1.00	1.21	1.20	1.15	1.13	1.15	1.16

Table F.9. Average Shear Stress Measurements

$$\tau_w / \bar{\tau}_w$$

$\frac{x}{\lambda}$	Run 13	Run 14	Run 15	Run 16	Run 17	Run 18
0.00	1.16	1.12	1.16	1.20	1.18	1.09
0.05	1.06	1.04	1.08	1.08	1.02	1.04
0.10	0.94	0.91	0.97	0.95	1.04	0.93
0.15	0.81	0.81	0.88	0.84	0.83	0.83
0.20	0.71	0.74	0.78	0.72	0.67	0.69
0.25	0.67	0.66	0.68	0.70	0.67	0.68
0.30	0.60	0.64	0.65	0.66	0.67	0.67
0.35	0.63	0.63	0.65	0.71	0.66	0.69
0.40	0.62	0.62	0.68	0.71	0.69	0.72
0.45	0.66	0.63	0.72	0.74	0.71	0.77
0.50	0.73	0.76	0.77	0.83	0.83	0.83
0.55	0.88	0.80	0.81	0.95	0.97	0.96
0.60	1.03	1.07	0.95	1.09	1.02	1.04
0.65	1.17	1.22	1.14	1.18	1.20	1.22
0.70	1.32	1.37	1.29	1.27	1.31	1.30
0.75	1.37	1.39	1.30	1.31	1.33	1.32
0.80	1.37	1.45	1.36	1.25	1.35	1.31
0.85	1.39	1.41	1.34	1.29	1.29	1.31
0.90	1.39	1.34	1.34	1.26	1.31	1.28
0.95	1.30	1.26	1.27	1.15	1.18	1.19
1.00	1.19	1.14	1.16	1.11	1.08	1.13

Table F.10. Average Shear Stress Measurements

$$\tau_w / \bar{\tau}_w$$

$\frac{x}{\lambda}$	Run 19	Run 20	Run 21	Run 22	Run 23	Run 24
0.00	1.22	1.16	1.14	1.18	1.07	1.06
0.05	1.15	1.09	1.06	1.02	1.04	1.02
0.10	1.00	0.96	0.94	0.95	0.90	0.91
0.15	0.91	0.85	0.83	0.79	0.80	0.81
0.20	0.78	0.77	0.75	0.74	0.76	0.70
0.25	0.75	0.69	0.68	0.68	0.66	0.68
0.30	0.71	0.66	0.67	0.67	0.68	0.67
0.35	0.69	0.69	0.67	0.70	0.67	0.72
0.40	0.71	0.71	0.65	0.76	0.69	0.75
0.45	0.79	0.74	0.63	0.81	0.77	0.78
0.50	0.81	0.76	0.75	0.85	0.87	0.85
0.55	0.90	0.85	0.89	0.96	0.94	0.95
0.60	1.03	1.01	1.12	1.13	1.15	1.09
0.65	1.03	1.20	1.19	1.16	1.20	1.23
0.70	1.26	1.30	1.35	1.34	1.33	1.32
0.75	1.26	1.31	1.33	1.25	1.31	1.30
0.80	1.20	1.35	1.38	1.29	1.34	1.31
0.85	1.26	1.30	1.31	1.24	1.26	1.30
0.90	1.22	1.27	1.37	1.25	1.29	1.23
0.95	1.21	1.20	1.21	1.15	1.17	1.18
1.00	1.10	1.14	1.07	1.10	1.10	1.14

Table F.11. Average Shear Stress Measurements

$\frac{x}{\lambda}$	$\tau_w/\bar{\tau}_w$					
	Run 25	Run 26	Run 27	Run 28	Run 29	Run 30
0.00	1.10	1.05	1.09	1.13	1.08	1.10
0.05	1.04	0.98	1.07	1.02	0.95	1.00
0.10	0.92	0.86	0.94	0.91	0.93	0.95
0.15	0.81	0.81	0.84	0.81	0.81	0.86
0.20	0.73	0.74	0.73	0.76	0.77	0.79
0.25	0.69	0.69	0.63	0.71	0.71	0.71
0.30	0.67	0.70	0.68	0.71	0.74	0.72
0.35	0.74	0.72	0.70	0.75	0.76	0.74
0.40	0.74	0.75	0.78	0.81	0.81	0.81
0.45	0.77	0.80	0.81	0.84	0.83	0.87
0.50	0.83	0.86	0.84	0.87	0.93	0.92
0.55	1.00	0.98	0.92	1.01	1.01	0.97
0.60	1.11	1.15	1.09	1.08	1.12	1.17
0.65	1.23	1.23	1.24	1.19	1.16	1.15
0.70	1.25	1.31	1.32	1.21	1.25	1.27
0.75	1.26	1.34	1.34	1.28	1.22	1.30
0.80	1.26	1.31	1.23	1.21	1.29	1.17
0.85	1.26	1.28	1.29	1.27	1.23	1.26
0.90	1.26	1.32	1.16	1.19	1.21	1.08
0.95	1.25	1.18	1.15	1.18	1.13	1.06
1.00	1.07	0.95	1.14	1.04	1.07	1.11

Table F.12. Average Shear Stress Measurements

$\frac{x}{\lambda}$	$\tau_w / \bar{\tau}_w$					
	Run 31	Run 32	Run 33	Run 34	Run 35	Run 36
0.00	1.16	1.05	1.10	1.12	1.12	1.14
0.05	1.02	0.98	1.04	1.06	1.07	1.09
0.10	0.94	0.88	0.93	0.94	0.91	0.93
0.15	0.80	0.83	0.88	0.85	0.88	0.86
0.20	0.77	0.76	0.80	0.76	0.77	0.78
0.25	0.70	0.75	0.74	0.78	0.74	0.66
0.30	0.72	0.75	0.75	0.75	0.71	0.69
0.35	0.74	0.75	0.81	0.80	0.76	0.67
0.40	0.79	0.75	0.80	0.83	0.71	0.86
0.45	0.80	0.85	0.83	0.87	0.75	0.86
0.50	0.85	0.90	0.89	0.87	0.84	0.88
0.55	0.95	0.97	0.95	1.02	0.94	0.94
0.60	1.08	1.13	1.03	1.08	1.12	1.10
0.65	1.14	1.19	1.22	1.15	1.17	1.23
0.70	1.22	1.25	1.14	1.20	1.26	1.25
0.75	1.25	1.31	1.24	1.23	1.28	1.29
0.80	1.25	1.28	1.27	1.18	1.26	1.21
0.85	1.25	1.25	1.25	1.23	1.19	1.20
0.90	1.25	1.29	1.16	1.18	1.25	1.10
0.95	1.21	1.16	1.09	1.11	1.14	1.20
1.00	1.12	0.93	1.08	0.98	1.12	1.07

Table F.13. Average Shear Stress Measurements

$\frac{x}{\lambda}$	$\tau_w / \bar{\tau}_w$					
	Run 37	Run 38	Run 39	Run 40	Run 41	Run 42
0.00	1.08	1.03	1.02	1.05	0.99	0.87
0.05	1.00	0.99	0.98	1.02	1.00	1.03
0.10	0.93	0.89	0.91	0.90	0.88	0.91
0.15	0.84	0.86	0.85	0.86	0.88	0.89
0.20	0.80	0.81	0.80	0.81	0.82	0.81
0.25	0.81	0.79	0.79	0.85	0.84	0.84
0.30	0.80	0.79	0.83	0.80	0.81	0.84
0.35	0.86	0.84	0.87	0.91	0.87	0.92
0.40	0.88	0.87	0.89	0.88	0.90	0.91
0.45	0.89	0.92	0.84	0.93	0.93	0.92
0.50	0.92	0.95	0.94	0.98	0.96	0.98
0.55	1.00	0.99	0.97	1.04	0.99	1.02
0.60	1.10	1.11	1.09	1.08	1.10	1.06
0.65	1.14	1.13	1.16	1.14	1.13	1.12
0.70	1.19	1.21	1.20	1.17	1.18	1.16
0.75	1.19	1.21	1.18	1.19	1.20	1.18
0.80	1.16	1.19	1.20	1.10	1.18	1.15
0.85	1.16	1.16	1.17	1.15	1.18	1.17
0.90	1.16	1.18	1.14	1.10	1.16	1.10
0.95	1.08	1.08	1.10	1.03	1.08	1.08
1.00	1.01	1.00	1.05	1.00	0.92	1.03

Table F.14. Average Shear Stress Measurements

$\frac{x}{\lambda}$	$\tau_w / \bar{\tau}_w$					
	Run 43	Run 44	Run 45	Run 46	Run 47	Run 48
0.00	0.97	1.01	1.07	1.00	1.05	1.02
0.05	0.98	1.01	1.01	1.01	0.97	0.97
0.10	0.86	0.89	0.92	0.91	0.90	0.91
0.15	0.89	0.92	0.87	0.92	0.85	0.90
0.20	0.81	0.87	0.84	0.85	0.83	0.86
0.25	0.87	0.87	0.85	0.89	0.84	0.82
0.30	0.84	0.85	0.82	0.86	0.86	0.86
0.35	0.86	0.92	0.90	0.93	0.90	0.85
0.40	0.87	0.86	0.91	0.90	0.90	0.91
0.45	0.89	0.88	0.93	0.93	0.91	0.96
0.50	0.91	0.96	0.96	0.96	0.95	0.99
0.55	0.99	0.98	1.01	1.00	1.01	0.97
0.60	1.07	0.99	1.08	1.03	1.06	1.06
0.65	1.17	1.18	1.12	1.14	1.12	1.07
0.70	1.14	1.06	1.15	1.13	1.15	1.18
0.75	1.26	1.19	1.18	1.16	1.17	1.19
0.80	1.16	1.16	1.14	1.12	1.14	1.14
0.85	1.21	1.21	1.13	1.16	1.15	1.11
0.90	1.16	1.08	1.11	1.08	1.13	1.19
0.95	1.12	1.06	1.06	1.07	1.09	1.06
1.00	0.97	1.05	0.96	1.00	1.01	0.99

Table F.15. Average Shear Stress Measurements

$$\tau_w / \bar{\tau}_w$$

$\frac{x}{\lambda}$	Run 49	Run 50	Run 51	Run 52	Run 53	Run 54
0.00	1.01	1.06	1.01	1.03	1.02	1.06
0.05	0.96	1.00	1.02	1.03	1.04	1.00
0.10	0.91	0.95	0.92	1.00	0.98	0.99
0.15	0.89	0.87	0.87	0.92	0.92	0.92
0.20	0.86	0.85	0.90	0.87	0.90	0.89
0.25	0.84	0.92	0.92	0.89	0.90	0.95
0.30	0.86	0.82	0.91	0.89	0.91	0.90
0.35	0.90	0.92	0.92	0.93	0.94	0.91
0.40	0.90	0.93	0.82	0.91	0.93	0.94
0.45	0.93	0.92	0.84	0.93	0.93	0.92
0.50	0.95	0.95	0.86	0.94	0.95	0.96
0.55	0.98	0.98	0.91	0.95	0.96	0.97
0.60	1.07	1.04	1.00	0.96	1.03	1.03
0.65	1.07	1.08	1.07	1.11	1.08	1.07
0.70	1.15	1.16	1.19	1.12	1.09	1.12
0.75	1.15	1.15	1.18	1.12	1.12	1.10
0.80	1.16	1.08	1.18	1.12	1.12	1.04
0.85	1.16	1.13	1.19	1.11	1.11	1.10
0.90	1.15	1.11	1.21	1.07	1.05	1.10
0.95	1.09	1.09	1.12	1.05	1.01	1.06
1.00	1.02	0.98	0.99	1.05	1.00	0.98

Table F.16. Average Shear Stress Measurements

$$\tau_w / \overline{\tau_w}$$

$\frac{x}{\lambda}$	Run 55	Run 56	Run 57	Run 58	Run 59	Run 60
0.00	0.99	1.04	1.02	1.07	1.04	1.01
0.05	1.00	0.98	1.04	1.04	1.01	1.02
0.10	0.94	0.93	0.94	1.02	0.97	0.97
0.15	0.95	0.88	0.89	0.94	0.92	0.98
0.20	0.93	0.90	0.98	0.89	0.91	0.97
0.25	0.92	0.94	0.93	0.92	0.90	0.94
0.30	0.90	0.85	0.92	0.90	0.90	0.92
0.35	0.95	0.93	0.84	0.93	0.94	0.96
0.40	0.94	0.95	0.86	0.89	0.94	0.93
0.45	0.92	0.94	0.87	0.94	0.94	0.92
0.50	0.96	0.91	0.84	0.96	0.96	0.93
0.55	0.97	0.97	0.87	0.99	0.96	0.96
0.60	0.98	1.01	0.96	1.05	1.02	0.99
0.65	1.09	1.05	1.05	1.08	1.04	1.07
0.70	1.10	1.16	1.16	1.08	1.10	1.08
0.75	1.11	1.16	1.16	1.07	1.08	1.09
0.80	1.13	1.07	1.21	1.07	1.10	1.11
0.85	1.09	1.12	1.16	1.08	1.10	1.07
0.90	1.06	1.11	1.19	1.03	1.11	1.05
0.95	1.04	1.09	1.09	1.01	1.07	1.03
1.00	1.04	1.00	1.02	1.02	0.99	1.02

Table F.17. Average Shear Stress Measurements

$$\tau_w / \bar{\tau}_w$$

$\frac{x}{\lambda}$	Run 61	Run 62	Run 63	Run 64	Run 65	Run 66
0.00	1.06	1.00	1.03	0.97	0.98	1.06
0.05	1.01	1.01	1.03	1.01	1.03	1.01
0.10	0.99	0.97	0.98	0.93	0.99	1.03
0.15	0.91	0.96	0.96	0.93	1.00	0.97
0.20	0.92	0.96	0.91	0.91	0.97	0.95
0.25	0.95	0.95	0.99	0.97	0.96	0.94
0.30	0.90	0.92	0.89	0.92	0.94	0.91
0.35	0.93	0.96	0.95	0.94	0.98	0.93
0.40	0.95	0.93	0.91	0.96	0.93	0.95
0.45	0.93	0.92	0.95	0.91	0.92	0.91
0.50	0.95	0.94	0.96	0.92	0.93	0.92
0.55	0.96	0.96	0.96	0.97	0.93	0.94
0.60	1.02	0.97	0.97	1.05	0.93	0.99
0.65	1.06	1.07	1.04	1.09	1.05	1.01
0.70	1.10	1.09	1.07	1.12	1.04	1.07
0.75	1.08	1.09	1.09	1.12	1.09	1.04
0.80	1.03	1.12	1.00	1.15	1.09	1.08
0.85	1.09	1.07	1.12	1.15	1.10	1.10
0.90	1.10	1.06	1.09	1.09	1.04	1.11
0.95	1.08	1.05	1.11	0.97	1.04	1.10
1.00	0.99	1.00	0.98	0.93	1.06	1.05

Table F.18. Average Shear Stress Measurements

$$\tau_w / \bar{\tau}_w$$

$\frac{x}{\lambda}$	Run 67	Run 68
0.00	1.03	1.04
0.05	1.08	1.09
0.10	1.06	1.06
0.15	1.02	1.03
0.20	0.97	0.97
0.25	1.01	1.00
0.30	0.93	0.93
0.35	0.96	0.97
0.40	0.94	0.94
0.45	0.96	0.92
0.50	0.94	0.94
0.55	0.93	0.93
0.60	0.95	0.96
0.65	0.98	1.01
0.70	1.03	1.03
0.75	1.05	1.03
0.80	1.02	1.03
0.85	1.03	1.03
0.90	1.02	1.02
0.95	1.04	1.03
1.00	1.02	1.01

Table F.19. Fluctuating Shear Stress Measurements

$$\sqrt{s_x'^2 / \bar{S}_x}$$

$\frac{x}{\lambda}$	Run 5	Run 6	Run 7	Run 8	Run 9	Run 15
0.00	0.29	0.31	0.32	0.28	0.28	0.30
0.05	0.29	0.31	0.30	0.30	0.29	0.30
0.10	0.27	0.29	0.27	0.26	0.26	0.29
0.15	0.30	0.30	0.27	0.27	0.26	0.28
0.20	0.25	0.27	0.24	0.24	0.25	0.27
0.25	0.27	0.26	0.26	0.25	0.25	0.26
0.30	0.26	0.26	0.24	0.24	0.28	0.26
0.35	0.25	0.28	0.26	0.26	0.27	0.28
0.40	0.24	0.26	0.27	0.28	0.27	0.28
0.45	0.27	0.29	0.29	0.31	0.29	0.30
0.50	0.28	0.31	0.29	0.28	0.29	0.31
0.55	0.28	0.31	0.31	0.29	0.28	0.31
0.60	0.32	0.32	0.32	0.34	0.33	0.31
0.65	0.36	0.38	0.33	0.34	0.36	0.33
0.70	0.37	0.35	0.34	0.36	0.36	0.34
0.75	0.37	0.34	0.36	0.36	0.36	0.34
0.80	0.33	0.34	0.34	0.31	0.36	0.34
0.85	0.35	0.34	0.30	0.34	0.34	0.32
0.90	0.34	0.31	0.34	0.36	0.33	0.32
0.95	0.33	0.52	0.34	0.28	0.32	0.32
1.00	0.30	0.31	0.31	0.31	0.30	0.29

Table F.20. Fluctuating Shear Stress Measurements

$$\sqrt{\frac{s_x^2}{\bar{s}_x}}$$

$\frac{x}{\lambda}$	Run 13	Run 16	Run 20	Run 21	Run 25	Run 26
0.00	0.30	0.29	0.29	0.28	0.27	0.25
0.05	0.29	0.28	0.29	0.29	0.29	0.25
0.10	0.28	0.27	0.28	0.27	0.26	0.25
0.15	0.26	0.25	0.27	0.27	0.25	0.25
0.20	0.25	0.26	0.27	0.26	0.24	0.24
0.25	0.25	0.24	0.26	0.25	0.25	0.24
0.30	0.25	0.25	0.26	0.26	0.25	0.25
0.35	0.27	0.26	0.27	0.27	0.28	0.28
0.40	0.26	0.27	0.27	0.26	0.28	0.28
0.45	0.28	0.26	0.28	0.26	0.29	0.30
0.50	0.28	0.31	0.29	0.28	0.29	0.28
0.55	0.31	0.27	0.31	0.29	0.30	0.30
0.60	0.33	0.34	0.32	0.34	0.32	0.32
0.65	0.35	0.35	0.33	0.33	0.31	0.31
0.70	0.36	0.38	0.33	0.35	0.32	0.31
0.75	0.35	0.36	0.32	0.34	0.31	0.32
0.80	0.35	0.35	0.33	0.33	0.29	0.30
0.85	0.35	0.34	0.31	0.32	0.29	0.29
0.90	0.34	0.33	0.30	0.33	0.30	0.30
0.95	0.33	0.31	0.30	0.30	0.30	0.29
1.00	0.31	0.29	0.29	0.27	0.26	0.24

Table F.21. Fluctuating Shear Stress Measurements

$$\sqrt{s_x'^2} / \bar{S}_x$$

$\frac{x}{\lambda}$	Run 27	Run 32	Run 35	Run 36
0.00	0.28	0.25	0.26	0.26
0.05	0.28	0.25	0.26	0.26
0.10	0.27	0.23	0.24	0.25
0.15	0.25	0.24	0.25	0.25
0.20	0.25	0.24	0.24	0.25
0.25	0.23	0.25	0.24	0.21
0.30	0.25	0.26	0.24	0.24
0.35	0.26	0.25	0.27	0.24
0.40	0.28	0.26	0.26	0.28
0.45	0.29	0.29	0.26	0.27
0.50	0.29	0.27	0.25	0.29
0.55	0.30	0.26	0.27	0.28
0.60	0.30	0.28	0.29	0.30
0.65	0.32	0.28	0.27	0.30
0.70	0.32	0.28	0.29	0.29
0.75	0.31	0.29	0.30	0.29
0.80	0.27	0.28	0.28	0.27
0.85	0.29	0.27	0.26	0.26
0.90	0.27	0.28	0.28	0.25
0.95	0.26	0.26	0.26	0.27
1.00	0.28	0.21	0.26	0.25

APPENDIX G

ELECTROCHEMICAL MEASUREMENTS

The physical and chemical properties of the electrochemical solution are given in this appendix.

Physical Properties

All the electrochemical measurements required the determination of the kinematic viscosity, density, concentration of active specie and mass diffusivity. The viscosity was measured after each run with a No. 50 Ostwald viscometer. The density was determined by hydrometer immersion. The concentration was obtained using standard titration for potassium iodide. The diffusion coefficient for the iodine was calculated from the following correlation (see Zilker [77]),

$$\log_{10} D = -1.07291 \log_{10} \nu - 7.15278 \quad (\text{G.1})$$

where ν is the kinematic viscosity. Table G.1 summarizes the physical and chemical properties of the electrolyte.

Table G.1.
Physical and Chemical Properties of Electrolyte

Property	
Viscosity (P)	0.00858
Density (g/cm ³)	1.023
Kinematic Viscosity (cm ² /s)	0.00839
Mass Diffusivity (cm ² /sec)	1.188×10^{-5}
Schmidt Number	707
KI Concentration (moles/liter)	0.103 - .2
I ₂ (I ₃ ⁻) Concentration (moles/liter)	0.00131 - 0.00146
Temperature (C°)	26

APPENDIX H
ANALYSIS OF RAW DATA

In this appendix the method used in analyzing the raw data is outlined. All electrodes are assumed to have the same area. The instantaneous current measured at the j th electrode is

$$I_j = \frac{E_j}{R_f} \quad (\text{H.1})$$

where $E_j = (V_o - V_{app})$. Here V_o is the instantaneous measured voltage and V_{app} is the applied voltage. The term R_f is the feedback resistance. The average current at the j th electrode is given by

$$\bar{I}_j = \frac{\sum_{i=1}^n E_j^i}{R_f n} \quad (\text{H.2})$$

where E_j^i is the i th voltage sampled by the A/D converter and n is the total number of samples gathered. The average shear stress at the j th electrode is obtained from equation (4.5)

$$(\bar{\tau}_{w_d})_j = C^3 \left(\frac{\sum_{i=1}^n E_j^i}{n R_f} \right)^3 \quad (\text{H.3})$$

$$= C^3 \frac{(\bar{E}_j)^3}{R_f^3} \quad (\text{H.3})$$

where $\bar{E}_j = \sum_{i=1}^n E_j^i / n$.

The wave averaged shear stress is obtained by summing $(\bar{\tau}_w)_j$ over all j ,

$$\langle \tau_{w_d} \rangle = \frac{\sum_{j=1}^m (\bar{\tau}_{w_d})_j}{m} \quad (\text{H.5})$$

where m is number of electrodes. The dimensionless quantity,

$(\tau_{w_j} / \bar{\tau}_w) = (\bar{\tau}_{w_d})_j / \langle \bar{\tau}_{w_d} \rangle$, is then

$$\left(\frac{\tau_w}{\bar{\tau}_w} \right)_j = \frac{(\bar{E}_j)^3}{\left[\sum_{j=1}^m (\bar{E}_j)^3 / m \right]} \quad (\text{H.6})$$

$$= \frac{(\bar{E}_j)^3}{(\bar{E}^3)_w} \quad (\text{H.7})$$

where

$$(\bar{E}^3)_w = \frac{\sum_{j=1}^m (\bar{E}_j)^3}{m} \quad (\text{H.8})$$

The local intensity of the fluctuating shear stress is found using equation (4.6) to be

$$\left(\frac{\tau'_x}{\tau_w} \right)_j = 3 \frac{(\bar{E}_j - \bar{E}_j)}{\bar{E}_j} \quad (\text{H.9})$$

The local root mean square value of the fluctuating shear stress is

$$\left(\frac{\sqrt{\tau_x'^2}}{\tau_w} \right)_j = 3 \frac{(\overline{E_j^2} - \overline{E_j}^2)^{1/2}}{\overline{E_j}} \quad (\text{H.10})$$

and the absolute root mean square value of the fluctuating shear stress is obtained by multiplying equation (H.9) by equation (H.6)

$$\begin{aligned} \left(\frac{\sqrt{\tau_x'^2}}{\tau_w} \right) &= 3 \frac{(\overline{E_j^2} - \overline{E_j}^2)^{1/2}}{(\overline{E_j})} \frac{\overline{E_j^3}}{(\overline{E^3})_w}, \\ &= \frac{\sqrt{s_x'^2}}{\overline{S_x}} \end{aligned} \quad (\text{H.11})$$

where $s_x' = \partial u' / \partial y$ and $\overline{S_x} = \partial \overline{U} / \partial y$ are respectively, the dimensionless fluctuating and wave averaged velocity gradient evaluated at the wall.

APPENDIX I

LEAST SQUARES ANALYSIS

The surface shear stress data are fitted with a Fourier series.

The computer program Data is set up to calculate the first four harmonics if necessary, however, only one harmonic was used in fitting the data. The Fourier coefficients are obtained by performing a least squares analysis as follows:

let $f(x)$ be a function that has a period $2\pi/\alpha$. Then the Fourier series representation of $f(x)$ is

$$f(x_j) = \bar{f} + \sum_1^N (a_n \cos(\alpha n x_j) + b_n \sin(\alpha n x_j)) \quad (\text{I.1})$$

$$\bar{f} = \frac{\sum_1^J f(x_j)}{J} \quad (\text{I.2})$$

where x_j is the location of j th electrode. The spacing between the electrodes is assumed constant in the analysis that follows.

The error function E is defined as

$$E = \sum_{j=1}^J e_j \quad (\text{I.3})$$

where

$$e_j = [f(x_j) - \bar{f} - \sum_1^N (a_n \cos(\alpha n x_j) + b_n \sin(\alpha n x_j))]^2 \quad (\text{I.4})$$

The constants a_n and b_n are found by minimizing the error function with respect to a_n and b_n

$$\frac{\partial E}{\partial a_n} = 0, \quad \frac{\partial E}{\partial b_n} = 0 \quad n = 1, 2, \dots, N. \quad (\text{I.5})$$

Substituting equation (I.4) into (I.3) and using equation (I.5) yields

$$\sum_1^J (f(x_j) - \bar{f}) \cos(\alpha x_j) = \sum_1^J \sum_1^N (a_n \cos(\alpha x_j) + b_n \sin(\alpha x_j)) \cos(\alpha x_j) \quad (\text{I.6})$$

$$\sum_1^J (f(x_j) - \bar{f}) \sin(\alpha x_j) = \sum_1^J \sum_1^N (a_n \cos(\alpha x_j) + b_n \sin(\alpha x_j)) \sin(\alpha x_j). \quad (\text{I.7})$$

Equations (I.6) and (I.7) represent $2N$ equations in $2N$ unknowns, a_n and b_n ($n = 1, \dots, N$). The function $f(x)$, can be written as follows

$$f(x) = \bar{f} + \sum_1^N (a_n^2 + b_n^2)^{1/2} \cos(\alpha x + \theta_n) \quad (\text{I.8})$$

where

$$\theta_n = \tan^{-1} (-b_n/a_n) \quad (\text{I.9})$$

APPENDIX J

CORRECTION OF INTENSITY DATA

In this appendix the measurements of $\sqrt{s_x'^2 / \bar{S}_x}$ are corrected for both frequency and spatial averaging as suggested by Mitchell and Hanratty [47]. The results are summarized in Tables J.1 and J.2, where L^+ is the effective electrode length, $W_m = 2\pi (0.009)$ is the median frequency of S_x in pipe turbulence, Sc is the Schmidt number and Λ is the circumferential scale for mass transfer fluctuations. Mitchell and Hanratty have suggested that for pipe turbulence $\Lambda \approx 12$. They have presented curves of $1/A^2$ vs. $(L^+ W_m^{1/2} Sc^{1/2})$ and $\sqrt{k'^2} / \sqrt{k_m'^2}$ vs. $(1/\Lambda)$ where $(1/A^2)^{1/2}$ is the correction factor which accounts for frequency averaging and $\sqrt{k'^2} / \sqrt{k_m'^2}$ is the correction factor which accounts for spatial averaging. Here $\overline{k'^2}$ is the corrected intensity of the mass transfer fluctuation and $k_m'^2$ is the measured intensity of the mass transfer fluctuations.

It should be noted that the values of $\sqrt{s_x'^2 / \bar{S}_x}$ listed in this appendix refer to the wave induced components of the fluctuating shear stress.

Table J.1.

Correction of Fluctuating Shear Stress Measurements

α	L^+	$L^+ W_m^{+3/2} Sc^{1/2}$	L/Λ	$\frac{\sqrt{k'^2}}{\sqrt{k_m'^2}}$	$\frac{1}{A^2}$
0.00787	6.442	3.355	.5369	-	1.09
0.00621	8.162	4.25	.6802	-	1.22
0.00565	8.974	4.674	.748	-	1.26
0.0045	11.267	5.868	.939	1.07	1.29
0.00367	13.816	7.915	1.151	1.11	1.40
0.00297	17.07	8.9	1.422	1.15	1.48
0.00287	17.66	9.201	1.472	1.155	1.5

Table J.2

Correction of Fluctuating Shear Stress Measurements

α	$\frac{\sqrt{s_x'^2}}{\bar{s}_x}$	$\frac{\sqrt{s_x'^2}}{\bar{s}_x}$	$\frac{\sqrt{k'^2}}{\sqrt{k_m'^2}}$	$\frac{\sqrt{s_x'^2}}{\bar{s}_x} \frac{1}{A}$	$\frac{\sqrt{s_x'^2}}{\bar{s}_x}$	$\frac{\sqrt{k'^2}}{\sqrt{k_m'^2}} \frac{1}{A}$
0.00787	0.0462	0.0462	0.0462	0.0483	0.048	0.048
0.00621	0.0482	0.0482	0.0482	0.053	0.053	0.053
0.00565	0.0465	0.0465	0.0465	0.0528	0.0528	0.0528
0.00435	0.0366	0.0366	0.0392	0.0416	0.0445	0.0445
0.00367	0.0305	0.0305	0.0338	0.0374	0.0397	0.0397
0.00297	0.0211	0.0211	0.0243	0.025	0.0295	0.0295
0.00287	0.0230	0.0230	0.0265	0.0280	0.0325	0.0325

APPENDIX K

NUMERICAL FORMULATION OF WAVE INDUCED EQUATIONS

In this appendix equations (3.13)-(3.17) are set up in a suitable form for numerical solution using the techniques described in Chapter 5.

The differential equation describing the wave induced flow using the zero equation turbulence models is a fourth order equation. Since the dependent variable, the stream function, F , is a complex quantity the differential equation is solved as an eighth order system. This is achieved by splitting F into its real and imaginary parts and introducing the following variables,

$$\begin{aligned}
 \phi_1 &= F_R & \phi_5 &= F_I \\
 \phi_2 &= F'_R & \phi_6 &= F'_I \\
 \phi_3 &= F''_R & \phi_7 &= F''_I \\
 \phi_4 &= F'''_R & \phi_8 &= F'''_I
 \end{aligned} \tag{K.1}$$

Equation (3.13) can be written as follows:

$$F'''' = a_0(y)F + a_1(y)F' + a_2(y)F'' + a_3(y)F''' + g(y) \tag{K.2}$$

where $a_0(y)$, $a_1(y)$, $a_2(y)$ and $a_3(y)$ are the complex coefficients of the derivatives of the stream function and $g(y)$ is the complex non-homogeneous term. Equation (K.2), can be expressed in real and imaginary form as follows.

$$F'''' = F_R'''' + iF_I'''' \quad (K.3.1)$$

$$= \left[a_{0R} F_R - a_{0I} F_I + a_{1R} F_R' - a_{1I} F_I' + a_{2R} F_R'' - a_{2I} F_I'' + a_{3R} F_R''' - a_{3I} F_I''' \right] \\ + i \left[a_{0I} F_R + a_{0R} F_I + a_{1I} F_R' + a_{1R} F_I' + a_{2I} F_R'' + a_{2R} F_I'' + a_{3I} F_R''' + a_{3R} F_I''' \right] \\ + g_R + i g_I \quad (K.3.2)$$

where

$$a_0 = a_{0R} + i a_{0I} \quad (K.4.1)$$

$$a_1 = a_{1R} + i a_{1I} \quad (K.4.2)$$

$$a_2 = a_{2R} + i a_{2I} \quad (K.4.3)$$

$$a_3 = a_{3R} + i a_{3I} \quad (K.4.4)$$

$$g = g_R + i g_I \quad (K.4.5)$$

Equation (K.3.2) can be written in a form similar to equation (5.61),

$$\frac{d}{dy} \begin{bmatrix} \phi_1 \\ \phi_2 \\ \phi_3 \\ \phi_4 \\ \phi_5 \\ \phi_6 \\ \phi_7 \\ \phi_8 \end{bmatrix} = \begin{bmatrix} 0 & 1 & 0 & 0 & 0 & 0 & 0 & 0 \\ 0 & 0 & 1 & 0 & 0 & 0 & 0 & 0 \\ 0 & 0 & 0 & 1 & 0 & 0 & 0 & 0 \\ a_{0R} & a_{1R} & a_{2R} & a_{3R} & -a_{0I} & -a_{1I} & -a_{2I} & -a_{3I} \\ 0 & 0 & 0 & 0 & 0 & 1 & 0 & 0 \\ 0 & 0 & 0 & 0 & 0 & 0 & 1 & 0 \\ 0 & 0 & 0 & 0 & 0 & 0 & 0 & 1 \\ a_{0I} & a_{1I} & a_{2I} & a_{3I} & a_{0R} & a_{1R} & a_{2R} & a_{3R} \end{bmatrix} \begin{bmatrix} \phi_1 \\ \phi_2 \\ \phi_3 \\ \phi_4 \\ \phi_5 \\ \phi_6 \\ \phi_7 \\ \phi_8 \end{bmatrix} + \begin{bmatrix} 0 \\ 0 \\ 0 \\ g_R \\ 0 \\ 0 \\ 0 \\ g_I \end{bmatrix} \quad (K.5)$$

The boundary conditions are

$$\begin{aligned} F = 0 \quad F' = 0 \quad \text{at } y = 0 \\ F = U \quad F' = \bar{U}' \quad \text{at large } y. \end{aligned} \tag{K.6}$$

In matrix notation these conditions are: at $y = 0$,

$$\begin{bmatrix} 1 & 0 & 0 & 0 & 0 & 0 & 0 & 0 \\ 0 & 1 & 0 & 0 & 0 & 0 & 0 & 0 \\ 0 & 0 & 0 & 0 & 1 & 0 & 0 & 0 \\ 0 & 0 & 0 & 0 & 0 & 1 & 0 & 0 \end{bmatrix} \begin{bmatrix} \phi_1 \\ \phi_2 \\ \phi_3 \\ \phi_4 \\ \phi_5 \\ \phi_6 \\ \phi_7 \\ \phi_8 \end{bmatrix} = \begin{bmatrix} 0 \\ 0 \\ 0 \\ 0 \end{bmatrix} \tag{K.7}$$

and at large y ,

$$\begin{bmatrix} 1 & 0 & 0 & 0 & 0 & 0 & 0 & 0 \\ 0 & 1 & 0 & 0 & 0 & 0 & 0 & 0 \\ 0 & 0 & 0 & 0 & 1 & 0 & 0 & 0 \\ 0 & 0 & 0 & 0 & 0 & 1 & 0 & 0 \end{bmatrix} \begin{bmatrix} \phi_1 \\ \phi_2 \\ \phi_3 \\ \phi_4 \\ \phi_5 \\ \phi_6 \\ \phi_7 \\ \phi_8 \end{bmatrix} = \begin{bmatrix} \bar{U} \\ \bar{U}' \\ 0 \\ 0 \end{bmatrix} \tag{K.8}$$

Since the number of boundary conditions at the wave surface and at large y are both equal to two, there is no preferred direction of integration. In the computations carried out in this thesis, the direction of integration is toward the wave surface. Hence $y = 0 = b$ and $y \rightarrow y_\infty = a$.

The particular solution F_p is generated by solving the system of equations (K.5) subject to the boundary condition

$$F_p = \begin{bmatrix} \bar{U} \\ \bar{U}' \\ 0 \\ 0 \\ 0 \\ 0 \\ 0 \\ 0 \end{bmatrix} \quad \text{at large } y. \quad (\text{K.9})$$

The required solution to equation (K.3.2) could be obtained by generating a particular solution satisfying equation (K.9) and eight independent homogeneous solutions. The required solution would then be obtained by forming a linear combination of the eight homogeneous solutions and the particular solution. However by suitable choice of the homogeneous solutions at y_∞ it is necessary to generate only four homogeneous solutions. This is demonstrated below.

Let the eight homogeneous solutions at y_∞ satisfy

$$\begin{array}{cccc}
 F_{H_1}(y_\infty) = \begin{bmatrix} 0 \\ 0 \\ 1 \\ 0 \\ 0 \\ 0 \\ 0 \\ 0 \end{bmatrix} & F_{H_2}(y_\infty) = \begin{bmatrix} 0 \\ 0 \\ 0 \\ 1 \\ 0 \\ 0 \\ 0 \\ 0 \end{bmatrix} & F_{H_3}(y_\infty) = \begin{bmatrix} 0 \\ 0 \\ 0 \\ 0 \\ 0 \\ 0 \\ 1 \\ 0 \end{bmatrix} & F_{H_4}(y_\infty) = \begin{bmatrix} 0 \\ 0 \\ 0 \\ 0 \\ 0 \\ 0 \\ 0 \\ 1 \end{bmatrix} \\
 \\
 F_{H_5}(y_\infty) = \begin{bmatrix} 1 \\ 0 \\ 0 \\ 0 \\ 0 \\ 0 \\ 0 \\ 0 \end{bmatrix} & F_{H_6}(y_\infty) = \begin{bmatrix} 0 \\ 1 \\ 0 \\ 0 \\ 0 \\ 0 \\ 0 \\ 0 \end{bmatrix} & F_{H_7}(y_\infty) = \begin{bmatrix} 0 \\ 0 \\ 0 \\ 0 \\ 1 \\ 1 \\ 0 \\ 0 \end{bmatrix} & F_{H_8}(y_\infty) = \begin{bmatrix} 0 \\ 0 \\ 0 \\ 0 \\ 0 \\ 1 \\ 0 \\ 0 \end{bmatrix}
 \end{array} \quad . \quad (K.10)$$

The required solution is,

$$\begin{aligned}
 F = F_p + c_1 F_{H_1} + c_2 F_{H_2} + c_3 F_{H_3} + c_4 F_{H_4} + c_5 F_{H_5} + c_6 F_{H_6} \\
 + c_7 F_{H_7} + c_8 F_{H_8} . \quad (K.11)
 \end{aligned}$$

The above combination must satisfy the boundary conditions at y_∞ , equation (K.8), hence using these conditions,

$$\begin{bmatrix} 0 & 0 & 0 & 0 & 1 & 0 & 0 & 0 \\ 0 & 0 & 0 & 0 & 0 & 1 & 0 & 0 \\ 0 & 0 & 0 & 0 & 0 & 0 & 1 & 0 \\ 0 & 0 & 0 & 0 & 0 & 0 & 0 & 1 \end{bmatrix} \begin{bmatrix} c_1 \\ c_2 \\ c_3 \\ c_4 \\ c_5 \\ c_6 \\ c_7 \\ c_8 \end{bmatrix} + \begin{bmatrix} U \\ \bar{U}' \\ 0 \\ 0 \end{bmatrix} = \begin{bmatrix} U \\ \bar{U}' \\ 0 \\ 0 \end{bmatrix} \quad (K.12)$$

In order for the above equations to be satisfied c_5 , c_6 , c_7 and c_8 must be zero. Therefore, it is necessary to generate only four independent homogeneous solutions. The constants, $c_1 - c_4$, are determined once $F_{H_1} - F_{H_4}$ and F_p have been integrated to $y = 0$, by satisfying the boundary conditions at $y = 0$.

The K- ϵ Model equations (3.72)-(3.77.2) was solved using the same technique outlined above. The K- ϵ Model requires the solution of an eighth order complex differential equation which is then converted into a sixteenth order real system. This is achieved by splitting the stream function, F , the kinetic energy, \hat{k} , and the dissipation rate, $\hat{\epsilon}$, into real and imaginary parts and introducing the following variables:

$$\begin{array}{ll}
\phi_1 = F_R & \phi_9 = F_I \\
\phi_2 = F'_R & \phi_{10} = F'_I \\
\phi_3 = F''_R & \phi_{11} = F''_I \\
\phi_4 = F'''_R & \phi_{12} = F'''_I \\
\phi_5 = \hat{k}_R & \phi_{13} = \hat{k}_I \\
\phi_6 = \hat{k}'_R & \phi_{14} = \hat{k}'_I \\
\phi_7 = \hat{\varepsilon}_R & \phi_{15} = \hat{\varepsilon}_I \\
\phi_8 = \hat{\varepsilon}'_R & \phi_{16} = \hat{\varepsilon}'_I
\end{array} \tag{K.13}$$

The K- ε Model equations (3.13), (3.72) and (3.73) can be organized in a similar manner to equation (K-3)

$$\begin{aligned}
F'''' &= a_0(y)F + a_1(y)F' + a_2(y)F'' + a_3F'''' \\
&+ a_4(y)\hat{k} + a_5(y)\hat{k}' + a_6(y)\hat{\varepsilon} + a_7(y)\hat{\varepsilon}' + g \quad , \tag{K.14}
\end{aligned}$$

$$\begin{aligned}
k'' &= b_0(y)F + b_1(y)F' + b_4(y)\hat{k} + b_5(y)\hat{k}' \\
&+ b_6(y)\hat{\varepsilon} + b_7(y)\hat{\varepsilon}' + f \quad , \tag{K.15}
\end{aligned}$$

$$\begin{aligned}
\varepsilon'' &= c_0(y)F + c_1(y)F' + c_4(y)\hat{k} + c_5(y)\hat{k}' \\
&+ c_6(y)\hat{\varepsilon} + c_7(y)\hat{\varepsilon}' + h \quad , \tag{K.16}
\end{aligned}$$

where the $a_i(y)$, $b_i(y)$ and $c_i(y)$ are the complex coefficients such that

$$F_I = \begin{bmatrix} 0 & 0 & 0 & 0 & 0 & 0 & 0 & 0 \\ 0 & 0 & 0 & 0 & 0 & 0 & 0 & 0 \\ 0 & 0 & 0 & 0 & 0 & 0 & 0 & 0 \\ a_{0I} & a_{1I} & a_{2I} & a_{3I} & a_{4I} & a_{5I} & a_{6I} & a_{7I} \\ 0 & 0 & 0 & 0 & 0 & 0 & 0 & 0 \\ b_{0I} & b_{1I} & 0 & 0 & b_{4I} & b_{5I} & b_{6I} & b_{7I} \\ 0 & 0 & 0 & 0 & 0 & 0 & 0 & 0 \\ c_{0I} & c_{1I} & 0 & 0 & c_{4I} & c_{5I} & c_{6I} & c_{7I} \end{bmatrix} \quad (\text{K.20})$$

The boundary conditions at $y = 0$ cannot be applied directly since equations (K.15) and (K.16) are singular. Therefore, this boundary condition is applied at a small distance, $y = \delta_d$, from the wave surface. In order to apply the boundary condition a Taylor series approximation is made:

$$F - \frac{\delta_d F'}{2} = 0, \quad F' - \delta_d F'' = 0 \quad \text{at } y = \delta_d$$

$$\hat{k} - \frac{\delta_d \hat{k}'}{2} = 0, \quad \hat{\varepsilon} - \frac{\delta_d \hat{\varepsilon}'}{2} = 0 \quad (\text{K.21})$$

$$F = \bar{U}, \quad F' = \bar{U}', \quad \hat{k} = 0, \quad \hat{\varepsilon} = 0 \quad \text{at large } y. \quad (\text{K.22})$$

In matrix notation the conditions at $y = y_\infty$ are,

$$\begin{bmatrix} A_R & -A_I \\ A_I & A_R \end{bmatrix} \begin{bmatrix} \phi_1 \\ \vdots \\ \phi_{16} \end{bmatrix} = \begin{bmatrix} \bar{U} \\ \bar{U}' \\ \vdots \\ 0 \end{bmatrix} \quad (\text{K.23})$$

where

$$A_R = \begin{bmatrix} 1 & 0 & 0 & 0 & 0 & 0 & 0 & 0 \\ 0 & 1 & 0 & 0 & 0 & 0 & 0 & 0 \\ 0 & 0 & 0 & 0 & 1 & 0 & 0 & 0 \\ 0 & 0 & 0 & 0 & 0 & 0 & 1 & 0 \end{bmatrix}, \tag{K.24}$$

$$A_I = \begin{bmatrix} 0 & \dots & 0 & \dots & 0 \\ 0 & \dots & 0 & \dots & 0 \\ 0 & \dots & 0 & \dots & 0 \\ 0 & \dots & 0 & \dots & 0 \end{bmatrix}, \tag{K.25}$$

and at $y = \delta_d$,

$$\begin{bmatrix} B_R & -B_I \\ B_I & B_R \end{bmatrix} \begin{bmatrix} \phi_1 \\ \vdots \\ \vdots \\ \phi_{16} \end{bmatrix} = \begin{bmatrix} 0 \\ \vdots \\ \vdots \\ \vdots \\ 0 \end{bmatrix}, \tag{K.26}$$

$$B_R = \begin{bmatrix} 1 & -\frac{\delta_d}{2} & 0 & 0 & 0 & 0 & 0 & 0 \\ 0 & 1 & -\delta_d & 0 & 0 & 0 & 0 & 0 \\ 0 & 0 & 0 & 0 & 1 & -\frac{\delta_d}{2} & 0 & 0 \\ 0 & 0 & 0 & 0 & 0 & 1 & -\frac{\delta_d}{2} & 0 \end{bmatrix} \tag{K.27}$$

$$B_I = \begin{bmatrix} 0 & \dots & 0 & \dots & 0 \\ \vdots & & \vdots & & \vdots \\ \vdots & & \vdots & & \vdots \\ \vdots & & \vdots & & \vdots \\ 0 & \dots & 0 & \dots & 0 \end{bmatrix} \tag{K.28}$$

The required solution to equations (K.18)-(K.28) is obtained by generating a particular solution and eight homogeneous solutions. The particular solution is chosen to satisfy the known boundary conditions at y_{∞} . The initial vectors needed to generate the eight homogeneous solutions are obtained in a similar manner described for equation (K.5).

APPENDIX L

RELATIONSHIP BETWEEN TURBULENT ENERGY
AND VELOCITY GRADIENT AT THE WAVE SURFACE

In this appendix the wave induced kinetic energy is related to the root mean square level of the fluctuating velocity gradient, $\sqrt{s_x'^2} / \bar{s}_x$. All quantities are made dimensionless with wall parameters. The fluctuating velocity close to the wave surface is related to the fluctuating velocity gradient as

$$u' = \frac{s_x'}{\bar{s}_x} y. \quad (\text{L.1})$$

Therefore,

$$\sqrt{u'^2} = \frac{\sqrt{s_x'^2}}{\bar{s}_x} y \quad (\text{L.2})$$

where

$$\overline{u'^2} = -R_{xx}. \quad (\text{L.3})$$

Now R_{xx} can be decomposed into a wave averaged and fluctuating component

$$\overline{u'^2} = -(\bar{R}_{xx} + a \hat{r}_{xx} e^{i\alpha x}). \quad (\text{L.4})$$

Hence:

$$\sqrt{\overline{u'^2}} = (-\bar{R}_{xx})^{1/2} - \frac{a \hat{r}_{xx} e^{i\alpha x}}{(-\bar{R}_{xx})^{1/2}}, \quad (\text{L.5})$$

where $-\frac{a \hat{r}_{xx}}{2(-\bar{R}_{xx})^{1/2}} e^{i\alpha x}$ is the wave

induced component of, $y \sqrt{s_x'^2} / \bar{S}_x$. The turbulent kinetic energy K is related to $\overline{u'^2}$ as follows

$$K = \frac{\overline{u'^2} + \overline{v'^2} + \overline{w'^2}}{2} \quad (L.6)$$

Since $\frac{\overline{w'^2}}{2} < \frac{\overline{u'^2}}{2}$ and $\frac{\overline{v'^2}}{2} \ll \frac{\overline{u'^2}}{2}$ in the neighborhood of the wall

$$K = \frac{\overline{u'^2}}{2} \quad (L.7)$$

The turbulent kinetic energy can be written in terms of a wave averaged and fluctuating component as

$$K = \bar{K} + a \hat{k} e^{i\alpha x} \quad (L.8)$$

Therefore,

$$\sqrt{\overline{u'^2}} = 2^{1/2} \bar{K}^{1/2} + \frac{1}{2^{1/2} \bar{K}^{1/2}} \hat{k} a e^{i\alpha x} \quad (L.9)$$

Equations (L.5) and (L.9) gives the desired result.

$$a \hat{k} e^{i\alpha x} = \left(\frac{-\hat{r}_{xx}}{2(-\bar{R}_{xx})^{1/2}} \right) 2^{1/2} \bar{K}^{-1/2} a e^{i\alpha x} \quad (\text{L.10})$$

or

$$\text{Real} (a \hat{k} e^{i\alpha x}) = \left| \frac{-a \hat{r}_{xx}}{2(-\bar{R}_{xx})^{1/2}} \right| 2^{1/2} \bar{K}^{-1/2} \cos(\alpha x + \theta_K) \quad (\text{L.11})$$

where θ_k is the phase angle of the wave induced variation of

$$\sqrt{\frac{s_x^2}{\bar{S}_x}} .$$

NOMENCLATURE

a	Dimensionless wave amplitude
a_d	Wave amplitude (in.)
A	Van Driest parameter, see equation(3.47)
\bar{A}	Average value of Van Driest parameter.
\hat{A}	Complex function related to the wave induced component of the Van Driest Parameter, see equation (3.48.1)
A_e	Electrode area (cm^2)
C_1	Constant associated with K- ϵ Model defined in equation (3.62)
C_2	Constant associated with K- ϵ Model defined in equation (3.62)
C_3	Constant associated with K- ϵ Model defined in equation (3.64)
C_4	Constant associated with K- ϵ Model defined in equation (3.63.2)
C_μ	Constant associated with K- ϵ Model defined in equation (3.66)
C_b	Concentration of diffusing species in bulk (moles/liter)
D	Diffusion coefficient for mass (cm/sec)
D_m	Damping function, see equation (3.35)
f_d	Function associated with K- ϵ Model
f_o	Function associated with K- ϵ Model
F	Dimensionless complex function related to the wave induced stream function
F_a	Faradays constant (coulombs/equivalent)
h	Channal height (in.)
h_x	Dimensionless metric in the x direction
h_y	Dimensionless metric in the y direction
I	Cathode current (amps)
\hat{k}	Dimensionless complex function related to the wave induced turbulent kinetic energy

k_1, k_2	Coefficients defined in equation (3.47)
k_L	Lag parameter defined in equation (3.53)
k_R	Lag parameter defined in equation (3.56)
k_c	Lag parameter defined in equation (3.82)
K	Dimensionless turbulent kinetic energy
\bar{K}	Dimensionless wave averaged turbulent kinetic energy
K_m	Mass transfer coefficient defined in equation (4.1)
ℓ	Dimensionless mixing length; modified for streamline curvature
$\hat{\ell}$	Dimensionless complex function related to the wave induced mixing length; modified for curvature
ℓ_o	Dimensionless plane shear mixing length
$\hat{\ell}_o$	Dimensionless complex function related to the wave induced plane shear mixing length
L_e	Equivalent length of electrode (cm.)
n_e	Number of electrons transferred in reaction
p	Dimensionless instantaneous pressure
p'	Dimensionless fluctuating pressure
\hat{p}	Dimensionless complex function related to the wave induced pressure
P	Dimensionless time averaged pressure
$\frac{\partial P}{\partial x}$	Dimensionless value of pressure gradient in x direction
$\overline{\frac{\partial P}{\partial x}}$	Dimensionless average value of pressure gradient in x direction
$\frac{\partial P}{\partial y}$	Dimensionless value of pressure gradient in y direction
$\overline{\frac{\partial P}{\partial y}}$	Dimensionless average value of pressure gradient in y direction
q^2	Dimensionless trace of Reynolds stress tensor
\hat{r}_{ij}	Dimensionless function related to the wave induced components of the turbulent stress tensor

R_{ij}	Dimensionless components of the turbulent stress tensor
\overline{R}_{ij}	Dimensionless average components of the turbulent stress tensor
R_c	Dimensionless radius of curvature of streamlines
Re	Channel Reynolds number based on U_b and channel half width
R_f	Feedback resistance (ohms.)
R_{i_c}	Dimensionless curvature Richardson number defined on equation (3.80)
\hat{R}_{i_c}	Dimensionless complex function associated with the wave induced Richardson number
R	Dimensionless composite term representing turbulent stress terms, see equation (3.14)
s_x	Dimensionless fluctuating component of velocity gradient at the wall
\hat{s}_{ij}	Dimensionless complex function related to the wave induced rate of stress tensor
S_{ij}	Dimensionless components of the rate of strain tensor
\overline{S}_{ij}	Dimensionless average rate of strain
S_x	Dimensionless velocity gradient at the wall
\overline{S}_x	Dimensionless wave averaged velocity gradient at the wall
u	Dimensionless instantaneous velocity in x direction
u'	Dimensionless fluctuating component of turbulent velocity in x direction
\hat{u}	Dimensionless complex function related to the wave induced velocity in the x direction
u^*	Friction velocity (ft/sec)
U	Dimensionless time averaged velocity in the x direction
\overline{U}	Dimensionless wave averaged velocity in the x direction
U_b	Bulk average channel velocity (cm/sec)
V	Dimensionless instantaneous velocity in the y direction

v'	Dimensionless fluctuating component of turbulent velocity in the y direction
\hat{v}	Dimensionless complex function related to the wave induced velocity in the y direction
V	Dimensionless time averaged velocity in the y direction
V_{app}	Applied voltage (volts)
V_o	Instantaneous measured voltage (volts)
x	Dimensionless boundary layer coordinate along wave
y	Dimensionless boundary layer coordinate perpendicular to wave

Greek

α	Dimensionless wave number
β_c	Coefficient defined in equation (3.80)
γ	Coefficient defined in equation (3.91)
δ	Boundary layer thickness
δ_d	Small distance from wave surface defined in equation (3.78.1)
$\hat{\epsilon}$	Dimensionless complex function associated with wave induced turbulent dissipation rate
ϵ	Dimensionless turbulent dissipation rate
$\bar{\epsilon}$	Dimensionless average turbulent dissipation rate
θ	Phase angle ($^\circ$)
κ	Curvature of wave surface
κ	Von Karman constant used in equations (3.35), (3.41), (3.43), (3.50), (3.58), (3.71), (3.86) and (3.89)
λ	Wave length (in.)
μ	Viscosity of fluid (poise)
ν	Kinematic viscosity (cm^2/sec)

ν_t	Turbulent viscosity (cm^2/sec)
$\hat{\nu}_t$	Complex function related to the wave induced turbulent viscosity (cm/sec)
$\bar{\nu}_t$	Average turbulent viscosity (cm/sec)
Π	Coefficient defined in equation (3.89)
ρ	Density of fluid (gm/cm^3)
τ	Dimensionless shear stress
$\hat{\tau}$	Dimensionless complex function related to the wave induced shear stress
$\bar{\tau}$	Dimensionless wave averaged shear stress
τ_w	Dimensionless wall shear stress
$\bar{\tau}_w$	Dimensionless wave averaged wall shear stress
τ'_x	Dimensionless fluctuating shear stress in x direction
τ_{wd}	Instantaneous wall shear stress (dynes/cm^2)
$\bar{\tau}_{wd}$	Time averaged wall shear stress (dynes/cm^2)
τ'_{xd}	Fluctuating component of turbulent shear stress in the x direction (dynes/cm^2)
ψ	Dimensionless stream function

REFERENCES

1. Abrams, J. (1979), "A Nonlinear Boundary Layer Analysis for Turbulent Flow Over a Solid Wavy Surface," M.S. Thesis, Department of Chemical Engineering, University of Illinois, Urbana.
2. Abrams, J., Frederick, K. A. and Hanratty, T. J. (1981), "Interaction Between a Trubulent Flow and a Wavy Surface," presented at National Meeting of the A.I.Ch.E., Det oit, Michigan; to be published in Physico Chemical Hydrodynamics.
3. Anderson, P. S., Kays, W. M. and Moffat, R. J. (1972), "The Turbulent Boundary Layer on a Porous Plate: An Experimental Study of the Fluid Mechanics for Adverse Free-Stream Pressure Gradients," Stanford University, Thermosc. Div. Rep. HMT-15.
4. Badri Narayanan, M. A. and Ramjee, V. (1968), "On the Criteria for Reverse Transition in a Two Dimensional Boundary Layer Flow," India Inst. Sci. Rep. AE68FMI.
5. Bellman, R. E. and Kalaba, R. E. (1965), "Quasilinearization and Nonlinear Boundary Value Problems," Elsevier, New York.
6. Benjamin, T. B. (1959), "Shearing flow over a wavy boundary" J. Fluid Mech., 6, 161.
7. Bradshaw, P. (1969), "The analogy between streamline curvature and buoyancy in turbulent shear flow," J. Fluid, Mech., 36, 177.
8. Bradshaw, P. (1973), "Effects of Streamline Curvature on Turbulent Flow," AGARDograph., No. 169.
9. Buckles, J. J. (1983), "Turbulent Separated Flow Over Wavy Surfaces," Ph.D., Thesis, Department of Chemical Engineering, University of Illinois, Urbana.
10. Caponi, E. A., Fornberg, B., Knight, D. D., Mclean, J. W., Saffman, P. G. and Yuen, H. C. (1982), "Calculations of laminar viscous flow over a moving wavy surface," J. Fluid. Mech., 124, 347.
11. Cary, A. M., Jr., Weinstein, L. M. and Bushnell, D. M. (1980), "Drag reduction characteristics of small amplitude rigid surface waves," in Viscous Flow Drag Reduction (ed. by G. R. Hough), Amer. Inst. Aero. Astro., New York, 144.
12. Cebeci, T. and Smith, A. M. O. (1974), Analysis of Turbulent Boundary Layers, Academic Press, New York, New York.

13. Chien, K. Y. (1980), "Prediction of channel and boundary layer flows with a low Reynolds number two-equation model of turbulence," AIAA Paper, 80-034.
14. Conte, S. D. (1966), "The Numerical Solution of Linear Boundary Value Problems," SIAM Review, 8, 309.
15. Cook, G. W. (1970), "Turbulent Flow Over Solid Wavy Surfaces," Ph.D. Thesis, Department of Chemical Engineering, University of Illinois, Urbana.
16. Davis, R. E. (1972), "On the Prediction of Turbulent Flow Over a Wavy Boundary," J. Fluid Mech., 52, 287.
17. Davey, A. (1973), "A Simple Numerical Method for Solving Orr-Sommerfeld Problems," Quatt. J. Mech. Appl. Math, 26, 401.
18. Ellis, L. B. and Joubert, P. N. (1974), "Turbulent shear flow in a curved duct," J. Fluid Mech., 62, 54.
19. Eskinazi, S. and Yeh, H. (1956), "An Investigation of Fully Developed Turbulent Flows in a Curved Channel," J. of Aero Science, Vol. 23, No. 1.
20. Fox, L. (1980), "Numerical Methods for Boundary Value Problems," in Computation Techniques for Ordinary Differential Equations," edited by Gladwell, I. and Sayers, D. K., Academic Press Inc., New York, New York.
21. Frederick, K. A. (1982), "Wave Generation At a Gas-Liquid Interface," M.S. Thesis, Department of Chemical Engineering, University of Illinois, Urbana.
22. Gersting, J. M. and Jankowski, D. F. (1972), "Numerical Methods for Orr-Sommerfeld Problems," Int. J. Num. Methods in Eng., 4, 195.
23. Gersting, J. M. (1977), "Numerical Methods for Eigensystems: the Orr-Sommerfeld Problem," Comp. Maths. Applics., 3, 47.
24. Gillis, C. J., Johnston, J. P., Kays, W. M. and Moffat, R. J. (1980), "Turbulent Boundary Layer On A Convex, Curved Surface," Stanford University Thermosc. Div. Rep. HMT-31.
25. Godunov, S. (1961), "On the Numerical Solution of Boundary-Value Problems for Systems of Linear Ordinary Differential Equations." Uspekhi Mat. Nauk, 16, 171.
26. Hsu, S. and Kennedy, J. F. (1971), "Turbulent flow in wavy pipes," J. Fluid Mech., 47, 481.

27. Hussain, A. K. M. F. and Reynolds, W. C. (1970), "The Mechanics of a Perturbation Wave in Turbulent Shear Flow," Stanford University, Thermosc. Div. Rep. FM-6.
28. Jones, W. P. (1967), "Strongly Accelerated Turbulent Boundary Layers," M.Sc. Thesis, Imperial College.
29. Jones, W. P. and Launder, B. E. (1972), "The Prediction of Laminarization With A Two-Equation Model of Turbulence," Int. J. Heat Mass Transfer., 15, 301.
30. Jones, W. P. and Launder, B. E. (1972), "Some properties of sink flow turbulent boundary layers." J. Fluid Mech., 38, 817.
31. Jones, W. P. and Launder B. E. (1973), "The Calculation of Low-Reynolds-Number Phenomena With A Two-Equation Model of Turbulence," Int. J. Heat Mass Transfer., 16, 1119.
32. Julien, H. L., Kays, W. M., and Moffat, R. J. (1969), "The Turbulent Boundary Layer over a Porous Plate: Experimental Hydrodynamics of Favorable Pressure Gradient Flows," Stanford University, Thermosc. Div. Rep. HMT-4.
33. Kays, W. M. and Moffat, R. J. (1975), "Behavior and Transpired Turbulent Boundary Layers," in, "Studies in Convection," edited by Launder, B. E., Academic Press Inc., New York, New York.
34. Kendall, J. M. (1970), "The turbulent boundary layer over a wall with progressive surface waves," J. Fluid Mech., 41, 259.
35. Langley Field, (1981), Private communication.
36. Larras, J. and Claria, A. (1960), "Recherches en soufflène sur l'action relative de la houle et du vent," La Houille Blanche, 6, 674.
37. Launder, B. E. and Stinchcombe, H. S. (1967), "Sink Flow Turbulent Boundary Layers," Imperial College, Mech. Engng. Dept. Rep. TWF/TN/21.
38. Launder, B. E. and Jones, W. P. (1968), "On the prediction of Laminarization," presented at a meeting of the ARC Heat and Mass Transfer Sub - Committee, April 5, 1968.
39. Launder, B. E. and Jones, W. P. (1969), "Sink-Flow Turbulent Boundary Layers," J. Fluid Mech., 38, 817.
40. Launder, B. E., Pridden, C. H. and Sharma, B. I. (1977), "The Calculation of Turbulent Boundary Layers on Spinning and Curved Surfaces," J. Fluids Eng., 99, 237.
41. Lightfoot, E. J. (1983), Private communication.

42. Loyd, R. J., Moffat, R. J. and Kays, W. M. (1970), "The Turbulent Boundary Layer on a Porous Plate: An Experimental Study of the Fluid Dynamics with Strong Favorable Pressure Gradients and Blowing," Stanford University Thermosc. Div. Rep. HMT-13.
43. Lucas, T. R. and Reddisen, G. W. (1972), "Some Collocation Methods for Nonlinear Boundary Value Problems," SIAM Journal on Numerical Analysis, 9, 341.
44. Markatos, N. C. G. (1978), "Heat Mass and Momentum Transfer Across a Wavy Boundary," Comp. Meth. Appl. Mech. Eng., 14, 323.
45. Mclean, J. W. (1983), "Computation of turbulent flow over a moving wavy boundary," Phys. Fluids, 26, 2065.
46. Miles, J. W. (1959), "On the generation of surface waves by shear flows," J. Fluid Mech., 38, 181.
47. Mitchell, J. E., and Hanratty, T. J. (1966), "A Study of turbulence at a wall using an electrochemical wall shear-stress meter," J. Fluid. Mech., 26, 199.
48. Morrisroe, P. E. (1970), "Flow Over Solid Wavy Surfaces," M.S. Thesis, Department of Chemical Engineering University of Illinois, Urbana.
49. Motzfield, H. (1937), "Die Turbulente Strömung on welligen Wänden," Z. angew. Math. Mech., 17, 193.
50. Na, T. Y. (1979), "Computational Methods in Engineering Boundary Value Problems," Academic Press Inc., New York, New York.
51. Ng, B. S. and Reid, W. H. (1979), "An Initial Value Method for Eigenvalue Problems Using Compound Matricies." J. Comput. Phys., 30, 12S.
52. Ortega, J. M. and Poole, G. P. (1981), "An Introduction to Numerical Methods for Differential Equations," Pitman Publishing Inc., Marshfield Massachusetts.
53. Patankar, S. V. and Spalding, D. B. (1967), "Heat and Mass Transfer in Boundary Layers," Morgan-Grampian Press, London.
54. Patel, V. C., Rodi, W., Scheuerer, G. (1983), "Evaluation of Turbulence Models for Near-Wall and Low-Reynolds Number Flows," Subm. to AIAA-J.
55. Prenter, P. (1975), "Splines and Variational Methods," Wiley, New York.
56. Ramaprian, B. R. and Shivaprasad, B. G. (1978), "The structure of turbulent boundary layers along mildly curved surfaces," J. Fluid Mech., 85, 273.

57. Ramaprian, B. R. and Shivaprasad, B. G. (1982), "The instantaneous structure of mildly curved turbulent boundary layer." J. Fluid Mech., 115, 39.
58. Reis, L. P. (1960), "Mass Transfer to Small Sections of a Pipe Wall," M. S. Thesis, Department of Chemical Engineering, University of Illinois, Urbana.
59. Reynolds, W. C. (1974), "Recent advances in the computation of turbulent flows," Adv. Chem. Eng., 9, 193.
60. Reynolds, W. C. (1976), "Computation of turbulent flows," Annual Rev. Fluid Mech., 8, 183.
61. Russel, R. (1977), "A Comparison of Collocation and Finite Differences for Two-Point Boundary Value Problems," SIAM Journal on Numerical Analysis, 14, 19.
62. Scott, M. R. and Watts, H. A., (1975) "Support a Computer Code for Two-Point Boundary-Value Problems via Orthonormalization," Rep. Sand. 75-0198, Sandia Labs., Albuquerque, NM.
63. Scott, M. R. and Watts, H. A. (1977), "Computational Solution of Linear Two-Point Boundary Value Problems via Orthonormalization," SIAM Journal on Numerical Analysis, 14, 40.
64. Scott, M. R. (1981), Private communication.
65. Sigal, A. (1970), "An Experimental Investigation of the Turbulent Boundary Layer over a Wavy Wall," Ph.D. Thesis, Department of Aeronautical Engineering, California Institute of Technology.
66. So, R. M. C. and Mellor, G. L. (1973), "Experiment on convex curvature effects in turbulent boundary layers," J. Fluid Mech., 60, 43.
67. Stewart, G. W. (1973), "Introduction to Matrix Computations," Academic Press, New York.
68. Strang, G. and Fix, G. (1973), "An Analysis of the Finite Element Method," Prentice-Hall, Englewood Cliffs, N.J.
69. Tennekes, H. and Lumley, J. L. (1973), "A First Course in Turbulence," The MIT Press, Cambridge, Massachusetts.
70. Thorsness, C. B. (1975), "Transport Phenomena Associated with Flow Over a Solid Wavy Surface." Ph.D. Thesis, Department of Chemical Engineering, University of Illinois, Urbana.
71. Thorsness, C. B., Morrisroe, P. E. and Hanratty, T. J. (1978), "A Comparison of Linear Theory with Measurements of the Variation of Shear Stress Along a Solid Wave." Chemical Engineering Science, 33, 579.

72. Townsend, A. A. (1972), "Flow in a deep turbulent boundary layer over a surface distorted by water waves," J. Fluid Mech. 55, 719.
73. Van Driest, E. R. (1957), "On turbulent flow near a wall," J. Aero. Sci., 73, 1007.
74. Villadsen, J. and Michelsen, M. L. (1978), "Solution of Differential Equation Models by Polynomial Approximation," Prentice Hall, International series in the physical and chemical engineering sciences.
75. Watts, A., Scott, M. R. and Lord, M. E. (1979), "Solving Complex Valued Differential Systems," Rep. Sand. 75-1501, Sandia Labs., Albuquerque, N.M.
76. Zagustin, K., Hsu, F. Y., Street, R. L., and Perry, B. (1966), "Flow over a Moving Boundary in Relation to Wind-Generated Waves," Technical Report No. 60, Department of Civil Engineering, Stanford University.
77. Zilker, D. P. (1976), "Flow Over Wavy Surfaces," Ph.D. Thesis, Department of Chemical Engineering, University of Illinois, Urbana.
78. Zilker, D. P., Cook, G. W. and Hanratty, T. J. (1977), "Influence of the amplitude of a solid wavy wall on a turbulent flow. Part 1, Non-Separated flows." J. Fluid Mech., 82, 29.
79. Zilker, D. P. and Hanratty, T. J. (1979), "Influence of the amplitude of a solid wavy wall on a turbulent plate. Part 2. Separated Flows," J. Fluid Mech., 90, 257.

Distribution List

Professor W. W. Willmarth
The University of Michigan
Department of Aerospace Engineering
Ann Arbor, MI 48109

Office of Naval Research
Code 481
800 N. Quincy Street
Arlington, VA 22217

Professor Richard W. Miksad
The University of Texas at Austin
Department of Civil Engineering
Austin, TX 78712

Professor Stanley Corrsin
The Johns Hopkins University
Department of Mechanics and
Materials Sciences
Baltimore, MD 21218

Professor Paul Lieber
University of California
Department of Mechanical Engineering
Berkeley, CA 94720

Professor P. S. Virk
Massachusetts Institute of Technology
Department of Chemical Engineering
Cambridge, MA 02139

Professor E. Mollo-Christensen
Massachusetts Institute of Technology
Department of Meteorology
Room 54-1722
Cambridge, MA 02139

Professor Patrick Leehey
Massachusetts Institute of Technology
Department of Ocean Engineering
Cambridge, MA 02139

Professor Eli Reshotko
Case Western Reserve University
Department of Mechanical and
Aerospace Engineering
Cleveland, OH 44106

Professor S. I. Pai
University of Maryland
Institute of Fluid Dynamics
and Applied Mathematics
College Park, MD 20742

Computation and Analyses Laboratory
Naval Surface Weapons Center
Dahlgren Laboratory
Dahlgren, VA 2218

Dr. Robert H. Krichnan
Dublin, NH 03444

Professor Robert E. Falco
Michigan State University
Department of Mechanical Engineering
East Lansing, MI 48824

Professor E. Run Lindgren
University of Florida
Department of Engineering Sciences
231 Aerospace Engineering Building
Gainesville, FL 32611

Mr. Dennis Bushnell
NASA Langley Research Center
Langley Station
Hampton, VA 23365

Dr. A. K. M. Faz Hussain
University of Houston
Department of Mechanical Engineering
Houston, TX 77004

Professor John L. Lumley
Cornell University
Sibley School of Mechanical
and Aerospace Engineering
Ithaca, NY 14853

Professor K. E. Shuler
University of California, San Diego
Department of Chemistry
La Jolla, CA 92093

Dr. E. W. Montroll
Physical Dynamics, Inc.
P. O. Box 556
La Jolla, CA 92038

Librarian Station 5-2
Coast Guard Headquarters
NASSIF Building
400 Seventh Street, SW
Washington, DC 20591

Library of Congress
Science and Technology Division
Washington, DC 20540

Dr. A. L. Slafkosky
Scientific Advisor
Commandant of the Marine Corps
Code AX
Washington, DC 20380

Maritime Administration
Office of Maritime Technology
14th & E Streets, NW
Washington, DC 20230

Maritime Administration
Division of Naval Architecture
14th & E Streets, NW
Washington, DC 20230

Dr. G. Kulin
National Bureau of Standards
Mechanics Section
Washington, DC 20234

Naval Research Laboratory
Code 2627
Washington, DC 20375 6 copies

Library
Naval Sea Systems Command
Code 09GS
Washington, DC 20362

Mr. Thomas E. Peirce
Naval Sea Systems Command
Code 03512
Washington, DC 20362

Dr. Gary Chapman
Ames Research Center
Mail Stop 227-4
Moffett Field, CA 94035

Dr. Louis Schmidt
Assistant for Engineering Technology
Assistant Secretary of the Navy (RE&S)
Department of Navy
Washington, D.C. 20310

Mr. Stanley W. Doroff
Mechanical Technology, Inc.
2731 Prosperit Avenue
Fairfax, VA 2031

Dr. Charles Watkins
Head, Mechanical Engineering Department
Howard University
Washington, DC 20059

Dr. Denny R. S. Ko
Dynamics Technology, Inc.
22939 Hawthorne Boulevard, Suite 200
Torrance, CA 90505

Professor Thoma J. Hanratty
University of Illinois at Urbana-
Champaign
Department of Chemical Engineering
205 Roger Adams Laboratory
Urbana, IL 61801

Air Force Office of Scientific
Research/NA
Building 410
Bolling AFB
Washington, DC 20332

Professor Hsien-Ping Pao
The Catholic University of America
Department of Civil Engineering
Washington, DC 20064

Dr. Phillip S. Klebanoff
National Bureau of Standards
Mechanics Section
Washington, DC 20234

Dr. G. Kulin
National Bureau of Standards
Mechanics Section
Washington, DC 20234

Dr. J. O. Elliot
Naval Research Laboratory
Code 8310
Washington, DC 20375

Mr. R. J. Hansen
Naval Research Laboratory
Code 8441
Washington, DC 20375

Library
Naval Weapons Center
China Lake, CA 93555

Technical Library
Naval Surface Weapons Center
Dahlgren Laboratory
Dahlgren, VA 22418

Technical Documents Center
Army Mobility Equipment Research Center
Building 315
Fort Belvoir, VA 22060

Technical Library
Webb Institute of Naval Architecture
Glen Cove, NY 11542

Dr. J. P. Breslin
Stevens Institute of Technology
Davidson Laboratory
Castle Point Station
Hoboken, NJ 07030

Professor Louis Landweber
The University of Iowa
Institute of Hydraulic Research
Iowa City, IA 52242

R. E. Gibson Library
The Johns Hopkins University
Applied Physics Laboratory
Johns Hopkins Road
Laurel, MD 20810

Lorenz G. Straub Library
University of Minnesota
St. Anthony Falls Hydraulic Laboratory
Minneapolis, MN 55414

Library
Naval Postgraduate School
Monterey, CA 93940

Technical Library
Naval Underwater Systems Center
Newport, RI 02840

Engineering Societies Library
345 East 47th Street
New York, NY 10017

The Society of Naval Architects and
Marine Engineers
One World Trade Center, Suite 1369
New York, NY 10048

Technical Library
Naval Coastal System Laboratory
Panama City, FL 32401

Professor Theodore . Wu
California Institute of Technology
Engineering Science Department
Pasadena, CA 91125

Director
Office of Naval Research Western Regional
1030 E. Green Street Office
Pasadena, CA 91101

Technical Library
Naval Ship Engineering Center
Philadelphia Division
Philadelphia, PA 19112

Army Research Office
P. O. Box 12211
Research Triangle Park, NC 27709

Editor
Applied Mechanics Review
Southwest Research Institute
8500 Culebra Road
San Antonio, TX 78206

Technical Library
Naval Ocean Systems Center
San Diego, CA 92152

ONR Scientific Liaison Group
American Embassy - Room A-407
APO San Francisco 96503

Librarian
Naval Surface Weapons Center
White Oak Laboratory
Silver Spring, MD 20910

Defense Research and Development Attache
Australian Embassy
1601 Massachusetts Avenue, NW
Washington, DC 20036

Dr. Steven A. Orszag
Cambridge Hydrodynamics, Inc.
54 Baskin Road
Lexington, MA 02173

Professor Tuncer Cebeci
California State University
Mechanical Engineering Department
Long Beach, CA 90840

Dr. C. W. Hirt
University of California
Los Alamos Scientific Laboratory
P. O. Box 1663
Los Alamos, NM 87544

Professor Frederick K. Browand
University of Southern California
University Park
Department of Aerospace Engineering
Los Angeles, CA 90007

Professor John Laufer
University of Southern California
University Park
Department of Aerospace Engineering
Los Angeles, CA 90007

Professor T. R. Thomas
Teesside Polytechnic
Department of Mechanical Engineering
Middlesbrough TS1 3BA, England

Dr. Arthur B. Metzner
University of Delaware
Department of Chemical Engineering
Newark, DE 19711

Professor Harry E. Rauch
The Graduate School and University
Center of the City University of
New York
Graduate Center: 33 West 42 Street
New York, NY 10036

Mr. Norman M. Nilsen
Dyntec Company
5301 Laurel Canyon Blvd., Suite 201
North Hollywood, CA 91607

Professor L. Gary Leal
California Institute of Technology
Division of Chemistry and Chemical
Engineering
Pasadena, CA 91125

Professor H. W. Liepmann
California Institute of Technology
Graduate Aeronautical Laboratories
Pasadena, CA 91125

Professor A. Roshko
California Institute of Technology
Graduate Aeronautical Laboratories
Pasadena, CA 91125

Dr. Leslie M. Mack
Jet Propulsion Laboratory
California Institute of Technology
Pasadena, CA 91103

Professor K. M. Agrawal
Virginia State College
Department of Mathematics
Petersburg, VA 23803

Technical Library
Naval Missile Center
Point Mugu, CA 93041

Professor Francis R. Hama
Princeton University
Department of Mechanical and
Aerospace Engineering
Princeton, NJ 08540

Dr. Joseph H. Clarke
Brown University
Division of Engineering
Providence, RI 02912

Professor J. T. C. Liu
Brown University
Division of Engineering
Providence, RI 02912

Chief, Document Section
Redstone Scientific Information Center
Army Missile Command
Redstone Arsenal, AL 35809

Dr. Jack W. Hoyt
Naval Ocean Systems Center
Code 2501
San Diego, CA 92152

Professor Richard L. Pfeffer
Florida State University
Geophysical Fluid Dynamics Institute
Tallahassee, FL 32306

Defense Technical Information Center
Cameron Station
Alexandria, VA 22314 12 copies

Professor Bruce Johnson
U.S. Naval Academy
Engineering Department
Annapolis, MD 21402

Library
U.S. Naval Academy
Annapolis, MD 21402

Technical Library
David W. Taylor Naval Ship Research
and Development Center
Annapolis Laboratory
Annapolis, MD 21402

Professor C. -S. Yih
The University of Michigan
Department of Engineering Mechanics
Ann Arbor, MI 48109

Professor T. Francis Ogilvie
The University of Michigan
Department of Naval Architecture
and Marine Engineering
Ann Arbor, MI 48109

Office of Naval Research
Code 200B
800 N. Quincy Street
Arlington, VA 22217

Office of Naval Research
Code 438
800 N. Quincy Street
Arlington, VA 22217 3 copies

Office of Naval Research
Code 473
800 N. Quincy Street
Arlington, VA 22217

NASA Scientific and Technical
Information Facility
P. O. Box 8757
Baltimore/Washington International
Airport
Maryland 21240

Professor Paul . . . Naghdi
University of California
Department of Mechanical Engineering
Berkeley, CA 94720

Librarian
University of California
Department of Naval Architecture
Berkeley, CA 94720

Professor John V. Wehausen
University of California
Department of Naval Architecture
Berkeley, CA 94720

Library
David W. Taylor Naval Ship Research
and Development Center
Code 522.1
Bethesda, MD 20084

Mr. Justin H. McCarthy, Jr..
David W. Taylor Naval Ship Research
and Development Center
Code 1552
Bethesda, MD 20084

Dr. William B. Morgan
David W. Taylor Naval Ship Research
and Development Center
Code 1540
Bethesda, MD 20084

Director
Office of Naval Research Eastern/Central
Building 114, Section D Regional Office
666 Summer Street
Boston, MA 02210

U 211413